SCIENCE ▪ PASSION ▪ TECHNOLOGY

TU Graz

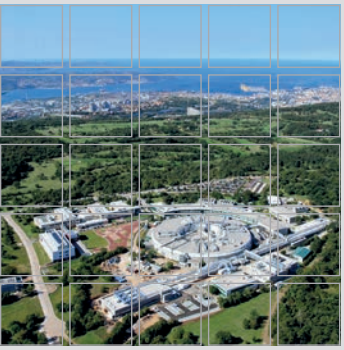
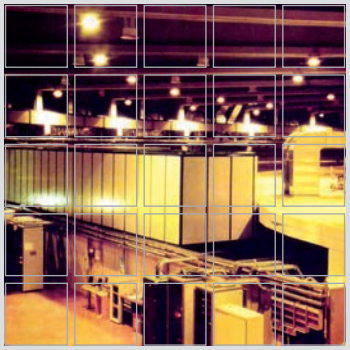
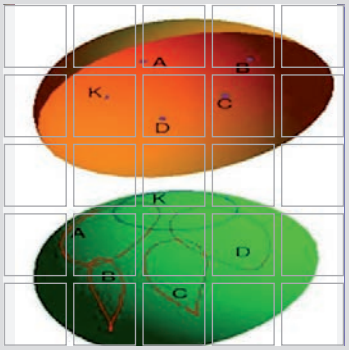
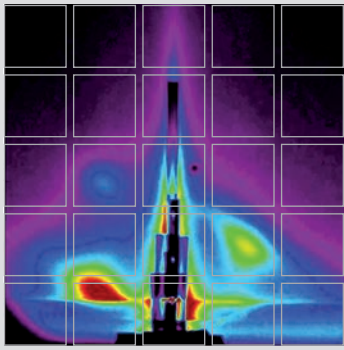

TCVB

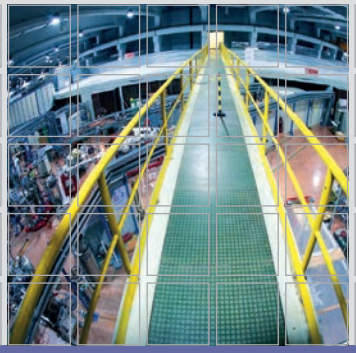
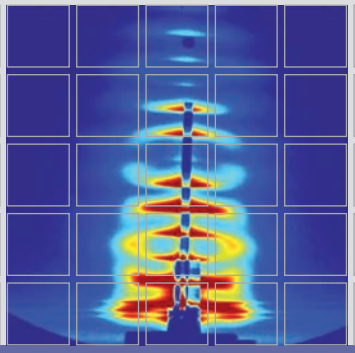
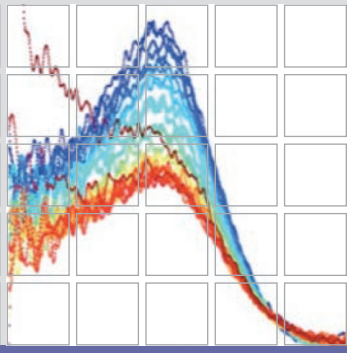

ANNUAL REPORT 2013

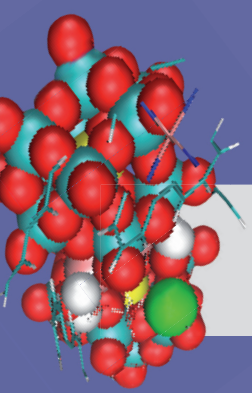

Austrian SAXS Beamline at Elettra Sincrotrone Trieste

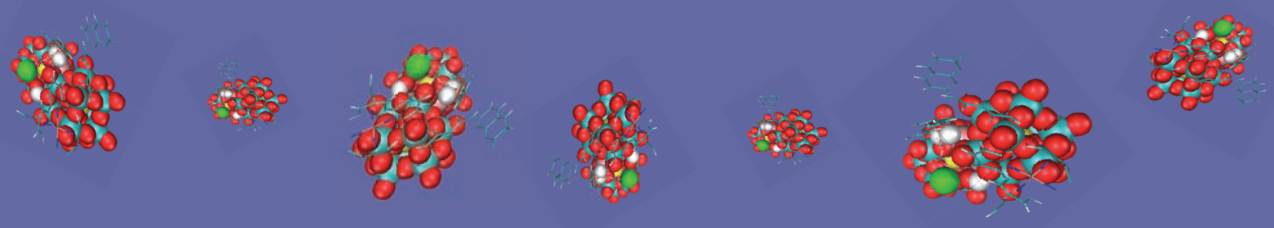

Austrian Small Angle X-ray Scattering (SAXS) Beamline at ELETTRA

Annual Report 2013

Compiled by Sigrid Bernstorff & Heinz Amenitsch

Cover pictures taken from the user contributions:

Z. Syrgiannis et al., pages 78-81 (front cover: background picture)

M. D'Acunto et al., pages 48-49 (front cover: middle-right up)
M. Buljan et al., pages 44-45 (front cover: right up)
M. Jerčinović et al., pages 55-56 (front cover: middle-right down)
M. Manno et al., pages 98-99 (front cover: right down)
L. Sapir et al., pages 102 (back cover: middle right up)
M. Jerčinović et al., pages 55-56 (back cover: right up)
A. Yaghmur et al., pages 106-107 (back cover: middle right down)
K.V. Sarathlal et al., pages 68-70 (back cover: right down)

Table of Contents

Preface

Frank Uhlig
Head of the Institute of Inorganic Chemistry *and*
Dean of the Faculty of Technical Chemistry,
Chemical & Process Engineering and Biotechnology
Graz University of Technology, Graz

2013 was the first full year for the Austrian Beamlines at ELETTRA as members of the Graz University of Technology (TU Graz). As mentioned last year on this place such a transfer carries its own opportunities, new environments, new colleagues, and thus new scientific challenges resulting finally into new projects. I´m proud to declare here that our team in Trieste handled all these new challenges highly motivated and highly committed leading to an ongoing and partially increasing high performance of our beamlines. We were able to initiate novel projects not only within our own university but also by attracting new partners from Austria and beyond.

CEO of ELETTRA-Sincrotrone Trieste Alfonso Franciosi, TU Graz Rector Harald Kainz, President of ELETTRA-Sincrotrone Trieste Carlo Rizzuto, Head of the Institut for Inorganic Chemistry of TU Graz Frank Uhlig, and Head of the outstation of TU Graz in Trieste Heinz Amenitsch (from right to left) at the handing over of the new Pilatus3 1M detector from Dectris (Nov 2013)

Also in 2013 as Graz University of Technology we are able to significantly increase the quality of the scientific equipment and hence the quality of the scientific output of the Austrian Beamlines at ELETTRA. The most visible sign for this was the solemn handover of the DECTRIS detector by our Rector Harald Kainz to our beamline team in November 2013.

On this occasion also the new formal agreements between our university and ELETTRA were signed transferring now also officially the responsibilities for the Austrian programs involving the SAXS and DXRL beamlines at Elettra to the Graz University of Technology.

President of ELETTRA-Sincrotrone Carlo Rizzuto and TU Graz Rector Harald Kainz (right to left) after signing the collaboration agreements between Elettra-Sincrotrone Trieste and Graz University of Technology in November 2013.

I want to thank especially our Italian partners at ELETTRA for their outstanding support during the process of finalizing the agreements. Nevertheless, within these negotiations we learned to understand and to respect each other in a much better way. As result, a further strengthening of our collaboration has been achieved also with the participation in the novel European Research Infrastructure Consortium CERIC-ERIC hosted by Italy. Together with the Czech Republic, Italy, Romania, Serbia and Slovenia, Austria is one of the founding members of this infrastructure consortium. Our Austrian commitment to CERIC-ERIC consists on one hand of the AUSTRIAN SAXS Beamline in Trieste and on the other hand of our light and X-ray scattering laboratories at the Institute for Inorganic Chemistry in Graz. In line with the traditions as well as the strategic goals of the Graz University of Technology the concentration of the available resources - coming with projects such as CERIC-ERIC - is the only way to further strengthen our research capabilities within the existing financial framework. Therefore in the upcoming years, we expect from CERIC-ERIC new impulses in the European scenery of infrastructures for science and technology, for us but as well also for our partners.

Alfonso Franciosi
President and Chief Executive Officer
Elettra-Sincrotrone Trieste S.C.p.A.

Elettra-Sincrotrone Trieste is delighted to have found a new and enthusiastic partner in the Technical University of Graz (TUG), as this activity report clearly shows. On November 21, 2013, new formal agreements between TUG and Elettra were signed transferring responsibility for the Austrian programs involving the SAXS and DXRL beamlines at Elettra from the Austrian Academy of Sciences to TUG. The impressive scientific production summarized in this report, the continued success of Austrian researchers in their beamtime applications at Elettra, with a success rate that almost doubles the average success rate, and the implementation of a new important joint venture, the Central European Research Infrastructure Consortium (CERIC-ERIC), testify both to the quality of Austrian science, and to the creativity and effectiveness of the TUG personnel at Elettra.

Last year the users of Elettra were able to take full advantage of the increase in machine stability and reproducibility resulting from the top-up operating mode, that was available for 97.1% of the user-dedicated beamtime. In particular, the increase in thermal stability of the different machine components deriving from the full-energy injection yielded a drastic reduction in component failures and the overall machine uptime reached 96.9%, the highest ever recorded at Elettra. The mean time between beam losses went from 45 to 60 hours.

The new x-ray fluorescence (XRF) beamline in collaboration with the International Atomic Energy Agency was opened to users in the Fall of 2014. The superconductive wiggler that is to provide photon energies up to 25 keV was successfully tested on the storage ring at high field (3.5 T) during top-up operation. The second diffraction beamline for structural biology (XRD2) and the new beamline for high pressure diffraction studies (XPRESS) - under construction in collaboration with the Indian Institute of Science in Bangalore - which will utilize the superconductive wiggler radiation are scheduled to be completed in February and April 2015, respectively. Together with the implementation of the XRF beamline in collaboration with the IAEA, they will substantially extend the range of facilities available to Elettra users.

A new branch-line designed to allow users to install their own experimental station has been implemented on the SuperESCA beamline. As a result of the approval of a long-term proposal by the peer-review panels, the surface physics group of the National Institute of Materials Physics from Magurele, Romania, a CERIC-ERIC partner, has installed on the SuperESCA branch-line an experimental station that includes a spin-resolved photoemission spectrometer, a scanning tunneling microscope and a molecular beam epitaxy chamber. This new experimental station will be accessible also to other user groups, substantially expanding the sample growth and characterization facilities available at SuperESCA.

A number of preliminary studies for a long-term upgrade of the Elettra light source have begun in 2014. The goal was to explore the technical feasibility of converting the existing storage ring to a minimum emittance source, provisionally designated as Elettra 2.0, that could be housed in the existing Elettra tunnel, utilizing the existing top-up capable injection system, and preserving as much as possible the source points of the existing beamlines, in order to minimize the required infrastructural changes and therefore minimize cost and installation time.

Our machine physicists and engineers have examined a numer of different technical solutions for the lattice of Elettra 2.0, from a 4-bend achromat to a 9-bend achromat, and our initial costs/benefits analysis made us tentatively select a 6-bend achromat lattice, that would allow us to achieve an emittance 250 pm, i.e., 28 times lower than the present Elettra emittance, and still utilize the existing injection system. These initial results were presented to our international Scientific Advisory Council (SAC) and Machine Advisory Committee (MAC), obtaining very positive reactions. In the next few months, our machine physicists and engineers will refine the initial analysis by defining the technical specifications and costs of the required new crucial components, while our beamline scientists, in collaboration with our key partners, will be developing a scientific case for Elettra 2.0. Our Austrian partners are already at work planning the doubling of the SAXS beamline and the upgrade of the beamline optics as an essential step to enable a full exploitation of the planned Elettra upgrade.

The implementation of the FERMI FEL facility has continued in 2013-2014 in three parallel directions: i) optimizing FEL-1 operation for external users; ii) commissioning of FEL-2 at shorter wavelengths; iii) increasing pump-probe capabilities and the number and range of applications of the FERMI beamlines.

In 2013 FERMI was in operation for 6136 hours, with 57% of the time devoted to LINAC and FEL *commissioning* and 43% of the time devoted to beamline *commissioning* and users' experiments. FEL-1 routinely achieved energies of several hundreds μJ/pulse and design specifications were achieved or surpassed throughout the operating wavelength range and down to the minimum design wavelength of 20 nm. Last year FERMI users could apply for beamtime on the EIS-TIMEX, DiProI and LDM experimental stations, while contruction continues for the EIS-TIMER, TeraFERMI and MagneDyn beamlines, which should gradually become operational in 2015-2016. A new hutch adjacent to the TeraFERMI hutch is also under construction to house the table-top laser sources and experimental stations of the T-ReX laboratory, which will be operated as a user facility complementary to FERMI.

Since the beginning of user operations 125 experimental proposals were received as a result of three calls for proposals. Some 40% of the proposals were submitted from Italian institution, while 60% came from some 14 additional countries. A total of 50 experiments were selected by the FERMI peer-review panel and received beamtime. Unfortunately, no proposals were received from Austrian institutions and we at Elettra look forward to expanding the scope of our collaboration with TUG to enhance Austrian participation in the exploitation of the unique scientific potential of FERMI.

The FEL resulted available for 85% of the planned users' beamtime, as compared to the original 50% target, highlighting the constant improvement in reliability that derived from the strict collaboration between machine physicists and internal and external user groups. New machine operating modes also derived from such a collaboration. As an example, two-color experiments have been perfomed using two FEL pulses generated by two seed laser pulses

spaced by a few hundred femtoseconds, with negligible time jitter and the undulators tuned at the same resonance. More recently a two-color, double resonance mode has been successfully tested, exploiting the modulator bandwidth with two seed laser pulses and tuning the two groups of radiators at two different resonances. This technique can be used with the two seed laser pulses separated by as much as 2% in wavelength. All this has been made possible by the unprecedented control obtained for the time jitter, of low as 7 fs, which is, to our knowledge, a world record for any operating FEL.

The commissioning of FEL-2 has continued, yielding high quality spectra at 14.4 and 10.8 nm with pulse energies of the order of 100 μJ. In March, photon wavelengths of 8.1 and 6.5 nm were produced with relatively high intensity. To achieve even shorter wavelegths the LINAC energy was increased to 1.5 GeV and in June laser emission at the minimum design wavelength of 4 nm in the first harmonic was produced, with several μJ of pulse energy. We expect FEL-2 to be open to users with the fourth call for proposals, to be issued by the end of 2014.

Some of the new strategic directions opening up for us and for our partners with the ongoing developments at Elettra and FERMI will be addressed by a number of thematic events, including the workshop: INTEGRATING TABLE-TOP LASER, SEEDED-FREE ELECTRON LASER AND STORAGE RING SOURCES FOR TIME-RESOLVED SPECTROSCOPIES (December 1-2), and two workshops that will take place in sequence as part of the XXII Elettra Users' Meeting: NOVEL SUPERCONDUCTORS AND SYNCHROTRON RADIATION (December 10-11), and ADVANCES IN X-RAY IMAGING (December 11-12). Such workshops will serve the purpose of engaging a broader user community, and our partner institutions will have prominent roles in the above events.

A new major institutional development involves directly Elettra-Sincrotrone Trieste and the Technical University of Graz. CERIC-ERIC, a European Research Infrastructure Consortium hosted by Italy, with statutory seat in Trieste and Elettra-Sincrotrone Trieste as a Representing Entity of Italy has been established through a Decision of the European Commission on June 24, 2014. Austria, the Czech Republic, Italy, Romania, Serbia and Slovenia are the initial participanting countries, while Croatia and Hungary are scheduled to join at a later date. CERIC-ERIC is a new European legal entity and a pan-european user facility that offers a common entry point and integrated services for international users, a single proposal evaluation system, free and open access by quality selection only, and will implement common support and logistic services as required, joint IPR and industrial policy, and joint educational and outreach activities across the different facilities. Two CERIC-ERIC calls for proposals have already been published, offering access to several of the Elettra beamlines, the Austrian SAXS and TU Graz Laboratories, the Czech Materials Science beamline and the Prague Laboratory, the Budapest Neutron Center, the TEM Magurele Laboratory in Romania, and the national Slovenian NMR Center.

The Chair of the General Assembly and Executive Director of CERIC-ERIC is Professor Carlo Rizzuto, who moved from being President of Elettra Sincrotrone Trieste to the stewardship of this new European Institution. Professor Giovanni Comelli, former Vice-President of Elettra-Sincrotrone Trieste, will now maintain relations between CERIC-ERIC and Elettra, in addition to serving as Vice-President of the Elettra Strategic Committee. We take this opportunity to thank both Carlo e Giovanni for the capital role they have had in creating and making Elettra-Sincrotrone Trieste a worldwide success and look forward to continuing the fruitful collaboration that we have maintained for the past 15 years.

We thank our Austrian partners at the Technical University of Graz for their professionalism and steady dedication over the years. We at Elettra look forward to expanding the scope and depth of our collaboration and exploring together the frontiers that the new upgraded Elettra, FERMI and CERIC-ERIC will open for all of us.

The SAXS Group

SCIENTISTS: Heinz Amenitsch [1)]

e-mail: amenitsch@elettra.eu

Sigrid Bernstorff [2)]

e-mail: bernstorff@elettra.eu

Benedetta Marmiroli [1)]

e-mail: benedetta.marmiroli@elettra.eu

Michael Rappolt [1)] (until 31.3.2013)

e-mail: michael.rappolt@elettra.eu

POST DOCS: Fernando Cacho [1)] (until 31.7.2013)

e-mail: fernando.cacho@elettra.eu

SCIENTIFIC ASSISTANT: Barbara Sartori [1)]

e-mail: barbara.sartori@elettra.eu

TECHNICIAN: Christian Morello [2)]

e-mail: christian.morello@elettra.eu

1) Until 30.9.2012: Institute for Biophysics and Nanosystems Research, Austrian Academy of Sciences, Schmiedlstraße 6, 8042 Graz, Austria

Since 1.10.2012: Institute of Inorganic Chemistry, Graz University of Technology, Faculty of Technical Chemistry, Chemical and Process Engineering, Biotechnology - TCVB, Stremayrgasse 9/IV, 8010 Graz, Austria
Tel 0043-316-873 32145
Fax 0043-316-873 32102
WEB: http://ac.tugraz.at

and: Institute Outstation c/o Elettra - Sincrotrone Trieste

2) Elettra - Sincrotrone Trieste, Strada Statale 14, km 163.5, 34149 Basovizza (TS), Italy
Tel 0039-040-375 8572
Fax 0039-040-938 0902
WEB: http://www.elettra.eu

The SAXS-Beamline in General

Small Angle X-ray Scattering has become a well known standard method to study the structure of various objects in the spatial range from 1 to 1000 Å, and therefore instruments capable to perform such experiments are installed at most of the synchrotron research centers. The high-flux SAXS beamline at ELETTRA is mainly intended for time-resolved studies on fast structural transitions in the sub-millisecond time region in solutions and partly ordered systems with a SAXS-resolution of 10 to 1400 Å in real-space.
The photon source is the 57-pole wiggler whose beam is shared and used simultaneously with a Macromolecular Crystallography beamline. The wiggler delivers a very intense radiation between 4 and 25 keV of which the SAXS-Beamline accepts 3 discrete energies, namely 5.4, 8 and 16 keV. The beamline optics consists of a flat double crystal monochromator and a double focusing toroidal mirror.
A versatile SAXS experimental station has been set-up, and an additional wide-angle X-ray scattering (WAXS) detector monitors simultaneously diffraction patterns in the range from 1 to 9 Å. The sample station is mounted move-able onto an optical table for optimising the sample detector distance with respect to SAXS resolution and sample size.
Besides the foreseen sample surrounding the users have the possibility to install their own specialised sample equipment. In the design phase, besides technical boundary conditions, user friendliness and reliability have been considered as important criteria.
The optimisation of the beamline with respect to high-flux and consequently high flux density, allows to perform the following experiments:

- Low Contrast Solution Scattering
- Grazing Incidence Scattering and Surface Diffraction
- Micro-Spot Scanning
- X-ray Fluorescence Analysis
- Time-Resolved Studies ≥ 11 μs
- Simultaneously Performed Small- and Wide-Angle Measurements (SWAXS) on:
    - Gels
    - Liquid Crystals
    - (Bio) Polymers
    - Amorphous Materials
    - Muscles

Furthermore, using 5.4 and 16 keV energies, the beamline is widely applicable also to very thin, e.g. single muscle fibers, and optically thick (high Z) specimen, as often used in e.g., material science and solid state physics.

THE INSERTION DEVICE

The wiggler for the SAXS beamline consists of three 1.5 m long segments, each having 19 poles. The device can work with a minimum gap of 20 mm, which corresponds to K=20 at 2 GeV. The main parameters of the wiggler are:

- Critical Energy 4.1 keV
- Radiation Power 8.6 kW
- Flux 3.5×10^{14} ph/s/mrad/0.1%BW (at 400 mA)

The wiggler radiation cone has a horizontal width of 9 mrad. From this the SAXS-beamline accepts vertically 0.3 mrad, and horizontally +/-0.5 mrad at a 1.25 mrad off-axis position. The resulting source size for 8 keV photons is 3.9 x 0.26 mm^2 (horiz. x vert.).

THE OPTICS

The optics common with the diffraction beamline consists of:

- C-Filter and Beryllium window assembly to reduce the power load on the first optical elements by a factor of 2 and to separate the beamline vacuum from the storage ring.
- Beam defining slit chamber which allows to define the SAXS beam on three sides before the monochromator in order to reduce the straylight in the downstream beamline sections.

The SAXS beamline optics consists of:

- A double-crystal monochromator consisting of four individual chambers, in which three interchangeable asymmetric Si(111) crystal pairs are used to select one of three fixed energies. Each of the crystal pairs is optimised for the corresponding energy to accomplish a grazing angle of 2°. The energy resolution $\Delta E/E$ of the monochromator is in the range of 0.7 - 2.5 10^{-3}.
- A baffle chamber after the monochromator is used as an adjustable straylight fenditure.
- A segmented toroidal mirror focuses the light in horizontal and vertical direction with a 1/2.5 magnification onto the SAXS-detector.
- An aperture slit reduces the straylight after the monochromator and the toroidal mirror.
- A guard slit defines the illuminated region around the focal spot. The spot size on the detector is 1.6 mm horizontally and 0.6 mm vertically. The calculated flux at the sample is in the order of 10^{13} ph/s at 400 mA. For a maximum sample size of 5.4 x 1.8 mm^2 correspondingly a flux density of 10^{12} ph/s/mm^2 has been calculated.

SAMPLE STAGE

The multipurpose sample stage allows to perform fast time-resolved relaxation studies based on temperature- or pressure-jumps as well as stopped flow experiments. Shear jump relaxation experiments are planned. Specifically, T-jumps can be induced by an infra-red light pulse (2 ms) from an Erbium-Glass laser, raising the temperature about 20 °C in an aqueous sample volume of 10 µl. A hydrostatic pressure cell with a maximal accessible angular range of 30° for simultaneous SAXS and WAXS measurements is available. P-jumps are realised by switching fast valves between a low and a high pressure reservoir, increasing or decreasing the hydrostatic pressure in the range from 1 bar to 2.5 kbar within a few ms. A Differential Scanning Calorimeter (DSC) allows for DSC-scans simultaneously to SWAXS measure-ments. In an overview, the following sample manipulations are possible (for further details, see pages 30-38):

- Temperature Manipulations: Ramps, Jumps and Gradient Scans
- Pressure Manipulation: Scan and Jumps
- Stopped Flow Experiments
- SWAXS Measurements Applying Mechanical Stress
- Calorimetric measurements

Scientific Applications	Low Contrast Solution Scattering, Grazing Incidence Surface Diffraction, Micro-Spot Scanning, X-ray Fluorescence Analysis, Time-Resolved Studies ≥ 11 μs and Simultaneously Performed Small- and Wide-Angle Measurements (SWAXS) on: Gels Liquid Crystals (Bio) Polymers Amorphous Materials Muscles
Source characteristics	Wiggler (NdFeB Hybrid): Period 140 mm No. full poles 57 Gap 20 mm B_{max} 1.607 T Critical Energy ε_c 4.27 keV Power (9 mrad) 8.6 kW Effective source size FWHM 3.9 x 0.26 mm^2(h x v)
Optics	Optical elements: *Double crystal monochromator*: Si (111) asym. cut, water cooled. *Mirror*: two–segment,toroidal, Pt coated. Distance from source: 18.4 m 26.5 m Acceptance 1 mrad/0.3 mrad (h x v) Energy (3 selectable) 5.4, 8, 16 keV (0.77, 1.54, 2.3 Å) Energy resolution ΔE/E 0.7-2.5 x 10^{-3} Focal spot size FWHM 1.2 x 0.6 mm^2 (h x v) Spot at Sample FWHM 5.4 x 1.8 mm^2(h x v) Flux at sample 7.5 x 10^{12} ph s^{-1}(2 GeV, 300 mA, 8 keV)
Experimental apparatus	Resolution in real space: 10-1400 Å (small-angle), 1- 9 Å (wide-angle) Sample stage: temperature manipulations: ramps, jumps and gradient scans, pressure manipulation: scan and jumps, stop flow experiments, SWAXS measurements applying mechanical stress, SWAXS measurements applying magnetic fields. In-line calorimetric measurements simultaneously with SWAXS. Detectors: 1D gas-filled detectors for simultaneous small- and wide-angle (Gabriel type), 2D CCD (Photonic Science) and Mar300 Image Plate for small-angle, Vantec-1D (Bruker AXS), Pilatus 2D detector.
Experiment control	Beamline control: Program-units written in LabView for Windows 1 D detector control: PC-card and software from Hecus X-ray Systems GmbH, Graz. 2 D detector control: Software from corresponding detector system.

CURRENT STATUS

The beamline has been built by the Institute for Biophysics and Nanosystems Research (IBN), Austrian Academy of Science in collaboration with staff members from Sincrotrone Trieste, and is in user operation since September 1996. The set-up of the beamline started at the beginning of January 1995 with the installation of the support structure. Until the end of 1995, the 8 keV single energy system had been realised. The upgrade to the full three energy system was finished in spring 1998. Time resolved experiments require fast X-ray detectors and data acquisition hard- and software. Depending on the desired resolution in time and in reciprocal space, on isotropic or anisotropic scattering of the sample, one-dimensional position sensitive (delay-line type) or two-dimensional CCD detectors are employed.

In August 2002 our chemistry and X-ray laboratory went into operation. The chemistry unit serves mainly for sample preparation and analysis for both, in house research and external user groups, whereas the X-ray laboratory allows on-site testing of samples before moving on to the SR beamline (see page 40).

In May 2008 we extended about 3 m also our experimental hutch. It is now possible to increase the sample to detector distance and therefore improve our minimum SAXS resolution or maximise the flux density at sample position for certain experiments.

On 1st October 2012 the beamline was transfered from the Institute of Biophysics and Nanosystems Research, Austrian Academy of Sciences, to the Institute of Inorganic Chemistry, Graz University of Technology. Elettra-Sincrotrone Trieste and Graz University of Technology (TU Graz) strengthened their collaboration as they signed a scientific cooperation agreement on 21st November 2013 in Trieste, Italy. TU Graz is now officially the leading coordinator for two Austrian beamlines: SAXS (Small Angle X-ray Scattering) and DXRL (Lithography). Accompanying the signing of the contract, Harald Kainz, Rector of TU Graz, handed over a new Pilatus3 1M X-ray detector (see page 26), which now significantly broadens the research opportunities at the Austrian SAXS beamline.

from the left: Prof. Frank Uhlig, Dean of the Faculty of Technical Chemistry (TU Graz); Prof. Harald Kainz, Rector (TU Graz); Prof. Carlo Rizzuto, President of Elettra; Prof. Alfonso Franciosi, CEO of Elettra (picture taken on 21st November 2013).

Application for Beamtime at ELETTRA

1. Beamtime Policy at SAXS beamline

According to the agreement from March 2001 regarding the co-operation between the Austrian Academy of Sciences and Sincrotrone Trieste, at the Austrian SAXS-beamline the available beamtime of about 5000 hours/year is distributed as follows:

- 35% for Austrian Users, type: "CRG" (Collaborating Research Group)
- 35% for Users of Sincrotrone Trieste (General Users (GU))
- 30% is reserved for beamline maintenance and in-house research

In both user beamtime contingents also any industrial, proprietary and confidential research can be performed according to the "General User Policy" of Sincrotrone Trieste.

To apply for CRG and GU user beamtime proposals must be submitted according to the rules of Sincrotrone Trieste. The international review committee at ELETTRA will rank the proposals according to their scientific merit assessment. Based on this decision beamtime will be allocated according to the specific quotes for the beamtimes (CRG/GU) either for the following semester ("normal application") or for the next two years ("long term application"). However, at the moment no more than a maximum of 10% of the beamtime will be assigned to "long term" projects.

2. How to apply for beamtime

2A. Applications for SAXS-beamtime only

There are two deadlines each year for proposals, namely August 31st and February 28th. Accepted proposals will receive beamtime either in the then following first or second half year period, respectively. The Application Form must be completed on-line according to the following instructions.

ELETTRA USERS OFFICE
Strada Statale 14 - km 163.5
34012 Basovizza (Trieste), ITALY
Tel: +39 040 375 8628 / 8538- fax: + 39 040 375 8565
e-mail: useroffice@elettra.trieste.it

INSTRUCTIONS GIVEN BY THE USERS OFFICE
(see also http://www.elettra.trieste.it/userarea/apbt.html)

1. Read carefully the General Guidelines.

2. Connect to the Virtual Unified Office: https://vuo.elettra.trieste.it/pls/vuo/guest.startup using your favorite browser with JavaScript enabled.

3. Select the Virtual Unified Office link. Login with your ID and password. If you are a new user fill in the registration form with your data and choose your institution with the search button; in case your institution does not appear in the list, please contact useroffice@elettra.trieste.it giving all the details about it. When registered, you will receive an acknowledgment with your ID and password. You can change your password, if you wish. In case you forget your password, please don't register again but contact useroffice@elettra.trieste.it. At any moment you can select the help button and view more detailed instructions. By inserting your ID and password you will be able to continue.

4. Select the proposals button in the User functions group.

5. Select add and fill in on-line the proposal form. Please, type your proposal in English. Repeat this procedure for each proposal you intend to submit.

6. In case of continuation proposal: a) attach the experimental report of previous measurements; b) give your previous proposal number.

7. When finished, submit the proposal electronically, selecting the save button.

8. Print all safety forms (related to your proposal form).

9. Sign the safety form(s).

10. Mail all printed and signed safety form(s) to the (real) Users Office.

2B. Applications for a combination of SAXS-beamtime AND access to other laboratories (CERIC-ERIC proposals)

CERIC, the Central European Research Infrastructure Consortium, is a distributed research facility, set up as an ERIC, by Austria, Czech Republic, Italy, Romania, Serbia, Slovenia and open to other interested countries.
The specific scope of this ERIC concerns the offer as an integrated service to external researchers of the access to synchrotron light and other analytical techniques notably for materials preparation and characterization, structural investigations and imaging in Life Sciences, Nanoscience and Nanotechnology, Cultural Heritage, Enviroment, Chemistry and Materials Science.
CERIC-ERIC integrates the most competitive instrumental, technical and research resources complementary analytical and preparation methods like NMR, Synchrotron light, Neutrons, electron Microscopy and other Surface and Interface analytical instruments. For a detailed description on the available facilities visit CERIC's website.
Access to its services is awarded free of charge to any Researcher upon submission of a proposal to be selected by an external International peer review committee. Proposals should address challenging scientific or technological problems that require the use of several methods offered by the partners for sample growth and characterization. CERIC-ERIC features a completely innovative approach focusing on the scientific or technological value of

the project allowing to request access to different integrated facilities in a single step, through a single access point.

How to Apply
Detailed information can be found at
http://www.c-eric.eu/index.php?n=Main.HomePage
http://www.c-eric.eu/index.php?n=CallZero.Homepage

NOTE:

For administrative questions related to the proposal submission, contact useroffice@elettra.trieste.it

For scientific or technical questions related to the possibility of performing a given SAXS experiment, contact bernstorff@elettra.eu or amenitsch@elettra.eu

Users and institutes performing experiments in 2013

Austria

Laboratory of Polymer Engineering LKT-TGM, Vienna, and University of Vienna, Research Group Physics of Nanostructured Materials

WILHELM Harald

Graz University of Technology, Institute of Inorganic Chemistry, Graz

AMENITSCH Heinz
BINDER, Judith
CACHO-NERIN Fernando
KRIECHBAUM Manfred
MARMIROLI Benedetta
RAPPOLT Michael
SARTORI Barbara
UHLIG Frank
ZEPPEK Cathrin

Graz University of Technology, Institute for Chemistry and Technology of Organic Materials, Graz

GOLLAS Bernhard

Graz University of Technology, Institute for Chemistry and Technology of Organic Materials, Graz

BUCHMAIER Christine
DUNST Sebastian
EHMANN Heike M.A.
KNALL Astrid-Caroline
RATH Thomas
SPIRK Stefan
STELZER Franz
TRIMMEL Gregor

Graz University of Technology, Institute for Electron Microscopy and Nanoanalysis, Graz, & Centre for Electron Microscopy, Graz

REICHMANN A.

Graz University of Technology, Institute of Materials Science and Welding, Graz

POLETTI Cecilia
SCHLACHER Christian
TAENDL Johannes

Karl-Franzens Universität Graz, Institute of Chemistry

MOHAN T.

Karl-Franzens Universität Graz, Insitute of Pharmaceutical Technology

WERZER Oliver

Medical University of Graz, Institute of Biophysics
KORNMUELLER Karin
PRASSL Ruth

Montanuniversity Leoben, Department of Physics
LECHNER Rainer T.
MORAK Roland
PARIS Oskar
PREHAL Christian
SHARIFI RAJABI Parvin

Technische Universität Graz, Institut für Festkoerper Physik, Graz
AMTMANN Christoph
PACHMAJER Stefan
RESEL Roland
WERZER Oliver

University of Graz, Institute of Molecular Biosciences, Biophysics Division
KOLLMITZER Benjamin
HEFTBERGER Peter
PABST Georg
RIEDER Alexander

University of Graz, Institute of Molecular Biosciences, Structural Biology Group
KELLNER Thomas

University of Vienna, Faculty of Physics, Dep. Physics of Nanostructured Materials
POLT Gerald
SPIECKERMANN Florian
ZAREGHOMSHEH Mohammad
ZEHETBAUER Michael J.

University of Vienna, Faculty of Physics, Dynamics of Condensed Systems, Vienna
AKBARZADEH Johanna

Brazil

Universidade de Brasília, Instituto de Física, Núcleo de Física Aplicada, Brasília
LEóN FéLIX L

Croatia

Institute of Physics, Zagreb
DELAč MARION Ida
GRGIčIN Danijel
KRALJ Marko
SALAMON Krešimir
VULETIć Tomislav

"Ruđer Bošković" Institute, Zagreb

BOGDANOVIĆ-RADOVIĆ Ivancica
BULJAN Maya
DUBČEK Pavo
JERčINOVIč Marko
KARLUšIć Marko
PIVAC Branko
RADIć Nikola
ŠANTIć Ana

University of Zagreb, Faculty of Science, Department of Physics

UTROBICIC Antonija

Czech Republic

Charles University, Faculty of Mathematics and Physics, Prague

HOLY Václav
HORAK, L.
VALEŠ Václav

Denmark

University of Copenhagen, Department of Pharmacy, Faculty of Health and Medical Sciences, Copenhagen

ULDALL JONASSEN A.L.
WENG LARSEN S
YAGHMUR Anan

Finland

University of Helsinki, Viikki Drug Discovery and Development Technology Center

BURMESTER Mechthild
TASAKA Fumitaka

Germany

DESY, HASYLAB, Hamburg

SARATHLAL Koyiloth Vayalil

Helmholtz Research Center Rossendorf, Dresden

BäHTZ Carsten
GRENZER Jörg
HüBNER René
MüCKLICH Arndt
ROSCHUPKINA O.

INM, Leibniz-Institut für Neue Materialien GmbH, Energy Materials Group, Saarbrücken

PERRE Emilie
WEINGARTH Daniel
PRESSER Volker

Martin-Luther University Halle-Wittenberg, Institute of Chemistry, Chair of Macromolecular Chemistry, Halle

BINDER Wolfgang H.
DöHLER Diana
MICHAEL Philipp
STOJANOVIC Anja

Technische Universität München, Dept. of Physics, Lehrstuhl für Funktionelle Materialien, Garching

KöRSTGENS Volker
MAGERL David
MüLLER-BUSCHBAUM Peter
RUI Yichuan
SCHAFFER Christoph J.
SCHLIPF Johannes
SONG Lin
SU Bo

University of Erlangen-Nuremberg, Institute of Crystallography and Structural Physics, Erlangen

GERTH Stefan
MAGERL Andreas
SCHIENER Andreas
WILLNAUER Kerstin

University of Ulm, Division of Inorganic Chemistry II

LINDéN Mika
RAFAI Christopher

India

Center for Spintronic Materials, Amity University, Noida

GUPTA Ajay

Saha Institute of Nuclear Physics, Surface Physics Division, Kolkata

CHATTERJEE Paramita
DATTA Sruti
HAZRA Satyajit
JANA Sayanee

Inter University Consortium for DAE Facilities, University Campus, Indore

PANDIT Pallavi
SHARMA Gagan

Israel

Hebrew University of Jerusalem, Institute of Chemistry and the Fritz Haber Research Center

HARRIES Daniel
SAPIR Liel

University of Tel-Aviv, School of Physics & Astronomy

BECK Roy
KORNREICH Micha
SHAHARABANI Rona

Italy

CNR (National Research Council), Institute of Biophysics, Palermo

BULONE Donatella
CARROTTA Rita
LIBRIZZI Fabio
MANGIONE Maria Rosalia
MANNO Manno
MARTORANA Vincenzo
NICASTRO M.C.
NOTO R.
RAPPA G.C.
SAN BIAGIO Pier Luigi
SPIGOLON Dario
VILASI Silvia

CNR, Institute of Crystallography, Monterotondo (Rome)

CAMPI Gaetano

CNR-ISM, Istituto di Struttura della Materia, Rome

D'ACUNTO Mario
SUBER Lorenza

Elettra-Sincrotrone Trieste S.C.p.A., Trieste

BERNSTORFF Sigrid
BOSCO Alessandro
DE MARCH Matteo
IANESELLI Luca
MORELLO Christian
ONESTI Silvia Caterina Elvira

INSTM - Consorzio Interuniversitario Nazionale per la Scienza e Tecnologia dei Materiali & Elettra-Sincrotrone Trieste

CASALIS Loredana
PARISSE Pietro

IOM - CNR National Laboratorio TASC, Trieste
RADIVO Andrea
SOVERNIGO Enrico
TORMEN Massimo

SISSA, and CNR, Istituto Officina dei Materiali, Trieste
PICCIN S.
FABRIS Stefano

University of Camerino, Department of Chemical Sciences
NOBILI Francesco

Università "G.D'Annunzio" di Chieti - Pescara
SINIBALDI Raffaele

University of Messina, Department of Chemical Sciences, and Centro Interuniversitario per la Conversione Chimica dell'Energia Solare, Messina
CAMPAGNA S..
LA GANGA G.
PUNTORIERO F.

Università di Padova, Dipartimento di Biologia, Padova
GONNELLI Adriano

University of Padova, Department of Chemical Sciences, and ITM-CNR, Padova
SARTOREL Andrea
CARRARO Mauro
BONCHIO Marcella

University of Padova, Department of Chemical and Pharmaceutical Sciences, and ITM-CNR, Padova
GRIGOLETTO Antonella
MERO Anna
PASUT Gianfranco

Polytechnic University delle Marche, Department of Life and Environmental Sciences, and National Interuniversity Consortium for the Physical Sciences of Matter, Ancona
MOSCATELLI Silvia
ORTORE Maria Grazia

Polytechnic University delle Marche, Department of Life and Environmental Sciences, Ancona
BALDASSARRI Enrico
CAMPANELLA Gabriele
RICCI C.
SPINOZZI Francesco

University of Pisa, Department of Civil and Industrial Engineering
DI PUCCIO F.

University of Rome “La Sapienza”, Department of Molecular Medicine
CARACCIOLO Giulio
POZZI Daniela

University of Trieste, Department of Chemical and Pharmaceutical Sciences, & Center of Excellence for Nanostructured Materials (CENMAT), & INSTM, Trieste
Da ROS Tatiana
PRATO Maurizio
BONASERA Aurelio
SYRGIANNIS Zois

University of Trieste, Department of Chemical and Pharmaceutical Sciences, Trieste
CORVAGLIA Stefania
MARANGONI Tomas

Morocco

LPS, Physics Department, Faculty of Sciences, Fès
KARZAZI Ouiame

Peru

Universidad Nacional Mayor de San Marcos, Facultad de Ciencias Físicas, Lima
BUSTAMANTE DOMíNGUEZ Angel

Universidad Nacional Mayor de San Marcos, Facultad de Ciencias Físicas, & TECSUP, Lima
ESPINOZA SUAREZ Silvia Marisel

Portugal

University of Minho, Department of Physics, Braga
GOMES Maria J.M.
LEVICHEV Sergey
SEKHAR Koppole Chandra

Romania

Institute of Macromolecular Chemistry " Petru Poni", Iasi
MARIA Ignat

Switzerland

Ecole Polytechnique Fédérale de Lausanne, Faculté des Sciences de Base, Lausanne
MOGLIANETTI Mauro
STELLACCI Francesco

United Kingdom

University of Cambridge, Cavendish Laboratory, Department of Physics, Cambridge

BARNES C.H.W.
DE LOS SANTOS VALLADARES Luis

Diamond Light Source, Didcot

CACHO-NERIN Fernando

Keele University, Department of Physics, Keele

ARUMUGAM Mahendrasingam
SWANN Nichola
WYE Steven

University of Leeds, School of Food Science and Nutrition, Leeds

RAPPOLT Michael

USA

University of Delaware, Dept. of Chemical and Biomolecular Engineering, Newark, Delaware

ROBERTS C.J.
BARNETT Gregory
BLANCO Marco

List of Performed Experiments

2013 (first half year)

Proposal	Proposer	Institute	Country	Title	Research Field
20125013	GUPTA Ajay	Inter Univ. Consortium for DAE Facilities, Indore	India	GISAXS study of Co film on nanorippled Si substrate	Materials Science
20125045	BURMESTER Mechthild	Univ. of Helsinki, Viikki Drug Discovery & Develop. Technology Center	Finland	In situ gelation of ocular drug nanocarriers based on cubosomes and hexosomes	Life Sciences
20125052	CARACCIOLO Giulio	Sapienza Univ., Dep. of Chemistry, Rome	Italy	Effect of human plasma on the nanostructure of cationic liposome/DNA complexes	Life Sciences
20125089	LINDEN Mika	Ulm Univ., Inorganic Chemistry II	Germany	In Situ SAXS studies of the formation of cylindrical mesoporous silica nanoparticles	Chemistry
20125091	BINDER Wolfgang	Martin Luther Univ., Halle-Wittenberg	Germany	Autocatalysis in multivalent "click" cycloaddition reactions towards self-healing polymeric materials: investigation of time-dependent cluster formation via SAXS	Chemistry
20125097	D'ACUNTO Mario	CNR, Institute of Materials Structure, Rome	Italy	Synchroton radiation SAXS study on enhanced toughness of polymers filled with electrospun nanofibers	Materials Science
20125139	BULJAN Maja	Ruder Bošković Insitute, Zagreb	Croatia	Structural properties and growth mechanism of Si nano-objects in amorphous alumina mutlilayers	Materials Science
20125142	PARIS Oskar	Dep. of Physics, Montanuniv. Leoben	Austria	Deformation of ordered mesoporous materials due to protein adsorption	Materials Science
20125152	PARIS Oskar	Dep. of Physics, Montanuniv. Leoben	Austria	Deformation of ordered mesoporous thin films due to water adsorption and condensation	Materials Science
20125153	PARIS Oskar	Dep. of Physics, Montanuniv. Leoben	Austria	In-situ SAXS studies on the charge/discharge behavior of electrochemical double -layer capacitors	Materials Science
20125184	PABST Georg	Univ. of Graz, Inst. of Molecular Biosciences, Division of Biophysics	Austria	Kinetics of Domain Formation in Lipid Bilayers	Life Sciences
20125212	MARMIROLI Benedetta	Technical Univ. Graz, Dept. of Inorganic Chemistry	Austria	Scanning SAXS studies of Pt catalyst degradation on large areas of Membrane Electrode Assemblies in HT-PEM Fuel Cells	Materials Science
20125218	MARMIROLI Benedetta	Technical Univ. Graz, Dept. of Inorganic Chemistry	Austria	SAXS studies of confinement effect on calcium carbonate formation in presence of additives using custom made micromixers	Materials Science
20125241	ORTORE Maria Grazia	Politechn. Univ. delle Marche, Dep. Sciences Applied to complex systems, Ancona	Italy	Looking for re-alloying signature in tin nanoparticles embedded in carbon cylinder	Life Sciences
20125261	YAGHMUR Anan	Univ. of Copenhagen, Faculty of Pharmaceutical Sciences	Denmark	In situ characterization of drug-loaded liquid crystalline formulations	Life Sciences

20125296	ONESTI Silvia	Elettra-Sincrotrone Trieste	Italy	Structural analysis of human proteins involved in DNA replication	Life Sciences
20125347	GOMES Maria	Dep. of Physics, Univ. of Minho	Portugal	GID and GISAXS investigation of the effect of cobalt concentration on the structural properties of $Zn_{1-x}Co_xO$ /Al_2O_3 multilayered nanostructures	Materials Science
20125383	SCHIENER Andreas	Univ. Erlangen-Nürnberg, Dep. für Kristallographie und Strukturphysik	Germany	In-situ SAXS study on the influence of EDTA on the formation of CdS quantum dots	Materials Science
inhouse research	AMENITSCH Heinz & MIKHLIN Yury	TU Graz & Russian Academy of Sciences, Inst. of Chemistry and Chemical Technology, Siberia	Austria & Russian Federation	Small-angle X-ray scattering examination of liquid intermediates preceeding nucleation of metal nanoparticles in aqueous solutions	Chemistry
inhouse research	AMENITSCH Heinz & MOGLIANETTI Mauro	TU Graz & EPFL - Faculté des Sciences de Base	Austria & Switzerland	2D gold nanoparticles supracrystals	Materials Science
inhouse research	BERNSTORFF Sigrid & RADIC Nikola	Elettra-Sincrotrone Trieste & Ruder Bošković Insitute, Zagreb	Italy & Croatia	A 2D and 3D arrays of Ni nanoparticles formed by magnetron sputtering	Materials Science
inhouse research	BERNSTORFF Sigrid & DUBCEK Pavo	Elettra-Sincrotrone Trieste & Ruder Bošković Insitute, Zagreb	Italy & Croatia	Silicon quantum dots from PLD produced SiO2/SiO multilayers	Materials Science
inhouse research	BERNSTORFF Sigrid & PIVAC Branko	Elettra-Sincrotrone Trieste & Ruder Bošković Insitute, Zagreb	Italy & Croatia	Si quantum dots production in silicon carbide/Si and silicon carbide/Ge multilayers	Materials Science
inhouse research	AMENITSCH Heinz & BONASERA Aurelio	TU Graz & Univ. di Trieste, Dip. Scienze Farmaceutiche	Austria & Italy	Structural analysis of perylene-tetracarbocylic acid bisimides (PDIs) nano-aggregates deposited on glass surface	Materials Science
inhouse research	AMENITSCH Heinz & SYRGIANNIS Zois	TU Graz & Univ. di Trieste, Dip. Scienze Farmaceutiche	Austria & Italy	Stability measurements for perylene-tetracarbocylic acid bisimides (PDIs) nano-aggregates suitable for electronics	Materials Science
inhouse research	BERNSTORFF Sigrid & Peter Mueller-Buschbaum	Elettra-Sincrotrone Trieste & Techn. Univ. München, Physics Dept.	Italy & Germany	Decoration of silica nanoparticles with silver	Materials Science
inhouse research	AMENITSCH Heinz & PARISSE Pietro	TU Graz & INSTM (Consorzio Interuniv. Nazionale per la Scienza e Tecnologia dei Materiali)	Italy	GISAXS on supported lipid bilayers::the role of hydration	Life Sciences

2013 (second half year)

Proposal	Proposer	Institute	Country	Title	Research Field
20130007	CAMPI Gaetano	CNR, Inst. for Chrystallography, Montelibretti, Rome	Italy	Control of hierarchic assembling of silver nanoparticles in organic-inorganic micro-structures	Chemistry
20130019	PASUT Gianfranco	Univ. Padova, Dep. of Farmaceutical Sciences	Italy	SAXS studies of human growth hormone conjugated to polyglutamic acid	Life Sciences
20130073	PARISSE Pietro	INSTM (Consorzio Interuniv. Nazionale per la Scienza e Tecnologia dei Materiali	Italy	GISAXS on supported lipid bilayers: the role of hydration	Life Sciences
20130103	KORNREICH Micha	Univ. of Tel-Aviv, School of Physics & Astron.	Israel	Structure and self-assembly of neural intermediate filament protein	Life Sciences
20130129	ESPINOZA SUAREZ Silvia Marisel	TECSUP	Peru	Study of the formation of hollow hematite spheres without the use of templates	Life Sciences
20130133	BINDER Judith	Technical Univ. Graz, Dept. of Inorganic Chemistry	Austria	Silicon thin film formation by thermal decomposition of organosilanes	Chemistry
20130138	TAENDL Johannes	TU Graz, Inst. für Werkstoffkunde und Schweißtechnik	Austria	In-situ investigation of the Al3Sc precipitation kinetics in an Al-Mg-alloy with large Sc-content	Materials Science
20130153	EHMANN Heike M. A.	Universität Graz, Inst. for Physikalische Chemistry	Austria	Order in cellulose model thin films	Materials Science
20130190	PARIS Oskar	Montanuniversity Leoben, Physics Department	Austria	Deformation of ordered mesoporous thin films due to water adsorption and condensation: The influence of film thickness and film perfection	Materials Science
20130200	SWANN Nichola	Keele University, Dept. of Physics	United Kingdom	Investigation of the dehydration mechanisms and kinetics of thehalose dihydrate and theophylline monohydrate using time-resolved SAXS/WAXS/DSC techniques	Chemistry
20130221	BULJAN Maja	Ruder Bošković Insitute, Zagreb	Croatia	Growth of anisotropic Ge and Ge/Si quantum dot lattices in amorphous oxide matrices	Materials Science
20130275	TRIMMEL Gregor	TU Graz, Inst. for Chem. and Technology of Organic Materials	Austria	Nanoimprinted comb structures for inorganic-organic hybrid solar cells	Materials Science
20130296	VILASI Silvia	CNR, Istituto di Biofisica, Palermo	Italy	Intrinsic disorder and chaperon-like activity of different caseins: an extensive in-solution SAXS study	Life Sciences
20130314	CARROTTA Rita	CNR - Istituto di Biofisica, Palermo	Italy	Interaction of amyloid beta protein aggregates and model cellular membranes: Study on the double layer phase behavior and structure.	Life Sciences
20130327	ORTORE Maria Grazia	Politechn. Univ. delle Marche, Sez. Sciences Applied to complex systems, Ancona	Italy	Investigating the controversial role of Hsp60: an extensive in solution SAXS study	Life Sciences
20130346	SPINOZZI Francesco	Politechn. Univ. delle Marche, Sez. Scienze Fisiche	Italy	SAXS investigation of the quaternary structure of human N-ethylmaleimide-Sensitive Factor after ATP binding and phosphorylation	Life Sciences

20130419	MARMIROLI Benedetta	Technical Univ. Graz, Dept. of Inor-ganic Chem.	Austria	GISAXS studies of the structural change of mesoporous materials upon controlled X-ray irradiation	Materials Science
20130456	SPIECKERMANN Florian	Univ. Vienna, Inst. for Material-physics	Austria	In situ study of microstrains during post yield deformation of polyethylene	Materials Science
20130469	HAZRA Satyajit	Saha Institute of Nuclear Physics - Surface Physics Division	India	Formation of P123-mediated AU-nanoparticles in aqueous solution: in-situ X-ray scattering study	Materials Science
20130481	DUBCEK Pavo	Ruder Bošković Insitute, Zagreb	Croatia	Aluminium nano particles for future photovoltaic applications	Materials Science
20130499	SARTORI Barbara	Technical Univ. Graz, Dept. of Inorganic Chemistry	Austria	In-situ study of mesostructured silica synthesized in the gas phase	Materials Science
20130505	HARRIES Daniel	Hebrew Univ. of Jerusalem, Inst. of Chemistry	Israel	X-ray scattering studies of macromo-lecular solvation in choline/urea based deep eutectic solvents	Life Sciences
20130506	MARTORANA Vincenzo	CNR, Institute of Biophysics, Palermo	Italy	Interaction potential of an amyloido-genic protein.	Life Sciences
Inhouse	BERNSTORFF Sigrid & SHAHARABANI Rona	Elettra-Sincrotro-ne Trieste & Univ of Tel-Aviv, School of Physics & Astronomy	Italy & Israel	Self-assembly in Myelin-sheaths: structural changes in lipid-MBP complexes	Life Sciences
Inhouse	BERNSTORFF Sigrid & SALAMON Kresimir	Elettra-Sincrotro-ne Trieste & Institute for Physics	Italy & Croatia	SAXS study of microphase separated DNA/hyaluronic acid mixtures	Life Sciences
Inhouse	BERNSTORFF Sigrid & RADIC Nikola	Elettra-Sincrotro-ne Trieste & Ruder Bošković Insitute, Zagreb	Italy & Croatia	Self-assembled growth of nickel nanoparticles in amorphous alumina matrix	Materials Science
Inhouse	BERNSTORFF Sigrid & MUELLER-BUSCHBAUM Peter	Elettra-Sincrotro-ne Trieste & TU München, Physics Dept.	Italy & Germany	The role of solvent-additives on polymer-fullerene layers for organic photovoltaics	Materials Science
Inhouse	AMENITSCH Heinz & GOLLAS Bernhard	TU Graz, Dept. Inorganic Chem. & Inst. for Chem. and Technology of Organic Mate-rials	Austria	Structure and dynamics of the electrode/electrolyte interface in deep eutectic solvents.	Chemistry
Inhouse	AMENITSCH Heinz & MARANGONI Tomasd	TU Graz & Univ. of Trieste, Dep. of Farmaceutical Sciences	Austria & Italy	Structure of different chiral R-Binol derivatives in solution	Life Sciences
Inhouse	AMENITSCH Heinz & CARACCIOLO Giulio	TU Graz & Sapienza Univ., Dep. of Chemi-stry, Rome	Austria & Italy	Effect of human plasma on the nanostructure of cationic liposome / DNA complexes	Life Sciences
Inhouse	AMENITSCH Heinz & KORNMUELLER Karin	TU Graz & Medi-cal Univ. of Graz, Inst. of Biophysics	Austria	Studies on the membrane-activity of surfactant-like designer-peptides	Life Sciences

User Statistics

1. Number of submitted proposals and assigned shifts from 1995 until December 2014

The Austrian SAXS-beamline at ELETTRA opened to users in September 1996. Since then many experiments have been performed related to the fields of life science, materials science, physics, biophysics, chemistry, medical science, technology and instrumentation.

The assignment of beamtime at this beamline is done separately for the group of "General Users" (GU) and the "Collaborating Research Group" (CRG), i.e., the Austrian users. Beamtime was assigned to the proposals of each group in the order of the rating received by the Scientific Committee, and up to the maximum number of shifts available to each group according to the contract between "The Austrian Academy of Sciences" and the "Sincrotrone Trieste". Until December 1997 up to 30 % of the beamtime was given to CRG, up to 55 % to GU, and 15% was reserved for maintenance purposes. From January 98 to June 2001 the quota for beamtime was up to 35 % for CRG, up to 50 % for GU, and again 15% reserved for maintenance purposes. From July 2001 on the two contingents for user proposals from CRG and GU receive up to 35% of the beamtime each. The remaining 30 % of beamtime are used for inhouse research projects as well as for maintenance purposes. From July 2014 on, access to the Austrian SAXS-beamline can also be obtained by submitting a proposal via the new CERIC-ERIC channel (see page 8).

Figure 1 gives an overview of the numbers of received proposals, the numbers of requested and assigned shifts, as well as the percentage between assigned and requested shifts during the last years. As can be seen in Fig.1, the request for beamtime at the SAXS-beamline increased strongly until the first half year of 1999. Then, probably due to the high rejection rates, the number of submitted proposals decreased somewhat during 2001, which resulted in a better ratio of accepted / rejected proposals. This oscillating behaviour of beamtime request can also be seen for the period 2002 – 2014 where after higher numbers of submitted proposals slightly reduced request periods follow. The numbers for the second semester of 2007 and first of 2008 reflect also that, due to the long shut-down from 1.10.2007 to 3.03.2008 (for the new booster-electron-injector installation) less proposals were submitted, and less beamtime was available.

In 2013, in total 83 proposals (14 from CRG, and 69 from GU) were submitted. From these 3 CRG and 17 GU proposals were submitted by "new" usergroups, i.e. groups which so far had never beamtime at the SAXS beamline. From these, 4 GU and all 3 CRG proposals were accepted by the review committee.

Figure 1 (Next page). The statistical information about the beamtime periods since end of 1995 are given for the groups "CRG", and "GU" separately, as well as for both together ("Total"). Shown are, for all beamtime periods (from top to bottom):
● Number of received proposals, ● Number of requested shifts,
● Number of assigned shifts, and ● Relation between assigned and requested shifts

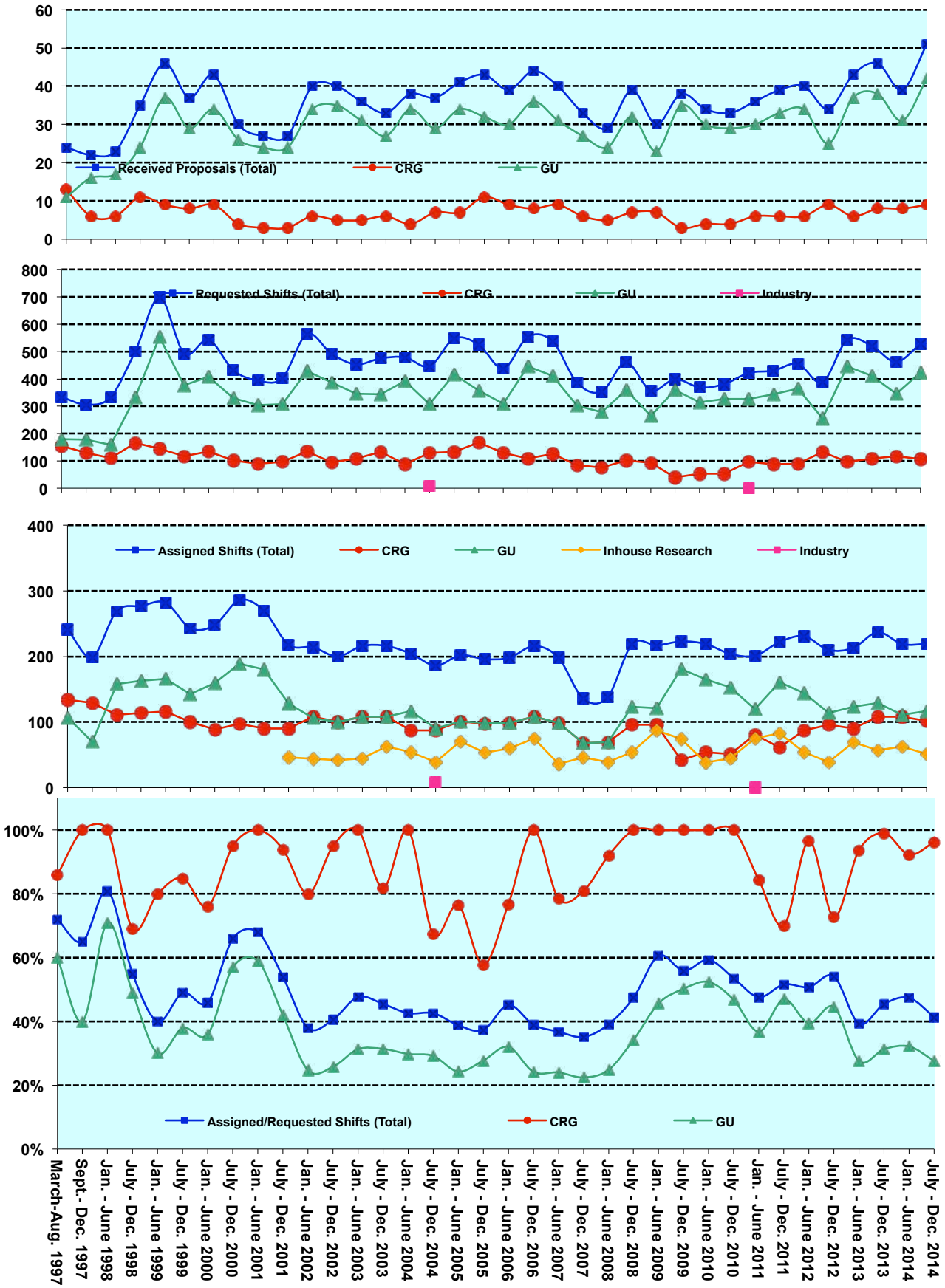
Received Proposals (Total)
CRG
GU
Requested Shifts (Total)
CRG
GU
Industry
Assigned Shifts (Total)
CRG
GU
Inhouse Research
Industry
Assigned/Requested Shifts (Total)
CRG
GU
March-Aug. 1997
Sept.- Dec. 1997
Jan. - June 1998
July - Dec. 1998
Jan. - June 1999
July - Dec. 1999
Jan. - June 2000
July - Dec. 2000
Jan. - June 2001
July - Dec. 2001
Jan. - June 2002
July - Dec. 2002
Jan. - June 2003
July - Dec. 2003
Jan. - June 2004
July - Dec. 2004
Jan. - June 2005
July - Dec. 2005
Jan. - June 2006
July - Dec. 2006
Jan. - June 2007
July - Dec. 2007
Jan. - June 2008
July - Dec. 2008
Jan. - June 2009
July - Dec. 2009
Jan. - June 2010
July - Dec. 2010
Jan. - June 2011
July - Dec. 2011
Jan. - June 2012
July - Dec. 2012
Jan. - June 2013
July - Dec. 2013
Jan. - June 2014
July - Dec. 2014

2. Provenience of users

During 2013, 181 users from 63 institutes in 17 countries have performed experiments at the SAXS beamline. In Fig. 2 are shown both the provenience of these users, and of their respective institutes. Each user or institute was counted only once, even though many users performed experiments in both beamtime periods of 2013.

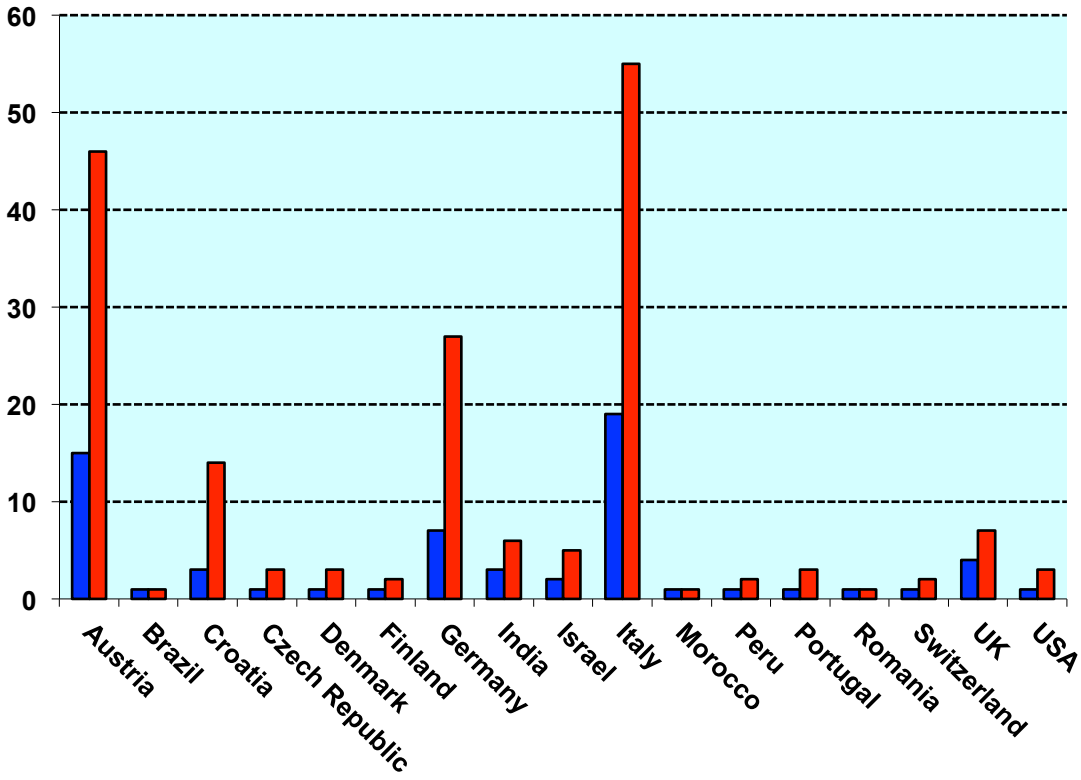

Figure 2. Nationality of the Austrian SAXS beamline users in the year 2013. The number of users (red) and the corresponding number of institutes (blue) are shown for each country.

3. Documentation of experimental results

As could be expected, with the start of user-operation at the SAXS-beamline the number of contributions to conferences started to increase strongly. With a delay of one year - the average time needed for paper publications - also the number of publications increased accordingly, as can be seen in Fig. 3.

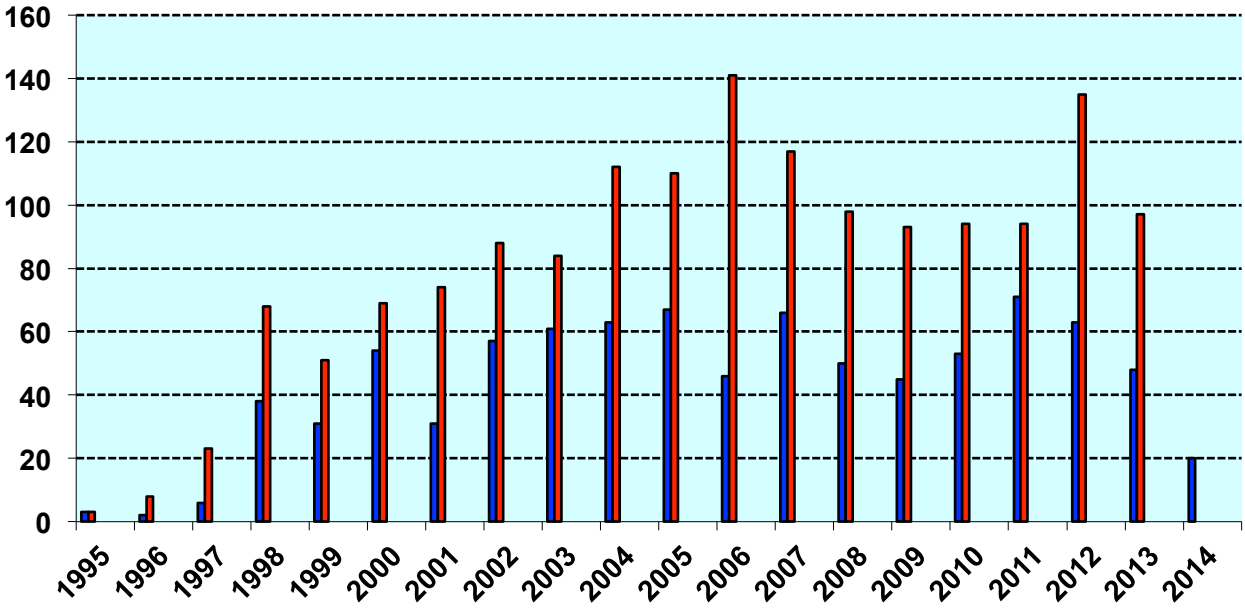

Figure 3. Number of conference contributions (red) and of refereed paper publications (blue) for the years 1995-2013. Also paper publications until July 2014 are included.

In addition, from 1995 until August 2014, the following documentations based on instrumentation of the SAXS-beamline, or on data taken with it, have been produced:

Technical Reports on Instrumentation: 5
Contributions to Elettra Newsletters: 15
Contributions to Elettra Highlights: 48
Habil Thesis: 4
PhD Thesis: 100
Master Thesis: 42
Bachelor Thesis 1

Experimental Possibilities at the SAXS-beamline

1. NEW DEVELOPMENTS AND INSTRUMENTATION

New Pilatus3 1M detector system

A Pilatus3 1M X-ray Detector System from Dectris Ltd. (Baden, Switzerland, 650 kEuro, financed by Austria) arrived in November 2013, and is available for users since Decembre 2013. It is now routinely used for SAXS measurements, while our older, smaller Pilatus 100K Detector System can now be used simultaneously for monitoring tthe wide angle scattering (WAXS) range, in order to detect the eventual crystalline amount of the samples.

The Pilatus3 1M detector system [1] system has a large sensitive area (168.7 x 179.4 mm^2), operates in "single photon counting" mode and is based on the CMOS hybrid pixel technology: the X-rays are directly transformed into electric charge, and processed in the CMOS readout chips. This rather new design has no dark current or readout noise, a high dynamic range of 20 bits (~1 million counts), a read-out time of less than 1 ms, a frame rate of up to 500 images/s and an excellent point spread function of 1 pixel. The data are stored in TIF format and can be directly processed with FIT2D [2]

Technical specifications:

	Pilatus3 1M	**Pilatus 100K**
Area [mm^2]	168.7 x 179.4	83.8 x 33.5
Number of detector modules	2 x 5	1
Pixel size [μm^2]	172 x 172	172 x 172
Number of pixels	981 x 1043 = 1 023 183	487 x 195 = 94 965
Intermodule gap	x: 7 pixels, y: 17 pixels, 7.2 % of total area	-
Dynamic range [Bits]	20 (1:1,048,573)	20 (1:1,048,573)
Counting rate per pixel [incoming X-ray photons/sec]	10^7	$> 2 \times 10^6$
Readout time [ms]	0.95	2.7
Maximum framing rate [Hz]	500	300
Point-spread function [FWHM]	1 pixel	1 pixel
Data formats	Raw data, TIF, EDF, CBF	Raw data, TIF, EDF, CBF
External trigger / gate	5V TTL, 3 different modes	5V TTL, 3 different modes

Thus this combination of the two Pilatus detectors has now significantly broadened the research opportunities at the Austrian SAXS beamline. It is now possible to follow the current trends in scattering experiments, namely: 1. to perform faster 2D time-resolved measurements (ms range) on e.g. phase transitions or chemical reactions. And 2. to perform grazing incidence (GISAXS) experiments on surfaces or on thin films, where a large detector area and large dynamic range is essential due to the contemporanea presence of very strong central (near the reflection plane) and very weak (in the larger q-range) signals.

[1] https://www.dectris.com/pilatus3_specifications.html#main_head_navigation
[2] A.P. Hammersley, "Fit2D: an introduction and overview", ESRF Internal Report, ESRF97HA02T, 1997

SFM – 20 Stopped flow module

A SFM-20 stopped-flow module (Bio-Logic) is available for single mixing rapid kinetics experiments at the beamline. This system is dedicated to kinetics or conformational studies on biological samples, such as protein folding, enzyme kinetics, water (or solute) transport across the membranes of small vesicles.
The two glass, gas tight syringes (10 ml) are controlled by independent stepper motors; the instrument can be set to obtain completely variable mixing ratio, and can be used to mix solutions of different viscosity.
The SFM-20 is controlled from a PC using the included Bio-Kine software and a USB connected control module. The software provides powerful and simple menus to design mixing sequence and multi-concentration experiments.
This new device has the big advantage of a smaller dead volume with respect to the old device SFM4, which is now dedicated mainly to material sciences, in which the sample volume is not a critical factor.

Specifications

- *dead time*: 0.6 ms
- *Mixing ratio:* 1:1 to 1:40
- *Priming volume:* 50 µl per syringe
- *Flow rate range:* 0.003 to 5.8 ml/s
- *Mixing ratio:* fully variable from 1:1 to 1:40
- *Minimum injection volume in stopped*-flow mode: 10-30 µl depending on the syringe

Server

In order to use the new Pilatus Detektor properly and to cope with the expected high data throughput, we have installed a big 50 TB server at the SAXS beamline. The current system architecture is shown in Fig. 1. The data acquisition is initiated by sending a command from the detector GUI running on the beamline control computer to the detector camserver. The detector aquires single or multiple images, which are automatically transferred from the detector CPU-RAM-disk to the mini PPU RAM-disk by a demon FURKA. The ELETTRA-IT group installed an additional demon which stores the data locally at the PPU and transfers the data to the 50 TB SAXS-server. For online post processing a new tool SAXSDOG running on the fast CPU core of the 50TB SAXS-server was developed by our group together with support from the SAXS group in Graz in order to integrate the data on the fly, and additional options are foreseen to visualize the data as soon they arrive. These options are currently tested and optimized partly also during user operation of the beamline.

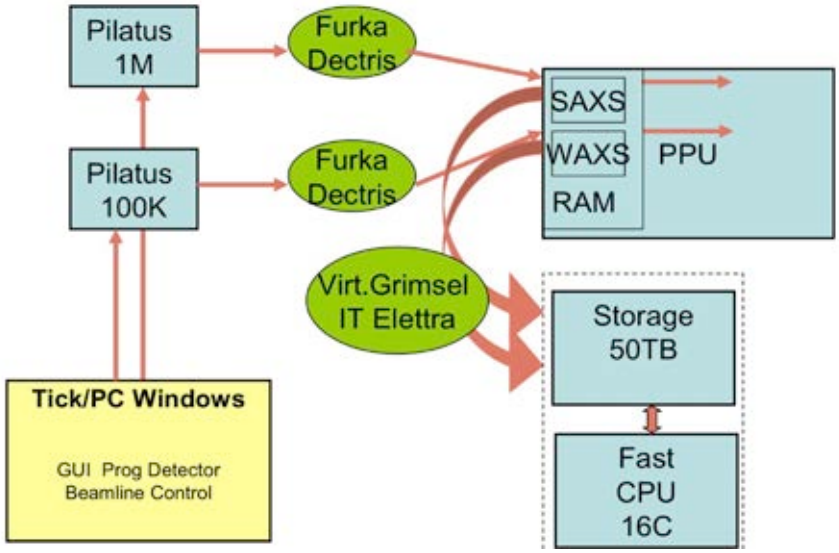

Schematic of the data transfer scheme for the Pilatus SWAXS set-up

2. ACCESSIBLE SAXS AND WAXS RANGES

The accessable **SAXS-range** depends on the requirements of each specific experiment: the required SAXS resolution (minimum q-value needed) defines the minimum possible sample-to-detector distance, which in turn limits the maximum reachable q-value due to the limited detector and vacuum-tube sizes. Also the required time-resolution can limit the effectively accessable SAXS-range, depending of the active size of the most suitable detector from our pool (see pages 27-28, 37-38). Therefore, first-time users should contact their local contact in usefull time before coming to ELETTRA in order to design their experiment accordingly.
Generally, the sample-to-detector distance can vary between a minimum of ca. 20 cm, and a maximum of 3 m. Thus, depending on the photon energy, maximum SAXS resolutions of 2000 Å (5.4 keV), 1400 Å (8 keV) or 630 Å (16 keV) are available.

Simultaneous SAXS- and WAXS-measurements can be performed using two different detectors at the same time. The accessable **WAXS-range** depends also on the requirements for each specific experiment, namely on the size of the required WAXS-detector, and the vacuum chambers needed for the SAXS-range. Maximum angles ($2\boldsymbol{\theta}$) of about 80^{o} are possible.

A specially designed vacuum chamber (SWAXS-nose, see Annual Report of 1996/97, p. 32) allows to use both scattering areas below (for SAXS) and above (for WAXS) the direct beam, respectively. The overall length of the SWAXS-nose in the horizontal direction, measured from the sample position, is 512 mm and the fixed sample to WAXS-detector distance is 324 mm. With a SAXS camera-length of $\leq$ 1.25 m an overlap in the d-spacings covered by the SAXS- and WAXS-detectors, respectively, is possible: then, the common regime lies around 9 Å d-spacing.

3. CALIBRATION OF THE S-AXIS AND FLAT FIELD CORRECTION

At the SAXS beamline various standards are used for the angular (s-scale) calibration of the different detectors:

- Rat tail tendon for the SAXS detector - high resolution (rtt*.dat)
- Silver behenate for the SAXS detector – medium and low resolution (agbeh*.dat)
- Para-bromo benzoic acid for the WAXS detector – WAXS range 1 and 2 (pbromo*.dat)
- Combination of Cu, Al foils and Si powder for the WAXS detector – WAXS range 2 and higher

In Figure 1 a typical diffraction pattern of rat tail tendon is shown, depicting the diffraction orders (from the first to the 14th order) measured with a "high" resolution set-up (2.3 m) and the delay-line gas detector. The d-spacing is assumed to be 650 Å, but this value can vary depending on humidity up to 3%. Thus, the rat tail tendon is often used only to determine the position of the direct beam (zero order), while the absolute calibration is performed using the diffraction pattern of Silver behenate powder. Fig. 2 depicts a diffraction pattern of Silver behenate measured with "medium" resolution set-up (1.0 m) from the first to the 4th order (repeat spacing 58.4 Å) [1].

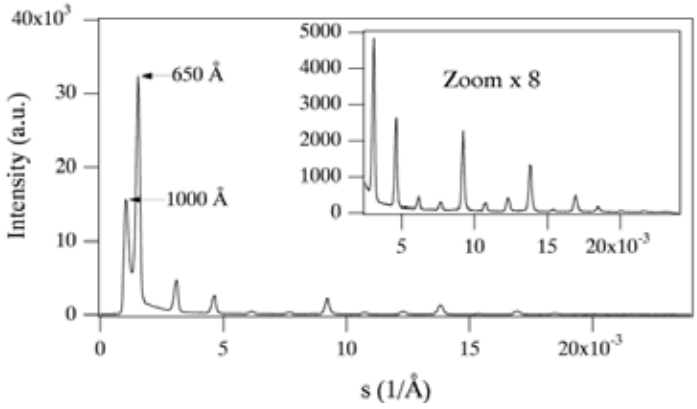

Figure 1. SAXS diffraction pattern of the collagen structure of rat tail tendon fibre at a distance of 2.3 m

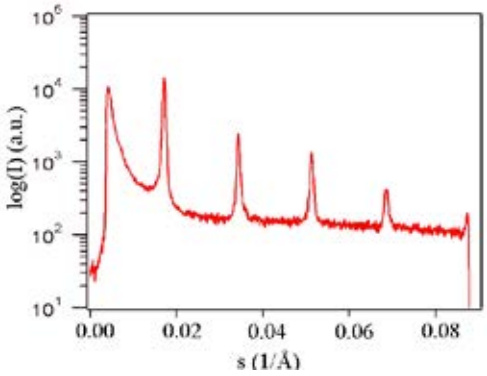

Figure 2. SAXS diffraction pattern of Ag behenate powder at a distance of 1.0 m

In Figure 3 a typical WAXS pattern of p-bromo benzoic acid is shown. The diffraction peaks are indexed according to the values given in Table 2, taken from [2].

d-spacing/Å	rel. intensity	d-spacing/Å	rel. intensity
14.72	18000	4.25	490
7.36	1200	3.96	2380
6.02	330	3.84	10300
5.67	980	3.74	26530
5.21	6550	3.68	1740
4.72	26000	3.47	760

Table 2. d-spacings and relative intensities of p-bromo benzoic acid according to [2].

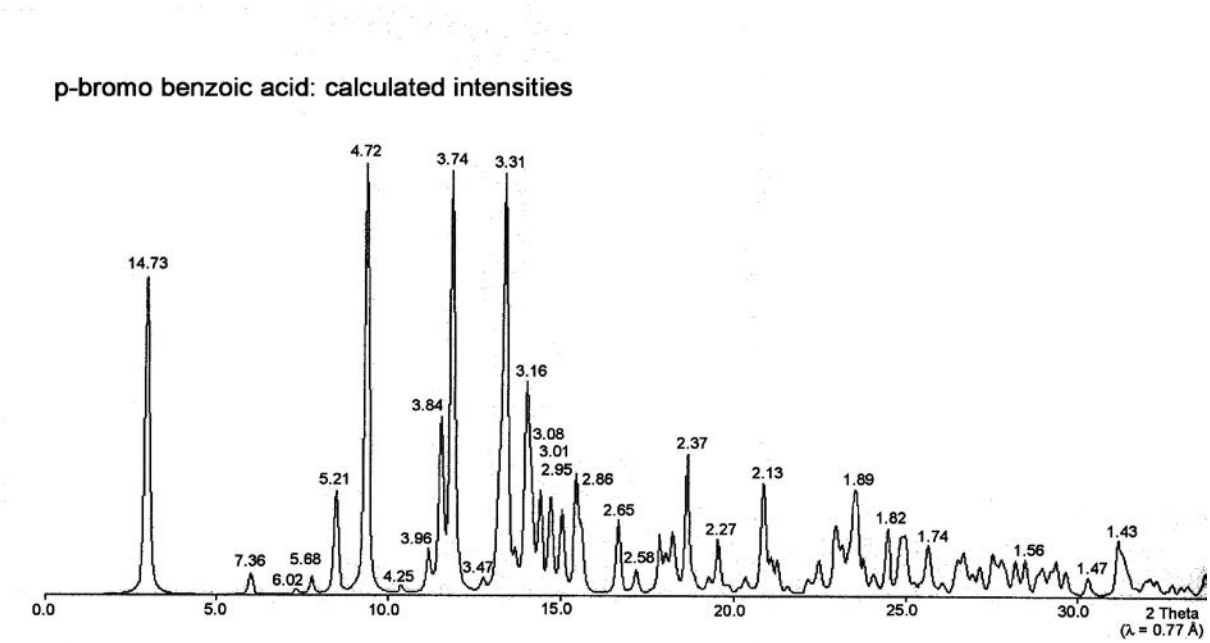

Figure 3. Calculated diffraction pattern of p-bromo benzoic acid. d-spacings are given in Å.

The s-scale for both, the SAXS and the WAXS range, can be obtained by linear regression, i.e., the linear relation between the known s-values of the calibrant versus the measured peak positions has to be found.

A further correction is regarding the flat field response (efficiency) of the detectors. For this correction, the fluorescence light of various foils are used to illuminate the detectors rather homogeneously:

At 8 keV: iron foil (100 μm thick), fluorescence energy: 6.4 keV K_{α}, 7.1 keV K_{β}(effic*.dat)
At 16 keV: copper foil (> 100 μm thick), fluorescence energy: 8.028 keV $K_{\alpha 2}$, 8.048 keV $K_{\alpha 1}$, 8.905 keV K_{β} (effic*.dat)

The measured scattering pattern are corrected for the detector efficiency simply by dividing them by the fluorescence pattern. Note: The average of the detector efficiency data should be set to unity and a small threshold should be applied to avoid any division by zero.

[1] T.N. Blanton et. al., Powder Diffraction 10, (1995), 91
[2] K. Ohura, S. Kashino, M. Haisa, J. Bull. Chem. Soc. Jpn. 45, (1972), 2651

4. AVAILABLE SAMPLE MANIPULATIONS STAGES

1. General

Usually the sample is mounted onto the sample alignment stage which allows the user to place the sample into the beam with a precision of 5µm (resolution: 1µm). In Fig. 5 the ranges for vertical and horizontal alignment as well as the maximum dimensions of the sample holders are given. The maximum weight on the sample stage is limited to 10 kg. In case the envelope dimensions of a sophisticated sample station provided by the users are slightly larger than those given in Fig. 5, the user can ask the beamline responsible for a check up of his space requirements. If it does not fit at all to these specifications, user equipment can also be mounted directly onto the optical table, which allows much larger spatial dimensions.

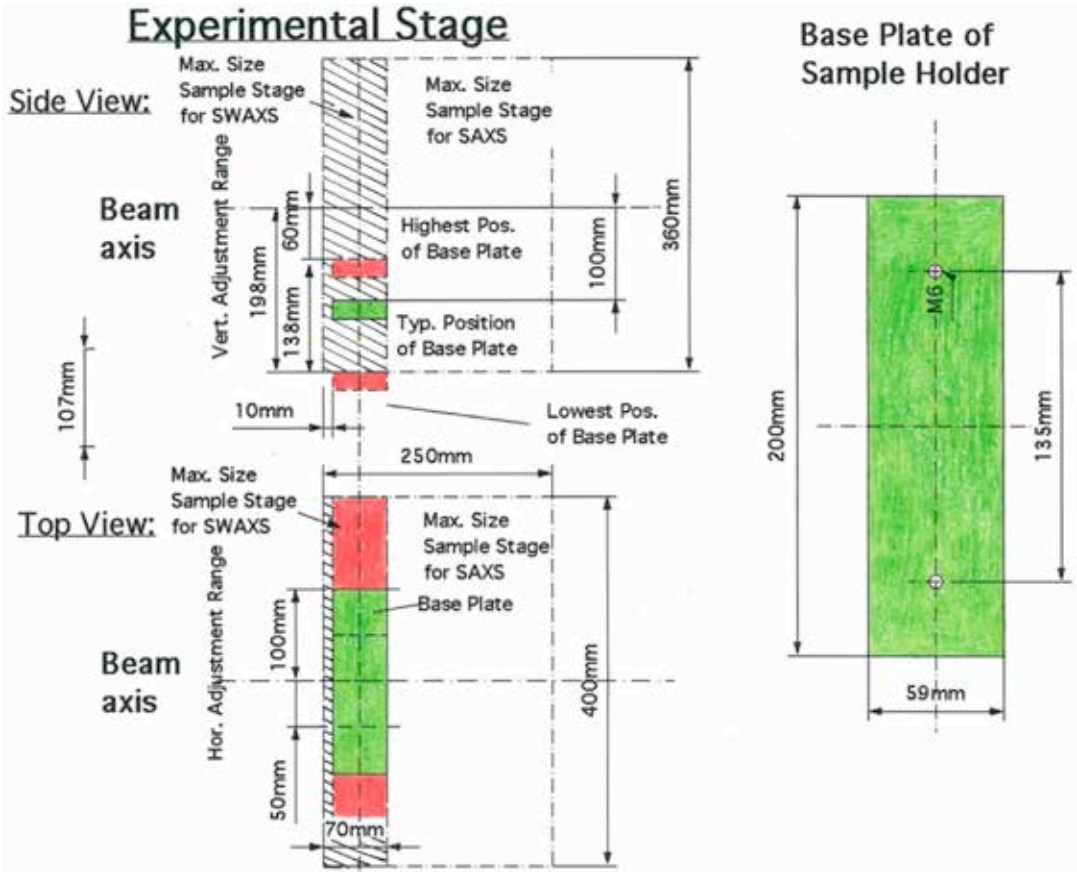

Figure 5. Maximum dimensions and alignment range of the sample holder to be mounted via a base-plate onto the standard alignment stage (left), and dimensions of the base-plate (right).

2. Sample Holders

As standard equipment for liquid samples Paar capillaries (diameter: 1 and 2 mm) are used thermostated with the KPR (Peltier heating/cooling) sample holders (Anton Paar, Graz, Austria). For use in these sample holders flow through capillaries and Gel holders are standard equipment. Temperature scans can be performed with KPR (-30-70 °C). Typically the precision and the stability of this systems is 0.1 °C. Additionally thermostats for temperature control or cooling proposes can be used at the beamline (-40 - 200 °C). Helium and Nitrogen gas bottles are available at the beamline, for other gases please contact the beamline responsible.

Multiple-sample holders can be mounted onto the standard sample manipulator. At present holders are available for measuring in automatic mode up to 30 solid samples at ambient temperature or up to 4 liquid or gel samples in the temperature range 0 – 95 °C.

3. Online Exhaust System

At the experimental station is available a custom-built fume cover and chemical exhaust system for toxic gases. Thus it is possible to e.g. study in-situ chemical reactions, during which toxic gases might develop.

4. Stopped Flow Apparatus

A commercial stopped flow apparatus (manufactured by Bio-Logic, Paris, France), especially designed for Synchrotron Radiation SAXS investigations of conformation changes of proteins, nucleic acids and macromolecules, is available. The instrument consists of a 4-syringe cell with 3 mixer modules manufactured by Bio-Logic. Each syringe is driven independently from the others by an individual stepping-motor, which allows a high versatility of the mixing sequence (flow-rate, flow duration, sequential mixing). For example, injection sequences using one or up to 4 syringes, unequal filling of syringes, variable mixing ratio, reaction intermediate ageing in three- or four-syringe mode etc.. The solution flow can be entirely software-controlled via stepping motors, and can stop in a fraction of a millisecond.

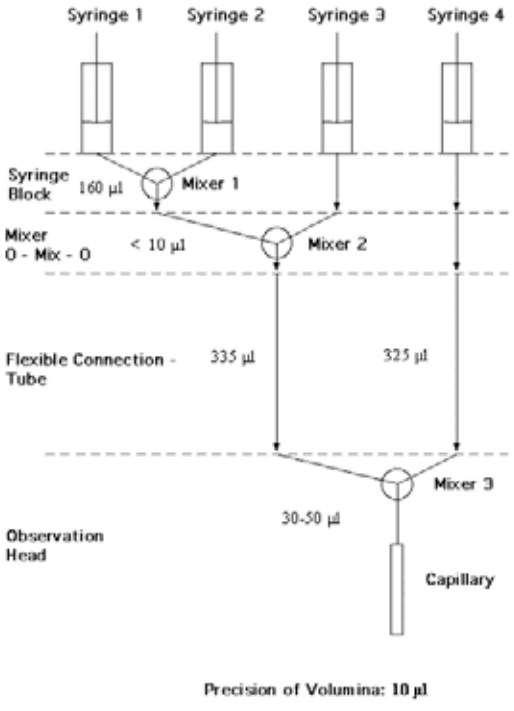

The software allows the set-up of the shot volumes of each of the 4 syringes in a certain time interval. Up to 20 mixing protocols can be programmed. Additionally macros for the repeated execution of individual frames can be defined. Furthermore, the input and output trigger accessible for user operation can be programmed. In the usual operation modus the start of rapid mixing sequence is triggered from our X-ray data-acquisition system (input trigger).

After the liquids have been rapidly mixed, they are filled within few ms into a 1 mm quartz capillary - situated in the X-ray beam- , which is thermostated with a water bath. Depending on the diffraction power of the sample time resolutions of up to 10 ms can be obtained.

Figure 6. Sketch of the stop flow system.

The main parameter of the system are:

- Thermostated quartz capillary (1 mm)
- Temperature stability 0.1 °C
- Total sample used per mixing cycle (shot volume): 100 µl
- Maximum 2θ angle of 45°
- Total Volume 8 ml
- Dead volume 550 µl
- Flow rate: 0.045 – 6 ml/s
- Duration of flow 1 ms to 9999 ms/Phase
- Dead time: 1 ms
- Reservoir volume: 10 ml each

Further information can be found at the webpage: http://www.bio-logic.fr/

5. Grazing Incidence Small Angle X-ray Scattering

Grazing incidence studies on solid samples, thin film samples or Langmuir-Blodget-films can be performed using a specially designed sample holder, which can be rotated around 2 axes transversal to the beam. Furthermore the sample can be aligned by translating it in both directions transversal to the beam. The precisions are 0.001 deg for the rotations and 5 µm for the translations. Usually the system is set to reflect the beam in the vertical direction. According to the required protocol and the actual assembly of the rotation stages ω, θ, 2θ and φ scans can be performed.

6. Temperature Gradient Cell

A temperature gradient cell for X-ray scattering investigations on the thermal behaviour of soft matter manybody-systems, such as in gels, dispersions and solutions, has been developed. Depending on the adjustment of the temperature gradient in the sample, on the focus size of the X-ray beam and on the translational scanning precision an averaged thermal resolution of a few thousands of a degree can be achieved.

7. Flow-through Cell

The flow through cell works in a simple manner: Special quartz capillaries (Glas Technik & Konstruktion, Schönwalde/Berlin) of 1.5 mm diameter and wide openings of about 3 mm at each end, can be inserted into the standard Anton Paar sample holder, which allows various temperature treatments (T-range 25-300 or –30-70 °C, respectively). Thin tubes are connected directly to the capillary ends and a constanst flow is achieved by a peristaltic pump.

8. IR-Laser T-Jump System for Time-Resolved X-ray Scattering on Aqueous Solutions and Dispersions

The Erbium-Glass Laser available at the SAXS-beamline (Dr. Rapp Optoelektronik, Hamburg, Germany) delivers a maximum of 4 J per 2ms pulse with a wavelength of 1.54 μm onto the sample. The laser-beam is guided by one prism onto the sample, which is filled in a glass capillary (1 or 2 mm in diameter) and Peltier or electronically thermostated in a metal sample holder (A. Paar, Graz, Austria). With a laser spotsize of maximal 7 mm in diameter a sample-volume of maximal 5.5 μl or 22 μl, respectively, is exposed to the laser-radiation. In a water-solutions/dispersions with an absorption coefficient of A = 6.5 cm^{-1} T-jumps up to 20°C are possible.

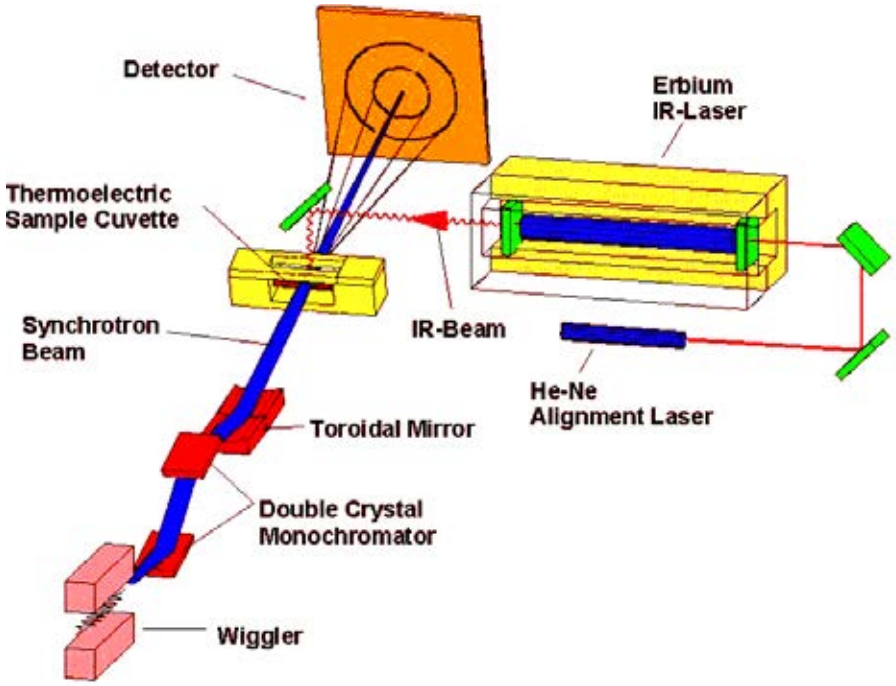

Figure 7. Sketch of the T-jump set-up.

9. High Pressure Cell System

SWAXS measurements of samples under pressure can be performed from 1 to 2500 bar, from 0 to 80 °C in the scattering angle region up to 30 degrees, both in the static or time-resolved mode, e.g. p-jump or p-scan, with a time-resolution down to the ms range. Precise pressure scans of any speed within a broad range (e.g. ca. 1.0 bar/s - 50 bar/s in the case of water as pressurising medium, and a typical sample volume) can be performed. Alternatively, dynamic processes can be studied in pressure-jump relaxation experiments with jump amplitudes up to 2.5 kbar/10ms in both directions (pressurising and depressurising jumps).
In most applications diamond windows of 0.75 mm thickness (each) are used. The transmission of one pair (entrance and exit window) is 0.1 at 8 keV, i.e. lower than 0.3, the value for the originally used 1.5 mm thick Be-windows. However the loss in intensity is more than compensated for by the considerably lower background scattering of diamond thus leading to higher q-resolution in the experiments.
The sample thickness can be 0.6-4.0 mm, with a volume of approximately 0.5-3 mm^3 completely irradiated by pin-hole collimated (< 1.0 mm diameter) X-rays.

The pressure cell system is flexible and can be built according to the needs of the particular experiment. Normally, a liquid (water, ethanol or octanol) is used as pressurising medium. But in principle, also gaseous media can be employed as well. N_2 has been successfully tested, and measurements in supercritical CO_2 became frequent.
Beside bulk measurements on samples in transmission set-up, also grazing incidence experiments using silicon wafer with highly aligned samples on its surface inserted in the high-pressure cell have been carried out successfully.

10. Oxford Cryostream Cooler

The Cryostream cooler creates a cold environment only a few millimeters from the nozzle position. The temperature and the flow of the nitrogen gas stream is controlled and regulated by a Programmable Temperature Controller based on an 'in stream' heater and a thermo-sensor before it passes out over the sample.

The system has been especially developed for X-ray crystallography to perform diffraction experiments on e.g. shock frozen bio-crystals. However, the programmable temperature controller allows further implication for SAXS-experiments, e.g., rapid temperature drops in solvents. The design of the Cryostream Cooler facilitates:

- Nitrogen stream temperatures from -190 to 100 °C
- Stability of 0.1 °C,
- Refill without any disturbance of the temperature at the sample
- Temperature ramps can easily be carried out remotely controlled with scan rates up 6 °C/min
- Individual temperature protocols can be cycled
- T-jumps in both directions can be performed by rapid transfer of the sample in a pre-cooled or -heated capillary using an fast syringe driver reaching a minimum temperature of -80 °C. Here, typical scan rates are about 15 °C/sec with a total process time in the order of 10 sec.

Further information can be found at the webpage: http://www.oxfordcryosystems.co.uk/

11. In-line Differential Scanning Calorimeter (DSC)

The in-line micro-calorimeter built by the group of Michel Ollivon (CNRS, Paris, France) allows to take simultaneously time-resolved synchrotron X-ray Diffraction as a function of the Temperature (XRDT) and high sensitivity DSC from the same same sample.
The microcalorimetry and XRDT scans can be performed at any heating rate comprised between 0.1 and 10 °C/min with a 0.01 °C temperature resolution in the range -30/+130 °C. However, maximum cooling rates are T dependent and 10°C/min rates cannot be sustained below 30°C since cooling efficiency is a temperature dependent process. Microcalorimetry scans can be recorded independently, and also simultaniously, of X-ray patterns. The microcalorimeter head can also be used as a temperature controlled sample-holder for X-ray measurements while not recording a microcalorimetry signal. Isothermal microcalorimetry is also possible when a time dependent thermal event such as meta-stable state relaxation or

self-evolving reaction, is expected. The sample capillaries have a diameter of 1.5 mm and are filled over a length of 10 mm.

12. Tension Cell

Together with the external user group Schulze-Bauer/Holzapfel the research team constructed a general-purpose tension cell. This particular cell was designed for *in-situ* tensile testing with the particular feature that the sample could be completely immersed in a solvent (e.g. physiological solution), which is of particular interest for the blood vessel or collagen fiber testing. The sample container can be attached to a thermal bath to control the temperature in the range from 5 to 95 ºC. A screw with an appropriate opening for the passage of the X-ray beam can adjust the optical thickness of the sample container continuously and optimize the set-up for different sample geometries.
The fully remote controlled system allows to control not only the fiber extension from 0 to 50 mm, but also it records simultaneously the force signal in the range from 0 to 25 N and as an option the optically determined Video extensometer signal to measure the transversal contraction of the sample.

13. Domed Hot Stage

The domed hot stage (model DHS1100 from Anton Paar, Graz, Austria) for in-situ temperature studies operates in the temperature range from 25 to 1100°C, and gas connections allow sample measurements in vacuum or inert gas to avoid oxidation or other chemical reactions of the sample at high temperatures.

The special, dome-shaped X-ray window is made of graphite, which exhibits an excellent combination of good mechanical properties, high temperature resistance and X-ray transmission. Moreover a custom made cover with Kapton windows has been constructed which allows GISAXS measurements at lower temperatures with reduced window background. This cell allows e.g. for variable humidity environment or inert gas flow. Below 200 °C heater temperature, the instrument can be run without dome. The hot stage is light weight, and can be mounted onto our goniometer craddle for GISAXS measurements on thin films or surfaces, as well as on the XY stage for transmission measurements. A transmission cell for 1.5 mm diameter capillaries has been constructed.

Due to the design of dome, heater and sample fixing, very low angles of incidence can be reached and the following types of X-ray measurements can be carried out: grazing incidence small angle scattering, pole figures, grazing incidence diffraction as well as grazing incidence in-plane diffraction. The main applications for the DHS 1100 are to investigate the temperature dependence of crystalline textures, crystal stress and strain, temperature-induced phase transitions as well as structural properties of thin films.

5. AVAILABLE DETECTORS

1. 2D Pilatus 3 1M Detector System

The new Pilatus 3 1M detector system is presented in detail on page 26. For more information: https://www.dectris.com/pilatus3_specifications.html#main_head_navigation

2. 2D Pilatus 100K Detector System

The Pilatus 100K detector system (http://www.dectris.com/sites/pilatus100k.html) operates in "single photon counting" mode and is based on the CMOS hybrid pixel technology: the X-rays are directly transformed into electric charge, and processed in the CMOS readout chips. This new design has no dark current or readout noise, a high dynamic range of 1000000 (20 bits), a read-out time of less than 3 ms, a framing rate of over 200 images/s and an excellent point spread function of < 1 pixel.

3. 2D Image Plate

The Mar300 Image Plate detector with a circular active area of 300mm in diameter is the largest-area detector available to users of the beamline, with a spatial resolution (pixel size) of 150μm. This detector has two modes of operation (180mm or 300mm), depending on the desired active area, which result in image sizes of 1200x1200 and 2000x2000, respectively. They are stored in the mar image format (16 bit for compactness, with higher precision extensions for values out of range), and can be processed and converted using the Fit2D program [1]. Typical applications are those that need a large Q-range with high dynamic range (typical values of 10^5), i.e. solution scattering from proteins and nanoparticles, temperature-step scans, slow processes like nanoparticle formation, mesophase formation, etc. The exposure time for the Image Plate is given in seconds, with typical values between 1 and 60. Readout time depends on the chosen active area (for 180mm mode, about 130 seconds; for 300mm mode, about 210 seconds), and therefore it is not suitable for samples where high time resolution is needed. Exposure information, number of images in the series and other information is automatically written to a summary file after each image.
So far the detector cannot be triggered by an external trigger input. Controlling an additional (external) device or experiment can only be done by hardware wiring of the TTL shutter signal.

4. 2D CCD-Camera System

The CCD (Phtotonic Science, GemStar/XIDIS model) is a high resolution and sensitivity camera, providing a high dynamic range (16 bit) and advanced features such as on-camera binning and external triggering. The camera is fully software-controlled using the Image Pro Plus software, and connects to the controlling computer via a Hi-Speed USB interface.

Camera specifications:

Sensitive area	82 x 74 mm (110 mm diagonal)
Image size	2048 x 2048
Pixel size	43 μm
Dynamic range	16 bit (20 bit in exposure fusion mode)
Binning	x1, x2, x4, x8 (independent X and Y, on-chip and in software)
Interface	external triggering, external gating (3.3V TTL)
Intensifier gain	12 bit (0-4095 levels, approx 200:1 max gain)
Exposure time	<1ms to 30 min
Frame rate	at x1 binning, ~800 ms readout time per frame at x8 binning (on-chip), ~145 ms readout time per frame
Image format	16bit TIFF native (Image Pro Plus allows exporting to other formats as well)

5. 1D Vantec Detector

Two identical one-dimensional high-count rate capable Vantec-1 Detectors from BrukerAXS Inc. are available. They have each an active area of 50 x 16 mm, and can be used together mounted in-line to increase the active area. They have a spatial resolution of about 50 μm, which is smaller than the resolution obtained by the presently used Gabriel Type Gas detectors. Moreover its new gas amplification principle based on the Microgap technology [1] allows much higher count rates compared to the old system. Now the main limitation is the data acquisition system with its maximum integral count rate of about 1 MHz. In the present data acquisition system HCI (Hecus X-ray Systems, Graz, Austria) the detector has the following performance:

- Minimal time resolution: 11 μs
- Maximum No. of frames: 512 (depending on the no. of channels)
- Maximum integral count rate: 1 MHz

6. 1D Gabriel-type Detector System

Two 1D Gabriel-type detectors are available, which feature both 1024 pixels. The smaller detector has an entrance window size of 8 x 100 mm, and an active length of 86.1 mm with a resolution of 0.135 mm/channel. The larger detector has an entrance window size of 10 x 150 mm, and an active length of 134 mm with a resolution of 0.159 mm/channel. They can be used simultaneously, and are run with the data acquisition system HCI (Hecus X-ray Systems, Graz, Austria). This detector system has the following performance:

- Minimal time resolution: 11 microsec
- Maximum No. of frames: 512
- Maximum integral count rate: 40 kHz

6. OFFLINE SAXS SUPPORT LABORATORY

The laboratory consists of two rooms: the chemistry lab, which has been renewed during 2013, serves mainly for sample preparation and analysis for both, in house research and external SAXS user groups. In the X-ray laboratory is available a SWAXS camera for simultaneous small and wide-angle scattering (Hecus X-ray Systems, Graz, Austria: www.hecus.at), which allows on-site testing of samples before moving on to the SR beamline.

Figure 4. View of the Chemistry laboratory (left) and X-Ray laboratory (right).

Standard glassware, syringes and needles of different sizes, µ-pipettes (p10 - p100 - p200 - p1000), as well as some standard chemical reagents (e.g., chloroform, ethanol, methanol) and deionized water (milli-RO and ultrapure milli-Q water) is available.

The chemistry lab is further equipped with:

- micro centrifuge (max. 13200 rpm; model 5415D from Eppendorf, Hamburg, Germany)
- Chemical fume hood, equipped with a carbon filter for general organic solvents (model GS8000 from Strola, Italy)
- vacuum drying oven (min. pressure 1 mbar; max. T: 200 °C, precision +/- 0.4 °C; Binder WTB, Tuttlingen. Germany)
- balance (min.-max.: 0.001 - 220 g; model 770 from Kern & Sohn, Balingen, Germany)
- Magnetic stirrer with heating plate and thermometer, temp max 260 °C
- vortex for microtubes (model REAX from Heidolph, Schwabach, Germany)
- two water baths :
  - Unistat CC, freely programmable in the range from -30 to 100°C (Huber, Offenburg, Germany);
  - Lauda M3, available for heating only (Lauda-Könighofen, Germany)
- ultrasonic bath with water heater (VWR International, Milano, Italy)
- Ultrasonic processor equipped with a 3 mm probe (Sonics VCX130, SY-LAB Geräte GmbH, Germany)
- HPLC pump, Pharmacia LKB; working range, 0,01-9,99 ml/min, 0,1-40MPa
- HPLC pump, Gilson 307; working range, 0,01- 5 ml/min, 0,1-60MPa
- three-syringe pump, low pressure; flow rate range, 1µl/hr – 2120 ml/hr (TSE Systems GmbH, Germany)

- four-syringe pump, high pressure: P max ~ 60 bar (Harvard Apparatus, Holliston, Massachusetts, USA)
- three high pressure infusion modules: P max ~ 690 bar (Teledyne Isco, Lincoln, NE, USA)
- fridge (+ 4°C) and freezer (- 20 °C)

- **UV-VIS spectrometer:** Besides a standard 10 mm path length cuvette holder, the UV-VIS spectrophotometer (Cary 60, Agilent Technologies) is equipped with a Slide-Mounted External Specular Reflectance accessory which allows specular reflectance measurements to be made at a fixed angle of 30°. This accessory is suitable for studies of the film thickness on metallic substrates and measurements of epitaxial film thickness. Interchangeable masks for examining small samples or small areas of large samples are provided (3 mm, 6 mm and 13 mm diameters).
  The instrument can also be used for *in situ* measurement on liquid samples, through two optic fibers: a Torlon fiber probe, diameter 10 mm, for aggressive solutions, and a µprobe, 3.5 mm diameter, 10 mm fixed path length, for smaller volumes (approx. 500 µl).
  Specifications: double beam Czerny-Turner monochromator, wavelength range 190–1100 nm, fixed spectral bandwidth 1.5 nm, minimum scan rates of 24,000 nm/min (full wavelenght scan time <3s), maximum measurement rate 80 data points/sec

- **FT-IR spectrometer** (Alpha-T, Bruker Optics): equipped with the following modules for the analysis of different types of samples:
  - standard sample holder for transmission measurements,
  - single reflection diamond ATR sampling module for powder and solid analysis, which, due to the wide free working area around the crystal (approx. 350°), allows the analysis of large samples. Specifications: One-reflection Diamond crystal, spectral range: 375 - 7,500 cm^{-1}, working distance (max. sample height): >20 mm
  - sampling module for contactless reflection measurements in front of the spectrometer. Specifications: spectral range: 375-7.500cm^{-1}, measurement spot: 6 mm diameter, appr. 15 mm in front of the spectrometer

User Contributions

Material Science

GROWTH OF ANISOTROPIC GE QUANTUM DOT LATTICE IN ALUMINA MATRIX

M. Buljan[1], O. Roschupkina[2], A. Šantić[1], V. Holý[3], C. Baehtz[2], A. Muecklich[2], L. Horak[3], V. Valeš[3], N. Radić[1], S. Bernstorff[4], J. Grenzer[2]

1.) Ruđer Bošković Institute, Zagreb, Croatia
2.) Helmholtz-Zentrum Dresden-Rossendorf, Germany
3.) Department of Condensed Matter Physics, Charles University, Prague, Czech Republic
4.) Elettra - Sincrotrone Trieste S.C.p.A., Trieste, Italy

An anisotropic lattice of Ge quantum dots embedded in amorphous alumina was produced by magnetron sputtering deposition. A specific deposition geometry with oblique incidence of Ge and Al_2O_3 adparticles was used to achieve the anisotropy. The observed quantum dot ordering is explained by a combination of directional diffusion of Ge and Al_2O_3 adparticles and a shadowing process which occurs during deposition as a result of the specific surface morphology. The prepared material shows a strong anisotropy of the electrical conductivity in different directions parallel to the sample surface.

Simple processes for the preparation of regularly ordered lattices of semiconductor quantum dots (QDs) embedded in dielectric amorphous matrices play an important role in various nanotechnology applications. Of particular interest are QD lattices with properties that differ significantly in different directions parallel to the material surface.

In our past work [1-3] we have analysed the preparation and ordering properties of isotropic Ge QD lattices in different amorphous matrices produced by magnetron sputtering deposition. The regularity in the QD positions was achieved by a self-assembly process during the films growth, which is based on the surface morphology influence on Ge nucleation places. However, our previous depositions were all performed using a standard substrate stage which rotates during the deposition. This ensures the homogeneity of the films, but the regular ordering of QDs appears in domains, randomly rotated around the surface normal.

In our most recent work [4] we examined the ordering in ten period $(Ge+Al_2O_3)/Al_2O_3$ multilayer prepared also by magnetron sputtering deposition but under specific deposition geometry. We used small sputtering targets, a close distance between the substrate and targets, and a fixed substrate stage (held at a temperature of 573 K) during deposition. Under such conditions, the Ge and Al_2O_3 adparticles coming to the substrate from the sputtering targets have a preferential diffusion direction and a non-vanishing in-plane (tangential) component of their velocities. The growth of the Ge QDs and alumina matrix is not isotropic under such conditions due to the combination of directional diffusion of adparticles and shadowing effects caused by Ge QDs.

The result of such deposition is formation of an anisotropic lattice of Ge QDs embedded in amorphous alumina matrix. The details of the QD ordering properties in these films were investigated at the SAXS beamline of the synchrotron Elettra. Different directions of the probing x-ray beam with respect to the preferential diffusion direction of adparticles were used. Two specific cases, i.e. grazing incidence small angle x-ray scattering (GISAXS) maps taken with the x-ray beam set parallel and perpendicular ($\parallel$ and $\perp$) to the diffusion direction are demonstrated in Fig. 1a and Fig. 1b. The different arrangement of Bragg spots in them demonstrates clearly the anisotropy in the material structure. The anisotropy occurs along the diffusion direction of the Al_2O_3 adparticles. The anisotropy is also nicely visible in the TEM cross-sections of the film (Fig. 1c and Fig. 1d), where the correlation direction of the QD ordering is different for the parallel and perpendicular cross-sections. The GISAXS map of the film deposited under standard, isotropic conditions and using a rotational stage (Fig. 1e) is symmetrical and looks the same for all probing x-ray directions due to the existence of randomly distributed domains. The numerical analysis of the GISAXS maps obtained using

the paracrystal model [5], shows, that the resulting ordering in the system is a distorted body centred tetragonal (BCT) lattice, tilted toward the alumina target, which is schematically illustrated in Fig. 1f and Fig. 1h.

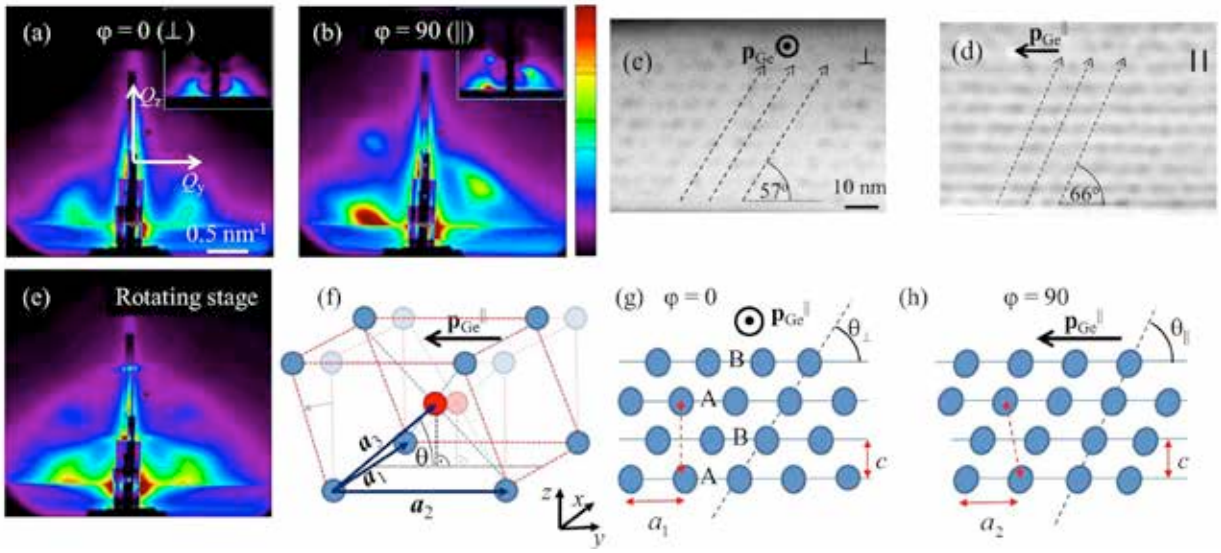

Figure 1. Structural properties of the films. (a), (b) GISAXS maps measured for parallel (||) and perpendicular (⊥) direction of the probing x-ray beam with respect to the main direction of the adparticle diffusion (the insets show the corresponding simulations), and (c), (d) the corresponding TEM images of the films cross-sections. (e) GISAXS map of a film deposited under standard isotropic conditions. (f) Structure of the anisotropic QD lattice. It is distorted along the *y* axis with respect to the ideal BCT lattice, which is shown by light symbols. (g) and (h) Simulations of the QD ordering found by GISAXS analysis. [M. Buljan *et al.* J. Appl. Cryst. 46, 709 (2013) Copyright (2013) IUCr Journals, International Union of Crystallography, http://dx.doi.org/10.1107/S0021889813008182].

The prepared materials show also a strong anisotropy in their electrical properties. The conductivities measured in directions parallel and perpendicular to the main diffusion direction differ by an order of magnitude. Such a big difference is explained by the structural properties of the films. More precisely, the conductivity in QD-based materials is highly influenced by the hoping probability between neighbouring QDs, and it decreases exponentially with the QD separation. The QD separations for various directions, found by GISAXS analysis, significantly differ. Due to difference in QD separations along the paths used for conductivity measurements, the large anisotropy in the electrical transport properties occurs.

References:

[1] M. Buljan, U.V. Desnica, G. Dražić, M. Ivanda, N. Radić, P. Dubček, K. Salamon, S. Bernstorff, V. Holý; Phys. Rev. B **79**, 035310 (2009)

[2] M. Buljan, N. Radić, I. Bogdanović-Radović, Z. Siketić, K. Salamon, M. Jerčinović, M. Ivanda, G. Dražić, S. Bernstorff, Phys. Status Solidi A, **210**, 1516–1521 (2013)

[3] M. Buljan, N. Radić, M. Ivanda, I. Bogdanović- Radović, M. Karlušić J. Grenzer, S. Prucnal, G. Dražić, G. Pletikapić, V. Svetličić, M. Jerčinović, S. Bernstorff, V. Holy. J. Nanoparticle Res. **15**, 1485 (2013)

[4] M. Buljan, O. Roshchupkina, A. Šantić, V. Holý, C. Baehtz, A. Mücklich, L. Horák, V. Valeš, N. Radić, S. Bernstorff , J. Grenzer, J. Appl. Cryst. **46** 709-715 (2013)

[5] M. Buljan, N. Radić, S. Bernstorff, G. Dražić, I. Bogdanović-Radović,V. Holý, Acta Cryst. A, **68**, 124 (2012)

FORMATION OF P123-MEDIATED AU-NANOPARTICLES IN AQUEOUS SOLUTION: IN-SITU X-RAY SCATTERING STUDY

P. Chatterjee[1], S. Datta[1], S. Jana[1], S. Hazra[1] and H. Amenitsch[2]

1.) Saha Institute of Nuclear Physics, 1/AF Bidhannagar, Kolkata 700064, India
2.) Insitute of Inorganic Chemistry, Graz University of Technology, NAWI Graz, Stremayrgasse 9, Graz, Austria

Metal nanoobjects are attracting significant attention because of their size dependent optical, magnetic, electronic, and catalytic properties. Among them, gold nanoparticles (AuNPs) with desirable structures and functions are of special interest due to their various applications in biology, medicine, catalysis and sensors [1,2]. There are various physical and chemical methods for the synthesis of AuNPs. Among them, the solution-phase chemical reduction method is one of the widely used methods to synthesize and stabilize monodispersed AuNPs. The whole process involves the use of four basic materials, namely solvent, metal salt, reducing agent and stabilizing agent. Recently, a lot of work is going on to develop simple, versatile, environment-friendly and economically viable methods for the preparation of AuNPs. In this direction, attempts are made to synthesize and stabilize AuNPs in a single step from aqueous solution of gold salt using water-soluble triblock copolymer (TBP) at ambient temperature [3-5]. TBPs belong to a special category of nonionic surfactants. The most widely used TBPs (with the commercial name of Pluronics) are polyethylene oxidepolypropylene oxide-polyethylene oxide (PEO-PPO-PEO) with different composition of hydrophilic PEO and hydrophobic PPO blocks. In the aqueous solution, TBPs form micelles. The hydrophobic PPO blocks form the core of these micellar aggregates, whereas the hydrophilic PEO ones form the corona. TBP can act as reducing and stabilizing agent and has been utilized to form nanoparticles. However, the control the size of the nanoparticles and their yield are poor, which need large improvement. For that monitoring the formation of the naoparticles, in-situ, using different complementary techniques, is very essential. X-ray scattering in general [6-9], while SAXS and WAXS in particular, can provide complementary information about polymer coated AuNPs and core AuNPs.

In order to monitor the formation of the nanoparticles, solutions were prepared by dissolving TBP and Au salt in water. P123 [PEO_{20}-PPO_{70}-PEO_{20}] is taken as TBP, while hydrogen tetrachloroaureate (III) hydrate [$HAuCl_4.3H_2O$] as Au salt. Solutions were prepared in glass beaker for 5 wt% of P123 and four different concentration (1, 2, 3 and 4 mM) of Au salt. After preparation, the solution was transferred quickly to a Kapton window based teflon cell and was placed to the sample stage of the goniometer (SAXS beam line, Elettra), where *in-situ* SAXS or WAXS measurements were carried out separately at energy 8 keV. For SAXS measurements a 2D detector (image plate mar300, Marresearch GmbH, having 2000 x 2000 pixels with pixel size 150 x 150 μm^2) was placed about 135 cm downstream of the sample, while for the WAXS measurements a 2D detector (PILATUS 100k, Dectris, having 487 x 195 pixels with pixel size 172 x 172 μm^2) was placed about 20 cm apart from the sample. The transparent colourless solution of P123 becomes colourful with time due to the AuNPs formation. Such coloration become fast compared to that observed in India, where UV-vis and DLS studies were carried out.

The SPR peak position obtained from the UV-vis spectra of the solutions increases with Au salt concentration, suggesting an increase in the AuNPs size. However, the intensity of the SPR peak increases with concentration up to 3 mM then decreases, indicative of some optimum value of Au salt concentration for conversion. LMCT peak intensity increases with Au salt concentration, however, for 1 and 2 mM solutions the intensity decreases gradually with time, while for 3 and 4 mM solutions the intensity increases up to about 30 min then decreases. A fast increase in the SPR peak intensity is also observed for 3 and 4 mM solutions

up to 30 min. This suggests that the LMCT complex formation continues up to 30 min, which is visible for the 3 and 4 mM solutions. The SPR peak intensity for all the solutions nearly saturate after 2 h. Considering different parameters, such as SPR and LMCT peak intensity for normalized concentration and corresponding P123 amount, optimum conversion observed for solution of 3mM Au salt. The size distribution of normal P123 micelles and after inclusion of Au salt are obtained from DLS measurements. The average size for the normal P123 micelles is found to be 18 nm. With the addition of Au salt large size particles (about 200 nm) are formed. This is due to the AuNPs loaded hybrid micelles. The amount of this hybrid particles increases with the Au salt concentration in expense of normal size micelles. Maximum amount is reached for 3 mM solution.

SAXS patterns show two peaks corresponding to two different size particles/clusters. The positions of the peaks remains fixed with time indicating no change in size of the particles/clusters, while a small increase in intensity is observed indicating an increase in the number of the particles/clusters. Such change is prominent within 20 min. WAXS patterns of the solution were also collected with time. After proper background subtraction, prominent (111) and weak (002) peaks of Au are visible. Almost no change in the width of the prominent peak, indicating no change in size of the Au particles, while a small increase in intensity is observed indicating an increase in the number of the particles. It can be noted that an increase in the background or amorphous intensity is found with time. Even considering that the peak (i.e. difference) intensity first increases and then saturates. Such change is again within 20 min. Similar is the situation for the other concentrations as well.

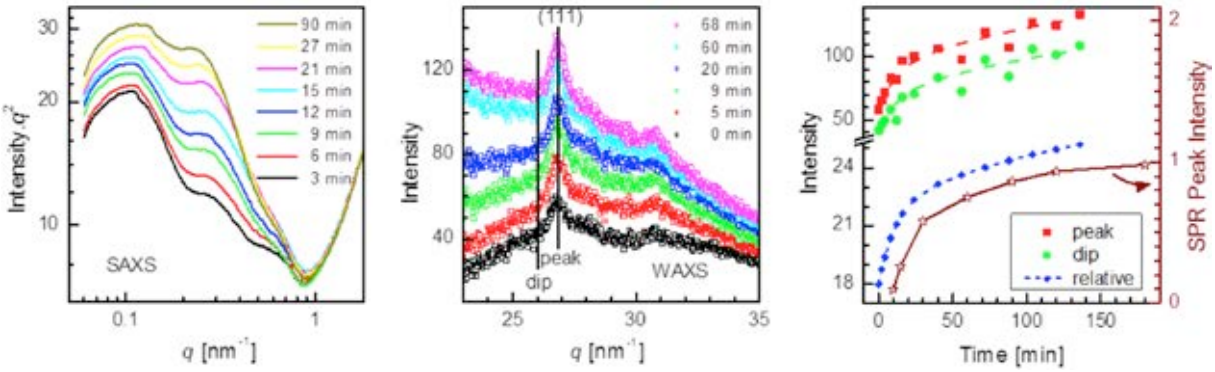

Figure 1. Left: Time-evolution of SAXS pattern of a P123 + $HAuCl_4$ + H_2O ternary mixture solution (intensity is multiplied with q^2 to enhance the features), Middle: Time-evolution of WAXS pattern of a P123 + $HAuCl_4$ + H_2O ternary mixture solution, Right: Corresponding variation of peak, dip and their expected difference in intensities with time. Also time-evolution of the SPR peak intensity as obtained from UV-vis spectra.

The Au NPs formation dynamics is found fast from the SAXS and WAXS studies, which is in contrary to the study carried out in India using in-situ UV-Vis and DLS techniques (see Fig. 1). We really need to understand the reason behind such fast dynamics. It is often found that light can also play some role in the growth of nanoparticles, which needs to be taken care. Thus the present experimental result is really interesting but needs further verification, which we are planning for next time. On the other hand, if the dynamics is really fast then special experimental arrangement is needed for proper understanding.

References:

[1] I. H. El-Sayed, X. Huang and M. A. El-Sayed, Nano Lett. **5**, 829 (2005)
[2] M.-C. Daniel and D. Astruc, Chem. Rev. **104**, 293 (2004)
[3] T. Sakai and P. Alexandris, Langmuir **20**, 8426 (2004)
[4] P. Khullar, A. Mahal, V. Singh, T. S. Banipal, G. Kaur and M. S. Bakshi, Langmuir **26**, 11363 (2010)
[5] D. Ray, V. K. Aswal and J. Kohlbrecher, Langmuir **27**, 4048 (2011)
[6] S. Hazra, Appl. Surf. Sci. **253**, 2154 (2006)
[7] P. Chatterjee, S. Hazra and H. Amenitsch, Soft Matter **8**, 2956 (2012)
[8] H. Koerner, R. I. MacCuspie, K. Park and R. A. Vaia, Chem. Mater. **24**, 981 (2012)
[9] P. Chatterjee and S. Hazra, J. Phys. Chem. C **118**, 11350 (2014)

SYNCHROTON RADIATION SMALL-AMGLE X-RAY SCATTERING STUDY ON ENHANCED TOUGHNESS OF UHMWPE

M. D'Acunto[1], F. Di Puccio[2] and H. Amenitsch[3]

1.) Istituto di Struttura della Materia, Consiglio Nazionale delle Ricerche, ISM-CNR, via Fosso del Cavaliere, 100, 00133, Rome, Italy
2.) Department of Civil and Industrial Engineering, University of Pisa, Largo Lucio Lazzarino, 56126 Pisa, Italy
3.) Insitute of Inorganic Chemistry, Graz University of Technology, NAWI Graz, Stremayrgasse 9, Graz, Austria

Wear of conventional Ultra High Molecular Weight Polyethylene (UHMWPE) has historically been recognized as the primary cause of soft-on-hard hip implant failure and revision. These implants are characterized by an acetabular cup made of UHMWPE and a femoral component of a cobalt–chromium alloy, figure 1. In the last fifteen years, understandings of the wear mechanisms of UHMWPE highlighted the fundamental role of multi-directional sliding, known as the Cross-Shear (CS) effect [3,4]. Several wear models have been proposed for taking into account such anisotropic surface damage. However, a precise validation has still not been achieved, because of the extreme complexity of the phenomenon and of the remarkable difficulties in the analysis of the microstructure of the material. Most observations are focused on pin-on-plate experimental tests, where a uniform wear behavior of the pin contact surface can be assumed, and were extended to the artificial joints from more global assessments (total wear volume, wear depth.
In this study, worn cups of UHMWPE were observed by means of different advanced instrumentations, to investigate the microstructure of the worn plastic surface. The aim of the present study was to employ some experimental techniques for topographical analysis to investigate the microstructure of UHMWPE cups specimens tested *in vitro* by means of a hip simulator. In order to ease the identification of the local loading/kinematic conditions experienced by the cup surface, a mathematical model developed by the authors in previous studies was applied.

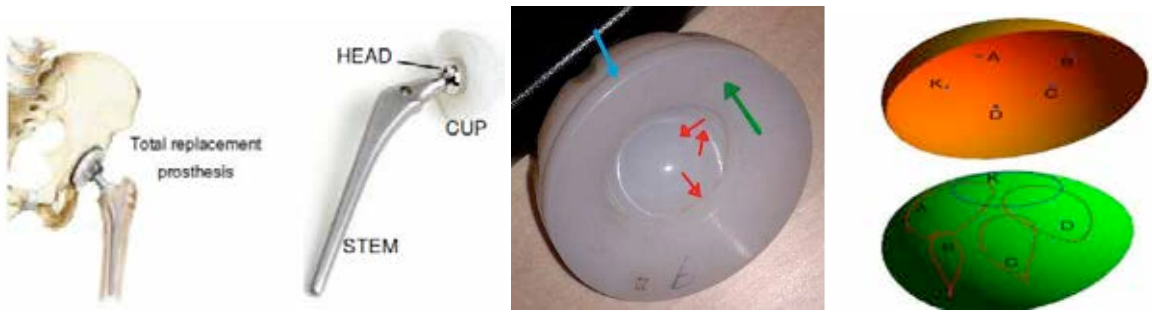

Figure 1. From left to right. Metal on Plastic Hip implant, left. Red arrows indicate the locations where the worn samples were taken, blue and green arrows represent the unworn sample locations, middle image. Selected cup points with different contact pressure, right. For details, see reference [1]

Among the different techniques used, FTIR, AFM, SEM, Small Angle X-ray Scattering (SAXS) can highlight lamellar periodic structures that are an indication of pre-fracture o pre-wear regimes. Finally, to assess the structural features of unworn and worn specimens, SAXS experiments were performed. The measurements were carried out at the Austrian SAXS beamline located at the Synchrotron Radiation Facility ELETTRA in Trieste, Italy, using an X-ray energy of 8 keV and an image plate detector (MAR 300) or a Pilatus 100K pixel detector. The peak position of periodic structures with long periods (*Lp*) can be found in agreement with the Bragg's law, $Lp = 2\pi/q$, where $q = (4\pi/\lambda)\sin\theta$, λ is the X-ray wavelength used and 2θ is the scattering angle. The results showed the presence of lamellar structures

with the long periods *Lp* for both worn and unworn samples, figure 2. SAXS data reveal periodic structures with periodicity Lp ≅ 4.8nm both for worn and unworn samples, but not lamellar periodic structures on larger spatial distances.

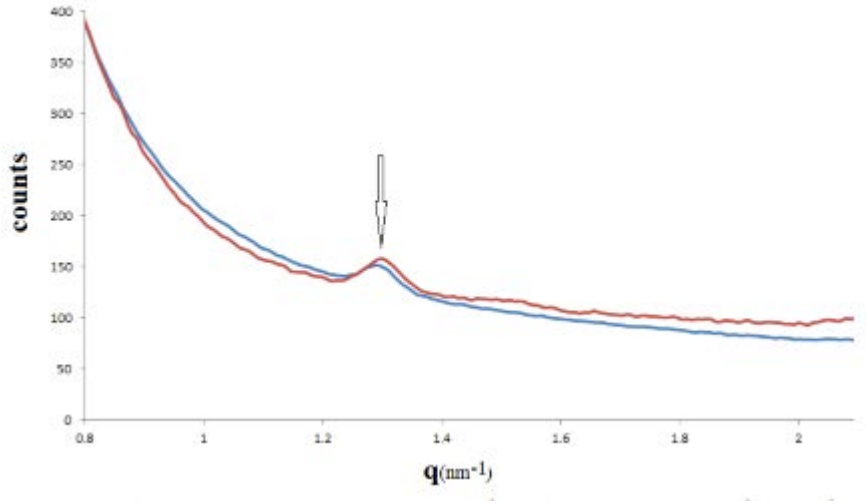

Figure 2. SAXS scattering plot for worn (red) and unworn (blue) UHMWPE samples

References:

[1] F. Di Puccio, L. Mattei, M. D'Acunto, S. Battaglia, S. Affattato, R. Ishak, S. Dinarelli, H. Amenitsch Experimental and Numerical Analysis of UHMWPE acetabular cups after wear test: a preliminary study. Proceedings of the World Tribology Conference 2013, Turin, Italy, 2013)

ALUMINIUM NANO PARTICLES FOR FUTURE PHOTOVOLTAIC APPLICATIONS

P. Dubček[1], B. Pivac[1], N. Radić[1] and S. Bernstorff[2]

1.) Ruđer Bošković Institute, Bijenička 54, 10000 Zagreb, Croatia
2.) Elettra - Sincrotrone Trieste, SS 14, km 163.5, Basovizza (TS), Italy

Doping of photovoltaic devices with plasmonic nanoparticles leads to a power conversion efficiency improvement that can reach 20%. Good control of size and space distribution is crucial for future device applications.

Silver nanoparticles have been introduced into photovoltaics in attempt to improve their efficiency. The success was partial: the photocurrent improved for longer wavelengths, but an additional loss was detected at shorter wavelenghts. Problems were encountered in the attempts to shift the plasmonic frequencies of silver towards higher energies. In this respect aluminium appears to be a better candidate, since its plasmonic frequencies are easily shifted from infra-red to ultra-violet, provided it is present in form of nanoparticles that have a well defined shape and size. Additionally native oxide of aluminium is more transparent to visible light than silver one.

Here we report an investigation of post-annealed magnetron sputtered aluminium thin film on monocrystalline silicon. Atomic Force Microscopy (AFM) and Grazing Incidence Small Angle X-ray Scattering (GISAXS) were employed in the size and size distribution investigation. Aluminium nanoparticles were prepared from post-annealed magnetron sputtered thin film on monocrystalline silicon. The deposition was carried out at room temperature, and the samples were annealed at different temperatures up to 500ºC for one hour.

Aluminium film is present at lower annealing temperatures (vertical fringes in GISAXS in Fig. 1.). At 450° C the film is dissolved. At that temperature, together with larger particles also smaller particles are still present and these are possibly oxide built out of native oxide when the sample is brought in contact with air.

The variation of the particle sizes with increasing film thickness and temperature is displayed in Fig. 2. We also found that up to 300° C, the formed particles are densely packed, and their sizes are increasing with the film thickness, although not at the same rate. Above 350-400° C a bimodal size distribution is observed, with sizes centered around 100-200 nm and 25-50 nm. The optimum initial thickness of the film appears to be in 10-20 nm range.

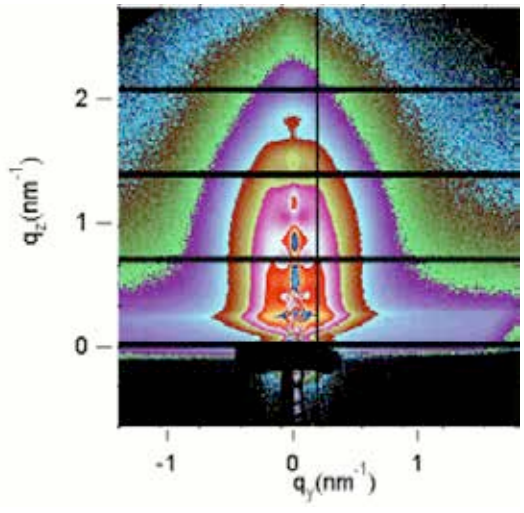

Figure 1. GISAXS from 20nm thick Al film annealed at 250°C

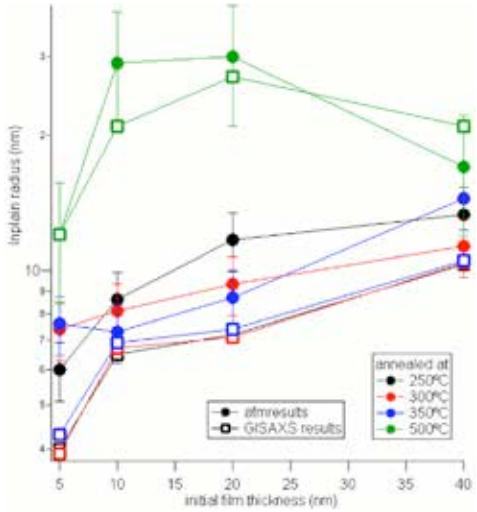

Figure 2. Al nanopaticle sizes vs initial film thickness for several annealing temperatures

NANOIMPRINTED COMB STRUCTURES FOR INORGANIC-ORGANIC HYBRID SOLAR CELLS

S. Dunst[1], T. Rath[1], A. Radivo[2], E. Sovernigo[2], M. Tormen[2], H. Amenitsch[3], B. Marmiroli[3], B. Sartori[3], A. Reichmann[4], A.-C. Knall[1], G. Trimmel[1]

1.) Institute for Chemistry and Technology of Materials, Graz University of Technology, Stremayrgasse 9, 8010 Graz, Austria
2) IOM CNR, Laboratorio TASC Area Science Park - Basovizza, S.S. 14 Km 163.5, 34149 Trieste, Italy
3) Institute of Inorganic Chemistry, Graz University of Technology, Stremayrgasse 9, 8010 Graz, Austria
4) Institute for Electron Microscopy and Nanoanalysis, Graz University of Technology & Centre for Electron Microscopy Graz, Steyrergasse 17, 8010 Graz, Austria

Hybrid solar cells have active layers which consist of conjugated polymers and inorganic semiconducting nanoparticles. They combine the beneficial properties of inorganic solar cell materials with the easy processability of polymeric materials and show already encouraging efficiencies of up to 5% [1].
Two major prerequisites for optimal function include large interfaces between these two materials, providing effective charge separation, but also continuous pathways for transporting the separated charge carriers to the respective electrodes. At present, blending both materials to bulk-heterojunctions is most effective; the complicated control of their morphology is one of the most essential topics in current research on hybrid solar cells.
A vertically bicontinuous and interdigititated heterojunction between the organic and inorganic phase is regarded to as an ideal structure for optimal charge separation as well as charge transport [2].
In this study, we investigate the possibility to realise interdigitated comb hybrid structures by the combination of nanostructured thin layers of a conjugated polymer (i.e. poly[9,9-dioctyl-2,7-silafluorene-co-alt-5,5-(4´,7´-di-2-thienyl-2´,1´,3´-benzothiadiazole)] – PSiF-DBT) prepared by nanoimprint lithography and the metal xanthate route for the preparation of metal sulphides by temperatures below 200 °C [3].
Thus in a first step the thermal stability of NIL-structured polymer layers was investigated by a time resolved GISAXS using a heating cell (DHS 1100 from Anton Paar GmbH) under nitrogen atmosphere. In Figure 1, a scanning electron microscopy image of such a NIL strudctured PSiF-DBT film is shown.

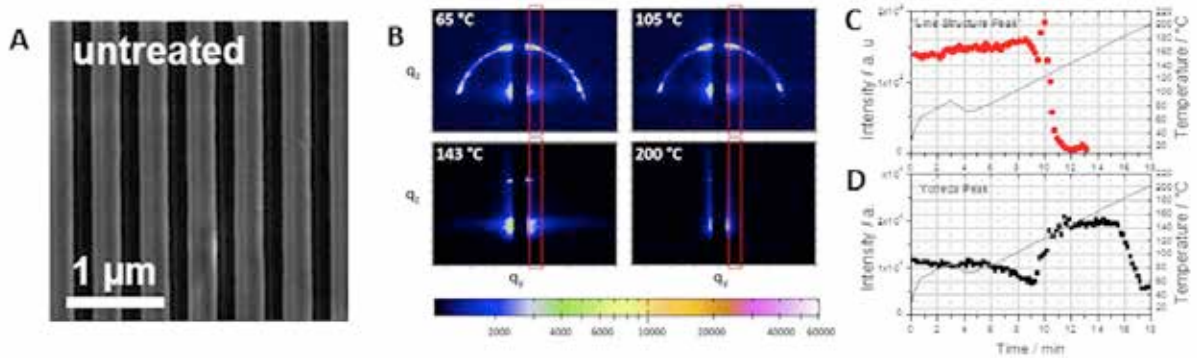

Figure 1. A: Scanning electron microscopy image of a NIL-structured polymer layer; B: GISAXS images of a NIL-structured PSiF-DBT film at 65, 105, 143 and 200 °C. The red boxes indicate the vertical areas for integration; C: Temperature-dependent changes in intensity of the "line structure peak" at approx. q = 0.9 nm^{-1}; D: Temperature-dependent changes in intensity of the Yoneda Peak at approx. q = 0.55 nm^{-1} (reproduced by permission from [4], copyright (2014) American Chemical Society)

Figure 1B shows the GISAXS patterns of a nanostructured PSiF-DBT film on a silicon substrate at different temperatures (65, 105, 143 and 200 °C) during the heating run to 200 °C (heating rate: 10 °C/min). At temperatures lower than 120 °C, a semicircle like chain of

intensity maxima is visible, which is typical for periodic line structures oriented parallel to the X-ray beam [5]. By further increasing the temperature, this semicircle like pattern vanishes and only a feature near to the beam stop, which represents also the most intense area of the semicircle at lower temperatures, remains.

At low temperatures, the scattering signal exhibits two distinct peaks, the Yoneda peak at around q = 0.55 nm^{-1} and the peak stemming from the periodic line structure at approx. q = 0.9 nm^{-1}. The latter is visible up to a temperature of 143 °C, before it vanishes. This is visualized in more detail in Figure 1C, where the temperature-dependent intensity of this peak (extracted from Lorentz fits) is plotted. The intensity stays almost constant up to a temperature of about 110 °C. At this temperature, the peak starts to become weaker until it decreases steeply at 130°C. In this temperature range, the glass transition temperature of PSiF-DBT is assumed to be. Above a temperature of 140-145 °C the peak is not detectable any more in the in-plane scattering signal. The intensity of the Yoneda peak with increasing temperature is shown in Figure 1D. The peak intensity increases in the same temperature range in which the "line structure peak" steeply decreases. The increase in intensity of the Yoneda peak indicates that the nanostructured polymer layer becomes rougher in this temperature range, which leads to the conclusion that the ordered well defined layer has changed to a rougher and more disordered structure. At about 180°C, the roughness decreases again, which might be an indication of a flattening effect caused by the softening of the polymer.

In further experiments, we used these NIL-templated thin films to realize nanostructured polymer/copper indium sulfide hybrid solar cells via the infiltration and thermal decomposition of a mixture of copper and indium xanthates. Although this step needs temperatures of more than 160 °C the nanostructures are retained in the final polymer/copper indium sulfide layers. These results have been published in Ref. [4].

References:

[1] R. Zhou amd J. Xue, *Chem. Phys. Chem*. ***13,*** 2471-2481 (2000)

[2] Y. Yang, K. Mielczarek, M. Aryal, A. Zakhidov and W. Hu, *ACS Nano*, **6**, 2877-2892 (2012)

[3] T. Rath, M. Edler, W. Haas, A. Fischereder, S. Moscher, A. Schenk, R. Trattnig, M. Sezen, G. Mauthner, A. Pein, D. Meischler, K. Bartl, R. Saf, N. Bansal, S.A. Haque, F. Hofer, E.J.W. List and G. Trimmel, Adv. Energy Mater. **1**, 1046-1050 (2011)

[4] S. Dunst, T. Rath, A. Radivo, E. Sovernigo, M. Tormen, H. Amenitsch, B. Marmiroli, B. Sartori, A. Reichmann, A.-C. Knall and G. Trimmel, ACS Appl. Mater. Interfaces **6**, 7633–7642 (2014)

[5] M. Yan and A. Gibaud, *J. Appl. Cryst*. **40**, 1050-1055 (2007)

ORDER IN CELLULOSE THIN FILMS

H.M.A. Ehmann[1], O. Werzer[2], S. Pachmajr[4], T. Mohan[3], R. Resel[4], F-Stelzer[1] and S. Spirk[1]

1.) Graz University of Technology, Institute for Chemistry and Technology of Materials, Stremayrgasse 9, 8010 Graz, Austria
2) Karl-Franzens Universität Graz, Institute of Pharmaceutical Technology,Heinrichstraße 28, 8010 Graz, Austria
3) Karl-Franzens Universität Graz, Institute of Chemistry,Heinrichstraße 28, 8010 Graz, Austria
4) Graz University of Technology, Institute of Solid State Physics, Petersgasse 6, 8010 Graz, Austria

As the most abundant of all available biopolymers, cellulose is utilized in many technological in most common organic solvents as well as in water. The preparation of homogeneous, amorphous cellulose thin films was studied extensively in the last decades using a trimethylsilyl (TMS) - derivate as precursor [1-3]. It is well known, that the film thickness and surface roughness of spin coated trimethylsilylcellulose (TMSC) thin films can be easily tuned by certain parameters, such as spinning speed and concentration whereby also the solvent in use crucially influences the quality of the so prepared films. The regeneration to pure cellulose thin films is induced using hydrochloric acid vapor, whereby the chlorine gas is responsible for cleaving off the TMS – groups as shown in Scheme 1.

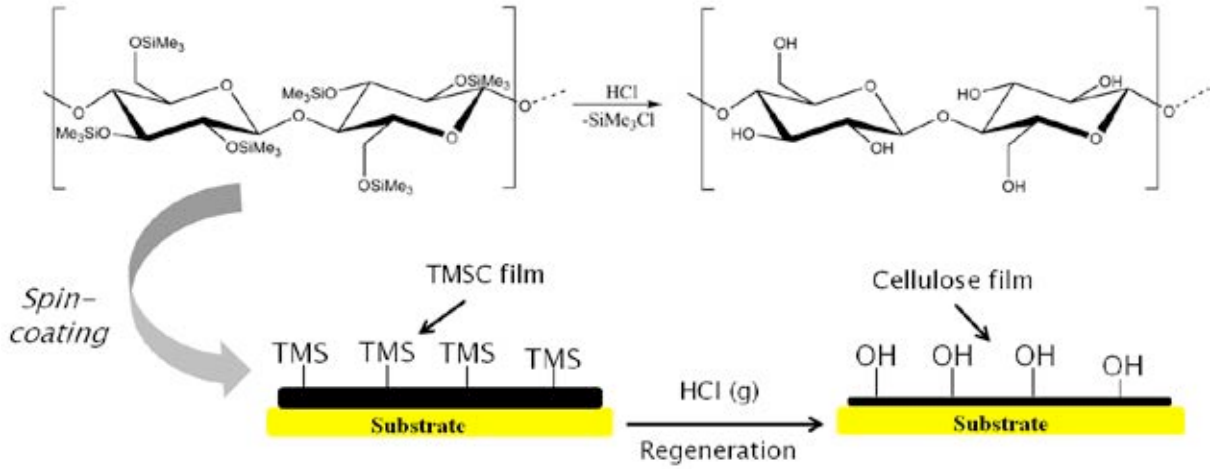

Scheme 1. Regeneration of TMSC to pure cellulose

This reaction is known to fully recover cellulose thin films in a time frame of about 12 minutes which was proven in a previous work using X-ray photoelectron spectroscopy as well as contact angle measurements [4-6]. Even if a lot was done to fully study the regeneration of such cellulosic thin films by chemical and physical means, less is known about the rearrangement taking place within such. Surface sensitive methods such as XPS and AFM were successfully employed to study the reconstructions at the surface but the elusive pore-restructuring within such thin films is still not fully understood. Further the subsequent temperature treatment induces a reformation of hydrogen bonds, leading to a change in the pore size distribution within the thin film.

In Fig. 1 the mean correlation lengths, extracted from the Yoneda region, are plotted as a function of the time. It can be seen that after the injection of HCl vapor (arrow) the mean correlation length increases; indicating that the cleavage of the silyl groups results in the formation of pores within the thin film. This is in excellent agreement with the proposed mechanism of the desilylation reaction whereby the total film density increases with decreasing film thickness (Fig. 2; XRR study with corresponding AFM images). After ~ 12 min the correlation length increase has reached a stable plateau. This can be correlated to the

point where all silyl groups are removed and a pure cellulosic film results. The corresponding XRR spectra are shown in Fig. 2 whereby the extracted thickness, roughness and density parameters are summarized in table 2. After the regeneration the film thickness decreased by 60 % while the film density increased by ~ 50 %.

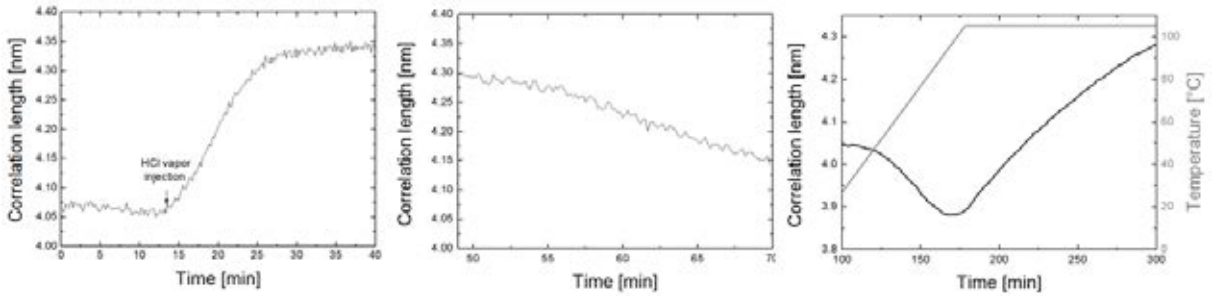

Figure 1. Mean correlation length of cellulose regeneration as a function of the regeneration time; (a) regeneration to pure cellulose (b) restructuring of the pore structure (c) heat treatment (105 °C)

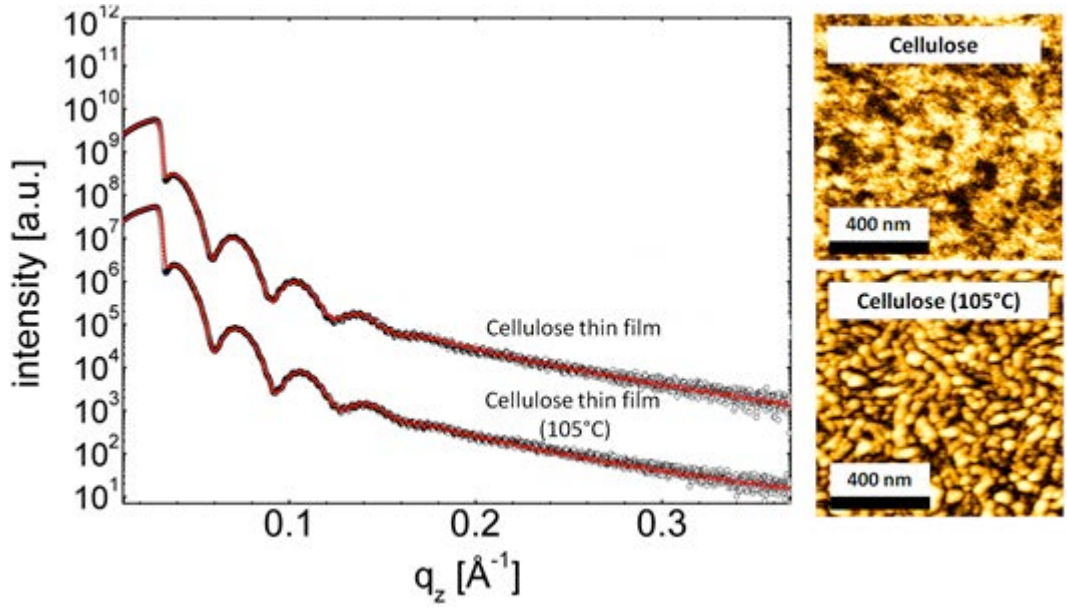

Figure 2. XRR (a) and AFM (b) of cellulose thin films; as-prepared, regenerated and heat treated

References:

[1] Rossetti, F. F., Panagiotou, P., Rehfeldt, Florian, Schneck Emanuel, Dommach, Martin, Funari, Sergio S., Timmann, Andreas, Müller-Buschbaum, Peter, Tanaka, Motomu; Biointerphases 1998, 3, 117-127

[2] Kontturi, E., Suchy, M., Penttilä, P., Jean, B., Pirkkalainen, K., Torkkeli, M., Serimaa, R. Biomacromolecules, 2011, 12, 770-777

[3] Ehmann H.M.A., Werzer O., Pachmajer S., Amenitsch H., Resel R., Stelzer F., Spirk S., *In Situ* Rearrangement in Cellulose Thin Films Followed by Synchrotron Grazing Incidence Small Angle X-Ray Scattering; 2014 (mansucript under prepration)

[4] Mohan, T.; Spirk, S.*; Kargl, R.; Doliska, A.; Vesel, A.; Salzmann, I.; Resel, R.; Ribitsch, V.; Stana-Kleinschek, K.: „Exploring the rearrangement of amorphous cellulose model thin films upon heat treatment" in Soft Matter, 2012, 8, 9807-9815

[5] Kargl, R., Mohan, T.; Köstler, StefS.an; Spirk, S.; Doliska, A.; Stana-Kleinschek, K.; Ribitsch, V.: "Functional patterning of biopolymer thin films using enzymes and lithographic methods" in Adv. Funct. Mat., 2013, 23, 308-315

[6] Mohan, T.; Spirk, S.*; Kargl, R.; Doliska, A.; Ehmann, H.M.A.; Köstler; S.; Ribitsch, V.; Stana-Kleinschek, K.: „Watching Cellulose grow - Kinetic Investigations on Cellulose Thin Film Formation at the Gas-Solid Interface using a Quartz Crystal Microbalance with Dissipation (QCM-D)", Coll. Surf. A-Physicochem. Eng. Asp., 2012, 400, 67-72

SELF-ASSEMBLED GROWTH OF NICKEL NANOPARTICLES IN AMORPHOUS ALUMINA MATRIX

M. Jerčinović[1], N. Radić[1], M. Buljan[1], J. Grenzer[2], I. Delač Marion[3], M. Kralj[3], I. Bogdanović Radović[1], R. Hübner[2], P. Dubček[1], K. Salamon[3] and S. Bernstorff[4]

1.) Ruđer Bošković Institute, Bijenička cesta 54, 10000 Zagreb, Croatia
2.) Helmholtz-Zentrum Dresden-Rossendorf, P O Box 510119, 01314 Dresden, Germany
3.) Institute of Physics, Bijenička cesta 46, 10000 Zagreb, Croatia
4.) Elettra-Sincrotrone Trieste, Strada Statale 14 km 163.5, 34149 Basovizza, Italy

Nanosized particles of ferromagnetic metals such as Fe, Co, and Ni have been extensively investigated [1] because of the rich diversity of their physical properties and the potential applications as catalysts, high-density magnetic recording, ferrofluids, medical diagnostics, drug delivery, multilayered capacitors, etc.

Small isolated ferromagnetic nanoparticles, arranged in regular lattices, are especially interesting for various spintronic devices. It is desirable to achieve the regular ordering by a self-assembly process due to its simplicity and cost-efficiency.

The Ni+Al_2O_3 nanocomposite system is particularly attractive and thus has been widely investigated in the last few decades because of its excellent mechanical properties like increased strength, hardness, toughness, and wear resistance, as well as its interesting size and particle separation dependent magnetic properties [2].

We present the formation of ordered 3D lattice of Ni nanocrystals/nanoparticles in amorphous alumina matrix achieved by a self-assembly process during a single-step magnetron sputtering deposition of Ni/Al_2O_3 multilayer at various substrate temperatures.

The structure of the films was analyzed using Grazing Incidence Small and Wide Angle X-ray Scattering, Transmission Electron Microscopy, Atomic Force Microscopy, Grazing Incidence Wide Angle X-ray Scattering, and Time-of-Flight Elastic Recoil Detection Analysis measurements.

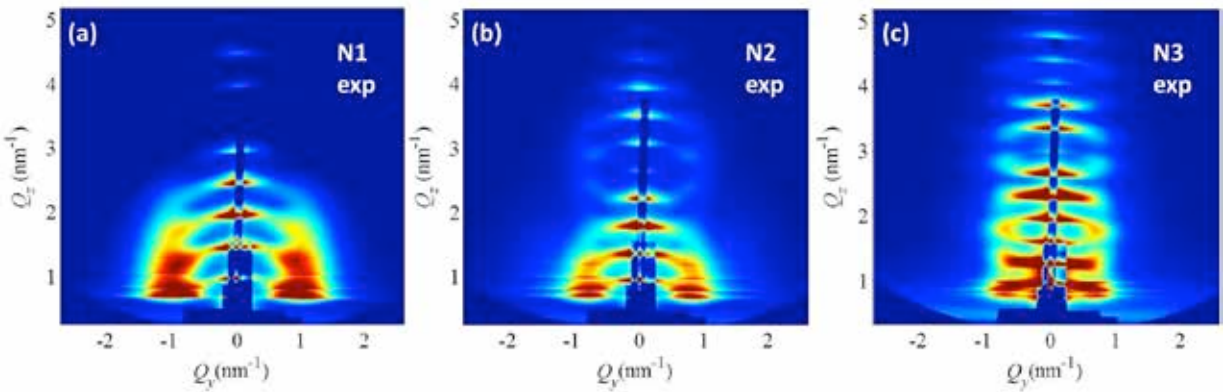

Figure 1. GISAXS intensity maps of samples with different nominal Ni layer thickness: a) 1.25 nm, b) 2.5 nm and c) 5.0 nm

GISAXS and GIWAXS measurements were performed at the Synchrotron Elettra in Trieste, with a photon wavelength of 0.154 nm and a two-dimensional image plate photon detector (Mar300) and a one-dimensional Gabriel-type gas detector, respectively. The incidence angle for all measurements was sligthly above the critical angle. The GISAXS results enabled the determination of the 3D positional ordering of the Ni nanoparticles [3], as well as their sizes and size distributions, while WAXS results gave insight into their crystalline structure.

The self-assembly is driven by surface morphology effects [4] and it results in a body-centered tetragonal (BCT) lattice of Ni particles with crystalline face-centered cubic (FCC) internal structure in amorphous Al_2O_3 matrix. The size distribution of the Ni NPs is

narrow, and the material has good mechanical properties due to the alumina matrix. We showed that the NP sizes and separations can be easily tuned by a suitable choice of the deposition conditions. Comprehensive sets of Ni/Al_2O_3 and $(Ni+Al_2O_3)/Al_2O_3$ multilayers have been examined by the GISAXS method. An example of the obtained results [5] is given in Fig. 1.

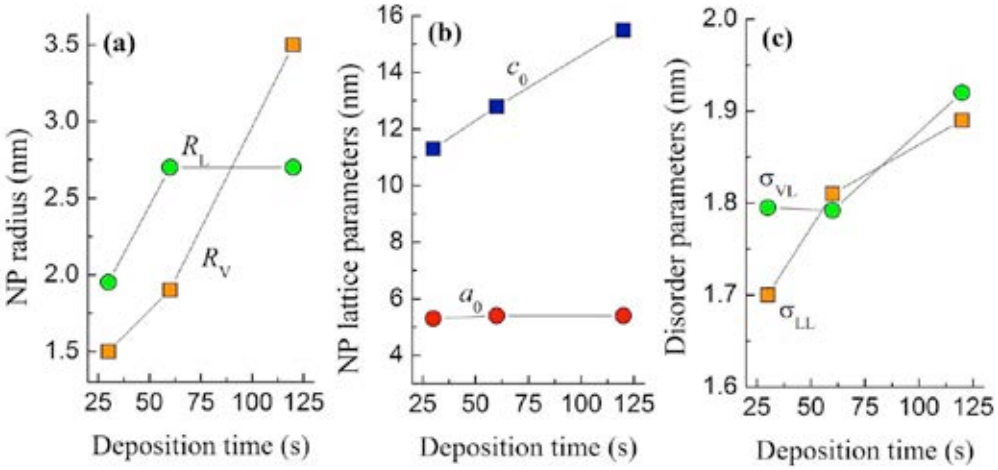

Figure 2. Ni particle size and arrangement properties. Dependence of: a) vertical and lateral particle radii (R_L and R_V); b) particle lattice parameters (a_0 and c_0); c) in-plane and interplane disorder parameters (s_{LL} and s_{VL})

The results of the analysis of the observed GISAXS patterns for the selected set [5] is given in Fig. 2, which shows plots of characteristic NP lattice parameters versus nominal Ni layer thickness.

The quality of the ordering achieved in the alumina matrix is found to be significantly better than the ordering of Ni particles in silica (Fig. 3). The obtained results are important for the understanding of the self-assembly process of metallic particles in amorphous matrices and the applications of such materials. The prepared materials are potentially interesting for spintronic applications.

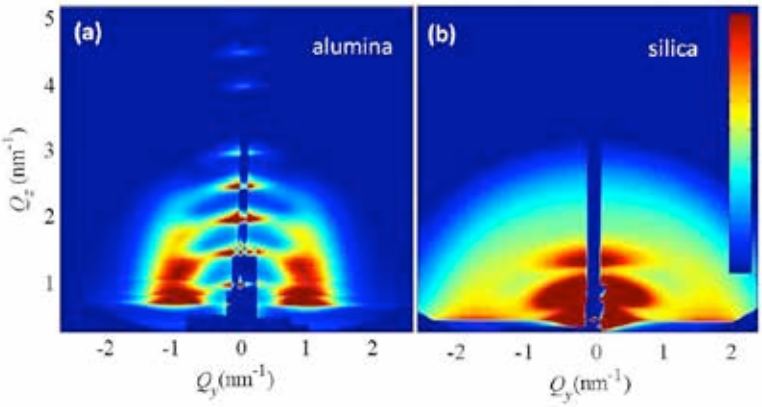

Figure 3. GISAXS maps of Ni particles formed in amorphous (a) alumina and (b) silica matrix

References:

[1] S.P. Gubin, A. Yu. Koksharov, G.B. Khomutov and G. Yu. Yurkov, Magnetic nanoparticles: preparation, structure and properties. Russ. Chem. Rev. **74**, 489–520 (2005)

[2] J. I. Gittleman, B. Abeles and S. Bozowski, Superparamagnetism and relaxation effects in granular Ni-SiO_2 and Ni-Al_2O_3films. Phys. Rev. B **9**, 3891–3897 (1974)

[3] M. Buljan, N. Radić, S. Bernstorff, G. Dražić, I. Bogdanović-Radović and V. Holý, Grazing incidence small angle X-ray scattering: application in study of quantum dot lattices. Acta Cryst. **A68**, 124–138 (2012)

[4] M. Buljan, U. V. Desnica, G. Dražić, M. Ivanda, N. Radić, P. Dubček, K. Salamon, S. Bernstorff and V. Holý, Formation of three-dimensional quantum dot superlattices in amorphous systems: experiments and Monte Carlo simulations. Phys. Rev. B **79**, 035310 (2009)

[5] M. Jerčinović, N. Radić, M. Buljan, J. Grenzer, I. Delač-Marion, M. Kralj, I. Bogdanović-Radović, R. Hübner, P. Dubček, K. Salamon and S. Bernstorff, Self-assembled growth of Ni nanoparticles in amorphous alumina matrix, J. Nanopart. Res. **16**, 2296 (2014)

EFFECT OF COBALT CONCENTRATION ON THE STRUCTURAL PROPERTIES OF $Zn_{1-x}Co_xO/Al_2O_3$ MULTILAYERED NANOSTRUCTURES

O. Karzazi[1], K. C. Sekhar[1], S. Levichev[1], M. Buljan[2], S. Bernstorff[3], and M.J.M.Gomes[1]

1.) Centre of Physics, University of Minho, Braga, 4710-057, Portugal
2.) Ruđer Bošković Institute, Bijenička cesta 54, 10000 Zagreb, Croatia
3.) Elettra-Sincrotrone Trieste, SS 14 km 163.5, 34149 Basovizza, Italy

$Zn_{1-x}Co_xO/Al_2O_3$ (x=0 to 0.3) multilayers were grown by pulsed laser deposition (PLD) with subsequent rapid thermal annealing in order to create layered ZnCoO nanocrystals (NCs) in an Al_2O_3 matrix. The influence of the Co concentration on the structural properties of the annealed nanostructures was investigated by grazing incidence small angle x-ray scattering (GISAXS). The measured 2D GISAXS maps of the as-grown and annealed multilayers containing different percentages of Co atoms are presented in Fig. 1. In the map of the as-grown film (Fig. 1(a)), several sheets of enhanced intensity elongated along the horizontal (Q_y) axis are clearly seen. These so-called Bragg sheets arise from the coherent superposition of x-rays scattered on different rough interfaces of the multilayer [1]. These sheets are still present in the maps of the annealed films (Fig. 1(b)-(d)), but they are much weaker and superimposed on a strong scattering signal stemming from the nanoparticles formed during annealing. The maps of annealed samples do not exhibit any correlation maxima, which allows us to conclude that there is no correlation in the NCs positions inside the layers.

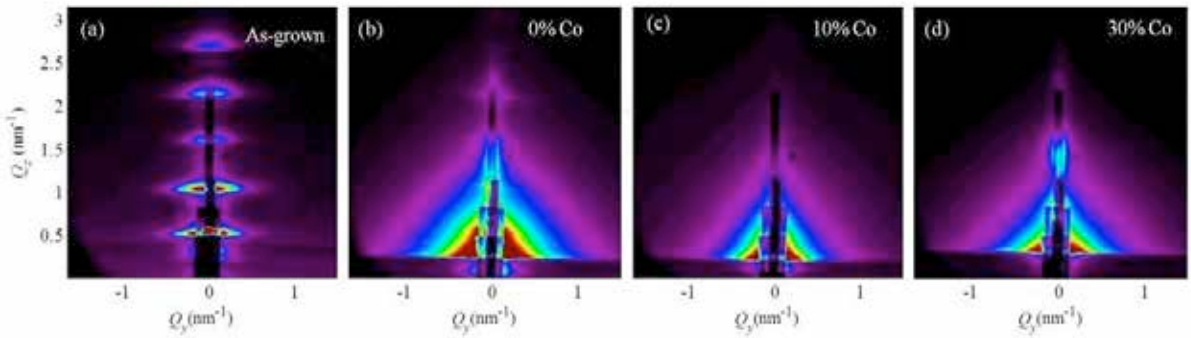

Figure 1. GISAXS maps of the as-grown film ZnO/Al_2O_3 multilayers (a) and annealed films with various percentages of Co doping in $Zn_{1-x}Co_xO/Al_2O_3$ (x=0 to 0.3) (b)-(d)

We have analyzed numerically the measured GISAXS pattern assuming no correlation in the NP positions. The shape of the particles is assumed spheroidal with the lateral (parallel to the substrate) and vertical (perpendicular to the substrate) radii R_L and R_V, respectively. We find that the radius R_L is in the range of 1.5 nm – 2.2 nm, where as Rv is in the range of 1.1 nm – 1.8 nm. It is noticed that the lateral NP radii are slightly larger than the vertical ones for all films. The NP radii increase with the Co percentage and have maxima at 15% of Co doping. GIWAXS patterns of annealed $Zn_{1-x}Co_xO/Al_2O_3$ nanostructures were simultaneously measured in the range of $2\theta = 20^0 - 45^0$. The presence of strong peaks reveals the high crystalline quality of the nanostructures. The peaks around $2\theta = 31.1^0 \pm 0.3^0$ and $36.7^0 \pm 0.3^0$ were attributed to ZnO (100) and alpha-Al_2O_3 (110) reflections, respectively. Within the WAXS limit, the nanostructures are only composed of ZnCoO and Al_2O_3, and no other secondary phases were detected.

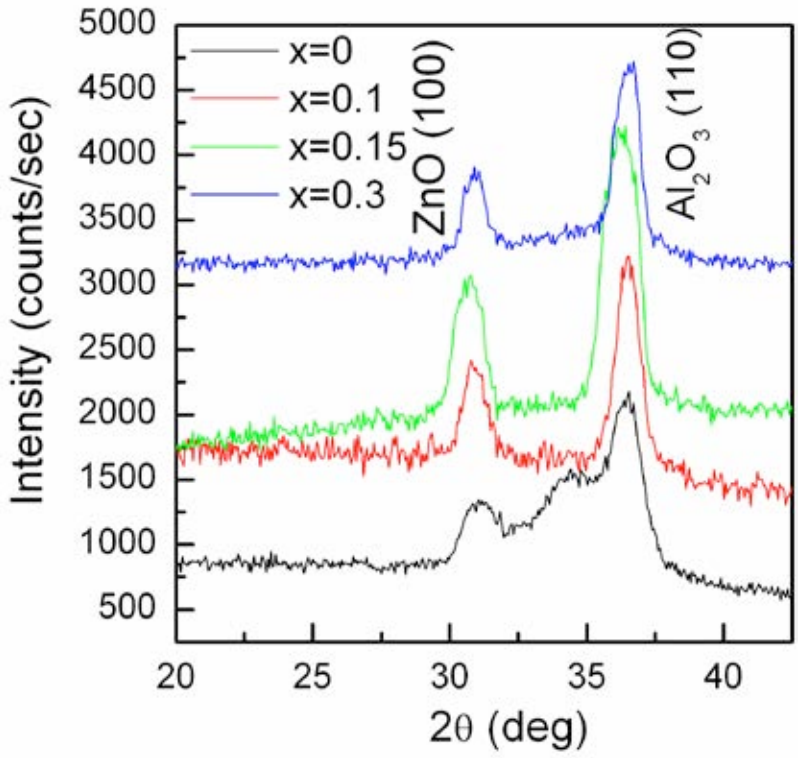

Figure 2. GIWAXS pattern of annealed $Zn_{1-x}Co_xO/Al_2O_3$ (x=0 to 0.3) multilayers

References:

[1] M. Buljan,N. Radić, S. Bernstorff,G. Dražić, et al, Acta Cryst. A **68,** 124 (2012)

DECORATION OF SILICA NANOPARTICLES WITH SILVER

V. Körstgens[1], D. Magerl[1], L.Song[1], B. Su[1], S. Bernstorff[2] and P. Müller-Buschbaum[1]

1.) Technische Universität München, Physik-Deptartment, Lehrstuhl für Funktionelle Materialien, James-Franck-Str. 1, 85748 Garching, Germany
2.) Elettra-Sincrotrone Trieste, S.S. 14 km 163.5 in Area Science Park, 34012 Basovizza, Trieste, Italy

Composite materials consisting of metallic nanoparticles distributed on the top an inorganic or polymer substrate, which has a nanostructure on its own show very interesting material properties. These kind of hierarchical structures are for example applicable as substrates for surface enhanced Raman scattering (SERS) [1].
Several approaches have been made to coat micro- and nanospheres with metallic nanoparticles in multistage processes in a fluid environment [2, 3]. These processes have in common that in a first step the adherence of metallic ions to the micro- and nanospheres has to be promoted. In a second step and optional further steps a reduction of metallic ions and growth of metallic nanoparticles on top of the micro- and nanospheres is induced by a reduction agent. This coating may proceed up to a closed metallic layer on the micro- and nanospheres. Usually afterwards several cleaning steps are necessary to obtain the pure metal coated particles from the dispersion with its reactants. In a final step the hierarchical particles are deposited onto substrates. The substrates are coated either to investigate single particles or obtain arrays or colloidal crystals of the coated spheres.
Our approach is different as we start with an array of nanoparticles (monolayer), which is pre-deposited, and conduct the chemical reaction directly on the coated substrate. The advantage of our method is, on one hand that less production steps are needed. On the other hand the order of the coated spheres in an array is constituted already with the initial array of uncoated spheres.
In figure 1 one example of the composite materials produced by our recipe is shown. On a glass substrate a dense monolayer of silica nanospheres (diameter 147 nm) was deposited and used as pre-structured layer. On top of the silica nanospheres successfully silver nanoparticles were grown.

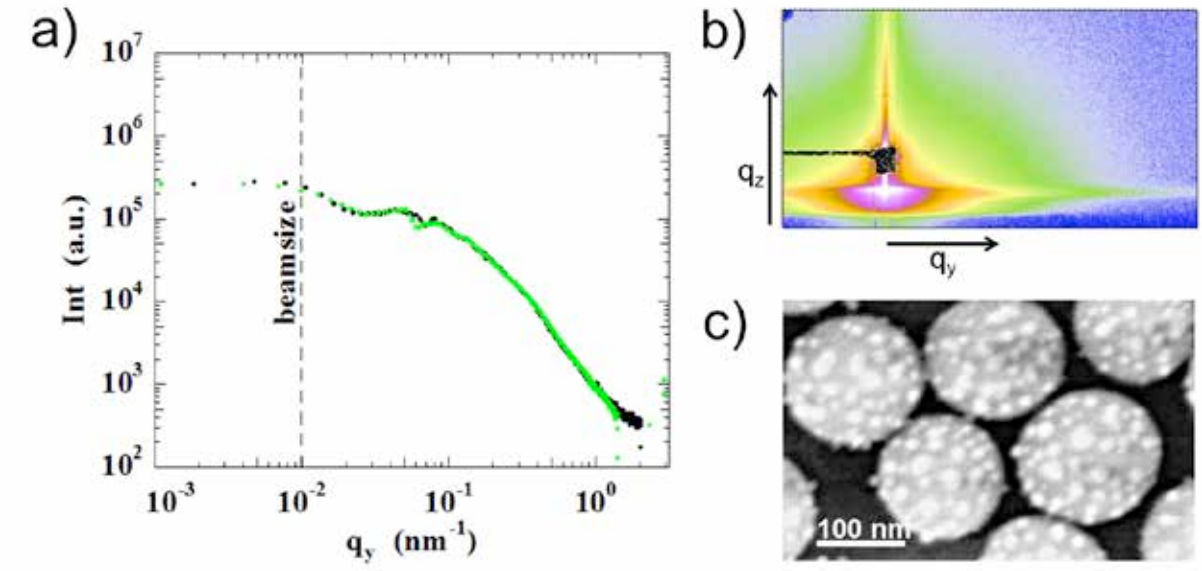

Figure 1. Monolayer of silica nanospheres decorated with silver nanoparticles on a glass substrate
a) Horizontal line cut from the 2D GISAXS data corresponding to the silver coated silica nanospheres. b) 2D GISAXS data measured at the Austrian SAXS beamline at Elettra after correction for the semitransparent beamstop and c) SEM image of the sample.

The GISAXS experiments have been performed at the Austrian SAXS beamline at the Elettra Sincrotrone, Trieste. In these GISAXS experiments an X-ray energy of 8 keV was used. The scattering data in figure 1 proves that it is possible to resolve 147 nm silica spheres in GISAXS. It can be observed that after the silver coating process the sphere form factor modulations are maintained and that the scattering signal has a larger contribution from smaller structures compared to the initial film. With further analysis information about the size distribution of silver nanoparticles will be obtained. This information is related to a large surface area of the sample whereas the complementary information gained by SEM is limited to local spots. Based on our initial experiments, we will investigate composite materials out of nanospheres with different sizes with a decoration of smaller metal nanoparticles where the coverage will be varied up to the situation of a core-shell particle. Beneficial for our studies will be the opportunity to obtain WAXS information simultaneously (during the GISAXS measurement) at the Austrian SAXS beamline. This will allow for the detection of metallic phases (e.g. silver) as well as potentially remaining reactants. The aim of our studies is to elucidate the structural morphology of the films and get information about the growth mechanisms involved by investigation of decorated samples after exposure to the reduction agent for different times. It has been shown that the development of metallic particles and the attachment to surfaces up to formation of closed layers can be described in detail by information gained from GISAXS measurements [4-6]. These procedures to achieve composite materials include liquid dispersion by flow techniques, spray deposition or sputter deposition techniques. With the chemical method of reduction metallic ions on the surface of an existing nanostructures composite materials can be obtained not accessible with other techniques.

References:

[1] S. M. Tabakman, Z. Chen, H. Sanchez Casalongue, H. Wang, and H. Dai; A new approach to solution-phase gold seeding for SERS substrates; Small **4**, 499-505 (2011)

[2] J. Zhang, J. Liu, S. Wang, P. Zhan, Z. Wang, and N. Ming; Facile methods to coat polystyrene and silica colloids with metal; Adv. Funct. Mater. **14**, 1089-1096 (2004)

[3] K. Wang, X. Zhang, C. Niu, and Y. Wang; Template-activated strategy toward one-step coating silica colloidal microspheres with silver; ACS Appl. Mater. Interfaces **6**, 1272-1278 (2014)

[4] E. Metwalli, J. F. Moulin, J. Perlich, W. Wang, A. Diethert, S. V. Roth, and P. Müller-Buschbaum; Polymer-template-assisted growth of gold nanowires using a novel flow-stream technique; Langmuir **25**, 11815-11821 (2009)

[5] M. Al-Hussein, M. Schindler, M. A. Ruderer, J. Perlich, M. Schwartzkopf, G. Herzog, A. Buffet, S. V. Roth, and P. Müller-Buschbaum; In situ X-ray study of the structural evolution of gold nano-domains by spray deposition on thin conductive P3HT films; Langmuir **29**, 2490-2497 (2013)

[6] G. Kaune, M. A. Ruderer, E. Metwalli, W. Wang, S. Couet, K. Schlage, R. Röhlsberger, S. V. Roth, and P. Müller-Buschbaum; In situ GISAXS study of gold film growth on conducting polymer films; ACS Appl. Mater. Interfaces **1**, 353-362 (2009)

GISAXS STUDIES OF THE STRUCTURAL CHANGE OF MESOPOROUS SILICA FILMS AFTER CONTROLLED X-RAY IRRADIATION

B. Marmiroli, B. Sartori, H. Amenitsch

Insitute of Inorganic Chemistry, Graz University of Technology, NAWI Graz, Stremayrgasse 9, Graz, Austria

Microfluidic systems for handling and sensing chemical and biological samples will improve their performance through the employment of materials with selected functionalities in tailored regions of the device. To obtain this goal, top-down techniques can be employed to pattern bottom-up synthesized functional materials.
Deep X-ray lithography (DXRL) is an effective top down technique to tune the porosity of mesoporous materials that can be used as "bricks" to build new generation lab on chips. DXRL induces chemical and structural changes in materials due to the effect of high energy X-rays (3–20 keV), thus providing high aspect ratios, almost vertical sidewalls after development, and 200 nm lateral resolution [1]. In the present experiment we have thoroughly investigated the effect of the X-ray irradiation dose on the structure of mesoporous materials based on silica films containing pores in the order of 2-10 nm.

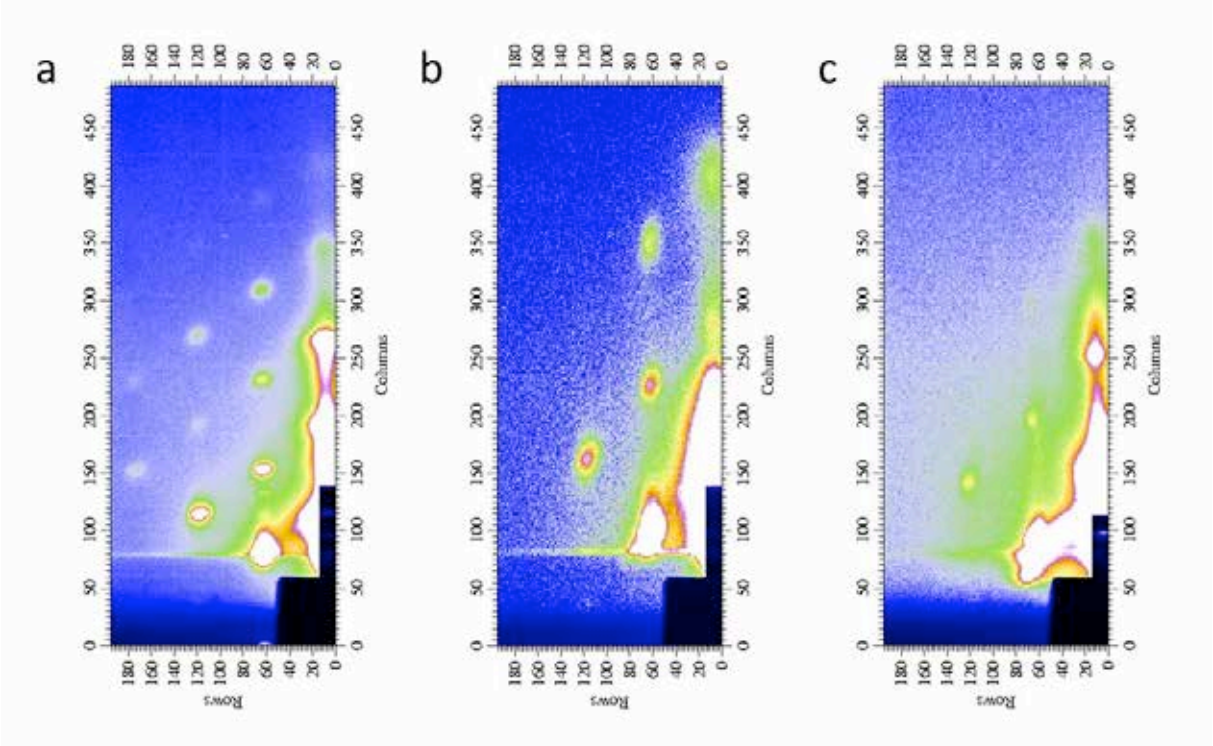

Figure 1. GISAXS pattern at the detector of mesoporous silica (a) still containing surfactant (b) after calcination at 450 °C for 0.5 h to remove surfactant, (c) after irradiation at a dose of 131 J/cm^2. The hexagonal structure is still present

Using DXRL as patterning technique, such materials can be used for example as DNA arrays [2,3], or can be functionalized with enzymes to achieve selective bioactive areas [4]. Usually, mesoporous silica presents a hexagonal arrangement of the pores parallel to the substrate, making them a good choice for microfluidics. With irradiation, such structure can undergo damage, leading to a wormlike arrangement of pores that are not connected. We have conducted the structural investigation through Grazing Incidence Small Angle X-Ray Scattering (GISAXS), leading to the optimization of the irradiation dose. The mesoporous silica film both as prepared and after irradiation still contains the surfactant. To remove the

surfactant from the unexposed samples, a thermal treatment has been performed at 450 C for 0.5 h. To remove the surfactant from the exposed ones, a mixture of different solvents (ethylen glycol, ethanol and acetone) has been used as developer, removing both the surfactant and the unexposed silica. With GISAXS it was possible to see that both the thermal treatment and the irradiation determine a loss of order (as seen in figure 1). Moreover, it seems that the structural loss is higher in the irradiated samples than in the thermally treated one. Anyway, a structural order is still evident also in the irradiated samples, leading to the possibility to obtain good quality patterned mesoporous structures using Deep X-ray lithography still maintaining a hexagonal structure to allow fluid flow.

References:

[1] M. Tormen, G. Grenci, B. Marmiroli, F. Romanato, X-ray Lithography: fundamentals and applications, in: S. Landis, ed., Nanolithography (ISTE-Wiley, London and Hoboken) 1-86 (2010)

[2] P. Falcaro, S. Costacurta, L. Malfatti, M. Takahashi, T. Kidchob, M. F. Casula, M. Piccinini, A. Marcelli, B. Marmiroli, H. Amenitsch, P. Schiavuta, P. Innocenzi, Fabrication of Mesoporous Functionalized Arrays by Integrating Deep X-Ray Lithography with Dip-Pen Writin, Adv. Mat. **20**, 1864-1869 (2008)

[3] P. Falcaro, L. Malfatti, L. Vaccari, H. Amenitsch, B. Marmioli, G. Grenci, and P. Innocenzi, Fabrication of Advanced Functional Devices Combining Soft Chemistry with X-ray Lithography in One Step ,Adv. Mater. **21**, 48, 4932 (2009)

[4] C. Doherty, Y. Gao, B. Marmiroli, H. Amenitsch, F. Lisi, L. Malfatti, K. Okada, M. Takahashi, A. Hill, P. Innocenzi, P. Falcaro, Microfabrication of Mesoporous Silica Encapsulated Enzymes using Deep X-Ray Lithography, J. Mater. Chem., **22** , 16191-16195 (2012)

IN SITU STUDY OF MICROSTRAINS DURING POST YIELD DEFORMATION OF POLYETHYLENE

G. Polt[1], M. Zareghomsheh[1], F. Spieckermann[1], H. Wilhelm[1,2], S. Bernstorff[3] and M. Zehetbauer[1]

1.) Research Group Physics of Nanostructured Materials, University of Vienna, Austria
2.) Laboratory of Polymer Engineering LKT-TGM, Wexstrasse 19-23, 1200, Vienna, Austria
3.) Elettra-Sincrotrone Trieste, Strada Statale 14 km 163.5 in AREA Science Park, 34149 Basovizza, Trieste, Italy

The mechanisms during plastic deformation in semicrystalline polymers, especially within the crystalline phase, are still a matter of discussion. However, many theoretical approaches take into account dislocation based deformation mechanisms for the post yield behaviour. In previous in-situ experiments performed at the Synchrotron ELETTRA (Trieste, SAXS-Beamline) it was not only possible to prove the existence of dislocations, but also to observe their evolution as a function of deformation [1, 2, 3]. An ideal tool for investigation of dislocation kinetics is the Multi-Reflection X-ray Profile Analysis (MXPA) method [4]. This method uses several reflections and their upper harmonics for the quantification of microstructural parameters such as dislocations or the coherently scattering domain size (CSD-size) which corresponds to the thickness of the crystalline domains in polymers. However, this method can not be applied to PE since this material only shows two high intensity reflections of the same phase, therefore the so called momentum- or variance-method [5] has to be considered. This method allows to determine parameters such as the presence and density of crystalline defects, such as dislocations and the grain size from only a single line profile, provided that the influence of the background on the intensity measurement is negligible [5].
In-situ deformation experiments during X-ray diffraction were performed on as received high density polyethylene (PE AR) and on high density polyethylene crystallized under high pressure in order to increase its crystallinity and lamellae thickness (PE cryst) [6]. The deformation was performed in uniaxial compression in order to avoid crazing. A transmission setup was used providing a large scattering volume using a 90° curved position sensitive linear detector of the type INEL CPS 590 with the sample located in the center. Diffraction patterns were recorded from the undeformed material up to a true strain of e=0.8.

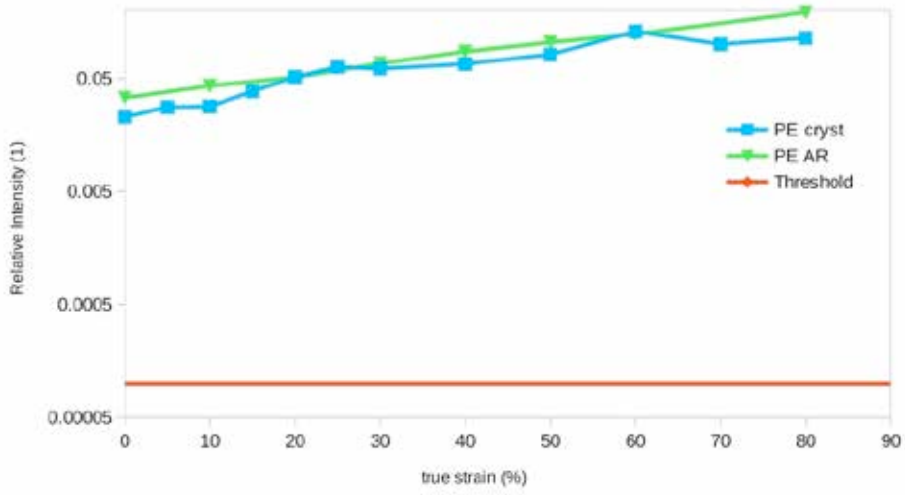

Figure 1. Relative intensity as a function of true strain. In order to apply the momentum method, the diffraction profile should be measured up to 10^{-4} relative intensity, represented by the threshold line. Although a high crystallinity was reached in the pressure crystallized sample (PE cryst), the diffuse scattering of the amorphous phase results in a high background to peak ratio

By plotting the relative background to peak intensities as a function of true strain it can be seen that the lowest value is in the order of 0.02 (figure 1) for the crystallized undeformed sample, increasing with increasing strain. This increase can be related to the formation of shear bands cutting through the crystallites leading to their amorphisation. Groma and Szekely [5] demonstrated that the development of the calculated moments at large q values is strongly influenced by the relation of the background to the peak intensity and pointed out that a threshold value of the relative intensity of at least 10^{-4} should be aimed in order to obtain reliable results [5]. Apparently, the nature of semicrystalline polymers, even if the crystallinity is in the order of 80%, such as for the crystallized PE sample, limits the relative intensity drastically due to diffuse scattering of the amorphous phase. Therefore, in order to apply the variance method on PE, a highly crystalline material such as PE single crystals need to be considered, however there is still a risk of an increasing background at higher deformations restricting the reliability of this method. Nonetheless by careful background subtraction, interpretation of the second and fourth order restricted moments might be possible. The related evaluation is in progress.

Additionally, the formation of a pressure induced hexagonal phase at 2θ=19° and 2θ=35° could be observed reaching a true strain of e=0.1 (figure 2). With increasing deformation the volume fraction of the pressure induced phase increases, while it is still present after unloading from e=0.8, most likely being stabilized by internal stresses. Nevertheless, a slight reduction in volume fraction is observed originating from relaxation processes.

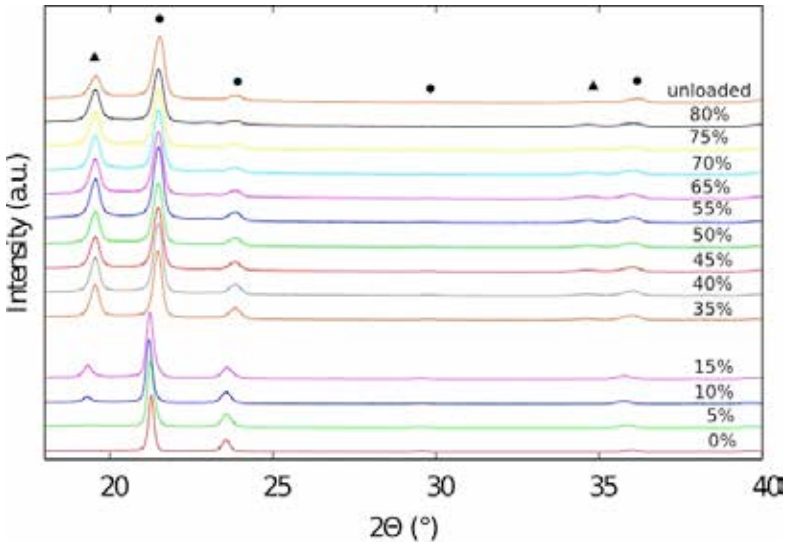

Figure 2. Diffraction patterns were recorded in-situ under load at different degrees of plastic deformation. In addition to the initial orthorhombic crystal structure, represented by (•), a pressure induced hexagonal phase develops at a true strain of e=0.1 (▲).

References:

[1] Wilhelm, H.; Paris, A.; Schafler, E.; Bernstorff, S.; Bonarski, J.; Ungar, T. & Zehetbauer, M.; Evidence of dislocations in melt-crystallised and plastically deformed polypropylene; Mater. Sci. Eng. A387-389, 1018-1022 (2004)

[2] Spieckermann, F.; Wilhelm, H.; Kerber, M.; Schafler, E.; Polt, G.; Bernstorff, S.; Addiego, F. & Zehetbauer, M.; Determination of lamella thickness distributions in isotactic polypropylene by X-ray line profile analysis', Polymer 51(18), 4195-4199 (2010)

[3] G. Polt, F. Spieckermann, H. Wilhelm, M. Kerber, E. Schafler, S. Bernstorff, M. Zehetbauer; The role of dislocations in gamma-iPP under plastic deformation investigated by X-ray line profile analysis; Mech. Mater. 67, 126-132 (2013)

[4] Ung, T. & Borby, A. ;The effect of dislocation contrast on x-ray line broadening: A new approach to line profile analysis; Appl. Phys. Lett., AIP, 69, 3173-3175 (1996)

[5] Groma I., Szekely F.A.; Analysis of the asymptotic properties of X-ray line broadening caused by dislocations; Appl. Cryst. 33, 1329-1334 (2000)

[6] Kazmierczak, T. Galeski, A.; Transformation of polyethylene crystals by high-pressure annealing; J. Appl. Polym. Sci. 86, 1337-1350 (2002)

IN-SITU SAXS STUDY ON THE ION TRANSPORT IN MICROPOROUS CARBON-BASED SUPERCAPACITORS

C. Prehal[1], E. Perre[2], D. Weingarth[2], R. T. Lechner[1], H. Amenitsch[3], O. Paris[1] and V. Presser[2]

1.) Institute of Physics, Montanuniversität Leoben, Franz-Josef Straße 18, Leoben, Austria
2.) Energy Materials Group, INM Saarbrücken, Campus D2 2, Saarbrücken, Germany
3.) Institute of Inorganic Chemistry, Graz University of Technology, Stremayrgasse 9/IV, 8010 Graz, Austria

Supercapacitors or Electrical Double-layer capacitors are devices used for efficient energy storage. If two electrodes are immersed into a liquid electrolyte and a voltage is applied a Double-layer will form on the electrode-electrolyte interface. The opposed charges of ions on the electrolyte and electrons/holes on the electrode side reveal capacitive behavior. The activated carbon electrodes used in this study exhibit specific surface areas up to 1800m^2/g, leading to capacities up to 100F/g. Since the average pore diameter in these materials is about 0.7-1.0 nm the ions have not enough space and the formation of a double-layer according to classical models is inhibited. It has been shown that ions partially lose their solvation shell when entering pores smaller than their hydrated ion size [1]. The arrangement and the transport of ions in such pores as a function of the electrical potential is still a matter of debate, and is the major motivation for our work in this field.

Using In-situ SAXS and WAXS we are able to track the change of ion concentrations as a function of the applied voltage in pores of different size regimes. Therefore a model supercapacitor was prepared in form of a thin multilayered stack soaked with an aqueous electrolyte, all inside a plastic casing. To be able to measure ion rearrangements with X-ray scattering within the micropores (<2nm) of the carbon working electrode only, all materials of the working EDLC contained a hole of 10 mm diameter, except of the investigated electrode. A potentiostate was installed at the Austrian SAXS beamline, allowing the control of the electrical potential and the measurement of the emerging current.

Small- and wide-angle X-ray scattering (SAXS/ WAXS) patterns of an activated carbon are shown in Fig. 1a. The sample infiltrated with 1M CsCl aqueous electrolyte show a similar scattering curve in the SAXS regime. In the WAXS regime the structure factor of the liquid electrolyte overlays the contribution of the carbon structure factor.

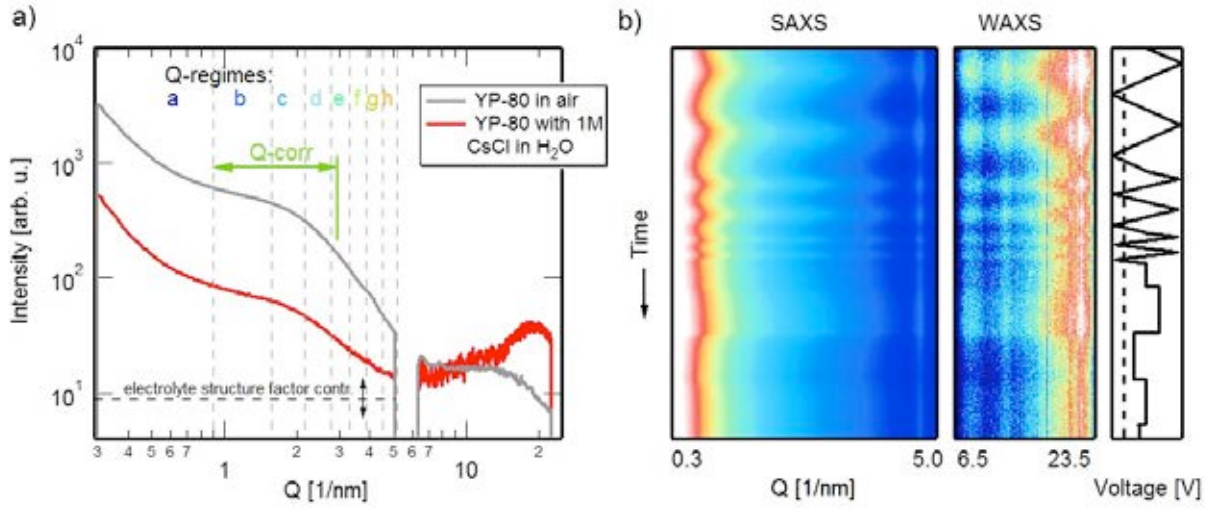

Figure 1. a) SAXS and WAXS intensity of the dry activated carbon YP-80 (grey) and the carbon infiltrated with electrolyte (red). The indicated Q-regimes are marked for further data analysis. b) The as-measured SAXS (left) and WAXS (middle) intensity is shown in a color coded scale as a function of the applied voltage signal (right).

First, the electrolyte structure factor contribution for the SAXS regime is evaluated and subtracted using a simple model. Then, integral parameters are calculated for specific regimes of the scattering vector length Q in the scattering curves (Fig. 1a). While the integrated intensity usually corresponds to a change in the average scattering contrast between electrolyte filled pores and carbon matrix, the correlation length - defined by the ratio of the first to the second moment of the scattering curve - is sensitive to structural changes within a certain length scale. The SAXS intensity covers mainly changes within the micro- and mesopores (Nanometer-regime). In contrast, the X-ray transmission signal, which was simultaneously measured using a photodiode, covers electron density changes within all pores (micro-, meso- and macropores). All these parameters are shown in Fig. 2 as a function of the applied electrical potential during two CV cycles.
The change in the transmission signal proves the change of the overall cation and anion concentration within the irradiated volume of the carbon electrode. Hence a macroscopic ion transport from one electrode to the other takes place as expected. Fig. 2b shows also that there is a clear "phase-shift" of the transmission signal with respect to the voltage signal. This shift enables ion transport to be analyzed in more detail. In particular, the small size of the X-ray beam (1x1mm) enables a measurement on different spots of the electrode within an about 10 mm diameter hole in the model device. A local dependence of the time-constants of the ion-concentration during CV cycling was found, depending on the distance the ions have to travel from one electrode to the other [2].

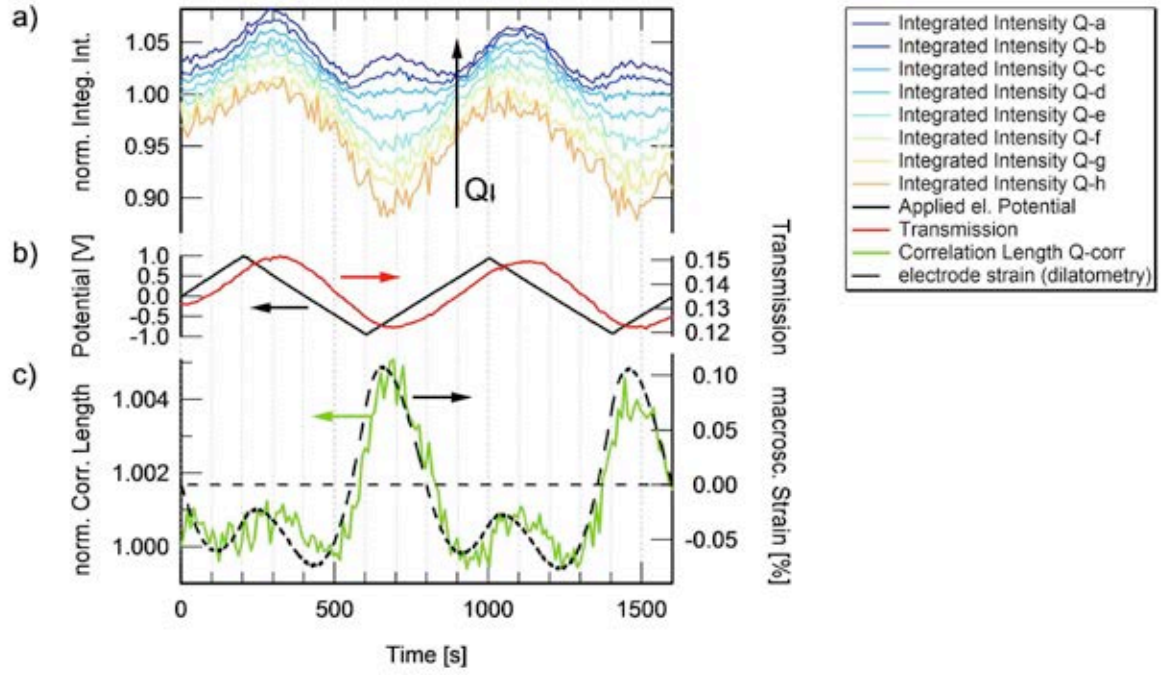

Figure 2. a) Integrated intensity as a function of time for different Q-regimes. b) Applied electrical potential signal (black) together with the measured X-ray transmission signal (red). c) SAXS correlation length (green) for the Q-regime "Q-corr" and macrosocopic electrode strain measured by dilatometry (dashed black).

Beside the study of the ion transport on different hierarchical levels, other phenomena like a mechanical response of the carbon electrode on ion electrosorption within confinement was found [2]. It is well known from literature that applying a voltage to the highly porous electrode can lead to its macroscopic expansion. This effect is often attributed to an increased electrolyte pressure within the smallest pores (<2 nm) [3] due to increased ion concentration. In other studies the expansion or contraction was exclusively explained by a change in the carbon interfacial energy due to the change of the binding situation for surface atoms when inserting electrons [4].

In general the change in the integrated intensity (Fig. 2a) is caused by the change of the electron density contrast between pores and carbon matrix. If Cs^+ ions with large scattering cross-section enter the pores at negative potential, the SAXS intensity is expected to decrease. This is the case at large values of Q, but additionally an intensity increase at small Q-values is observed at negative voltages (see Fig. 2a). By fitting the SAXS curves with the well-known Debye-Anderson-Brumberger model, it was demonstrated in [2] that this effect can be understood by the swelling of the electrode, which leads to an increase of the intensity particularly at intermediate and low Q-values. The swelling is directly observed in the SAXS correlation length in Fig. 2c, shown together with the macroscopic strain of the electrode measured with dilatometry. This provides independent evidence that the correlation length measured with SAXS has its origin in the change of the pore size. At negative voltages the pores expand while at positive potentials the pores basically shrink with respect to the 0V size, before they slightly expand around the voltage maximum. The asymmetric swelling behavior for positive and negative ions suggests at least two different physical mechanisms being responsible for the pore expansion behavior. A detailed analysis of the transmission and the electrical current signals allows the calculation of the absolute ion concentration change within the pores in dependence on the applied voltage. The total ion concentration was found to be constant for all potentials, while only the cation/anion ratio changes. Hence a direct correlation of the total ion concentration to the pore expansion was not found. Further systematic work - desirably on carbons with narrower size distribution - is required to better understand this interesting but hitherto unexplained swelling behaviour.
In conclusion, this study demonstrates for the first time the possibility of studying ion transport and pore expansion in highly disordered activated carbons by analyzing integrated SAXS parameters for defined Q-regions during in-situ voltage cycling in model supercapacitors.

References:

[1] Chmiola, J., et al.; Desolvation of ions in subnanometer pores and its effect on capacitance and double-layer theory; Angewandte Chemie - International Edition **47**, 3392-3395 (2008)
[2] Prehal, C.; In-situ SAXS study on the ion dynamics in microporous carbon based supercapacitors; Diploma Thesis at Institute of Physics, Montanuniversität Leoben, 104 (2014)
[3] Hantel, M.M., D. Weingarth, and R. Kötz; Parameters determining dimensional changes of porous carbons during capacitive charging; Carbon **69**, 275-286 (2014)
[4] Biener, J., et al.; Macroscopic 3D Nanographene with Dynamically Tunable Bulk Properties; Advanced Materials **24**, 5083-5087 (2012)

Co FILM ON NANORIPPLED Si SUBSTRATE: A GISAXS AND MOKE STUDY

K.V. Sarathlal[1], A. Gupta[2] and S. Bernstorff[3]

1.) Photon Science, DESY, Notkestr. 85, D-22607, Hamburg, Germany
2.) Center for Spintronic Materials, Amity University, Noida 201313, India
3.) Elettra-Sincrotrone Trieste, Strada Statale 14, km 163.5, 34149 Basovizza / Trieste, Italy

Tuning of magnetic properties of ultrathin films by means of the surface and interface modifications is an attractive issue from both fundamental and technological points of view. Controlling and manipulating of magnetic anisotropy in low dimensional systems such as ultra thin films are very important for optimization of the performance of thin film based devices. Magnetic anisotropies of ultra thin films are inherently related to their structure and morphology [1-3]. Various methods have been used to introduce magnetic anisotropy in a system. Scratched surfaces prepared by mechanical abrasion with groves separation of the order of 100 nm have been conventionally used for generating texture in Co films in order to achieve desired magnetic anisotropy [3]. A convenient way of manipulating uniaxial magnetic anisotropy in thin films is through depositing on an anisotropic substrate [1,2]. Therefore, rippled ferromagnetic thin films gained attraction in recent years and inspired usage in magnetic sensors [4].

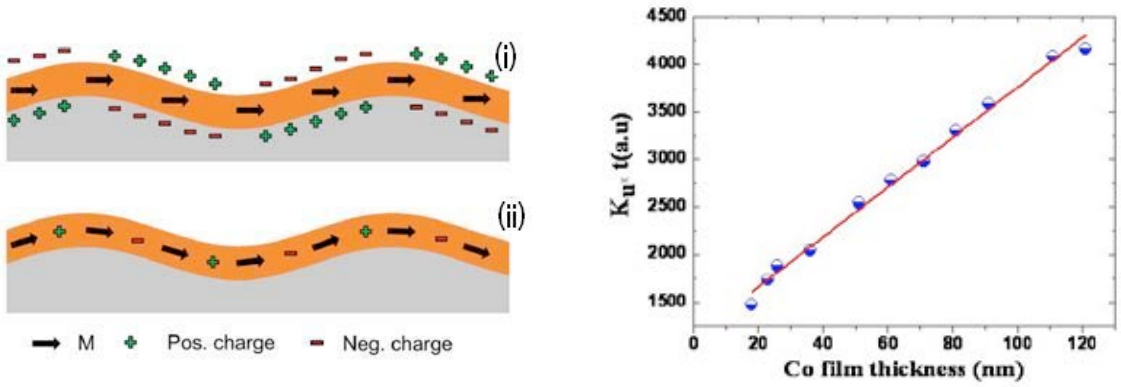

Figure 1. left: Sketch of two possible magnetic configurations for the magnetization oriented perpendicular to the ripples, as described in the text; right: Film thickness dependence of the magnetic anisotropy

Co film on nanorippled surface exhibits a strong uniaxial magnetic anisotropy, with its easy axis along the length of the ripples [5]. Objective of the present study is to understand the origin of this magnetic anisotropy. Two different models have been proposed for the generation of uniaxial anisotropy in magnetic films on nanorippled substrate, which are shown schematically in fig. 1(a) [6]. In the first case the stray dipolar fields generated at the surface/interface are responsible for the observed anisotropy, and can be written as [7]:

$$K_2^{dip} = 2\pi M_s^2 \frac{\pi \omega_{rms}^2}{\lambda D} \quad (1)$$

where ω_{rms} is the surface modulation amplitude, λ is the ripple wavelength, M_s is saturation magnetization and D is the ferromagnetic film thickness. In the second case, volume anisotropy has its origin in exchange energy.
In general, in ultra thin films the total observed uniaxial magnetic anisotropy per unit volume can be written as:

$$K_u^t = K_u^v + \frac{K_u^S + K_u^i}{t} \quad (2)$$

Where K_u^v, K_u^s and K^i_u represents the volume, surface and interface contributions respectively. Figure 1(b) gives the results of preliminary analysis of MOKE data as a function of film thickness. As expected on the basis of eq. (2), the plot of $K_u^t \times t$ versus t exhibits a linear variation with film thickness. Non-zero values of both the slope and the intercept of the straight line suggest that magnetic anisotropy has contributions from both volume as well as surface/interface terms.

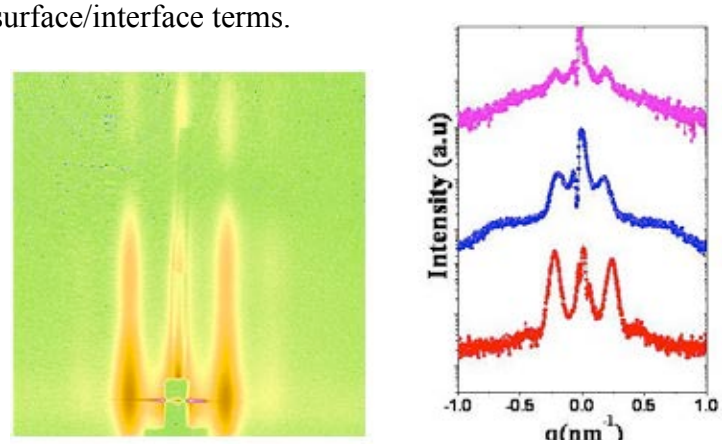

Figure 2. (a, left): typical 2D GISAXS pattern of Co film on nanorippled Si substrate; (b, right): Film thickness dependence of GISAXS pattern

Figure 2(a) shows a typical GISAXS pattern of Co film deposited on nanorippled Si substrate. Well defined sidebands on both sides of the direct beam signal the good quality of the ripples on the film surface. The intensity variation of the sidebands with film thickness is shown in figure 2(b). The height of the first sideband which is expected to be proportional to the square of modulation depth of the ripples, ω^2_{rms} , exhibits a linear decrease with film thickness and goes to zero around a thickness T= 55nm (Figure 3). As a result, the surface contribution to the magnetic anisotropy is also expected to decrease linearly. Thus, one can write for the surface contribution:

$$K_u^s = K_0^s - K_1^s t \qquad \text{(for } t \leq T\text{)} \tag{3}$$

where $K_0^s \equiv K_u^t$ is the surface contribution to the magnetic anisotropy in the limit of film thickness approaching zero, when the surface morphology is in perfect conformity with the morphology of the interface. Therefore, the total anisotropy can be written as:

$$\begin{aligned} K_u^t t &= (K_u^v - K_1^s)t + 2K_u^i && \text{for } t \leq T \\ &= K_u^v t + K_u^i && \text{for } t > T \end{aligned} \tag{4}$$

Thus, in the $K_u^t \times t$ versus t curve, one expects a change in slope as well as intercept at t=T. Preliminary analysis of the MOKE data (Fig. 2) does not show any such behavior, suggesting that for t<T, the film thickness dependence of volume and surface terms is complex. However for t>T, fig. 2 yields both the volume and interface contribution to the anisotropy.

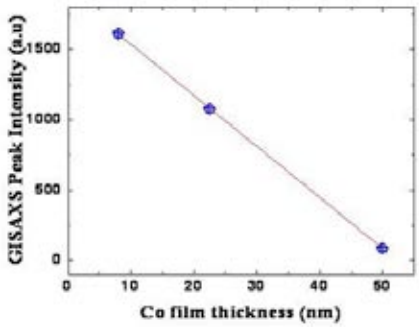

Figure 3. Variation of the intensity of GISAXS sidebands with film thickness

References:

[1] J. Fassbender et. al., New J. Phys. 11, 125002 (2009)
[2] R. Moroni, et. al., Phy.Rev.Lett. 91,167207 (2003)
[3] D. J. Twisselmann et al., J. Appl. Phys. 92, 3223 (2002); H. Kataoka et al., J. Appl. Phys. 73, 7591 (1993)
[4] M. J. Carey et al., U.S. patent no. 7,360,300 (22 April 2008); M. J. Carey et al.,U.S. patent no.7,529,066 (05 May 2009)
[5] K.V. Sarathlal et al., Appl. Surf. Sci. 258, 4116 (2012)
[6] Kai Chen et al., Phy. Rev.B 59 064432 (2012)
[7] E. Schlömann, J. Appl. Phys. 41, 1617 (1970)

IN-SITU STUDY OF MESOSTRUCTURED SILICA SYNTHESIZED IN THE GAS PHASE

B. Sartori, B. Marmiroli, F. Cacho-Nerin and H. Amenitsch

Graz University of Technology, Institute of Inorganic Chemistry, NAWI, Stremayrgasse 9/IV, 8010 Graz, Austria

Mesoporous nanoparticles are of great interest for a variety of applications, such as ion exchange, catalysis, or nanomedicine just to name a few [1], [2].
The spray-drying of aerosol droplets is an economically attractive method to obtain mesostructured nanoparticles: in the drying chamber the synthesis parameters can be easily controlled, making it possible to study the formation and organization of mesostructured nanoparticles in variuos conditions. We have focused our attention on silica nanoparticles.
Previous studies with a custom made aerosol system composed of an atomizer and a slidable inner reaction chamber with controllable temperature (drying part at room temperature and heating part with a temperature that can be selected) [3] showed that by altering the chemical composition of the precursors, or modifying the humidity and temperature conditions during the synthesis, it is possible to obtain mesoporous silica with different lattice constant of the hexagonal phase.
In the present experiment, we characterized with SWAXS the silica condensation during the evaporation process at different temperatures. The precursor solution droplets generated by the atomizer were driven into the drying zone, and then into the heating zone of the reaction chamber [4]. During the drying process, the non-volatile components concentration increases, and they coassemble in the droplets to form a well ordered nanostructure.

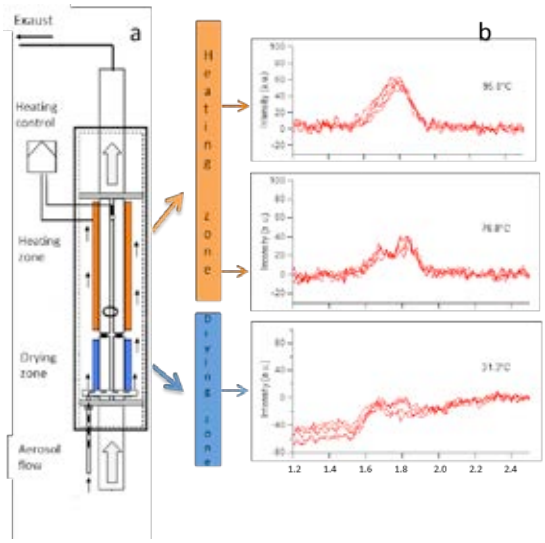

Figure 1. a) Scheme of the aerosol system; b) Scattering pattern of mesoporous silica collected at different temperature along the reaction chamber

The figure shows the SAXS pattern recorded at different positions during a multiple scan along the furnace: the heating temperature was set to 90°C. Each position was scanned five times, to check the influence of the recirculation of the solution in the aerosol generator. The scattering patterns show that the mesostructure formation starts already in the drying zone. Here, two peaks can be seen, suggesting a solvent demixing on the surface of the droplet due to their different evaporation rates, as previously described [5].

References:

[1] Davies, M.E., Nature (2002) 417
[2] Vallet-Regí, M., ISRN Matreial Science, 2012 (2012), ID 608548
[3] Shyjumon I. et al, Langmuir (2011), **27**, 5542-5548
[4] Jungnikl, K. et al, Aerosol Science and Technology (2011), **45**, 795-800
[5] Jiang X. et al, Ind. Eng. Chem. Res. (2012), **49**, 5631-5643

THE ROLE OF SOLVENT-ADDITIVES ON POLYMER-FULLERENE LAYERS FOR ORGANIC PHOTOVOLTAICS

C. J. Schaffer[1], J. Schlipf[1], B. Su[1], Y. Rui[1], S. Bernstorff[2] and P. Müller-Buschbaum[1]

1.) Technische Universität München, Physik-Deptartment, Lehrstuhl für Funktionelle Materialien, James-Franck-Str. 1, 85748 Garching, Germany
2.) Elettra-Sincrotrone Trieste, Strada Statale 14 km 163.5 in AREA Science Park, 34149 Basovizza, Trieste, Italy

Organic photovoltaic devices are more and more frequently reported to display power conversion efficiencies exceeding the milestone of 10% [1]. Such high efficiencies are typically achievable by the use of a blend from so-called push-pull polymers, which typically show a low optical band gap, giving rise to absorption in a large range of the visible spectrum and a fullerene derivative.

In order to gain an operational organic photovoltaic device, polymer and fullerene are mostly dissolved in a common solvent and subsequently applied as the active layer. Hereby, phase separation gives rise to an interpenetrating network of polymer and fullerene domains. When photons are absorbed in the polymer domains, excitons are generated which need to diffuse to a polymer/fullerene interface in order to be separated into two distinct charge carriers. This mechanism is efficient as long as the mean distance of such an interface is in the range of the exciton diffusion length (on the order of some 10 nm). As a consequence, the morphology of the active layer is of utmost importance for the device performance [2].

For the specific materials system consisting of poly[2,6-(4,4-bis-(2-ethylhexyl)-4H-cyclopenta [2,1-b;3,4-b′]dithiophene)-alt-4,7(2,1,3-benzothiadiazole)] and [6,6]-Phenyl C71 butyric acid methyl ester (PCPDTBT:$PC_{71}BM$) being processed with chlorobenzene (CB) it was found that the addition of a small (~ 3% wt in solvent) amount of 1,8-octanedithiol (ODT) leads to a significant increase of power conversion efficiency of solar cell devices from 2.8% to 5.5% [3].

In order to investigate the effect of ODT on the film morphology, blend films from PCPDTBT:$PC_{71}BM$ with different mass ratios (1:1.5, 1:2.0 and 1:2.7), processed from chlorobenzene with and without 3% wt ODT, have been fabricated. Using grazing incidence small angle X-ray scattering (GISAXS) the film morphology was investigated, since GISAXS is very powerful in extracting inner film information [4]. The GISAXS experiments have been performed at the Austrian SAXS beamline at the Elettra Sincrotrone, Trieste. In these GISAXS experiments an X-ray energy of 8 keV and a DECTRIS PILATUS 1M detector were used at a sample-detector distance of 2047 mm. The incident angle was set to 0.4°, which is well above the critical angle of the involved materials.

Figure 1a shows two exemplary images (raw data) of the two dimensional (2D) GISAXS data for the samples with a mass ratio of 1:2.7, which is reported to show highest performance, with and without the addition of ODT. In the images the transmitted information is included as the sample horizon is at the position $\alpha_i+\alpha_f=0.4$. A semi-transparent beamstop was used to protect the detector against the string intensity in the region of the Yoneda and specular peak. The 2D GISAXS look different for the films with and without ODT. It can be seen that, in the case where ODT was used, the lateral scattering is strongly enhanced as compared to the case without ODT. In order to gain more detailed information on the lateral structures present in the films, all patterns were corrected for the semi-transparent beamstop and the sample tilt. Horizontal line cuts from the 2D GISAXS data were taken at the Yoneda region corresponding to PCPDTBT to extract lateral structure information. These horizontal line cuts are shown in Figure 2b, together with model fit curves that reveal more quantitative details about the lateral structure. The latter ones have been obtained within the framework of the distorted wave Born approximation (DWBA) using the local monodisperse approximation

(LMA). The data clearly reveal, that the overall scattering intensity is strongly increased by the use of ODT as solvent additive. Furthermore, a pronounced shoulder at $q_y > 0.1$ nm^{-1} can be found for the three samples where ODT was used. Modeling of the curves reveals also that small objects with sizes up to some ten nanometers double their dimensions by the use of ODT. This is consistent with the idea of an enhanced phase separation in the films due to the additive. Thus our findings contribute to the better understanding of the efficiency enhancement of the organic solar cells.

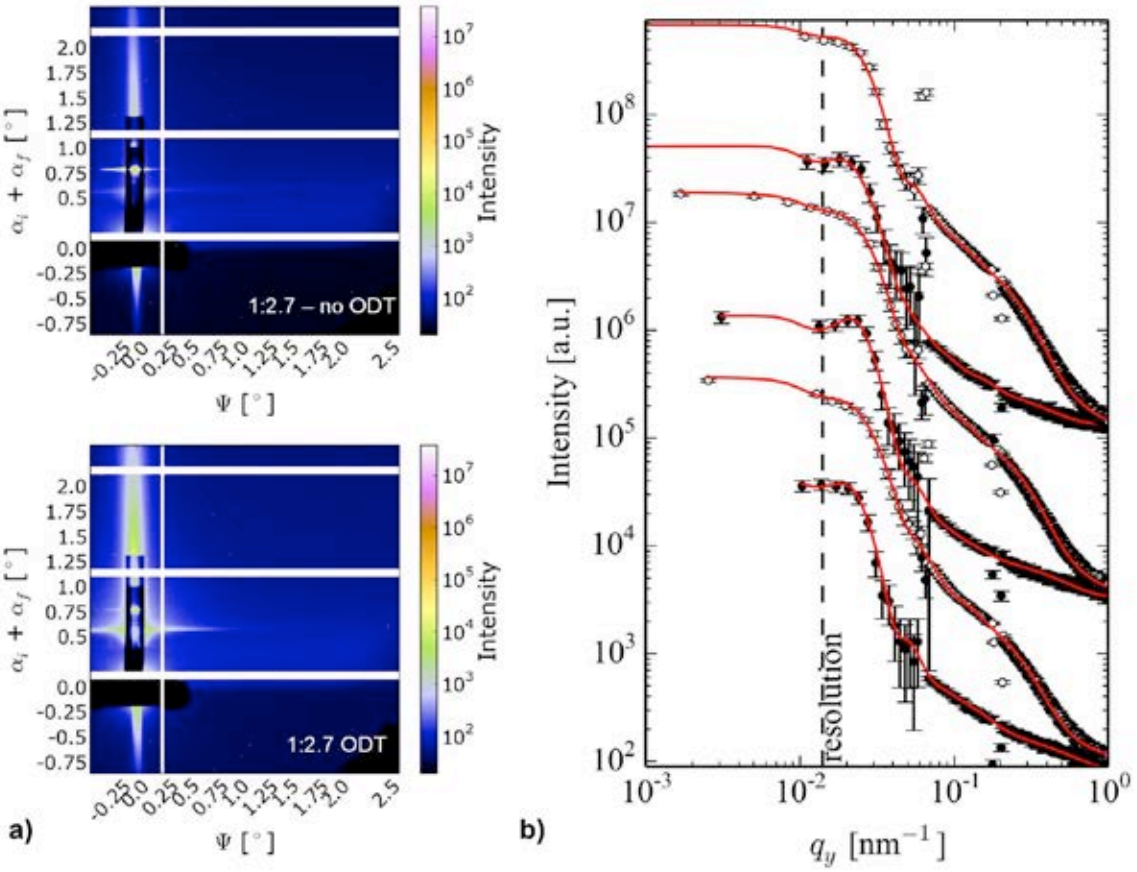

Figure 1. a) Raw 2D GIAXS data with a mass ratio of 1:2.7 (PCPDTBT:$PC_{71}BM$) without (top) and with (bottom) the use of ODT as solvent additive. b) Horizontal line cuts from the 2D GISAXS data of the samples without (full circles) and with (open circles) ODT. The mass ratio PCPDTBT:$PC_{71}BM$ from bottom to top is 1:1.5, 1:2.0,1:2.7 (pair wise with and without ODT). The data has been corrected for the beamstop attenuation and the sample tilt. Data is shifted pair wise along the y-axis for clarity. The dashed line indicates the resolution limit towards large scale structures

References:

[1] M. A. Green, K. Emery, Y. Hishikawa, W. Warta, E. D. Dunlop. Solar Cell Efficiency Tables (version 43). Progress in Photovoltaics: Research and Applications 22, Nr. 1 (2014)

[2] M.A. Ruderer, P. Müller-Buschbaum; Morphology of polymer-based bulk heterojunction films for oganic photovoltaics; Soft Matter 7, 5482-5493 (2011)

[3] J. Peet, J. Y. Kim, N. E. Coates, W. L. Ma, D. Moses, A. J. Heeger, G. C. Bazan; Efficiency Enhancement in Low-Bandgap Polymer Solar Cells by Processing with Alkane Dithiols; Nature Materials (2007)

[4] P. Müller-Buschbaum; Grazing incidence small-angle x-ray scattering - an advanced scattering technique for the investigation of nanostructured polymer films; Anal.Bioanal.Chem. 376, 3 (2003)

AN IN-SITU SAXS STUDY ON THE INFLUENCE OF EDTA ON THE FORMATION OF CdS QUANTUM DOTS

A. Schiener[1], K. Willnauer[1], H. Amenitsch[2] and A. Magerl[1]

1.) Crystallography and Structural Physics, Staudtstraße 3, Erlangen, Germany
2.) Institute for Inorganic Chemistry, Stremayrgasse 9/IV, Graz, Austria

Stabilized CdS quantum dots are already widely applied in different applications (e.g. chemistry or medicine) [1]. When the size becomes less than about 5 nm their physical properties become different from bulk material [2]. Most applications exploit the possibility to tailor electrical and optical properties as a function of particle size [3]. While various synthesis routes are already established and used, little is known about the nucleation and growth process. This understanding appears highly relevant when exploiting new synthesis routes to produce quantum dots of highest quality.

This study investigates the nucleation and growth of EDTA-stabilized (ethylene-diaminetetraacetic acid) CdS nanoparticles via in-situ SAXS (small angle X-ray scattering) using a stopped flow cell which has a starting dead time of 10 ms for the mixing of the reactants. From this we followed in-situ the particle formation up to 140 seconds at which time the reaction is supposed to be completed. This allows us to get a detailed insight into the evolution of the particle size and morphology, as well as their concentration in the solvent water. The stoichiometric addition of EDTA as a stabilizer is essential to slow down the reaction into the proper time regime, and to obtain stable EDTA-capped nanoparticles in solution.

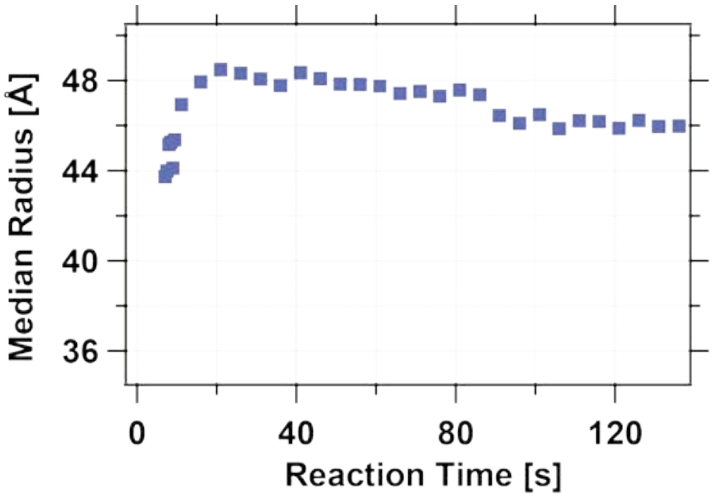

Figure 1. Median radius of the lognormal distributed spheres for a CdS concentration of 0.75 mM as a function of time

Figure 1 shows the behavior of the median particle size for EDTA stabilized 0.75 mM CdS nanoparticles as a function of time. A lognormal distributed spherical particle model was sufficient to achieve a proper fit to the data. To neglect a contribution of the change of the background due to coating of the capillary, to the fitted data, the first 0.5 s of every injection cycle were used as for background subtraction. Applying this we averaged the detector images over 40 cycles for every reaction time in order to obtain a reasonable scattering signal. The reduction and evaluation of the data were done using the Igor Pro extensions Irena [4] and Irena [5].

While the particle radius in this study remained constant after about 20 s the scattering volume increases over the entire observed time (see figure 2). This indicates that the reaction is not completed after 140 s.

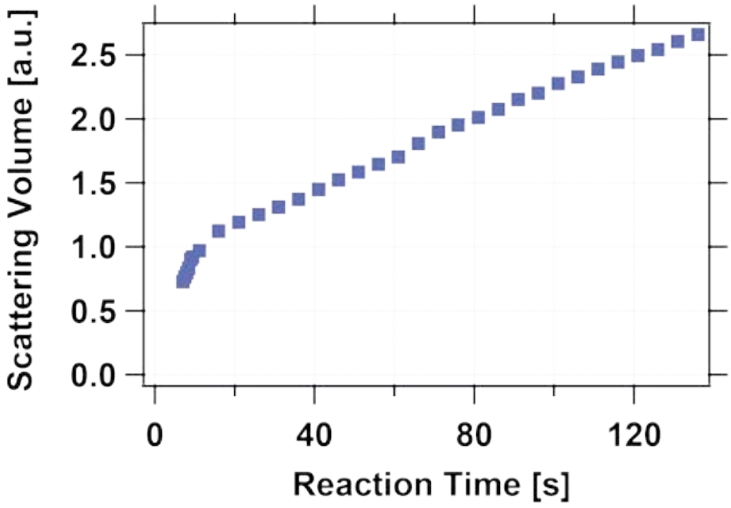

Figure 2. Scattering volume in arbitrary units for a CdS concentration of 0.75 mM as a function of time. The slope of the curve at measurement times exceeding the 100 s indicates, that the reaction is not jet completed after 140 s

Based on the experiences of this experiment we developed a novel containment free stopped – flow setup, which enables us to access times below 0.5 s, without a significant change of the background due to coating directly after the injection.

References:

[1] N.S. Kozhevnikova, A.S. Vorokh, A.A. Rempel, Preparation of Stable Colloidal Solution of Cadmium Sulfide CdS Using Ethylenediaminetetraacetic acid, Russian Journal of General Chemistry 80 (2010) 391–394

[2] Brus, L. E. Electron–electron and electron-hole interactions in small semiconductor crystallites: The size dependence of the lowest excited electronic state. J. Chem. Phys. 80, 4403 (1984)

[3] Trindade, T., O'Brien, P. & Pickett, N. L. Nanocrystalline Semiconductors: Synthesis, Properties, and Perspectives. Chem. Mater. 13, 3843–3858 (2001)

[4] Ilavsky, J. Nika : software for two-dimensional data reduction. J. Appl. Crystallogr. 45, 324–328 (2012)

[5] Ilavsky, J. & Jemian, P. R. Irena : tool suite for modeling and analysis of small-angle scattering. J. Appl. Crystallogr. 42, 347–353 (2009)

PRECIPITATION KINETICS OF $Al_3(Sc,Zr)$ IN AN AlMgScZr ALLOY

J.Taendl[1], H. Amenitsch[2] and C. Poletti[1]

1.) Institute of Materials Science and Welding, Graz University of Technology, 8010 Graz, Austria
2.) Institute of Inorganic Chemistry, Graz University of Technology, 8010 Graz, Austria

One of the most promising approaches to increase the specific strength of Al-alloys is the use of scandium as alloying element. When added to aluminum, Sc produces the highest increment of strengthening per atom, mainly due to the precipitation of nano-disperse, coherent, $L1_2$ type Al_3Sc precipitates. If appropriately aged, these phases have a size of 2-6nm which leads to strengthening of around 50MPa per 0.1wt% Sc. If, in addition, zirconium is alloyed in a Sc-to-Zr-weight ratio of around 2:1, $Al_3(Sc_x,Zr_{1-x})$ precipitates with improved thermal stability are formed [1]. The overall strengthening is even more pronounced if Sc and Zr are added to non-heat-treatable AlMg-alloys which results from the superposition of solid solution and precipitation strengthening [2].
In this work we perform an in-situ SAXS study of the precipitation kinetics of $Al_3(Sc,Zr)$ in an AlMg4Sc0.4Zr0.12 alloy in different initial conditions during isothermal ageing at 250, 325, and 400 °C for 3 hours. The initial sample conditions are summarized in Table 1. The samples with a size of 20 x 8 mm were cut and electrolytically polished to a final thickness of around 70µm. During measuring we clamped the samples in a molybdenum sample holder directly attached to a heating plate (Figure 1).

Table 1. Summary of the initial sample conditions

Condition	Applied treatment	Objective of the treatment
C1: As-cast (AC)	Casting and rapid cooling	Reference material
C2: Electron beam re-solidified (EBRS)	C1 + re-solidification in an EBW system	Increase the concentration of Sc in the supersaturated Al matrix
C3: Cold deformed (CD)	C1 + cold deformation in a Gleeble system	Study the influence of dislocations on the precipitation kinetics
C4: Hot deformed (HD)	C1 + hot deformation in a Gleeble system	Study the influence of partially restored microstructures in the kinetics of precipitation [3]

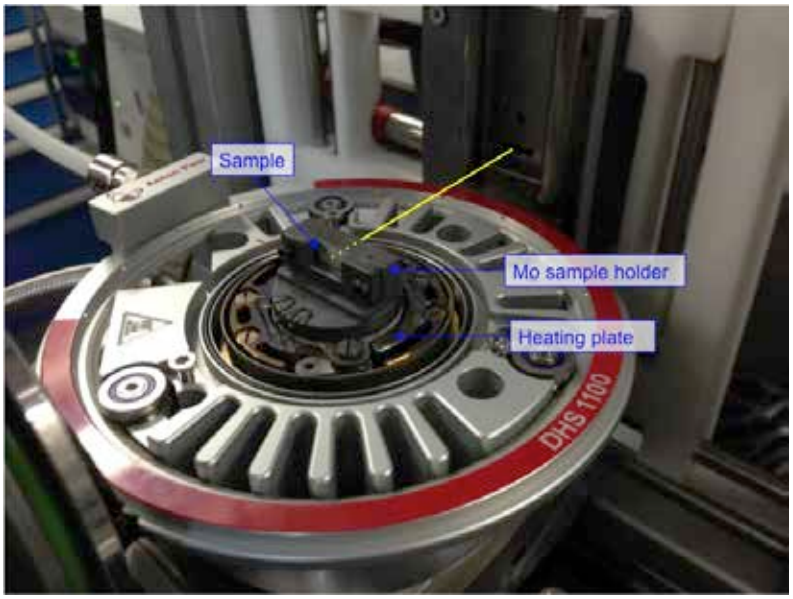

Figure 1. Measuring setup; Sample, sample holder and heating stage; The yellow line indicates the beam

Figure 1 shows SAXS spectra of a sample in C1 condition measured in-situ during isothermal ageing at 400°C for 3 hours. With increasing ageing time the shapes of the spectra change. At the beginning of the experiment they show a rather steady decrease of the intensity with increasing scattering angle q. With increasing ageing time, however, the curves develop two bumps, where the one is located at around 0.4nm^{-1} and the other one at 1.6nm^{-1}. In contrast, the intensity at scattering angles between 2.5 and 3 nm^{-1} is reduced during ageing. These observations indicate the formation of a bimodal precipitate structure. The mean size of the two precipitate populations at the end of the experiment can be roughly estimated with 15nm and 4nm, respectively. The plot of correlation length and temperature over time (Figure 3) further indicates structural changes due to isothermal ageing.

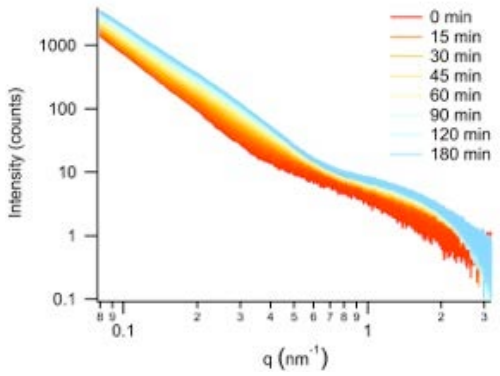

Figure 2. SAXS spectra of a sample in C1 condition isothermally aged at 400°C for 3 hours

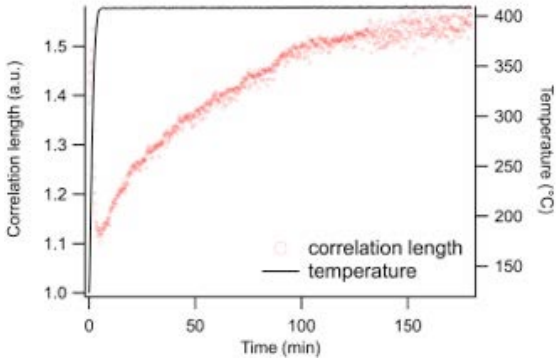

Figure 3. Plot of correlation length and temperature over time for a sample in C1 condition isothermally aged at 400°C for 3 hours

The obtained results will be combined with the results obtained from TEM analyses of heat treated samples and with calorimetry analyses as done for other alloys in [4]. Finally, the results will be used to validate MatCalc © simulations of the precipitation kinetics.

References:

[1] J. Royset and N. Ryum; Scandium in aluminium alloys; International Materials Reviews **50 (1)**, 19-44 (2005)

[2] E. A. Marquis, D. N. Seidman and D. C. Dunand; Effect of Mg addition on the creep and yield behavior of an Al-Sc alloy; Acta Materialia **51 (16)**, 4751-4760 (2003)

[3] J. Taendl, M. Dikovits and C. Poletti; Investigation of the hot deformation behavior of an Al-Mg-Sc-Zr alloy under plane strain condition; Key Engineering Materials **611-612**, 76-83 (2014)

[4] M. Kumar, C. Poletti and H.P. Degischer; Precipitation kinetics in warm forming of AW-7020 alloy; Materials Science and Engineering: A **561**, 362-370 (2013)

SELF-STRUCTURED PHOTOSYNTHETIC, FIBRE-LIKE SENSITIZER-CATALYST ARRAYS FOR HIGHLY EFFICIENT LIGHT-INDUCED WATER OXIDATION

Z. Syrgiannis[1], A. Bonasera[1], A. Sartorel[2], M. Carraro[2], F. Cacho-Nerin[3‡], H. Amenitsch[3], G. La Ganga[4], F. Puntoriero[4], S. Campagna[4‡], S. Piccin[5], S. Fabris[5], M. Bonchio[2] and M. Prato[1]

1.) Centre of Excellence for Nanostructured Materials (CENMAT) and INSTM, unit of Trieste, Department of Chemical and Pharmaceutical Sciences, University of Trieste, via L. Giorgieri n°1, 34127 Trieste, Italy
2.) CNR - ITM and Department of Chemical Sciences, University of Padova, via F. Marzolo n°1, 35131 Padova, Italy
3.) Institute of Inorganic Chemistry, Graz University of Technology, Stremayrgasse 9/IV, 8010 Graz, Austria;
4.) Centro Interuniversitario per la Conversione Chimica dell'Energia Solare, unit of Messina, Department of Chemical Sciences, University of Messina, viale F. Stagno D'Alcontres n°31, 98166 Messina, Italy
5.) SISSA, Scuola Internazionale Superiore degli Studi Avanzati, and CNR - IOM, Istituto Officina dei Materiali, Centro DEMOCRITOS, via Bonomea n°265, 34136 Trieste, Italy

‡ Current address: Diamond Light Source, Harwell Science and Innovation Campus, Didcot OX11 0DE, UK

Renewed attention has been addressed during the last 10 years towards polyoxometalates chemistry. Polyoxometalates (**POM**s) are an interesting typology of molecular inorganic scaffolds accessible with simple and well established synthetic protocols, which possess some relevant features such us catalytic activity towards a large variety of chemical transformations, such as water oxidation process [1]; moreover, the possibility to employ a supramolecular approach for the formation of novel poloxometalates-based superstructures which integrate chromophores make them suitable for artificial photosynthesis [2].
Recently, **Ru_4POM** specie has shown attitude to promote water oxidation in presence of photocatalyst $Ru(bpy)_3$ and its derivatives, with results worthy to note [3]. With the aim to improve the photocatalytic performances of the system described above, $Ru(bpy)_3$ has been modified by the covalent linkage on one (bpy) unit of a pyrene fragment; the presence of the new aromatic unit lengthens exited state lifetime of Ru centre so to make more effective the energy transfer towards POM unit. The novel supramolecular architecture produced by the interaction of the photosensitizer $Ru(pyrbpy)(bpy)_2$, **1**, and Ru_4POM, **2**, has shown improved catalytic activity, but also the formation of fibrous aggregates (Figure 1).

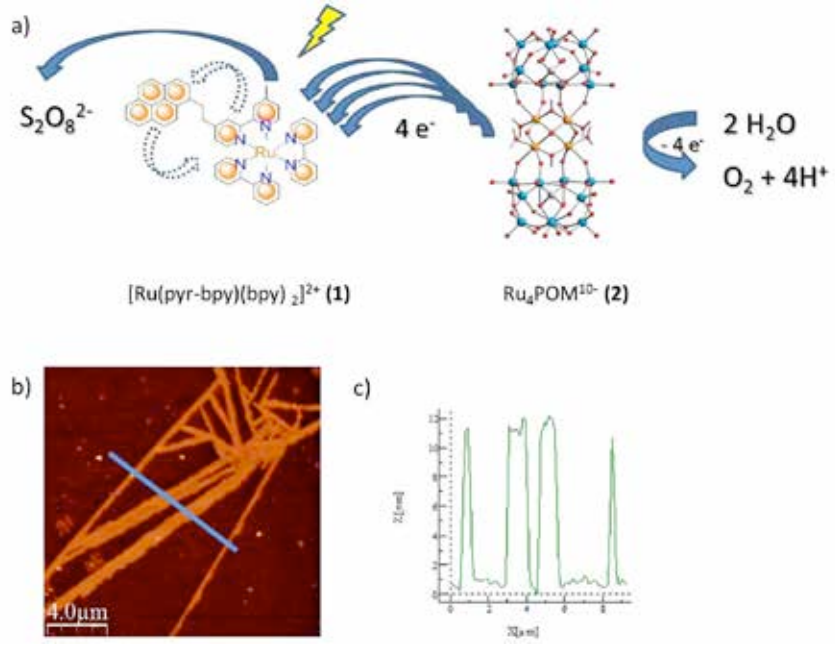

Figure 1. a) Structural *formulae* of **1** and **2** and cartoon representing electrons flow occurring during water oxidation process; b) representative AFM image of **1**@**2** deposited over glass surface and c) the height profile of the sample in the highlighted area

SAXS measurements have been performed in order to obtain information about the observed nanostructures. As blank experiment, solution of **2** has been analysed first, and we have found one correlation peak at q = 4.32 nm^{-1}, corresponding in a structural repeat distance of 1.45 nm, as shown in Figure 2; from this data, a natural tendency by **2** to self-organization has been put on evidence.

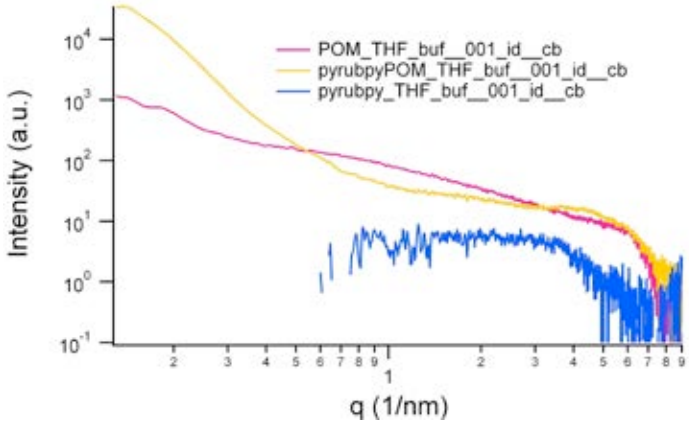

Figure 2. SAXS patterns of 1 (2.45 10^{-4} M, blue line) and 2 (6 10^{-5} M pink line) and the mixture of them in a mixed solvent THF/buffer phosphate 20 mM (1:1 v/v)

Moreover we have analysed the **1@2** mixed 1:4 molar ratio as suggested from conductivity experiments; scanning the sample at different times, we have observed an evolution of the system which, from small and spherical nanoparticles, evolves towards a 2-D system, with q = 4.27 nm^{-1} and q = 1.944 nm^{-1}. The first distance is closer to the value of **2** solution and can be recognized as the vertical distance between POMs, while the second is compatible with the distance between 2 POM units with 2 photosensitizer molecules.
Starting from SAXS data, Molecular Dynamics (MD) simulations have been performed in order to shape the architecture of the supramolecular system. In a first set of simulation we have explored the interaction between **1** and **2** molecules considering the presence of explicit water molecules in the simulation cell unit, and we have noticed that the interaction between 1 and **2** molecules is not selective to specific **2** molecular sites, because **1** molecules easily diffused over **2** surface, exploring several binding modes and configurations. The tendency of the **1** molecules to form aggregates is maintained also in presence of **2**. After the optimization of the minimal repetition unit of **1@2** superstructure, we have considered a periodically repeated three dimensional structure, with a unit cell containing 16 molecules of **2** and 64 molecules of **1**. As shown in Figure 3, fibrous structures are generated consisting of **2** molecules stacked along the z direction with their main axis orthogonal to the fibre axis. **1** molecules formed a disordered network shell around the **2** axis, with several π–π stacking units that provide additional structural axial cohesion to the fibre; π–π stacking also linked neighbouring fibres. Water molecules, which were initially distributed uniformly in the pores, accumulate on the regions of the **2** surface that remains exposed from the **1** network. There is clearly a strong driving force for water solvation of **2**, thus providing additional screening of the strong electrostatic Ru_4POM field. SAXS simulated spectra provided from the optimized final structure are in agreement with experimental data (Figure 4).

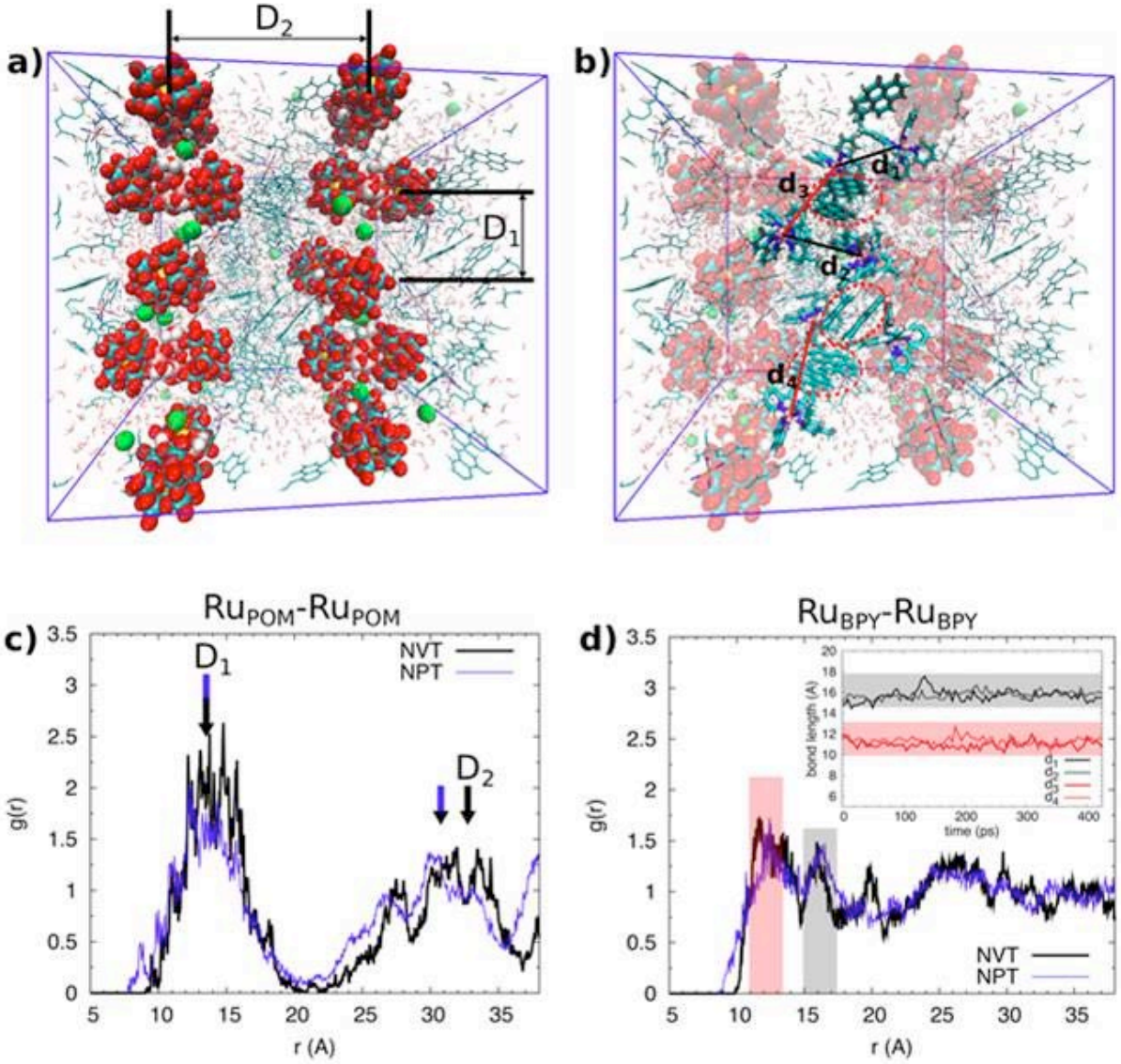

Figure 3. a) Snapshots of equilibrated configuration from the NVT MD simulation; for a clearer view, not all the 1 molecules are displayed. b) View along the z-axis. Water molecules atoms are represented in black. Grey spheres denote Na^+ counterions. c) and d), comparison between simulated and measured SAXS spectra

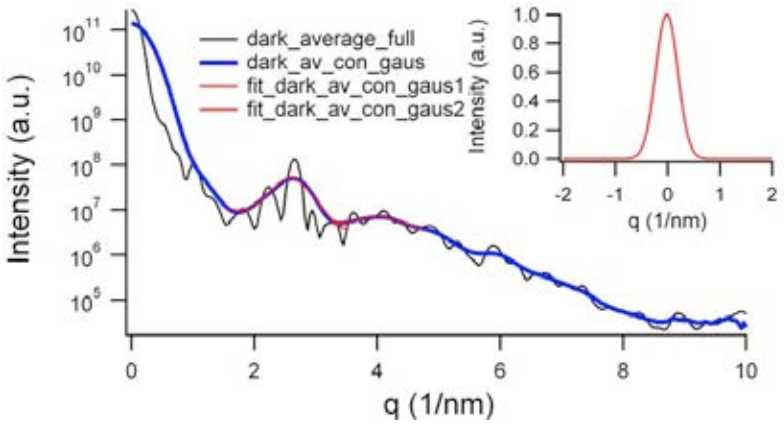

Figure 4. Averaged theoretical SAXS data (black) and (blue) convoluted with the Gaussian function shown in the insert in order to account for the additional disorder of the **1**@**2** supramolecular structure

Summarizing, we achieved the description of the architecture generated by the interaction of an organic photosensitizer with a molecular inorganic catalyst; SAXS experiment recognized an ordered regular arrangement of the components in the fibre-like aggregates and provided a good data set of data for the construction of theoretical models. MD simulations went beyond SAXS analysis and revealed an active role in the formation and stabilization of the fibrous structure.

Table 1. Short description of samples and relevant data extracted from SAXS spectra

Sample	POM/PS ratio (in moles)	d-spacing values
blank	**Ru_4POM** only	1.45 nm
1@2	4:1	1.47 nm 3.23 nm

References:

[1] A. Sartorel, M. Bonchio, S. Campagna, F. Scandola, Tetrametallic molecular catalysts for photochemical water oxidation, Chemical Society Reviews **42**, 2262-2280 (2013)

[2] N. D. McClenaghan, Y. Leydet, B. Maubert, M. T. Indelli, S. Campagna, Excited-state equilibration: a process leading to long-lived metal-to-ligand charge transfer luminescence in supramolecular systems, Coordination Chemistry Reviews **249**, 1336-1350 (2005).

[3] a) M. Orlandi, R. Argazzi, A. Sartorel, M. Carraro, G. Scorrano, M. Bonchio, F. Scandola, Ruthenium polyoxometalate water splitting catalyst: very fast hole scavenging from photogenerated oxidants, Chem. Commun. **46**, 3152-3154 (2010); b) M. Natali, M. Orlandi, S. Berardi, S. Campagna, M. Bonchio, A. Sartorel, F. Scandola, Photoinduced water oxidation by a tetraruthenium polyoxometalate catalyst: ion-paring and primary processes with $Ru(bpy)_3^{2+}$ photosensitizer, Inorganic Chemistry **51**, 7324-7331 (2012)

Life Sciences

STRUCTURAL CHARACTERIZATION OF CATIONIC LIPOSOME/POLY(I:C) COMPLEXES SHOWING HIGH ABILITY IN ELIMINATING PROSTATE CANCER CELLS

G. Caracciolo[1], D. Pozzi[1], and H. Amenitsch[3]

1.) Department of Molecular Medicine, "Sapienza" University of Rome, Viale Regina Elena 291, 00161 Rome, Italy
2.) Institute of inorganic Chemistry, Graz University of Technology, Stremayerg. 6/IV, 8010 Graz, Austria

Polyinosinic–polycytidylic acid (poly(I:C)) is a mimic of viral double-strand (ds)RNA that induces apoptosis in many cancer cells [1]. However, toxicity and stability issues so far prevented its application as it undergoes enzymatic degradation and bear the potential to trigger undue immune stimulation as well as autoimmune disorders. Encapsulation of antitumor drugs is frequently used to improve their effectiveness by lowering the necessary dosage. In this study we examined the ability of cationic liposomes to deliver poly(I:C) into PC3 and DU145 cell lines, derived from human bone and brain prostate cancer metastasis respectively. The first formulation was made of the cationic lipid 1,2-dioleoyl-3-trimethylammonium-propane (DOTAP) and the zwitterionic lipid dioleoylphosphocholine (DOPC). The second one was the binary lipid system made of the cationic 3β-[N-(N',N'-dimethylaminoethane)-carbamoyl]-cholesterol (DC-Chol) and the zwitterionic helper lipid dioleoylphosphatidylethanolamine (DOPE), while the third formulation was the multicomponent (MC) lipid system encapsulating the four lipid species simultaneously.
Since the structure of lipid membranes is directly related to their ability to encapsulate drugs and nucleic acids, a full knowledge of the membrane organization at the nanoscale is mandatory. In this regard, synchrotron SAXS allows to access structural parameters of lipid bilayers also when the lipid concentration is extremely low and nears that of typical cell culture experiments. In Fig. 1 the SAXS patterns of the bare cationic liposomes are shown.

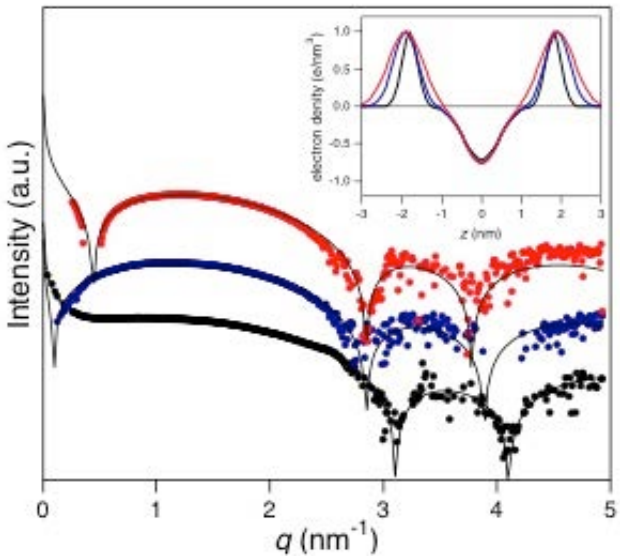

Figure 1. Synchrotron small angle X-ray scattering patterns of liposomal dispersions: DOTAP–DOPC (black circles), DC-Chol–DOPE (red circles) and MC (blu circles). A global analysis of the pattern (fit shown as solid line) reveals the electron density profile of the lipid/water system (inset) from which structural parameters, such as the membrane thickness can be derived

As evident, lipid vesicles exhibited only pure diffuse scattering, which is typical of uncorrelated bilayers. The scattered intensities were therefore fitted with a simple unilamellar

vesicle model based on the Gaussian-type representation of the electron density profile (EDP) as described in ref. 2. Fig. 2A, shows the SAXS patterns of cationic liposomes/poly(I:C) complexes (ρ=2.5). Comparing Fig. 2A with Fig. 1 it is clear that, upon mixing with poly(I:C), the diffraction patterns of cationic liposomes change from exhibiting pure diffuse scattering to showing Bragg peaks. This means that the lipid/water system changes from a state of positionally uncorrelated bilayers to a state of positionally correlated layers. The sharp periodically spaced Bragg peaks at q00l are due to a multilamellar structure with periodicity d=2π/q00l ranging from 6.90 nm (DC-Chol−DOPE/poly(I:C) complexes) up to 6.64 nm (DOTAP−DOPC/poly(I:C) complexes) (Table 1).

Table 1. Lamellar d-spacing, d, and lattice constant, dpoly(I:C), of cationic liposome/poly(I:C) complexes

	DOTAP-DOPC	**MC**	**DC-Chol-DOPE**
d (nm)	6.67±0.20	6.80±0.25	6.87±0.24
$d_{poly(I:C)}$ (nm)	4.39±0.12	3.93±0.10	3.35±0.12

The SAXS results of Fig. 2A suggest that mixing anionic poly(I:C) with cationic liposomes leads to an electrostatic-mediated topological transition into condensed complexes with a multilayer structure (Fig. 2B) composed of poly(I:C) layers sandwiched between cationic lipid bilayers with periodicity d=dB+dw (thickness of the lipid membrane plus the monolayer of poly(I:C) and water). Such arrangement is similar to that reported for both cationic liposome/DNA complexes and cationic liposome/short interfering RNA. From the thickness of lipid bilayers the water/poly(I:C) layer was found to vary from 2.3 nm up to 2.6 nm in size. Since poly(I:C) is structurally similar to double-stranded RNA, this means that the water channel is just large enough to accommodate a hydrated monolayer of poly(I:C). From the full width at half maximum (FWHM) of the first-order lamellar Bragg peaks, a domain lamellar size of about Lm=2π/FWHM~140 nm could be estimated. Since the lamellar d-spacings are roughly 7 nm in size, this finding suggests that multilamellar cationic liposomes/poly(I:C) complexes are made of about twenty repeating lipid/DNA layers. This domain size is in good agreement with that previously reported for DNA and siRNA lipoplexes. In the SAXS pattern of cationic liposomes/poly(I:C) complexes a broad peak (marked by an arrow) (Fig. 2A, inset) was also observed. This is most likely due to the in-plane correlation between poly(I:C) molecules that form a one-dimensional (1D) in-plane lattice with repeat distance dpoly(I:C)=2π/qpoly(I:C) between 3.40 nm (DC-Chol−DOPE/poly(I:C) complexes) and 4.33 nm (DOTAP−DOPC/poly(I:C) complexes). From a structural point of view, we observe that MC/poly(I:C) complexes exhibit structural properties (Table 1) intermediate between those of DOTAP−DOPC/poly(I:C) and DC-Chol−DOPE/poly(I:C) ones. This represents another similarity with cationic liposome/DNA complexes and suggests that the two-dimensional condensation of DNA is controlled by surface area of lipid membranes. In summary, synchrotron SAXS showed that: (i) cationic lipid/poly(I:C) complexes are multilamellar structure made of poly(I:C) molecules embedded within alternating lipid bilayers; (ii) in each water channel, poly(I:C) molecules are tightly packed and give rise to a well-ordered 1D lattice whose spatial unit is regulated by available surface area of lipid membranes.We further found that cationic liposomes/poly(I:C) complexes were up to 10 times more efficient in eliminating metastatic prostate cancer cells than the free drug. Most importantly, the ability of distinct lipid formulations to induce apoptosis did not correlate with their endosomal escape ability. This property of cationic liposome/poly(I:C) complexes contrasts to cationic liposome/DNA complexes, where the endosomal escape ability is rate-limiting step for the transfection efficiency [3].

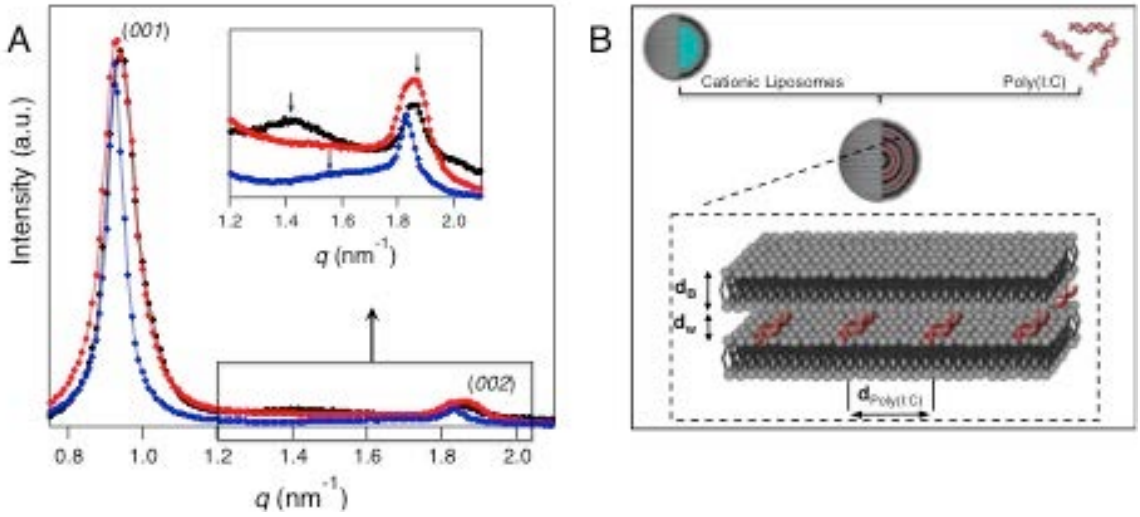

Figure 2. (A) Synchrotron SAXS patterns of DOTAP–DOPC/poly(I:C) (black circles), MC/poly(I:C) (blu circles) and DC-Chol–DOPE/poly(I:C) (red circles) complexes. (B) Mechanism of formation and nanostructure of cationic liposome/poly(I:C) complexes. Poly(I:C) molecules (right) are condensed in the mixture with unilamellar cationic liposomes (left), whereby both lipid and DNA undergo a complete topological transformation into compact complex multilayer complexes. Internally (dashed box), the complexes have ordered multilamellar structure made of water channels of thickness dw occupied by poly(I:C) molecules sandwiched between alternating lipid bilayers with thickness dB. Poly(I:C) molecules are spatially correlate and give rise to a one-dimensional in-plane lattice

References:

[1] B. Jasani, H. Navabi and M. Adams; Ampligen: a potential toll-like 3 receptor adjuvant for immunotherapy of cancer; Vaccine **27**, 3401-3404 (2009).

[2] G. Pabst; Global properties of biomimetic membranes: Perspectives on molecular features; Biophys. Rev. Lett. **1**, 57-84 (2006).

[3] S. Palchetti, D. Pozzi, A. Riccioli, E. Ziparo, V. Colapicchioni, H. Amenitsch and G. Caracciolo; Structural characterization of cationic liposome/poly(I:C) complexes showing high ability in eliminating prostate cancer cells; RSC Advances **3**, 24597-24604 (2013)

INTERACTION OF AMYLOID BETA PROTEIN AGGREGATES AND MODEL CELLULAR MEMBRANES: A STUDY ON THE DOUBLE LAYER STRUCTURE

R. Carrotta[1], F. Librizzi[1], M.C. Nicastro[1], D. Spigolon[1], M.G. Ortore[2], D. Bulone[1] and P.L. San Biagio[1]

1.) Institute of Biophysics, National Council of Research, Via U. La Malfa 153, 90146 Palermo, Italy.
2.) Department of Life and Environmental Sciences and National Interuniversity Consortium for the Physical Sciences of Matter, Marche Polytechnic University, Ancona, Italy

From a molecular point of view, Alzheimer's disease is characterized by the accumulation of a 39–42 amino acid peptide, the amyloid beta-peptide (Ab), in insoluble cerebral plaques, known as amyloid fibrils. However, Ab intermediates (oligomers/protofibrils), more than mature fibrils, have been proven to be the most toxic species, able to interfere with cellular membranes in many different ways [1]. We report here a study focused on the interaction of liposomes composed of OPPC:POPS (9:1) at different concentrations of cholesterol (0, 10% w/w) and with or without the ganglioside GM1 (5%, when cholesterol was 10% w/w), with different Ab species. We have a standard protocol to obtain samples rich of different aggregates, by quenching at different instants the aggregation of the amyloid-beta peptide [2]. Aim of this study was a comparison of the structure factor of the different ULVs bilayer before and after mixing with different Ab species, in order to get insight into the interaction. The SAXS patterns evidence two peaks in the region interesting the double layer structure. A detailed analysis of the data would allow to extract structural features and differences in the bilayer structure as a function of liposomes composition. As a first step, in order to highlight information contained in our data concerning the interaction, we performed a simple analysis by fitting a partial region of the collected data with two gaussians (see figure 1). In figure 2, we report the most significant parameter, i.e. the Q_{MAX} of the second Gaussian as a function of temperature.

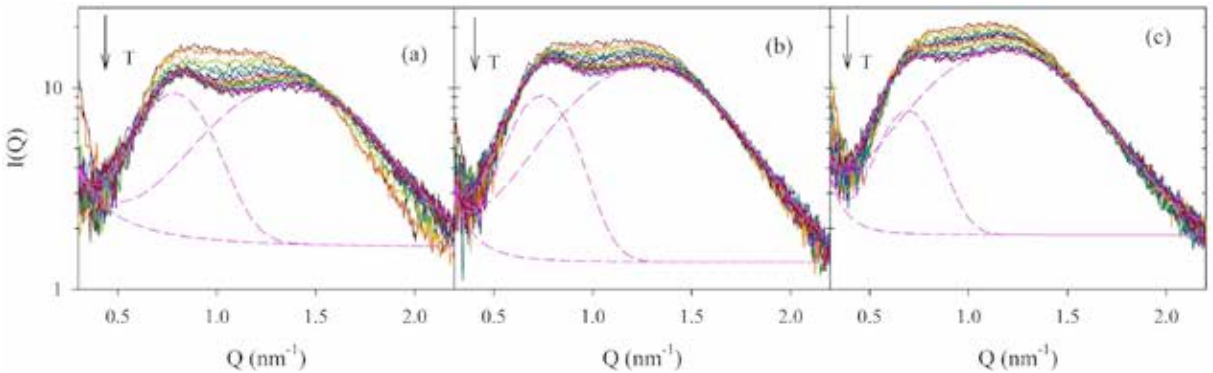

Figure 1. SAXS scattering pattern of sample OPPC:POPS (a), OPPC:POPS:Chol (b) and OPPC:POPS:Chol:GM1 (c) at different temperatures, from -10°C up to 20°C. The lines represent the Gaussian functions and a background used to fit the data, shown as an example for the highest temperature

A recent study showed that oligomers fraction, more than fibrils or native monomers, is able to interact with the lipid surface in a supported lipid bilayer system, as seen in liquid AFM observation [3]. Our results highlight a difference in the double layer depending on lipids-cholesterol-ganglioside composition (figure 1). We have recently found evidence through isothermal titration calorimetry that in our experimental conditions, if and only if a very small amount of ganglioside (5%) is present together with a 10% (w/w) of cholesterol, an interaction Ab-liposome occurs. When GM1 is absent no interaction is measured. Surprisingly, from a structural point of view, SAXS results did not evidence any change in the liposomes structure factor under addition of Ab species, even when GM1 was present (figure

2). We then argue that the interaction does not necessarily mean Ab insertion into the double layer or any measurable change in the double layer structure. We do not have a clear understanding of the experimental evidence that Ab species interact very differently with liposomes (100nm large) with respect to a supported "infinite" lipid bilayer, even though this could rise from the different geometry of the systems, a large bi-dimensional or smaller three-dimensional double layer respectively.

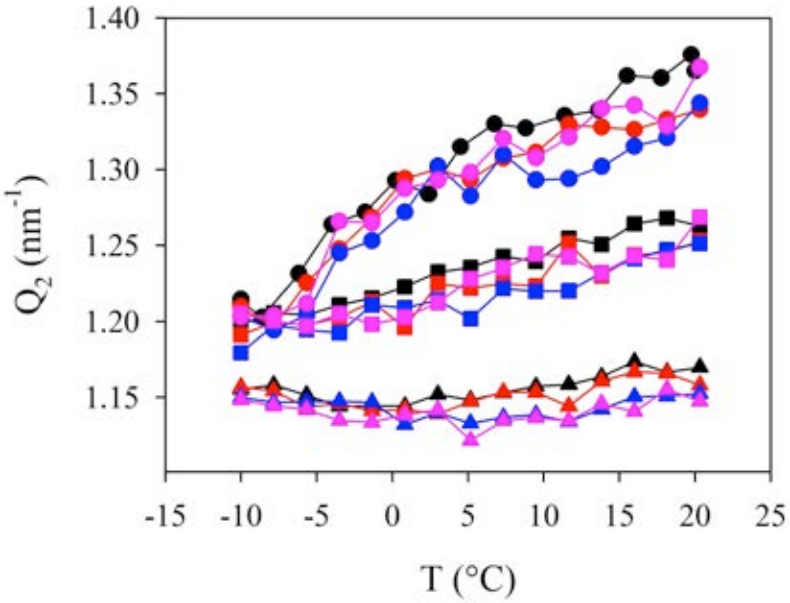

Figure 2. Q values, corresponding to the maximum of the second Gaussian, as a function of temperature: OPPC:POPS (circles), OPPC:POPS:Chol (squares) and OPPC:POPS:Chol:GM1 (triangles). For all samples: liposomes alone (black), liposomes with Ab-monomers (red), liposomes with oligomers (pink) and liposomes with fibrils (blue)

References:

[1] R. Kayed et al.; Annular protofibrils are a structurally and functionally distinct type of amyloid oligomer; Journal of Biological Chemistry, **284**, 4230-4237 (2009)
[2] R. Carrotta et al.; Inhibiting effect of αs1-casein on Aβ1-40 fibrillogenesis; BBA **1820**, 2, 124-132 (2012)
[3] C. Canale et al.; Different effects of Alzheimer's peptide Aβ(1–40) oligomers and fibrils on supported lipid membranes; Biophysical Chemistry **182**, 23–29 (2013

GISAXS ON SUPPORTED LIPID BILAYERS: THE ROLE OF HYDRATION

S. Corvaglia[1,2], L. Ianeselli[2], A. Bosco[2], H. Amenitsch[3], P. Parisse[4], and L. Casalis[2,4]

1.) University of Trieste, address, Trieste, Italy
2.) ELETTRA - Sincrotrone Trieste S.C.p.A., s.s. 14 km 163.5 in Area Science Park, Trieste, Italy
3.) TU Graz, Stremayrgasse 9/IV, Graz, Austria
4.) INSTM - ST Unit, s.s. 14 km 163.5 in Area Science Park, Trieste, Italy

We performed a series of GISAXS measurements on lipid bilayers of mixed composition as a function of humidity. In particular, we used this method to investigate the structural transition of dioleoylphosphatidylcholine (DOPC)/ sphingomyelin (SM) multi-bilayer in presence of a different percentage of cholesterol at different bilayer's hydration levels by changing the relative humidity (from 5% to 85% to 5%). Supported lipid bilayers have been prepared on silicon wafers by solvent spreading at 30 °C and 80% humidity chamber. After the complete solvent evaporation and hydration, in order to enhance the order and packing of the molecules, the samples have been put in a vacuum chamber to remove completely any solvent residue, that could have interfered with the GISAXS measurements.

We discuss here the case of DOPC/SM +10% cholesterol. In Fig. 1a we report, in a color scale, the variation of the scattered intensity as a function of the scattering vector q and the relative humidity. Bragg's peaks typical of a parallel lamellar structures were observed. In general, we observe two different series of Bragg's peaks corresponding to two distinct ordered phases (A1-A4, Liquid ordered, Lo, and B1-B4, Liquid disordered, Ld). As a function of humidity, the two phases change height and internal order thus changing the GISAXS spectra. Specifically, the number of orders of diffraction is an indication of packing and order of the lipid bilayer. We note here that the spectra are reversible as a function of humidity although after a complete cycle the A lines at orders higher than 1 split into two main components. At the moment, this behavior has not been completely understood and further investigation is required. In order to better understand the response of our lipid bilayers to humidity we plot two different scattering profiles vs q, collected at high and low humidity respectively (Fig. 1b). At high humidity the fourth order is evident for both phases (Fig. 1a, A1-A4 and B1-B4 peaks, blue curve), whereas at low humidity, only the Lo phase appears at the fourth order (A1-A4 peaks, red curve).

From these results, we conclude that by GISAXS it is possible to follow the response of different lipid bilayer phases to humidity variations. In particular, we observed that the shorter, liquid disordered domains (Ld) are more responsive than the higher, ordered phases (Lo). This can be attributed to the presence of a higher number of defects in the disordered fluid phase, together with a lower content of cholesterol and therefore a lower rigidity than in the ordered phase. The combination of these effects probably favors the insertion of water molecules in the Ld domains. It is clear from Fig. 1b that high humidity enhances the packing of the disordered layer while the height of the ordered one is almost unchanged. Notably, the effect of the humidity oh Ld domain height is perfectly reversible.

To reinforce our hypothesis we extrapolated the electron density distribution of the bilayer from the GISAXS patters. We expect that the electron density distribution of the bilayer shows maxima in correspondence to headgroup regions and minima at the methyl terminus of the hydrocarbon-chains. The electron density function can be computed when the GISAXS measurements present four or more orders of diffraction, as for the case of our data set but one (Ld at low humidity). In this way, using an inverse Fourier-transformation, one can distinguish among the different parts of the lipid bilayer. In particular, the lipid bilayer d-spacing can be decomposed into the different structural components such as the phosphate to phosphate distance (dpp), the water layer dimension (dw) and the monolayer thickness (d/2). The electron densities of Lo phase at low humidity (Fig. 2c red curve) and Lo-Ld phases at

high humidity (Fig. 1c dashed lines) are reported. For each curve, dpp, d/2 and dw have been calculated. For the Lo phase, it is possible to observe the increase of all the d parameters in the case of high hydration. In particular, dpp, i.e. the thickness of the bilayer, increases of about 0.16 nm, and the same trend is observed for d/2 (variation about 0.14 nm) and dw (variation about 0.1 nm) parameters, suggesting, as expected, an increase of the water layer thickness that covers the hydrophilic head groups of the layers.

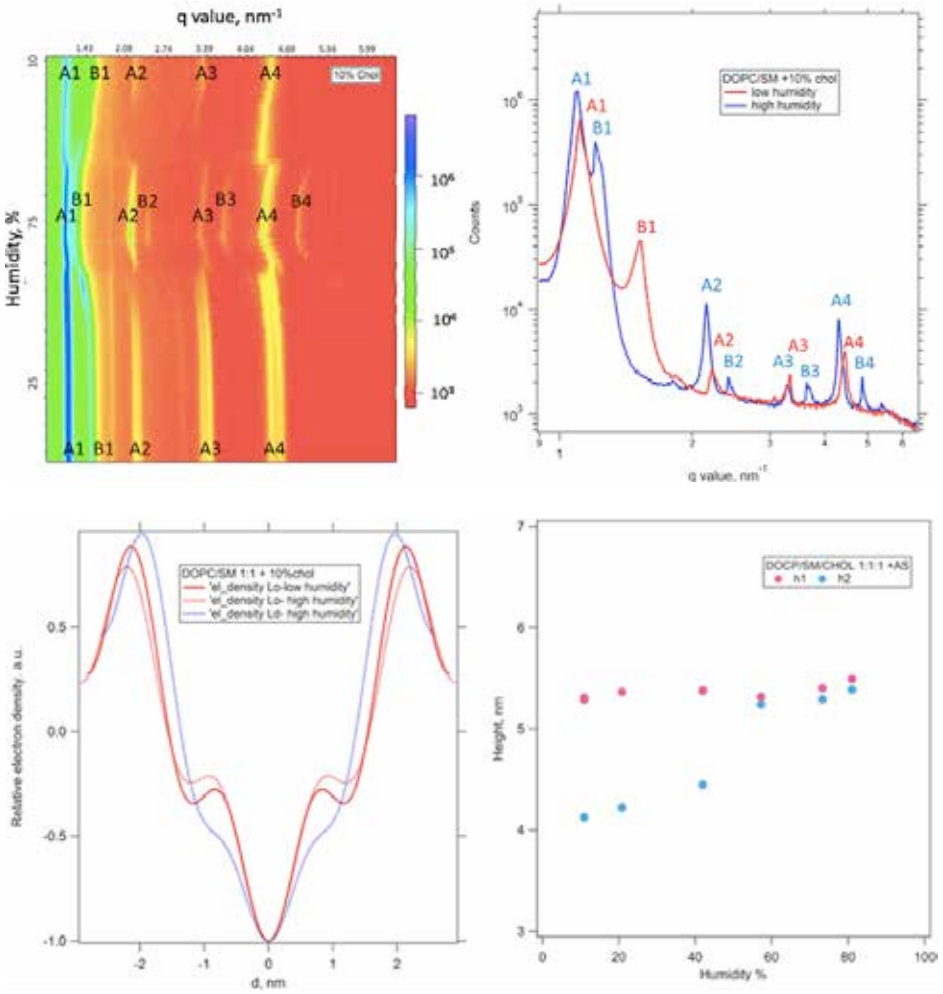

Figure 1. (a) Variation of the scattered intensity (in color scale) as a function of the scattering vector q and the relative humidity. A and B: Bragg's peaks of Lo and Ld phases respectively (b) Scattered intensity vs q, recorded for DOPC/SM + 10% chol. The red plot has been recorded at low humidity (~5%) whereas the blue curve at high humidity (~85%). A and B: Bragg's peaks of Lo and Ld phases respectively. (c) Electron density profile obtained from the sample composed by DOPC/SM +10% cholesterol. The graph has been obtained overlapping the higher phase (corresponding to the Lo phase) at low (hum ~5%, red line) and high humidity (hum ~85%, dashed red line). The blue dashed line corresponds to the Ld phase at high humidity. The lack of order for Ld phase at low humidity did not provide sufficient data for the calculation of the electron density map. (d) DOPC/SM/CHOL 1:1:1 after the incubation in presence of AS 3 μM. The plot reports the height of the two domains obtained by GISAXS measurements as a function of the humidity

GISAXS measurements have been also performed on a DOPC/SM/CHOL 1:1:1 after incubation in presence of AS. In this case, after the preparation of the sample by solvent evaporation of the lipid solution, the sample was covered by AS 3 μM in water solution until complete evaporation. Also in this case, before GISAXS analysis, the sample was placed in vacuum overnight. The results reported in Fig. 1d support our previous AFM measurements (not shown here) confirming an effect on the structure of the bilayer and the lipid phase

separation. Initially, at low humidity content, two main phases were observed, the higher (Lo) of about 5.28 nm and another of 4.12 nm (Ld). During the time of the experiment and upon increasing of the humidity, the height of the shorter phase increases until it reaches about the same value of the higher phase, which instead remains almost stable. The final 0.1 nm difference between the two phases is in agreement with the AFM topography measurements. We can then conclude that higher humidity favors the reorganization of the membrane into one phase only.

References:

[1] S. S.Corvaglia, "Nanoscale platform to study unstructured proteins interactions"; PhD Thesis in Nanotechnology - University of Trieste (2014)

MICROPHASE SEPARATED DNA/HYALURONIC ACID MIXTURES

I. Delač Marion[1], K.Salamon[1], D. Grgičin[1], S. Bernstorff[2] and T. Vuletić[1]

1.) Institute of Physics, Bijenička 46, 10000 Zagreb, Croatia
2.) Elettra-Sincrotrone Trieste, 34149 Basovizza (TS), Italy

We followed the effect of the concentration of hyaluronic acid (HA) and DNA on the structure of binary HA-DNA solutions. The structure of their aqueous solutions was investigated using the small angle X-ray scattering (SAXS) technique and polarizing (optical) microscopy.

In our recent paper [1], we applied SAXS experiments to single phase solutions (DNA or HA). For DNA solutions we showed – as expected in the framework of the scaling theory [2] – that the characteristic maximum in a scattering curve is shifted toward smaller scattering vectors, when DNA solution is diluted. The origin of this maximum is related to the repulsive interaction between polyelectrolyte (PE) chains and consequently formed short-range ordered PE mesh. The position of the scattering maximum, q*, provides insight into the characteristic length scale L of the DNA mesh, and is highly dependent on the monomer number concentration n_{DNA}: $q^*=2*\pi*(b_{DNA}n_{DNA})^{1/2}$, where b_{DNA}=0.34 nm is DNA monomer size.

Compared with DNA solutions, the HA solutions showed only a relatively weak and wide shoulder in the scattering intensities. There may be a reason for weaker scattering: the HA chain lacks the scattering power of relatively heavy P atoms present in the phosphate groups of a DNA chain. The absence of a clear scattering maximum is also a consequence of the more disordered mesh due to the weak electrostatic interaction between HA chains. Nevertheless, the position of this shoulder also follows the relation $2*\pi*(b_{HA}n_{HA})^{1/2}$. Thus, the scaling relation is equally applicable for both highly and weakly charged PE, while the local structure depends only on the total chain length in a given volume.

Thus, for DNA-HA binary mixtures the signal should be dominated by the DNA macroion partial scattering function. Moreover, taking into account the lack of a clear maximum for pure HA solutions, any appearance of a scattering maximum in SAXS spectra for DNA-HA solutions should have the origin in the DNA inter-chain arrangement. Therefore, the properties and the nature of binary DNA-HA solutions may be studied via the DNA scattering peak q* dependence on both the DNA and HA concentrations.

We note that for polymer mixture, there is an inherent tendency to demix because of the very small contribution from the entropy of mixing, resulting from the high molecular weight of the components. For charged polymers – PEs some compatibility enhancement may be due to the presence of the counterions, as the consequence of the osmotic pressures being regulated by the counterions and not the chains/coils and this issue was the motivation for the present study [3].

The SAXS measurements have been carried out at the high-flux SAXS beamline at ELETTRA. The scattering patterns were recorded with a 2D image plate detector (Mar300, MarResearch, Norderstedt, Germany). The detector covered the q-range ($q = 4\pi \sin\theta/l$, where l=1.54 Å is the wavelength and 2θ is the scattering angle) of interest from q_{min}=0.1 to q_{max}=5 nm^{-1}. The angular calibration of the detector was performed with silver behenate powder (d-spacing of 58.4 Å).

The sample solutions were measured either in quartz glass capillaries with a diameter of 1mm or in a specially designed gel-sample-holder, depending on the sample solution viscosity. The measurements were performed at 25°C.

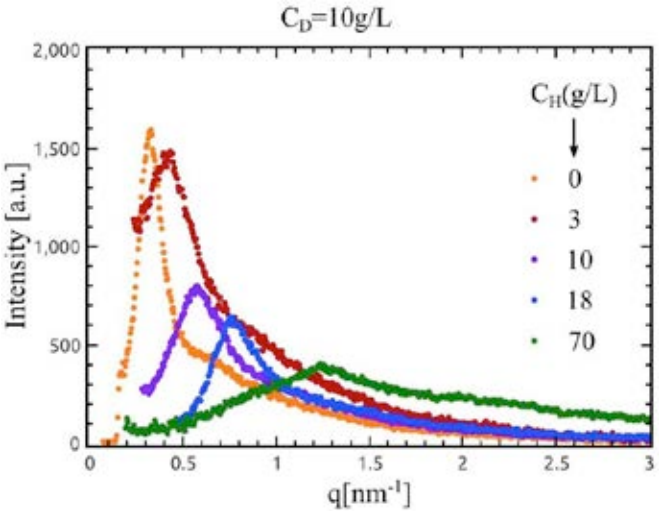

Figure 1. X-ray scattering pattern of binary mixtures of DNA (10g/L) with varying concentration of hyaluronic acid (HA) from 0 to 70 g/L. The increase in HA content "compresses" the DNA subphase – the DNA characteristic mesh size ξ becomes smaller and consequently the scattering maximum $q^*=2\pi/\xi$ moves to higher values

Before the analysis, the experimental 2D-images were corrected for the detector response, and the background scattering (pure H_20) was subtracted. From each 2D-image, 1D scattering profiles (curves) at several azimuths were extracted in order to obtain the average value of scattering peak position q* for each DNA-HA solution.

Polarizing microscopy observations were done between a slide and coverslip. To prevent dehydration, preparations were sealed by epoxy. The thickness of the preparations was ranging from 50 μm to 200μm. We used an Optika OptiPol B280 polarizing microscope with Optikam digital camera. In some cases, a quartz first order retardation plate (λ-plate) was inserted at 45° between crossed polars to analyze the orientations of molecules in the particular domains. Images were analysed to obtain the fraction of the birefringent phase, presumably DNA subphase. These data had to be corroborated by subphase fractions derived from SAXS data. Eventually, the correspondence was confirmed, which indicated a complete separation of DNA and HA despite intensive and thorough mixing.

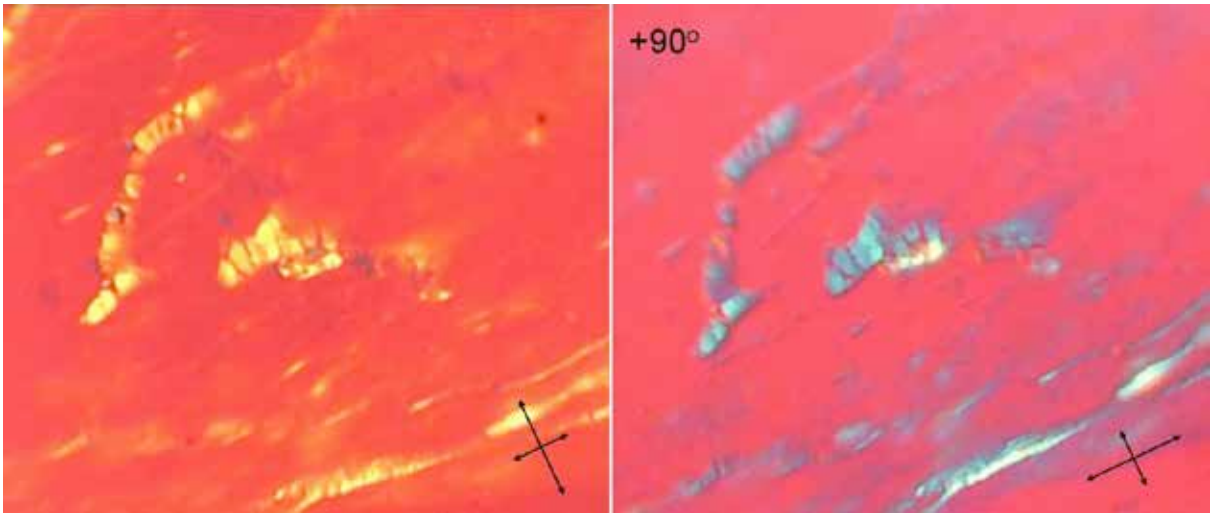

Figure 2. Binary mixture with concentrations of 90g/L HA and 10 g/L DNA (well below the concentration for precholesteric ordering of DNA which starts at 100g/L [4]). However, due to demixing the DNA subphase becomes highly concentrated and a lyotropic mesophase is formed and visualized by polarizing microscopy. Molecular orientations within a subphase may further be determined by the use of a quartz first order retardation plate (λ-plate) inserted at 45° between crossed polarizers. Negatively birefringent DNA gives yellow interference color when chains are perpendicular to the λ-plate fast axis (longer arrow). Red/magenta is the nonbirefringent, presumably HA subphase

The volume fraction of the DNA subphase was calculated from the scattering maxima q* that provides the effective DNA concentration. That is, we used the previously established relationship $q^* \sim 1/\xi \sim c^*_{DNA}{}^{1/2}$ [1,4]. The ratio between the nominal concentration of DNA c_{DNA} added in the mixture and the effective c^*_{DNA} that generates the scattering peak is the volume reduction ratio V_{DNA}/V_{total}. If we assume a complete separation then the volume available to the HA subphase is known which leads to an effective c^*_{HA}, higher than the nominal c_{HA}. Eventually, it turned out that c^*_{HA}/c^*_{DNA} is a constant ratio for the range of mixtures that we tested. The subphases should be in osmotic equilibrium $\Pi_{HA} \sim \Pi_{DNA}$, where the osmotic pressure of PEs is defined by the counterions released in solution. In other words, the HA equation of state has the same form as for DNA, $\Pi_{HA}=\phi\, k_B T c_{HA}{}^{9/8}$, however with a different prefactor ϕ. The prefactor for HA is 4 times lower than for DNA. In other words the number of counterions released by one HA monomer is only 0.25 instead 1. This is surprising as HA is a weak PE, with low linear charge density and no counterion condensation should take place.

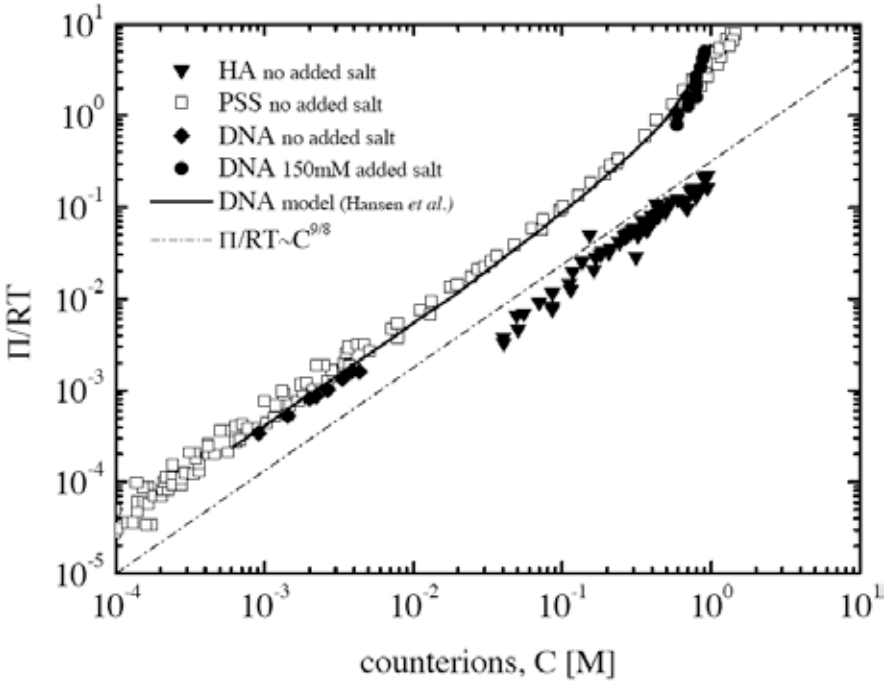

Figure 3. Spontaneous Equation of state for polyelectrolytes [5]: the osmotic pressure Π is regulated by the counterions concentration C released from the backbone. The reduction in C due to the Manning condensation was taken into account for all systems. However, the osmotic pressure for HA is further reduced).

References:

[1] K. Salamon, D. Aumiler, G. Pabst, T. Vuletić, Probing the Mesh Formed by the Semirigid Polyelectrolytes, *Macromolecules* **46**, 1107-1118 (2013)

[2] P.-G. de Gennes, P. Pincus, R.M. Velasco, F. Brochard, Remarks on polyelectrolyte conformation. *J. Phys. (Paris)* **37**, 1461-1473 (1976)

[3] A. R. Khokhlov' and I. A. Nyrkova, Compatibility Enhancement and Microdomain Structuring in Weakly Charged Polyelectrolyte Mixtures, *Macromolecules* **25**, 1493 (1992)
G.H.Lai, J.C.Butler,2 O.V. Zribi, I.I. Smalyukh, T.E. Angelini, K.R. Purdy, R.Golestanian, and G.C.L.Wong, Self-Organized Gels in DNA/F-Actin Mixtures without Crosslinkers: Networks of Induced Nematic Domains with Tunable Density *Phys.Rev Lett.* **101**, 218303 (2008)

[4] F. Livolant and A. Leforestier, Condensed phases of DNA:Structures and phase transitions *Prog.Polymer Sci.***21**, 1115-1164 (1996)

[5] L.Wang and V.A. Bloomfield, Osmotic Pressure of Polyelectrolytes without Added Salt, Macromolecules **23**, 804-809 (1990); P.L.Hansen, R.Podgornik, and V.A. Parsegian, Osmotic properties of DNA: Critical evaluation of counterion condensation theory, Phys.Rev. E **64**, 021907 (2001)

STUDY OF THE FORMATION OF HOLLOW HEMATITE SPHERES WITHOUT THE USE OF TEMPLATES

S. Espinoza Suarez[1,2], L. De Los Santos Valladares[3], H. Amenitsch[4], L. León Félix[5], A. Bustamante Domínguez[1], C.H.W. Barnes[3]

[1] Facultad de Ciencias Físicas, Universidad Nacional Mayor de San Marcos, Ap. Postal 14-0149, Lima, Peru
[2] TECSUP, Av. Cascanueces 2221, Sta. Anita, Lima 43, Peru
[3] Cavendish Laboratory, Department of Physics, University of Cambridge, Cambridge CB3 0HE, UK
[4] Institute of Inorganic Chemistry, Graz University of Technology, Stremayergasse 9/IV.A-8010 Graz, Austria
[5] Núcleo de Física Aplicada, Instituto de Física, Universidade de Brasília, Brasília DF 70910-900, Brazil

In this work we report the preparation and characterization of hollow spheres of hematite (α - Fe_2O_3). The preparation was performed by the sol gel method and thermal annealing. Ferric nitrate and citric acid were diluted in water to form the precursor gel consisting of amorphous iron hydroxide and it was oxidized by annealing at 600° C for 8 hours. The characterization was done by thermogravimetric and small angle X-ray scattering analysis. The size and morphology of the sample was analyzed further by scanning electronic microscopy, observing that it consists of hollow spheres with ~800 nm as inner diameter and ~60 nm thickness. The results suggest that hollow nanospheres obtained in this work are promising for applications in drug encapsulation.

Early stages of the precursors obtained by sol-gel nanoparticle formation are monitored by in situ synchrotron small-angle X-ray scattering (SAXS) experiments with a new set-up for capillaries based the Anton Paar DHS1100 in the temperature range RT to 1100 °C. A new strategy enables the preparation of hematite without templates from nine hydrate ferric nitrate and mono hydrated citric acid with distilled water. In Figure 1, the X-ray scattering pattern shows the structural evolution of the system. The data were taken *in situ* during heating of the precursor, from 30 to 525 °C with a heating rate of 3 °C/min and every 20 s an image was recorded. The kinetics of growth formation are clearly monitored by SAXS. Note that for most curves, an abrupt change in the intensity of the scattering vector, 0.2-0.3 nm^{-1}, is observed indicating the heat induced grain growth with a typical dimension of 25 nm (Bragg law), which is in the order of thickness parameter of the particles. Therefore the experiments support the hollow hematite shape of the resulting nanoparticles, which is also confirmed by scanning electron microscopy (figure insert).

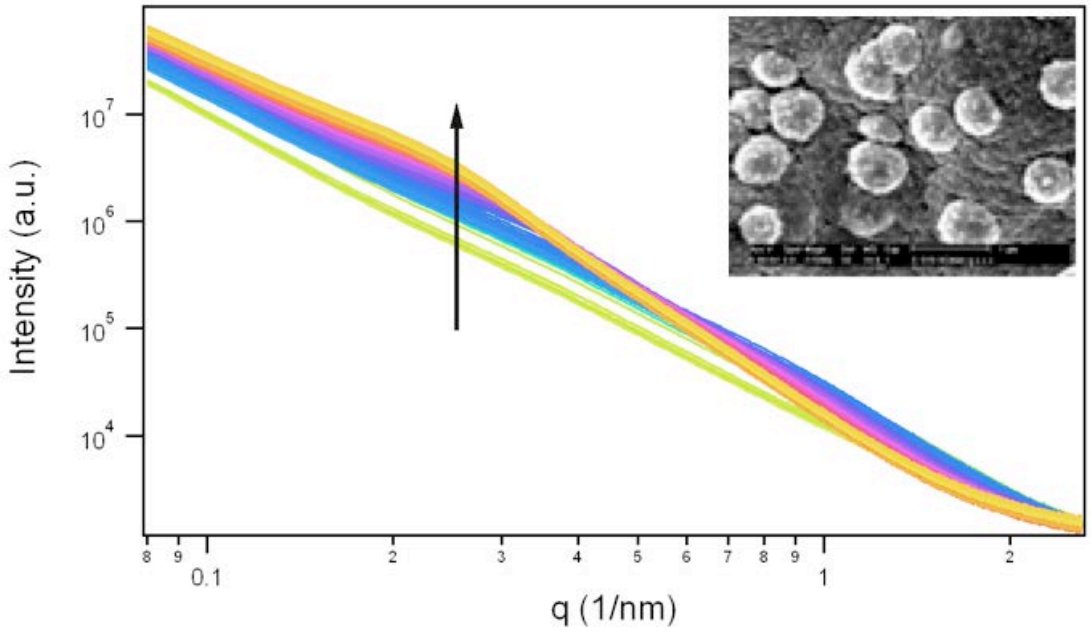

Figure 1. Time resolved scattering pattern of nanoparticle during the heating from 30 to 525°C with a heating ramp of 3ºC/min with 20 s time resolution. The insert shows the corresponding SEM image at the final stage

The Figure 2 shows the correlation length calculated from SAXS data shown in Figure 1. The grain growth after 100 min i.e. 350 °C is clearly seen due to the increase of the correlation length. The thermo-gravimetric (TG and DTA) measurement of the precursor obtained by sol-gel are shown in the insert. There are two strong endothermic peaks on the DTA and two corresponding weight losses on the thermal gravity curve between 150 and 200 ºC indicating a two-step mechanism of dehydration, which is not responsible for the grain growth as shown by the data of SAXS. Comparing with our previous work this reaction is accompanied with the formation of magnetite. The mass loss associated with the OH- ions on the maghemite surface is detected in the TG curve between 200 to 400 ºC [1]. Note that there is a corresponding weak exothermal peak in the DTA plot assigned to the hematite transition [2]. This transition might be accompanied with grain growth [3].

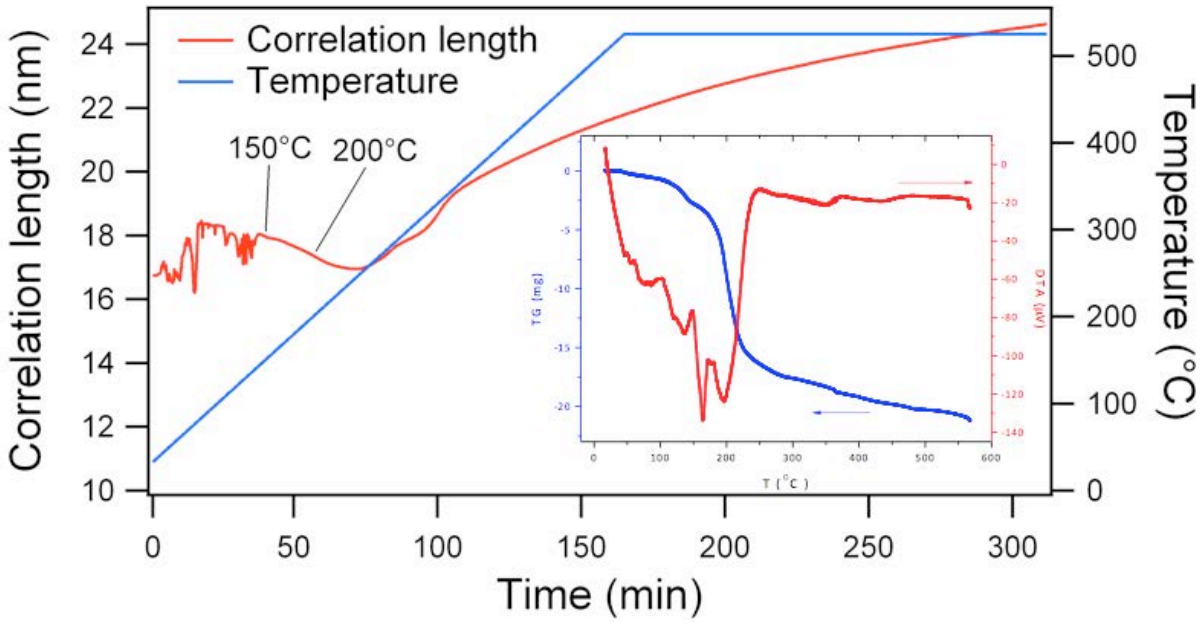

Figure 2. Correlation length calculated from the SAXS data versus time during heating of the sample from 30 to 525°C with the corresponding temperature evolution. The growth of the particles is observed after 100 min (i.e. ~ 350°C). The insert show the TG and DTA data measured from the same sample.

References:

[1] L. León, A. Bustamante, A. Osorio, G.S. Loarte, L. de los Santos Valladares, C.H.W. Barnes, Y. Majima, Hyperfine Interact. **202** 131-137 (2011)

[2] H. Karami J. Clust. Sci **21** 11-20 (2010)

[3] Y. Xisheng, S. Jian, S. Honngin, J. Zhengkuan, L. Guanglie, P. Zifei, Z. Lide, Chinese Sci. Bulletin **42** 894-897 (1997

TEMPERATURE DEPENDENCE OF LO/LD DOMAIN THICKNESS AND ELASTICITY BY GLOBAL SAXS DATA ANALYSIS

P. Heftberger[1], B. Kollmitzer[1], A. Rieder[1], H. Amenitsch[2], and G. Pabst [1]

1.) Institute of Molecular Sciences, Biophysics Division, University of Graz, Austria
2.) Institute of Inorganic Chemistry, Graz University of Technology, Austria

The spatial organization of lipids in biological membranes plays an important role in diverse cellular processes. Of particular interest are membrane rafts which are considered to enable cellular signaling and transport. Such membrane rafts are currently mimicked by liquid ordered (Lo) domains, observed in several lipid-only mixtures. The physical properties of Lo domains and the coexisting liquid disordered (Ld) phase are presently not entirely understood. We developed a global small-angle x-ray scattering data analysis for multilamellar vesicles that allows to determine membrane structural parameters and bending fluctuations of coexisting lipid domains. The analysis is based on a previously reported full q-range technique for multilamellar vesicles with high structural resolution [1]. Within this technique, volume distributions of quasi molecular lipid fragments are used to describe the electron density profile of the bilayer in more detail [1,2]. Furthermore, we apply separate electron density profiles for both phases in the bilayer for analyzing one combined scattering profile. This way we can get in-situ information about both phases without analyzing the corresponding single phase systems at their respective tieline endpoints, that is without the need to know their specific lipid compositions.

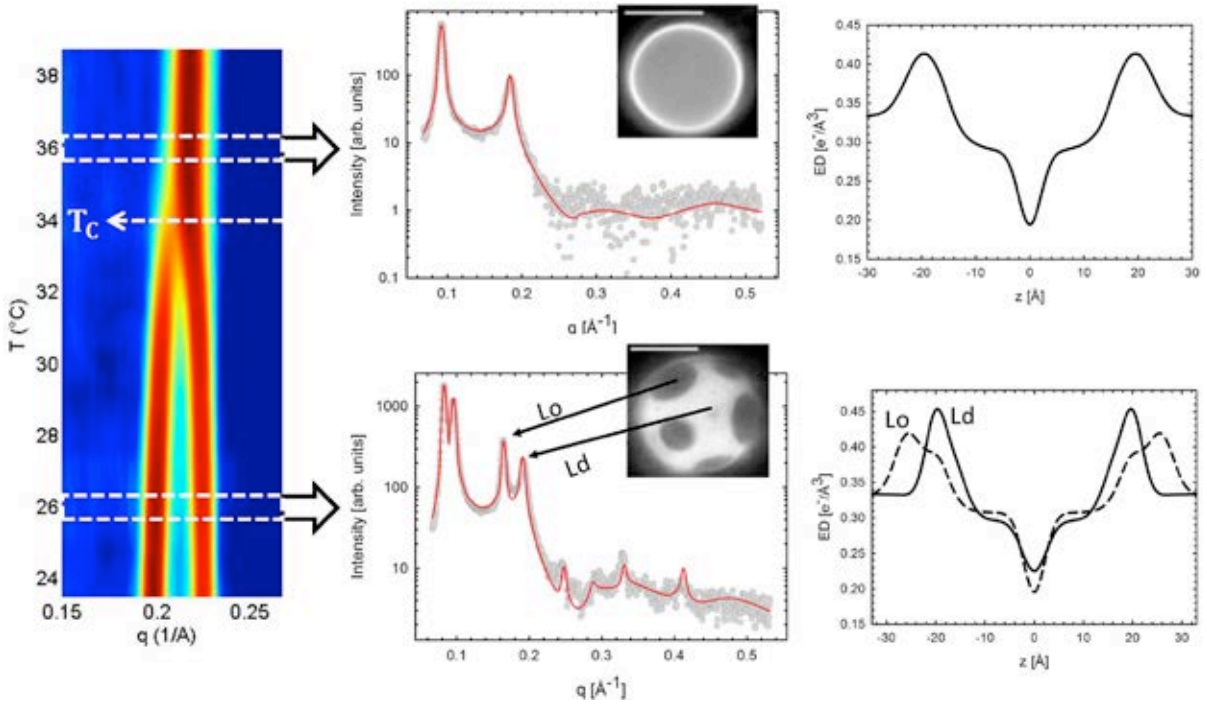

Figure 1. Analysis scheme of temperature dependent SAXS measurements of coexisting lipid domains. The left panel represents a height profile of a diffraction pattern as a function of temperature. Diffraction profiles at distinct temperatures are shown in the middle panel. The resulting electron density profiles are presented in the right panel. Images show corresponding fluorescence microscopy experiments on giant unilamellar vesicles using dyes that partition into Ld phases (scale bar: 20 µm)

The technique was applied to mixtures of DOPC/DPPC/Chol and DOPC/DSPC/Chol [3]. We determined membrane thickness as well as bending fluctuations for Lo and Ld phases as a function of lipid composition and temperature. In particular, we investigated changes in these parameters upon the transition to a homogeneous phase occurring at T_C (left panel in Fig.1).

This analysis is shown in Fig.1. Below T_C, two phases (Lo and Ld) coexist in the bilayer and contribute to a single, joined diffraction pattern. With our new method, we are able to deconvolute the individual phases. Below the transition temperature T_C the analysis is able to detect Lo and Ld phases, which differ mainly in their membrane thickness as seen from their electron density profiles (lower right panel). Above T_C only a single electron density profile is retrieved (upper right panel).

References:

[1] P. Heftberger, B. Kollmitzer, F. Heberle, M. Rappolt, H. Amenitsch, J. Pan, J. Katsaras, N. Kucerka, and G. Pabst, Journal of Applied Crystallography **47**, 173 - 180 (2014)

[2] N. Kucerka, J. F. Nagle, J. N. Sachs, S. E. Feller, J. Pencer, A. Jackson, and J. Katsaras, Biophys. J **95**: 2356–2367 (2008)

[3] DOPC…dioleoylphosphatidylcholine, DPPC…dipalmitoylphosphatidylcholine, DSPC…distearoylphosphatidylcholine, Chol…cholesterol

INTERACTION POTENTIAL OF AN AMYLOIDOGENIC PROTEIN

M. Manno[1], M. Blanco[2], R. Noto[1], C. J. Roberts[2] and V. Martorana[1]

1.) National Research Country of Italy, Institute of Biophysics, via Ugo La Malfa 153, 90146 Palermo, Italy
2.) Dept. of Chemical and Biomolecular Engineering, University of Delaware, Newark, Delaware 19716, USA

Amyloid fibrils are linearly elongated protein aggregates, characterized by a cross-β sheet quaternary structure running along the main fiber axis [1]. Amyloid fibrils and deposits have a high clinical relevance, because they are related to several diseases, including Alzheimer's and prion disease. In addition, they have a general biological importance as underlined by the existence of functional amyloids with a positive physiological activity. In both perspectives, it is of extreme interest to determine the mechanisms and the factors that are useful to inhibit, promote, and control the formation (or the disruption) of amyloid fibrils. A well-established relation exists between the capability of a protein to form amyloid fibrils and its molecular conformation and sequence [1]. On the other hand, the details of the intermolecular interaction potentials, which determine protein attraction and cause solution instability in fibril forming protein solutions, are still not completely explored, and a few studies explicitly focused quantitatively on these aspects [2-5], suggesting the fibrillation being regulated by a subtle balance between hydrophobicity and electrostatic repulsion [4].
Insulin is a model system for amyloid formation both for its medical importance and for the availability of a large amount of data in the literature [6]. Here, we aimed to determine the interaction potential of insulin monomers in acidic solution at low to high ionic strength, in conditions such that insulin may form amyloid fibrils upon heating.

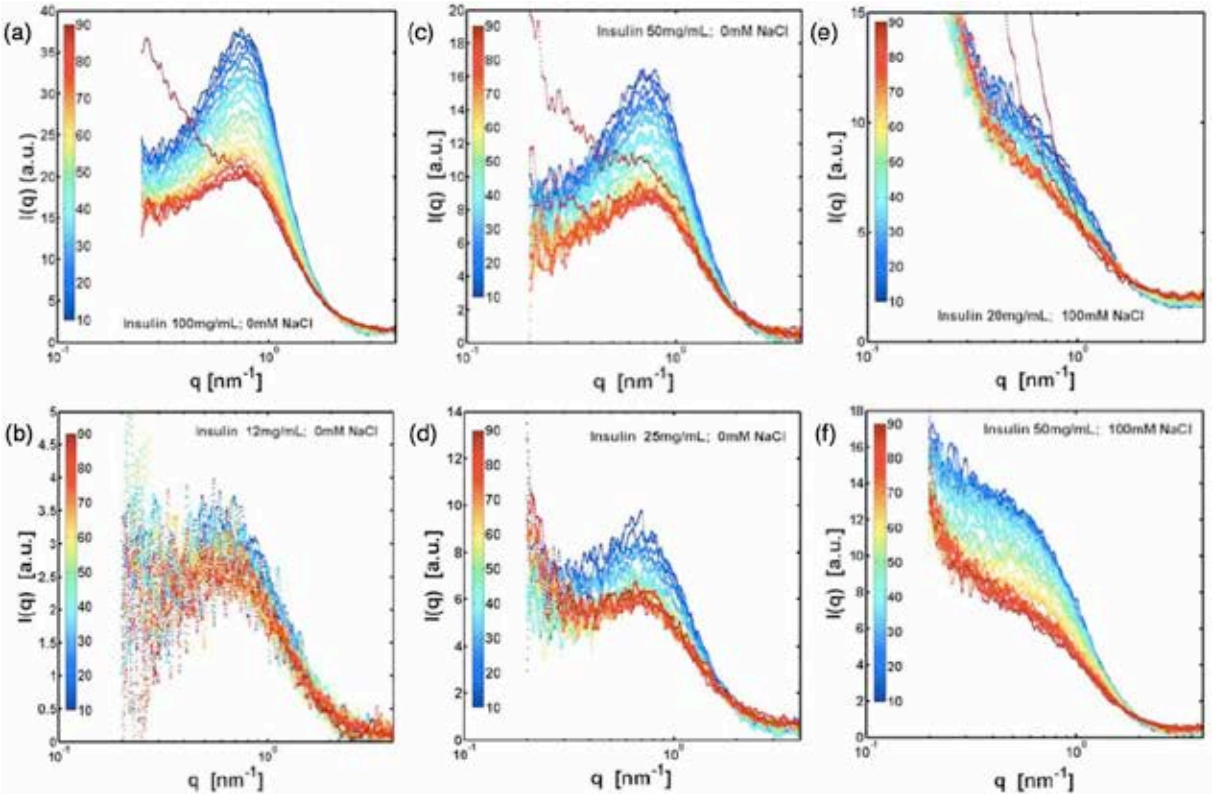

Figure 1. X-ray scattered intensity profiles I(q) for insulin at different protein and salt concentrations: (a) 0 mM NaCl, 100 mg/ml insulin; (b) 0 mM NaCl, 12 mg/ml insulin; (c) 0 mM NaCl, 50 mg/ml insulin; (d) 0 mM NaCl, 25 mg/ml insulin; (e) 100 mM NaCl, 20 mg/ml insulin; (f) 100 mM NaCl, 50 mg/ml insulin. Colors represent different temperatures ranging from 10C (blue) to 90C (red) as indicated on color bars in each panel

We exploited the possibility of the DSC module at the SAXS beamline at Electra to acquire scattering patterns of insulin solutions for a full temperature scan. Such approach allowed us to obtain several images by using the same capillary and the same sample, after a preliminary check that the effect of radiation damage was negligible in our conditions. The sample solvent was measured in parallel experiments with the same temperature scan rate. We explored a range of insulin concentration from 1 mg/ml (useful to measure the protein form factor) to 100 mg/ml.

In keeping with our preliminary results by light scattering experiments, insulin exhibits strong repulsive interaction condition at 0mM NaCl, when the electrostatic potential is not screened by counter-ions. This is highlighted in Figure 1 where the intensity profiles show the presence of correlation or the typical interaction peak at intermediate q. The interaction peak shifts to higher q by increasing the protein concentration (Fig. 1), as expected due to a shortening of the inter-molecular mean distance. Moreover, as the temperature increases, there is a decrease in the intensity signal at intermediate q as a consequence of a decrease in the strength of protein-protein interactions. At contrary, the addition of 100 mM NaCl causes the screening of electrostatic repulsion and the prevalence of attractive interacting condition, as evidenced by the absence of the interaction peak (Fig. 1e,f).

Furthermore, there is an increase in the intensity in the low-q range as the temperature increases, which is associated with protein aggregation. The intensity profiles reveal that protein aggregation is more prominent at intermediate protein concentration.

A detailed fitting of the SAXS profiles at different temperatures with theoretical S(q) will shed light on the inter-molecular interaction between insulin molecules in conditions leading to amyloid fibril formation.

References:

[1] F. Chiti, and C. M. Dobson; Protein Misfolding, Functional Amyloid, and Human Disease; Annu. Rev. Biochem. **75**, 333−366 (2006)

[2] N. Javid, K. Vogtt, C. Krywka, M. Tolan, and R. Winter; Capturing the Interaction Potential of Amyloidogenic Proteins; Phys. Rev. Lett. **99**, 028101_1−028101_4 (2007)

[3] S. E. Hill, T. Miti, T. Richmond, and M. Muschol; Spatial Extent of Charge Repulsion Regulates Assembly Pathways for Lysozyme Amyloid Fibrils; PLoS ONE **6**, e18171_1−e18171_12 (2011)

[4] S. Raccosta, V. Martorana, and M. Manno; Thermodynamic versus Conformational Metastability in Fibril-Forming Lysozyme Solutions; J. Phys. Chem. B **116**, 12078−12087 (2012)

[5] M. A. Blanco, T. Perevozchikova, V. Martorana, M. Manno, and C. J. Roberts; Protein−Protein Interactions in Dilute to Concentrated Solutions: α-Chymotrypsinogen in Acidic Conditions; J. Phys. Chem. B **118**, 5817-5831 (2014)

[6] M. Manno, E. F. Craparo, A. Podestà, D. Bulone, R. Carrotta, V. Martorana, G.Tiana, and P. L. San Biagio; Kinetics of Different Processes in Human Insulin Amyloid Formation; J. Mol. Biol. **366**, 258−274 (2007)

INVESTIGATING STABILITY AND DISASSEMBLY OF THE BACTERIAL CHAPERONIN PROTEIN GROEL AND ITS HUMAN HOMOLOG HSP60

C. Ricci[1], S. Vilasi[2], M.R. Mangione[2], D. Bulone[2], P. San Biagio[2], R. Carrotta[2], F. Spinozzi[1], H. Amenitsch[3] and M.G. Ortore[1]

1.) Dipartimento di Scienze della Vita e dell'Ambiente, Università Politecnica delle Marche, Ancona, Italy
2.) Istituto di Biofisica, IBF CNR, Palermo, Italy
3.) Institute of Inorganic Chemistry, Graz University of Technology, Austria

Recent results attribute to some chaperones, and in particular to Hsp60, an important role in amyloid neurodegenerative diseases and in particular in Alzheimer's disease (AD), even if with often controversial mechanisms that need to be clarified [1,2]. According to the "sink hypothesis", cellular toxicity may develop because chaperones and other proteins are being sequestered onto amyloid fibrils and re-directed from their normal tasks. However, basic knowledge about Hsp60 activity influence toward the beta-amyloid peptide (Aβ) aggregation is still lacking, and the molecular structure details, as well as the stability, of Hsp60 are not really established.

Hsp60 is a molecular chaperone known to assist protein folding in eukaryotic cells. It is produced in the cell cytoplasm (naïve Hsp60), but it is considered to be imported by losing a tail peptide to mitochondrial compartment (assuming the mitochondrial conformation called mtHsp60 or cpn60), in which it exerts its activity. It is a 60 kDa protein, and it was assumed that under normal physiological conditions it assemblies in a complex arranged as two stacked heptameric rings, on the basis of the structure of its bacterial homolog GroEL [3,4] one of the most exhaustively characterized molecular chaperones.

Some of us have recently discovered that in a wide range of concentrations, from 0.02 nM to 12.6 μM, naïve Hsp60 self assembles to form oligomeric species (like heptamers and tetradecamers) that, for mtHsp60 and its bacterial homolog GroEL, are considered to be the functional form of the chaperonins [5]. This result suggests that the investigated Hsp60, with its mitochondrial import signal, is not an aberrant protein that failed to enter mitochondria, but it could accumulate in the cytosol and be involved in physiological functions as oligomer. Hence, several hypothesis can be provided, concerning the possibility to participate in cellular functions as monomer at concentrations lower than that necessary for oligomerization.

In order to clarify this scenario, SAXS experiments at increasing GdnHCl concentration until Hsp60 and GroEL denaturations (between 1.5 and 2.5 M), have been performed. SAXS kinetic and equilibrium measurements (in agreement with previous literature results [6]) provide a deeper knowledge about conformational transition induced by chemical denaturation. In this experiment, human Hsp60 and bacterial GroEL were investigated, studying GdnHCl induced denaturation at 37°C and at different concentration values (between 0 M up 2 M). Preliminary information about molecular globularity were obtained from Kratky plots (Figure 1,2).

It is possible to immediately observe relevant qualitative differences between GroEL and Hsp60 structural response to the presence of increasing amounts of GdnHCl. The Kratky plots highlight the different stability of the two proteins: Hsp60 demonstrates less stability and a lower cooperativity in the chemical denaturation transition than GroEL at the same GdnHCl concentration. The presence of 1M GdnHCl modifies the features of Hsp60 SAXS pattern, while it does not affect at all SAXS curve corresponding to GroEL sample. Moreover, the 2M GdnHCl solvent solution manages to completely unfold Hsp60, while it is not able to denature GroEL structure. The kinetic response of the two homolog proteins to GdnHCl deserve further attention, too. In fact while Hsp60 SAXS patterns corresponding to 1M and 1.5M GdnHCl solutions present a continuous trend for a time between 15 and 30 minutes, the equivalent SAXS curves of GroEL show to quickly gain the equilibrium conditions (no

modifications can be revealed after 3 minutes). All these experimental evidences let us to suggest that Hsp60 and GroEL have very different stability features and further analyses are going on to detail the different oligomeric species present in solution both at different GdnHCl contents and at increasing time [7].

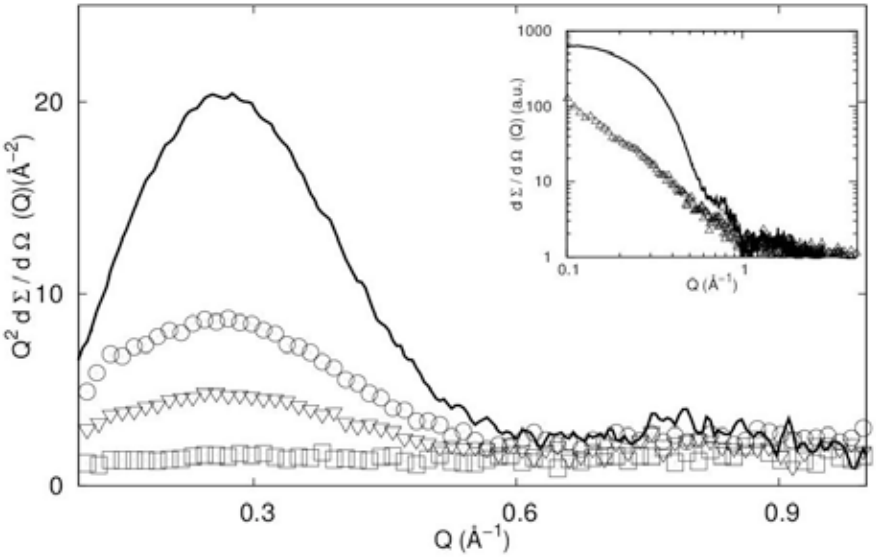

Figure 1. Kratky plots of Hsp60 at 0M (straight line), 1M (open circles), 1.5M (open triangles), and 2M GdnHCl (open squares). Inset shows SAXS curves at 0 M (straight line) and 1.5M GdnHCl (open triangles)

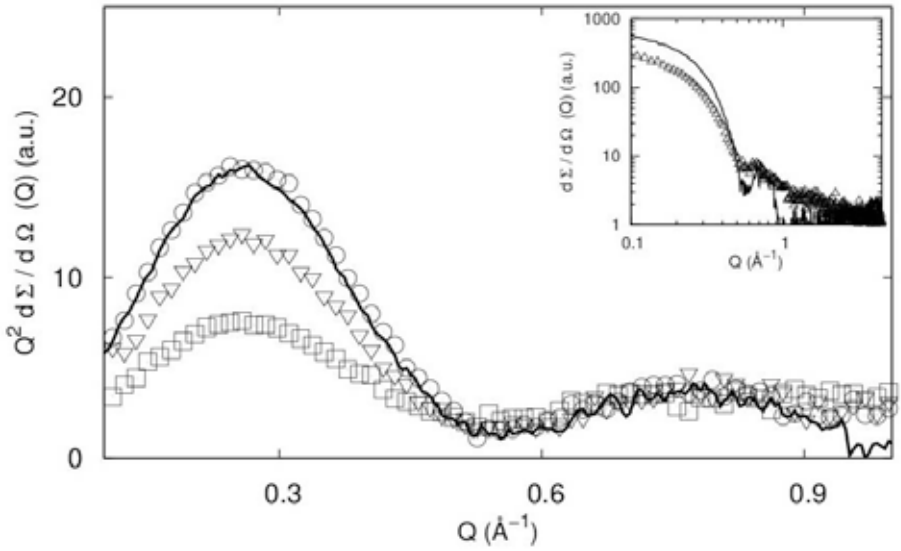

Figure 2. Kratky plots of GroEL at 0M (straight line), 1M (open circles), 1.5M (open triangles), and 2M GdnHCl (open squares). Inset shows SAXS curves at 0 M (straight line) and 2M GdnHCl (open triangles)

References:

[1] A. Nemirovsky et al.; Amyloid beta-HSP60 peptide conjugate vaccine treats a mouse model of Alzheimer's disease; Vaccine **29**, 4043-4050(2011)

[2] AAA Alexzander et al.; Heat Shock Proteins and the Brain: Implications for Neurodegenerative Diseases and Neuroprotection; Springer (2008)

[3] F.Cappello et al.; Hsp60 expression, new locations, functions and perspectives for cancer diagnosis and therapy; Cancer Biology and Therapy **7**(6), 801-809 (2008)

[4] C. Bartolucci, D. Lamba, S. Grazulis, E. Manakova, H. Heumann; Crystal structure of wild-type chaperonin GroEL; Journal of Molecular Biology **354**, 940-951(2005)

[5] S.Vilasi, R.Carrotta, et al; Human Hsp60 with its mitochondrial import signal occurs in solution as heptamers and tetradecamers remarkably stable over a wide range of concentrations; PLOS ONE, **9**(5) (2014)

[6] J. Chen and D.L.Smith; Unfolding and disassembling of the chaperonin GroEL occurs via a tetradecameric intermediate with a folded equatorial domain; Biochemistry **39**, 4250-4258 (2000)

[7] F.Spinozzi, M.Beltramini M. Quafit: A novel method for the quaternary structure determination from small-angle scattering data; Biophysical Journal **103,** 511–521 (2012)

X-RAY SCATTERING STUDIES OF MACROMOLECULAR SOLVATION IN CHOLINE CHLORIDE/UREA BASED DEEP EUTECTIC SOLVENTS

L. Sapir and D. Harries

Institute of Chemistry and The Fritz Haber Research Center, The Hebrew University, Jerusalem 91904, Israel

Our major interest is to understand the mechanisms by which Deep Eutectic Solvents act as solvating environment to biological macromolecules. Deep eutectic solvents (DES) are novel mixtures of two or more compounds that possess a drastically reduced melting temperature than any of the pure components. A prominent example is the mixture of urea and choline chloride, whereby the pure compounds melt well above 100°C, but a 2:1 molar mixture melts at a much lower temperature of 12°C [1]. Such DES at room temperatures have potential as green solvents for chemical reactions [2]: they are energy-efficient, nontoxic, environmentally friendly, and provide very different solvent properties to typical organic solvents or water. At the Elettra SAXS beamline, we studied DNA solvation in this unique DES. Specifically, we aim to probe the preferential interactions of different solvent components with the DNA, as well as the possible changes in DNA structure in this new type of solvent. Moreover, we are interested in resolving the structure of the pure solvent, which can be determined using WAXS.

Interestingly, DNA shows very different properties in DES than in aqueous solutions. The results for DNA in DES are shown in Fig. 1A. The preliminary measurements already demonstrate that the DNA form factor is significantly different in DES than in water. Moreover, the apparent cross-sectional radius of DNA decreases in DES. This data is currently being analyzed, in order to determine the spatial distributions of the different solvent components, as well as structural alterations in the DNA itself. The WAXS scattering profiles are also being analyzed, and will be compared with to our molecular dynamics computer simulations, Fig. 1B, to gain information on the structural features of the solvent itself.

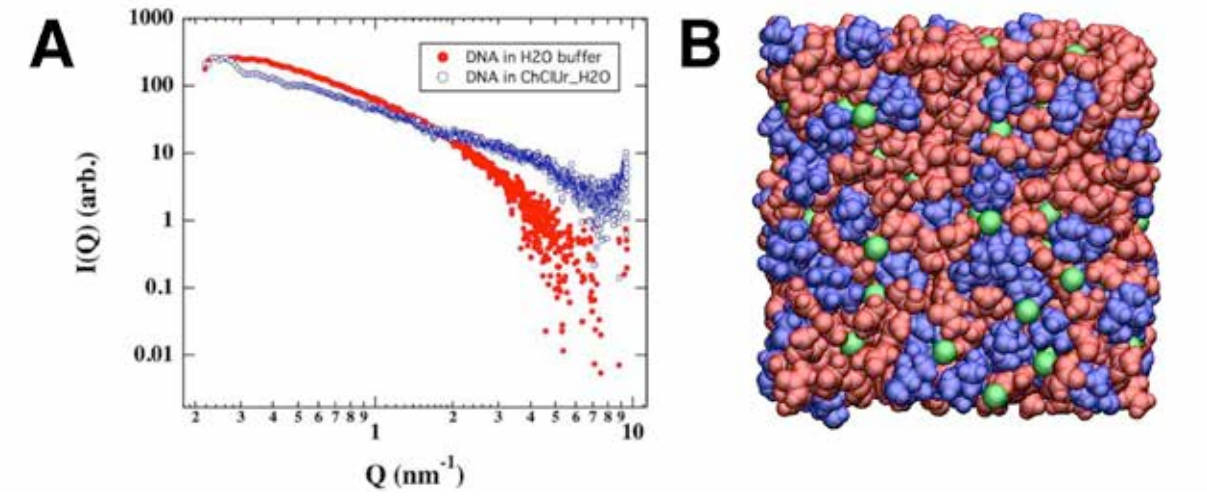

Figure 1. (**A**) DNA in water and in choline chloride urea DES (with a small amount of water). The scattering signal shows the different solvation properties of the two solvents in the way they affect the form factor of DNA. In DES the DNA is effectively "thinner and shorter" than in water. (**B**) A snapshot of the studied DES molecular dynamics simulation. The choline, urea, and chloride molecules are shown in blue, red, and green, respectively

References:

[1] A. Abbott, G. Capper , D.L. Davies, R.K. Rasheed, V. Tambyrajah; Novel solvent properties of choline chloride/urea mixtures; Chemical Communications **2003**, 70-71 (2003)

[2] A. Abbott, D. Boothby , G. Capper, D.L. Davies, R.K. Rasheed; Deep Eutectic Solvents Formed between Choline Chloride and Carboxylic Acids: Versatile Alternatives to Ionic Liquids; Journal of the American Chemical Society **126**, 9142-9147 (2004)

INTRINSIC DISORDER AND CHAPERON-LIKE ACTIVITY OF DIFFERENT CASEINS: AN EXTENSIVE IN-SOLUTION SAXS STUDY

S. Vilasi[1], M.G. Ortore[2], R. Carrotta[1], M.L. Mangione, G.C. Rappa[1], P.L. San Biagio[1], D. Bulone[1]

1.) Institute of Biophysics, National Research Council, Palermo, Italy; silvia.vilasi@pa.ibf.cnr.it
2.) Department of Life and Environmental Sciences, Marche Polytechnic University, Ancona, Italy

Casein is the best characterized milk protein and constitutes over 70–80% of total bovine milk protein. In milk, caseins exist as large micelle-like particles (100 nm in radius) that comprise four unrelated proteins (α_{s1}-, α_{s2}-, β-, and κ-casein) and calcium phosphate. Although α_{s1}-, α_{s2}, β-, and κ-casein present important structural differences, all of them adopt extremely open and flexible conformations, enough to be defined rheomorphic proteins [1] and considered full members of the class of intrinsically disordered proteins (IDPs) [2]. The structural intrinsic disorder of caseins, due to specific differential sequence features, is crucial for carrying out the various molecular activities attributed to them, including "holding" or "disaggregating" action consisting in recognizing protein misfolded regions, preventing their aggregation and disaggregating preformed aggregates by means of entropic pulling, mechanical unfolding or entropy energy transfer mechanisms [3].
SAXS experiments were aimed to evaluate caseins capability of preventing protein aggregation and amyloid formation by considering the caseins effect on 1-40 β-amyloid peptide ($A\beta_{1-40}$) fibrillogenesis. Preliminary experiments performed in our laboratory by thioflavin T fluorescence spectroscopy have shown that all caseins stabilize Aβ peptide against fibrillization, but k-casein provides the most significant effect on lag-phase, aggregation rate and fibrils amount (Figure 1). Differently from alpha and beta casein, k-casein is able to form amyloid fibrils and, according to the model proposed by Ecroyd et al, the dissociation from an oligomeric initial state, during the transition from 20 °C to 37 °C is the rate limiting step in the protein fibril formation [4] (Figure 2). The dissociated species would be amyloidogenic precursors of fibrillar assembly through a β-sheet stacking. Our hypothesis is that the inhibition of $A\beta_{1-40}$ amyloid aggregation is due to the binding of $A\beta_{1-40}$ peptide to these oligomeric surfaces, that, on one hand, reduces $A\beta_{1-40}$ monomer concentration thus influencing its amyloid concentration-dependent aggregation, and, on the other, inhibits k-casein dissociation. The mechanism would be a sort of dual chaperon-like activity involving two intrinsically disordered amyloid proteins, Aβ peptide and k-casein.

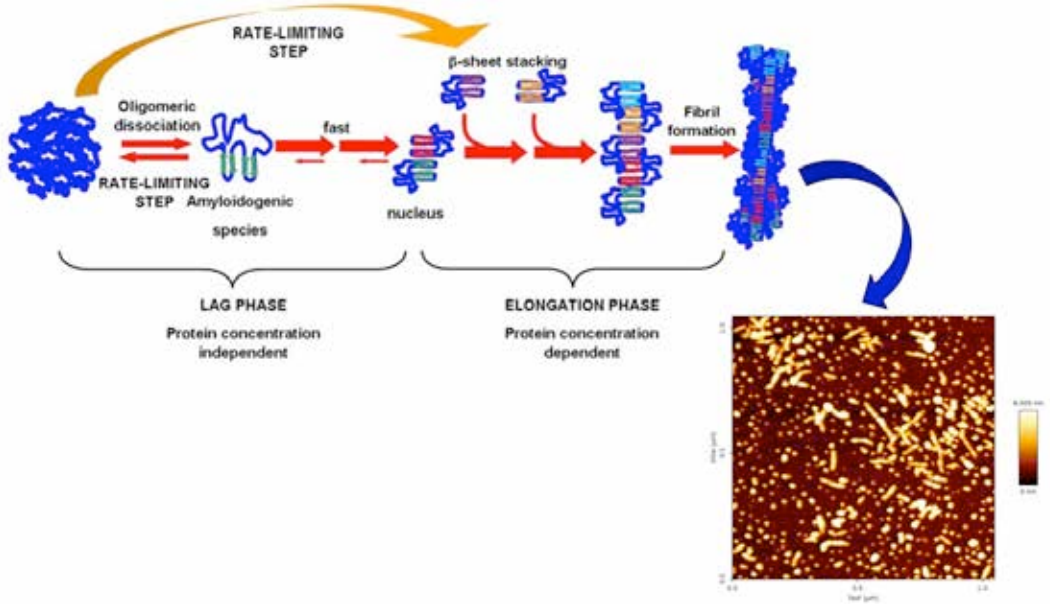

Figure 1. k-casein aggregation model. Adapted by Ecroyd et al. [4]

SAXS experiments were performed to characterize the effect of k-casein on Aβ amyloid aggregation process and clarify the molecular mechanisms underlying the chaperoning action of the milk protein.

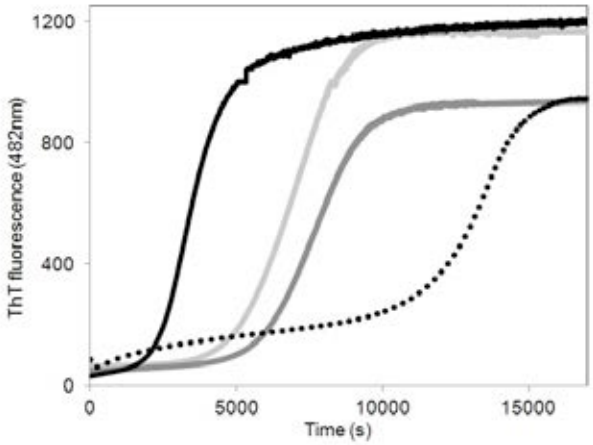

Figure 2. k-casein at increasing temperatures, as reported in the legend. The small differences between SAXS curves evidenced at high Q values underline the importance of the use of synchrotron light in order to detail these phenomena

Firstly, we aimed to understand how temperature influences the conformational transition toward ordered fibrillar structures for k-casein and how this behavior differs from the one traced in another milk protein, casein, as the temperature changes. SAXS spectra were acquired by varying temperature for both the proteins from 15 °C to 42 °C. While we assisted to the progressive variation of SAXS spectra for β casein towards species characterized by higher gyration radius (thus indicating protein aggregation process), surprisingly k casein did not exhibit any significant variation in the SAXS profile. Our idea, is that SAXS measurements temporal resolution, could be not able to detect the conformational change during protein dissociation, and the aggregates formed after the transition have the same characteristics, detectable by SAXS, of the initial aggregates.

Figure 3. Thioflavin T fluorescence used for monitoring the $A\beta_{1\text{-}40}$ alone (black) and $Ab_{1\text{-}40}$ incubated with α, β and k caseins (light grey, dark grey and dotted black respectively). Aβ concentration is 50μM and [Aβ]:[casein]=20:1. Samples are incubated under stirring at 37°C

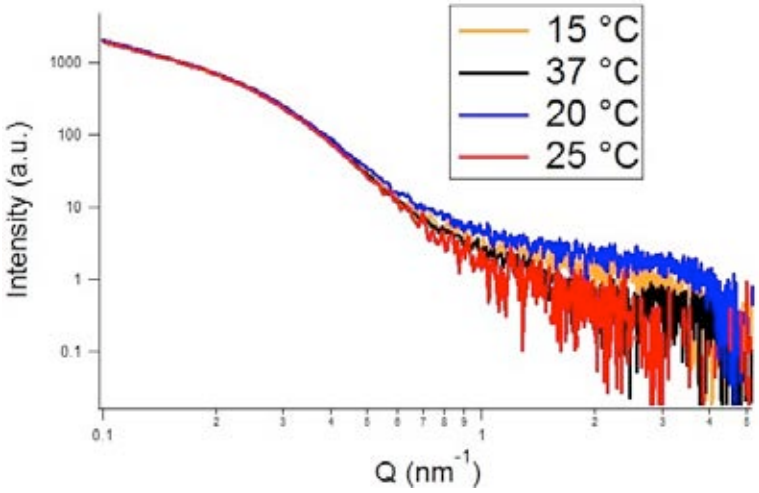

However, we report in figure 3 SAXS spectra corresponding to k casein at increasing temperatures because it is interesting to evidence that at 20 °C there is a small but not neglectable change at high Q values, which suggests that our hypothesis above mentioned should be better investigated by complementary techniques. A second series of SAXS measurements we performed was aimed to analyze the influence of the k-casein chaperones on $A\beta_{1\text{–}40}$ peptide aggregation process by the analysis of $A\beta_{1\text{–}40}$ peptide different aggregate species, corresponding to different stages from the beginning of the process, and formed in the presence and in the absence of κ-casein in monomeric, micellar or aggregated form [5]. SAXS curves corresponding to Aβ monomers (Figure 4) with and without k-casein are almost indistinguishable from one another, due to the low amount of k-casein in solution which

cannot evidence a remarkable SAXS signal from alone. Also, the large similarity of these SAXS curves assures that k-casein does not induce modification in Aβ monomers structure, neither in their aggregation number. On the other side, the comparison between the following Aβ aggregation stages in presence or in absence of k-casein deserves attention. The comparison between SAXS spectra corresponding to the oligomeric aggregates grown in presence and in absence of k-casein (Figure 4, in the middle), clearly indicates that bigger aggregates are found in the solution where k-casein is added. While the two SAXS curves are overlapped for Q>0.35 nm^{-1}, the intensities for lower Q values considerably change, until the extrapolation $\frac{d\Sigma}{d\Omega}(Q \cong 0)$ which in the presence of k-casein is about three times larger than in its absence. Because $\frac{d\Sigma}{d\Omega}(Q \cong 0)$ value is proportional to the square of the average volume of the scattering objects, it can be derived that k-casein modifies the first aggregation stages of Aβ inducing the formation of bigger aggregates. The similarity or the scattering curves for Q>0.35 nm^{-1} suggests the possibility that the smaller size Aβ oligomers are the same, with or without k-casein, but k-casein can act as a binding agent for these oligomers, giving rise to a population of average bigger size. This hypothesis could be confirmed considering SAXS curves relative to fibrils grown in presence or in absence of the milk protein (Figure 4, top). In this stage, the intensity of SAXS curves at Q≈0 is equal, while their morphology changes above all at intermediate Q values, demonstrating that although the average volume of the objects in solution is comparable, their structural features are markedly different.

The obtained results are promising to contribute to clear the evolutionary role and the action mechanism of proteins with chaperon-like activity that present intrinsically disordered regions, IDRs, that do not fit the standard sequence-structure-function paradigm. Moreover, this topic has important implications in the field of prevention and therapy in Alzheimer diseases, and, in general, of amyloid pathologies [6].

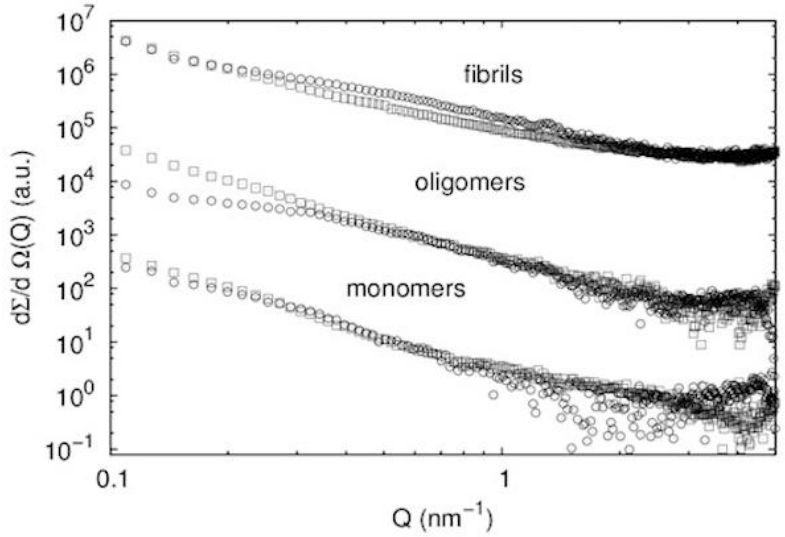

Figure 4. SAXS spectra obtained from different stages of Aβ aggregation pattern. Circles correspond to Aβ monomers (bottom, c=151μM), oligomers (middle, c=277μM) and fibrils (top, c=202μM). Squares correspond to Aβ monomers (c=400μM), oligomers (c=146μM) and fibrils (c=184μM), in presence of k-casein in a molar ratio k-casein:Aβ=1:20. Curves relative to the same aggregation step are normalized for their concentration in order to be compared. SAXS data corresponding to oligomeric and fibrillar stages are each one scaled by a factor 100 for the sake of clarity

References:

[1] Holt A and Sawyer L, J. Chem. Soc. Faraday Trans., 1993, 89 (15) 2683-2692
[2] Tompa P, Structure and Function of Intrinsically Disordered Proteins, CRC Press, 2009
[3] Uversky V, Protein Chaperones and Protection from Neurodegenerative Diseases, Wiley, 2011
[4] Ecroyd H et al., J Biol Chem. 283(14), 9012-22 (2008)
[5] Carrotta R et al., Biochim Biophys Acta, 2012, 1820(2):124-32
[6] Vilasi S et al. In preparation to be submitted to Febs Journal

IN SITU FORMATION AND CHARACTERIZATION OF DRUG DELIVERY SYSTEMS BASED ON LYOTROPIC LIQUID CRYSTALLINE PHASES

A. Yaghmur[1], M. Rappolt[2,3], A.L. Uldall Jonassen[1] and S. W. Larsen[1]

1.) Department of Pharmacy, Faculty of Health and Medical Sciences, University of Copenhagen, Universitetsparken 2, DK-2100 Copenhagen, Denmark
2.) Institute for Inorganic Chemistry, Technical University of Graz, Austria
3.) School of Food Science and Nutrition, University of Leeds, Leeds, UK

The stimuli-triggered *in situ* forming drug delivery systems are attractive due to their sustained release properties and they may offer also various advantages including ease of administration, the use of less invasive small needles, and the possibility of improving patient compliance due to a reduced frequency of administration [1-3]. Although different studies demonstrated the potential of this strategy in designing parenteral formulations, the dynamic behavior of the injectable drug preformulations and the effects of various parameters on the shape and size of the *in situ* formed depots as well as the sustained release characteristics have to be addressed. The optimal utilization of these drug delivery systems underscores the need of forming fast *in situ* the non-lamellar phases with an attempt of preventing burst drug release behavior during the involved stimuli-triggered phase transition.

In an interesting approach, the unique properties of inverted type non-lamellar liquid crystalline phases can be exploited to form *in situ* cubic and hexagonal delivery systems with sustained drug release properties at the administration site in response of injectable *low-viscous* stimulus-responsive precursors (drug preformulations) to the biological environmental stimuli [1-3]. Figure 1 presents a schematic for the *in situ* formation of drug-loaded highly viscous non-lamellar phase after subcutaneous administration. The proposed tolerability of these formulations and potential significant reduction in unwanted toxic effects upon injection, and also the possibility of controlling the release of solubilized drugs make these systems highly attractive for sustained drug release applications.

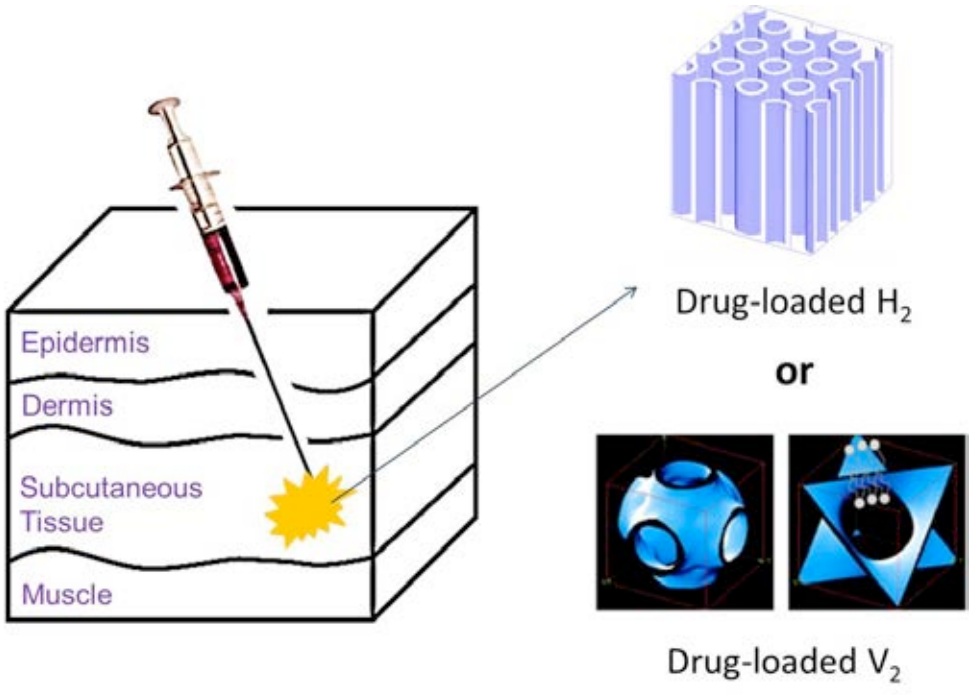

Figure 1. Hydration-triggered *in situ* formation of the drug-loaded inverted type bicontinuous cubic and hexagonal phases upon subcutaneous administration of the low-viscous precursors [3]

Our main attention was to focus on the structural characterization of these *in situ* formed depots under conditions mimicking the biological environment and also their drug release properties. The non-lamellar liquid crystalline phases are formed *in situ via* the self assembly of safe and biocompatible surfactant-like lipids with biological relevance upon direct exposure to excess of aqueous media or biological fluid. The adoption of the highly viscous bicontinuous cubic (V_2) and hexagonal (H_2) phases, which are attractive for the formation of stimuli-triggered drug delivery systems, is affected by different factors including the lipid molecular structure, the lipid composition, electrostatic interactions, hydration level, the presence of guest additives, and the applied experimental conditions. In one of these experiments, the dynamic behaviour of precursor (stock organic solution of a lipid mixture) was investigated upon rapid exposure to two different biological fluids under simulated body fluid environmental conditions at 37 °C [1]. To determine such structural events *in situ*, a combination of SAXS with remote controlled addition of biological fluid was used. This study attempted a detailed structural analysis of the role of the dynamical hydration under physiological conditions during the formation of nanoscaled non-lamellar structures. It is interesting to note that the obtained results reveal a relatively fast rearrangement of the lipid in excess biological fluids, see Figure 2.

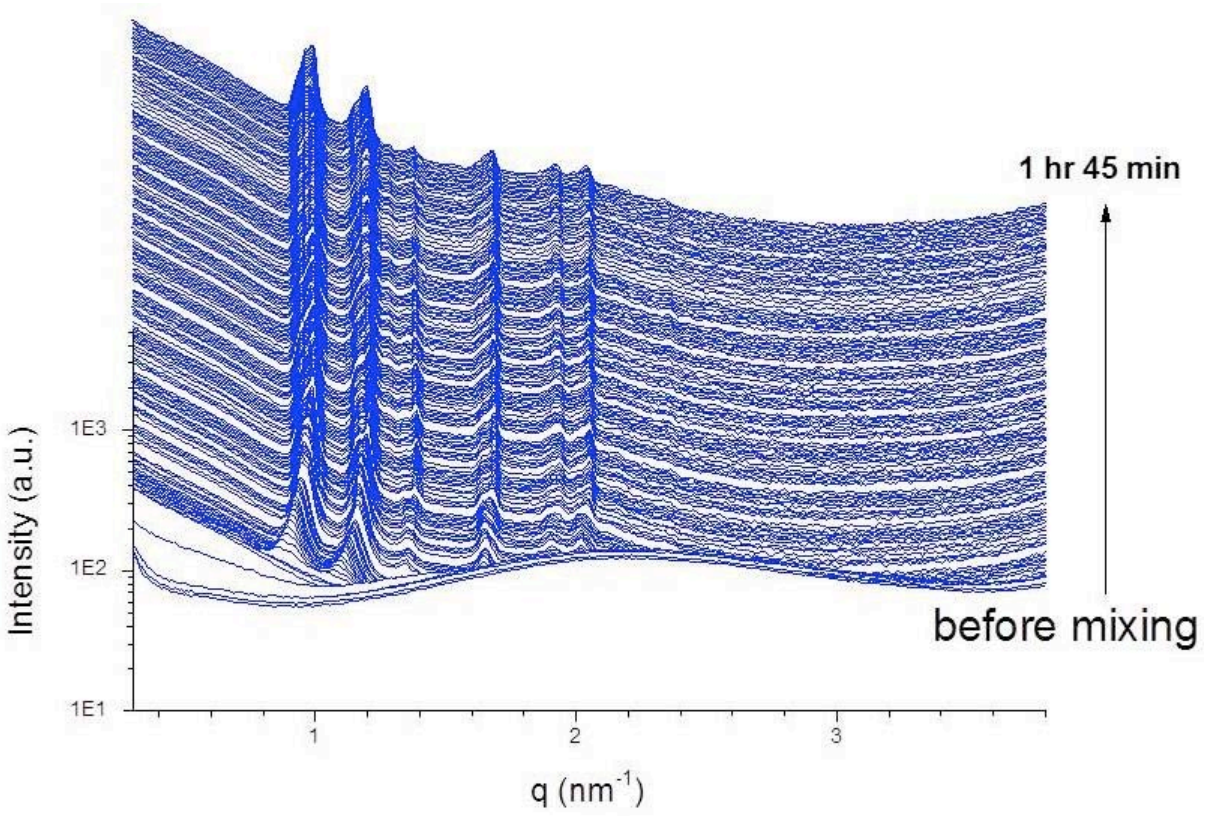

Figure 2. Direct exposure of organic solution of a lipid mixture to biologically relevant medium. A fast structural transition to inverted type bicontinuous cubic phase of the symmetry Pn3m is detected [4]

References:

[1] A. Yaghmur, S. Weng Larsen, M. Schmitt, J. Østergaard, C. Larsen, H. Jensen, A. Urtti and M. Rappolt; *In situ* characterization of lipidic bupivacaine-loaded formulations; Soft Matter **7**, 8291-8295 (2011)

[2] A. Yaghmur, M. Rappolt, J. Østergaard, C. Larsen and S. Weng Larsen; Characterization of bupivacaine-loaded formulations based on lyotropic liquid crystalline phases and microemulsions: effect of lipid composition; Langmuir **28**, 2881-2881 (2012)

[3] A. Yaghmur, M. Rappolt, S. W. Larsen, *J. Drug Del. Sci. Tech.* 2013, 23, 325-332

[4] A. Yaghmur, M. Rappolt, A. L. Uldall Jonassen, S. W. Larsen, *Manuscript in preperation*

Chemistry

AUTOCATALYSIS IN MULTIVALENT "CLICK" CYCLOADDITION REACTIONS TOWARDS SELF-HEALING POLYMERIC MATERIALS: INVESTIGATION OF TIME-DEPENDENT CLUSTER FORMATION VIA SAXS

W. Binder[1], P. Michael[1], A. Stojanovic[1], D. Döhler[1], J. Akbarzadeh[2] and S. Bernstorff[3]

1.) Institute of Chemistry, Chair of Macromolecular Chemistry, Faculty of Natural Sciences II (Chemistry, Physics and Mathematics), Martin-Luther University Halle-Wittenberg, von Danckelmann-Platz 4, Halle 06120, Germany
2.) Faculty of Physics, Dynamics of Condensed Systems, University of Vienna, Strudlhofgasse 4, 1090 Vienna, Austria
3.) Elettra-Sincrotrone Trieste S.C.p.A., Strada Statale 14, km 163.5 in AREA Science Park, I-34149 Basovizza / Trieste, Italy

The project aims to investigate “click” reactions between multivalent poly(isobutylene)s (PIBs) and poly(acrylate)s functionalized with azide- and alkyne-moieties, respectively to gain information of the crosslinking process and hence a deeper insight in the kinetics of nanocluster formation in self-healing polymers [1]. Basis is the autocatalytic copper(I)-catalyzed azide-alkyne click-reaction (CuAAC) [2,3], inducing transient nanosized 1,2,3-triazole-clusters, which are proposed to act as nucleus for the complexation of copper(I)-ions and thus the acceleration of the reaction [4,5].

Accordingly, temperature-dependent SAXS- and WAXS-measurements of micro-phase separated polymer networks including copper(I) clusters have been investigated on a reasonable time-scale of minutes. In order to identify the different influences on nanoclustering within the investigated networks they were analyzed in dependence on the molecular weight and the functional group density of the PIBs and poly(acrylate)s which have undergone crosslinking via CuAAC.

For the implementation of the SAXS and WAXS experiments with high resolution an asymmetric set-up of the camera in vertical direction with a sample to detector distance of 215 cm, leading to an accessible q-range of 0.1 – 20.0 nm^{-1} was used.

The already prepared and final polymeric networks were measured about 15 minutes each. Therefore they were placed either in quartz glass capillaries with a diameter of 1.5 mm and a wall thickness of 10 μm, or between two layers of commercially available aluminum foils. The experiments were performed in a temperature range from 25 °C to 100 °C using a holder cell with variable heating element with an external control element, utilizing a 8 keV energy beam (corresponding to a X-ray wavelength of 0.154 nm) and a 2D Pilatus 100K detector or a 2D Image plate for the SAXS-range and a 1D Gabriel type gas detector for the WAXS-range.

At room temperature networks formed between multivalent star-shaped PIBs functionalized with azide- and alkyne-moieties showed a broad scattering peak in the range between 0.8-1.5 nm^{-1} indicating a clear phase separation (see Figure 1a). The position as well as the broadness of the scattering peak strongly depended on the molecular weight and thus on the functional group density of the trivalent azide- and alkyne-functionalized PIBs which have undergone crosslinking via CuAAC.

While the polymeric network resulting from a PIB with a molecular weight of 4000 g/mol showed strong scattering around 1.3 nm^{-1}, the scattering peak for the investigated sample with a starting molecular weight of 11 600 g/mol shifted to 1.0 nm^{-1} indicating a larger distance between nanoclusters. Temperature-dependent measurements of PIB networks revealed the thermal stability of the investigated covalently bounded networks, since no order-disorder transition could be observed in the applied temperature range up to 100 °C.

The polymer networks formed between multivalent PIBs and poly(acrylate)s were analyzed in a similar manner. However, whereas in the case of pure PIB networks no scattering could be observed in the WAXS-range, poly(acrylate)-containing networks exhibited pronounced scattering in the WAXS-range (6-12 nm^{-1}, see Figure 1b). Thus, we assume that the observed

scattering peak in the WAXS-range is emerging due to interactions of active copper(I) centers with the carbonyl groups within the polymer backbone of poly(acrylate).

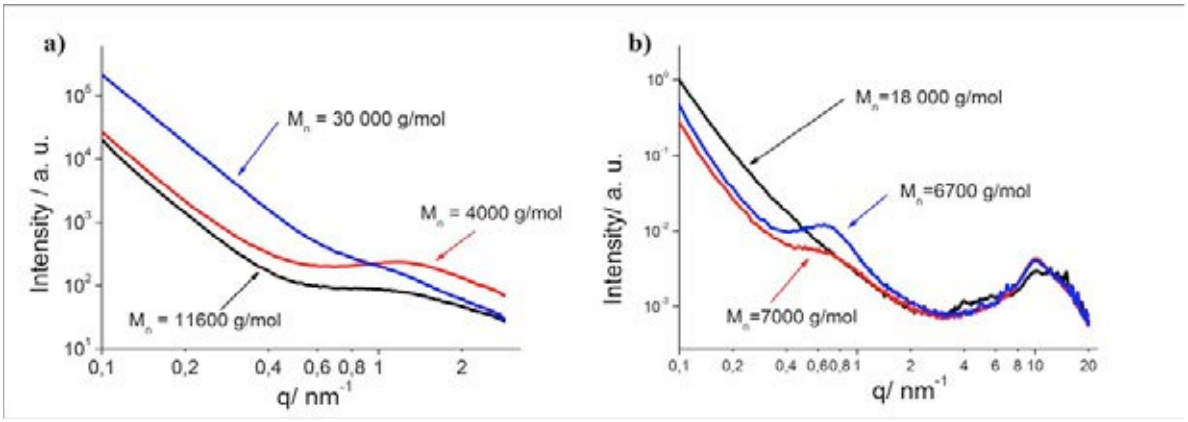

Figure 1. Dependence of phase separation within polymeric networks on the molecular weight of a) multivalent alkyne- and azide-functionalized PIBs which have undergone crosslinking via CuAAC and b) multivalent azide-functionalized PIBs and alkyne bearing poly(acrylate)s which have undergone crosslinking via CuAAC.

Additionally, scattering due to phase separation was observed in the range between 0.3 - 0.8 nm^{-1}, showing a strong dependence on the molecular weight and functional group density of the polymeric precursors. Similar to the aforementioned networks poly(acrylate) networks built up from a starting polymer with low molecular weight (6700 g/mol) show a stronger scattering peak at higher q-values whereas a high molecular weight starting polymer (18 000 g/mol) reveals no scattering at all due to the less amount of upcoming nanoclusters as well as their larger distance.

In order to investigate the kinetics of the nanocluster-formation via “click” chemistry more detailed further time-resolved *in-situ* SAXS investigations will be conducted in the future. Therefore PIBs as well as poly(acrylate)s with different starting molecular weights will be mixed with an appropriate copper(I) source to study the upcoming nanoclustering during the progress of reaction. Furthermore the influence of the concentration of active copper(I) centers on the reaction kinetics will be investigated by varying the amount of the applied copper(I) species.

References:

[1] W. H. Binder*, Ed., *Self-Healing Polymers. From Principles to Applications*, (Wiley-VCH Verlag GmbH & Co. KGaA, Weinheim, 2013), pp. 425
[2] V. O. Rodionov, V. V. Fokin, M. G. Finn, Angew. Chem. 117, 2250 (2005)
[3] T. R. Chan, R. Hilgraf, K. B. Sharpless, V. V. Fokin, Org. Lett. 6, 2853 (07/30, 2004)
[4] D. Döhler, P. Michael, W. H. Binder, Macromolecules 45, 3335 (2012)
[5] M. Gragert, M. Schunack, W. H. Binder, Macromol. Rapid Commun. 32, 419 (2011)

SITU SAXS STUDY OF THE FORMATION OF CYLINDRICAL MESOPOROUS SILICA NANOPARTICLES

C. Rafai[1], H. Amenitsch[2], M. Lindén[1]

1.) Inorganic Chemistry II, Ulm University, Albert-Einstein-Allee 11, 89081 Ulm, Germany
2.) Institute of Anorganic Chemistry, Graz University of Technology, Stremayrgasse 9/IV, 8010 Graz, Austria

Mesoporous silica nanoparticles are interesting for a variety of applications. During the last years huge progress has been made related to the use of mesoporous silica nanoparticles as carriers for drugs in vitro and in vivo, and also in the use of corresponding particles functionalized with an imagable group (fluorescent dyes, magnetic nanoparticles and complexes, etc.) for diagnostics and also for following disease progresses [1]. For example, the main proposer and co-workers have shown that spherical mesoporous silica nanoparticles can be targeted to cancer tumors in vivo and locally deliver drugs which otherwise would cause extensive negative side-effects [2]. It has also been shown that the shape of such nanoparticles is an important parameter for controlling biodistribution and cell-internalization kinetics of such particles [3]. Especially cylindrical particles are interesting in this respect, as their larger particle-cell surface contact area can be used to enhance cell penetration. There are several reports in the literature where syntheses resulting in monodisperse elongated mesoporous silica nanoparticles are described. However, the reason for the formation of cylindrical mesoporous silica nanoparticles is not well understood. We have used a flow-through setup previously used by us for in situ studies of the formation of mesoporous silica microparticles [4] with the aim of simultaneously monitoring the development of the mescoscopic order in the nanoparticles and the particle growth kinetics.

A typical SAXS pattern measured for a synthesis leading to cylindrical particles is shown in Figure 1.

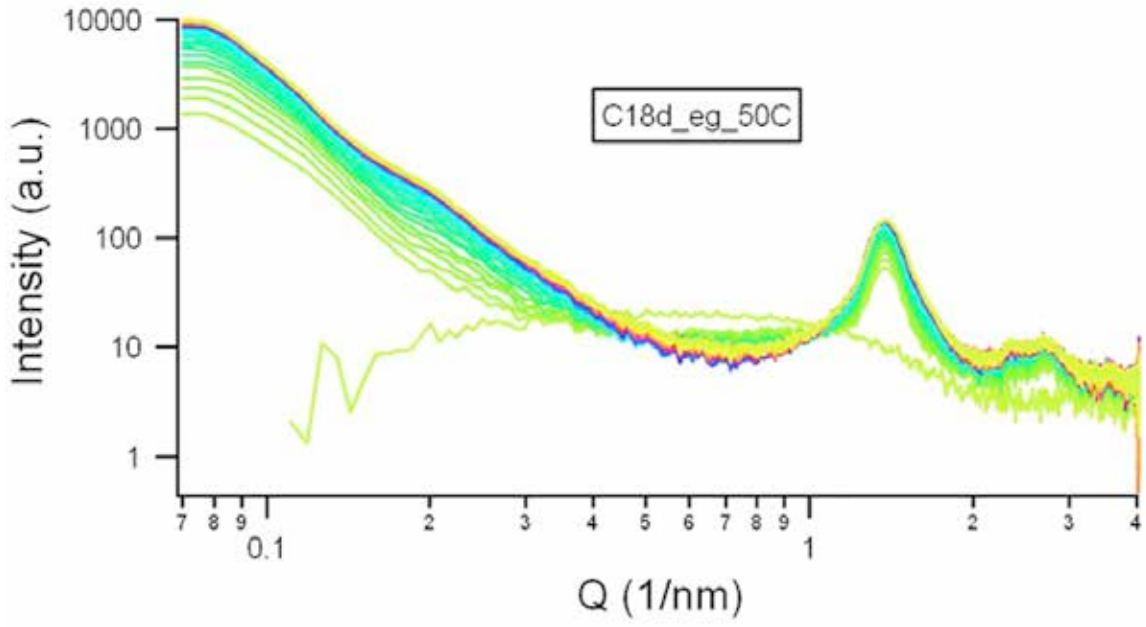

Figure 1. Time/resolved SAXS patterns measured for a synthesis leading to rod-like mesoporous silica nanoparticles with a 2D hexagonal arrangement of pores. The first scattering pattering was recorded 30 s after starting the reaction and the last scattering pattern was measured after a reaction time of 50 min.

Mesoscopic order, as indicated by the appearance of Bragg reflections, was observed after a reaction time of 60 s under these synthesis conditions. The Bragg reflections could be indexed as the (10), (11), (20), and (21) reflections of a 2D hexagonal phase. In the low-angle region, the slope of the scattering curve soon after the appearance of the Bragg reflections corresponds to what is expected for spherical particles. However, with time, a second region develops with clearly lower slope, which corresponds to the formation of elongated particles which evidently grow with time, as the knee shifts towards lower Q – growth. Thus, these results seem to indicate that the formation of the elongated mesoscopically ordered silica nanoparticles occurs through an initial formation of spherical mesoscopically ordered particles, which undergo secondary aggregation into the final cylindrical morphology.

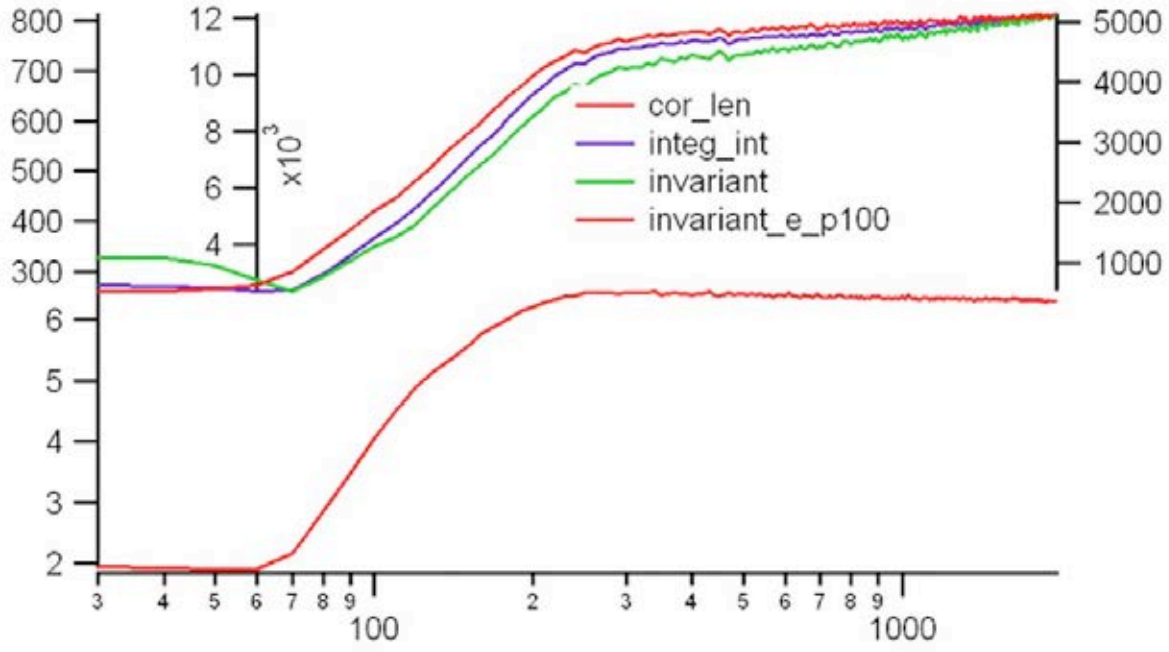

Figure 2. Correlation length, integrated intensity, and invariant as a function of time calculated based on the data shown in Figure 1.

Analysis of the correlation length, integrated intensity, and invariant as a function of time clearly indicated the onset of particle nucleation and growth, and also give evidence for an aggregation-driven process. Detailed quantitative analysis of the data is ongoing work, but already based on this semi-quantitative analysis, we can conclude that the formation of elongated silica particles is a two-step process, where the final particle dimensions are related to the initial size of the spherical nanoparticles formed, as well as their, most probably, electrostatically controlled, secondary aggregation.

References:

[1] J.M. Rosenholm, C. Sahlgren, M. Lindén, Cancer-cell targeting and cell-specific delivery by mesoporous silica nanoparticles, J. Mater. Chem., 20 (2010) 2707-2713

[2] V. Mamaeva, J.M. Rosenholm, L.T. Bate-Eya, L. Bergman, E. Peuhu, A. Duchanoy, L.E. Fortelius, S. Landor, D.M. Toivola, M. Lindén, C. Sahlgren, Mesoporous Silica Nanoparticles as Drug Delivery Systems for Targeted Inhibition of Notch Signaling in Cancer, Molecular Therapy, 19 (2011) 1538–1546

[3] X. Huang, X. Teng, D. Chen, F. Tang, J. He, The effect of the shape of mesoporous silica nanoparticles on cellular uptake and cell function, Biomaterials, 31 (2010) 438-448

[4] for example, K. Flodström, C.V. Teixeira, H. Amenitsch, V. Alfredsson, M. Lindén, An in situ Synchrotron Small Angle X-ray Scattering/X-ray Diffraction Study of the Formation of SBA-15 Mesoporous Silica, Langmuir, 20 (2004) 4885-4891.

SAXS STUDIES OF THE *IN SITU* DEHYDROGENATIVE COUPLING REACTION OF ARYLTIN TRIHYDRIDES

C. Zeppek, H. Amenitsch, F. Uhlig

Institute of Inorganic Chemistry, Graz University of Technology, Stremayrgasse 9/IV 8010 Graz, Austria

In the last decade, organotin dihydrides have been studied as precursors in the formation of polymeric materials exhibiting a linear backbone of covalently bonded tin atoms which can be seen as a molecular metal wire embedded in an organic jacket. These compounds feature an increased degree of electron delocalization by catenation. This leads to promising materials in charge-transfer devices. In particular, polyaryl stannanes have drawn a lot of attention attributed to their σ-π transitions, however these are not well characterized yet due to their insolubility [1,2]. Organotin hydrides undergo a catalytic dehydropolymerization using metal complexes [3,4]. More recently, cheap and easy to handle amine bases such as TMEDA (*N*,*N*,*N*',*N*'-tetramethylethylenediamine) have been reported to efficiently catalyze the polymerization reaction of organotin dihydrides leading to poly(diarylstannane)s [5]. While the use of amine bases as polymerization catalysts has been known since 1962, the mechanistic background or the role of TMEDA and the characteristics of the formed products has not been clarified [6].
Similarly to organotin dihydrides (R_2SnH_2), aryl trihydrides ($ArylSnH_3$) undergo Sn-Sn bond formation upon loss of hydrogen and the aryl group via a dehydrogenative coupling reaction when converted with TMEDA. This polymerization reaction leads to the formation of aryl decorated tin nanoparticles (Aryl@Sn) as insoluble, black solids (Scheme 1). HR-SEM imaging supposed that the nature of the reaction solvent used strongly affects the morphology of the resulting Aryl@Sn material. The specific impacts of the chosen solvent and educt concentration during the dehydrogenative coupling reaction in determining the morphology evolution of the resulting material is of high importance in the characterization of the product.
In our experiments the dehydrogenative coupling reaction of *o*-tolylSnH_3 with TMEDA was carried out under inert conditions and the particle formation monitored by SAXS (Scheme 1).

Scheme 1. Synthesis of aryl decorated nano particles Aryl@Sn *via* dehydrogenative coupling reaction of aryltin trihydrides (Aryl=*o*-tolyl).

The employed reaction solvents can be categorized in apolar-non aromatic (cyclohexane), apolar-aromatic (toluene) and apolar-donor solvents (diethylether, DME). Four different 0.4 M *o*-tolyltin tihydride solutions (diethylether, DME, toluene and cyclohexane) were prepared under inert conditions using degassed solvent. 50 μl of the solution were placed in a glass capillary and sealed with rubber septum. The capillary was then placed on the sample stage and measured as a blank ("static"). Afterwards, 20μl of degassed and dried TMEDA were added *via* the septum and the measurement started to follow the *in situ* formation and aggregation of nanoparticles. Further, the solutions were diluted with the corresponding degassed solvent (1:2 and 1:5) and the same sample treatment carried out in order to get information on the concentration dependency of the particle size.
It was observed that the lowest educt concentration of 0.08 M o-tolylSnH_3 in the respective solvent is the most suitable for monitoring the particle formation over time.

Fig.1 displays the scattering pattern for the dehydrogenative coupling reaction of *o*-tolyltin trihydride and TMEDA in diethylether (0.08M) over a reaction time of 2h.

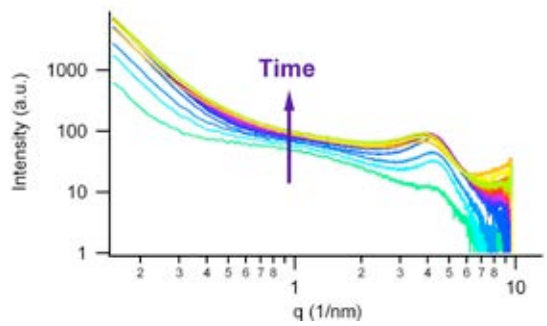

Figure 1. Scattering pattern of a *o*-tolylstannane/TMEDA reaction in Et_2O over the first 2 h. Time resolution for each pattern: 4 min

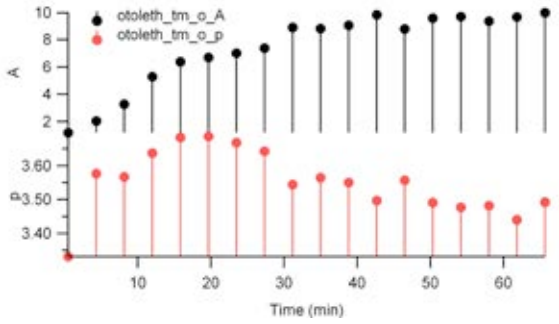

Figure 2. Porod constant A (a.u.) and Porod exponent p fitted on the low q part of the scattering pattern versus time^2 (min)

According to the *in situ* SAXS data, diethylether as solvent leads to the formation of spherical substructures with a diameter of 1.43 nm. The sphere formation process is completed after 20 min reaction time which is expressed by the constant height of the peak at 4.3 nm^{-1} (Fig. 1). As the intensity of the signals increases over reaction time an aggregation of these Aryl@Sn spheres takes places (Fig. 1). After approximately 20 min the Porod constant increases and the Porod exponent decreases caused by agglomeration of smaller spheres to the bigger aggregates (Scheme 2).

Scheme 2. Schematic growth process of the Aryl@Sn (Aryl= *o*-tolylSnH_3) in Et_2O

In the case of cyclohexane as reaction solvent rod like structures are formed and the Porod exponent reaches 1 already after 10 minutes reaction time. Thus, the principal rod formation is faster compared to the generation of spheres in Et_2O. The rods' cross section is 1.5 nm with a length of 8.6 nm. Upon reaction progress the Porod exponent converges to 1.5 which results from structural changes in the product. This might happen due to an agglomeration process of rods forming networks. In contrast to cyclohexane, a q^{-1} behavior is observed at the beginning of the dehydrogenative coupling reaction for aromatic solvents like toluene. Conclusively, rods of infinitive length are formed featuring a cross section of 1.5 nm with an average distance of 15.7 nm to each other.

As already suggested by HR-SEM imaging, our *in situ* SAXS data clearly confirm that the nano morphology of the aryl decorated Sn particles (Aryl@Sn) depends on the polarity and donor ability of the used solvent. This reveals a major feature in controlling the particle size and shape by simply adjusting the reaction conditions in order to tune the material for diverse applications as for instance anode material in lithium ion batteries.

References:

[1] F. Choffat, P. Smith, W. Caseri; Polystannanes: Polymers of a molecular, jacketed metal–wire structure; Adv. Mater. **20**, 2225-2229 (2008)

[2] F. Choffat, S. Fornera, P. Smith, W. Caseri, D. W. Breiby, J. W. Andreasen, M. M. Nilesen; Oriented poly(dialkylstannane)s; Adv. Funct. Mater. **18**, 2301-2308 (2008)

[3] F. Choffat, P. Smith, W. Caseri; Facile synthesis of linear poly(dibutylstannane); J. Mater. Chem. **15**, 1789-1792 (2005)

[4] H. K. Sharma, R. Aria-Ugarte, A. J. Metta-Magana, K. H. Pannell; Dehydrogenative dimerization of di-tert-butyltin dihydride photochemically and thermally Catalyzed by iron and molybdenum complexes; Angew. Chem. Int. Ed. **48**, 6309-6312 (2009)

[5] M.- L. Lechner, M. Trummer, I. Bräunlich, P. Smith, W. Caseri, F. Uhlig; From poly(dialkylstannane)s to poly(diarylstannane)s: comparison of synthesis methods and resulting polymers; Appl. Organomet. Chem. **25**, 769-776 (2011)

[6] a) W. P. Neumann; Darstellung und Struktur von Diphenylzinn; Angew. Chem. **6**, 215 (1962) b) W. P. Neumann; Neue Synthesen im Gebiet der Organozinnverbindungen (Über Zinn-dialkyle); Angew. Chem. **3**, 122 (1962)

Publications

Publications in Journals and Reviewed Proceedings 2013

H. Amenitsch, F. Benetti, A. Ramos, G. Legname, J.R. Requena
SAXS structural study of PrP^{Sc} reveals ~11 nm diameter of basic double intertwined fibers
prion, Vol. 7 - 1933-6896, pp. 496-500 (2013)

H. Amenitsch, D. Pozzi, F. Cardarelli, F. Salomone, C. Marchini, G. Caracciolo
Effect of cholesterol on the transfection efficiency of DOTAP-containing lipoplexes
Technical Proceedings of the NSTI-Nanotech 2013 Conference and Expo (2013), pp. 274 - 277

I. Andreou, H. Amenitsch, V. Likodimos, P. Falaras, P.G. Koutsoukos, E. Leontidis
Organized silica films generated by evaporation-induced self-assembly as hosts for iron oxide nanoparticles
Materials 6 (4), 1467-1484 (2013)

S. Bernstorff, V. Holy, J. Endres, V. Valeš, J. Sobota, Z. Siketić, I. Bogdanović-Radović, M. Buljan, G. Dražić
Co nanocrystals in amorphous multilayers - a structure study
Journal of Applied Crystallography 46 (6), pp. 1711-1721 (2013)

L. Bonaccorsi, P. Calandra, H. Amenitsch, E. Proverbio, D. Lombardo
Growth of fractal aggregates during template directed SAPO-34 zeolite formation
Microporous and Mesoporous Materials 167, pp. 3-9 (2013)

L. Bonaccorsi, P. Calandra, M.A. Kiselev, H. Amenitsch, E. Proverbio, D. Lombardo *Self-assembly in poly(dimethylsiloxane)-poly(ethylene oxide) block copolymer template directed synthesis of linde type A zeolite* Langmuir, Vol. 29 - 23, pp. 7079-7086 (2013) doi: 10.1021/la400951s

M. Buljan, N. Radić, M. Ivanda, I. Bogdanović-Radović, M. Karlušić, J. Grenzer, S. Prucnal, G. Dražić, G. Pletikapić, V. Svetličić, M. Jerčinović, S. Bernstorff and V Holý
Ge quantum dot lattices in Al_2O_3 multilayers
Journal of Nanoparticle Research 15 (3), article number 1485, 13 pages (2013)

M. Buljan, O. Roshchupkina, A. Šantić, V. Holý, C. Beahtz, A. Mücklich, L. Horák, V. Valeš, N. Radić, S. Bernstorff, J. Grenzer
Growth of a three-dimensional anisotropic lattice of Ge quantum dots in an amorphous alumina matrix
Journal of Applied Crystallography, Vol. 46, pp. 709-715 (2013)

M. Buljan, N. Radić, I. Bogdanović-Radović, Z. Siketić, K. Salamon, M. Jerčinović, M. Ivanda, G. Dražić, S. Bernstorff
Influence of annealing conditions on the structural and photoluminescence properties of Ge quantum dot lattices in a continuous $Ge+Al_2O_3$ film
Phys. Status Solidi A 210 (8), 1516–1521 (2013)

M. Buljan, M. Jerčinović, Z. Siketić, I. Bogdanović-Radović, I. Delač-Marion, M. Kralj, M. Ivanda, A. Turković, G. Dražić, S. Bernstorff, N. Radić.
Tuning the growth properties of Ge quantum dot lattices in amorphous oxides by matrix type
J. Appl. Cryst., Vol. 46, pp. 1490-1500 (2013)

G. Cordoyiannis, V.S.R. Jampani, S. Kralj, S. Dhara, V. Tzitzios, G. Basina, G. Nounesis, Z. Kutnjak, C.S.P. Tripathi, P. Losada-Perez, D. Jesenek, C. Glorieux, I. Muševič, A. Zidanšek, H. Amenitsch and J. Thoen
Different modulated structures of topological defects stabilized by adaptive targeting nanoparticles
Soft Matt. **9 (15)**, 3956-3964 (2013)

F. Di Puccio, L. Mattei, M. D'Acunto, S. Battaglia, S. Affattato, R. Ishak, S. Dinarelli, H. Amenitsch
Experimental and Numerical Analysis of UHMWPE acetabular cups after wear test: a preliminary study
Proceedings of the World Tribology Conference 2013, Turin, Italy, 2013

P. Dubcek, B. Pivac, S. Milosevic´, Niksa Krstulovic, Zlatko Kregar and S. Bernstorff
Texture of GaAs Nanoparticles Deposited by Pulsed Laser Ablation in Different Atmospheres
ISRN Nanomaterials, Vol. 2013, pp. 576506-1-576506-13 (2013)

L.F. Dumée, K. Sears, B. Marmiroli, H. Amenitsch, X. Duan, R. Lamb, D. Buso, C. Huynh, S. Hawkins, S. Kentish, M. Duke, S. Gray, P. Innocenzi, A.J. Hill, P. Falcaro
A high volume and low damage route to hydroxyl functionalization of carbon nanotubes using hard X-ray lithography
Carbon 51 (1), pp. 430-434 (2013)

P. Falcaro, F. Lapierre, B. Marmiroli, M. Styles, Y. Zhu, M. Takahashi, A.J. Hillad and C.M. Doherty
Positioning an individual metal–organic framework particle using a magnetic field
J. Mater. Chem. C, 2013,1, 42-45 (2013)

S. Haviar, M. Dubau, I. Khalakhan, M. Vorokhta, I. Matolinova, V. Matolin, V. Vales, J. Endres, V. Holy, M. Buljan, S. Bernstorff
X-ray small-angle scattering from sputtered CeO2/C bilayers
Journal of Applied Physics 113 (2), article 024301, 7 pages (Jan 2013)

M. Karlušić, M. Jakšić, M. Buljan, J. Sancho-Parramon, I. Bogdanović-Radović, N. Radić, S. Bernstorff
Materials modification using ions with energies below 1 MeV/u
Nuclear Instruments and Methods B317, pp. 143-148 (2013)

G. Khelashvili, B. Kollmitzer, P. Heftberger, G. Pabst, and D. Harries
Calculating the bending modulus for multicomponent lipid membranes in different thermodynamic phases
J. Chem. Theory Comput. 9: 3866 - 3871 (2013).

B. Kollmitzer, P. Heftberger, M. Rappolt, G. Pabst
Monolayer spontaneous curvature of raft-forming membrane lipids
Soft Matter, Vol. 9 - 45, pp. 10877-10884 (2013)

S. W. Larsen, J. Østergaard, A. Yaghmur, H. Jensen, C. Larsen
Use of in vitro release models in the design of sustained and localized drug delivery systems for subcutaneous and intra-articular administration
Drug Del. Sci. Tech. 23, 315-324 (2013)

M. Lavrič, V. Tzitzios, S. Kralj, G. Cordoyiannis, I. Lelidis, G. Nounesis, V. Georgakilas, H. Amenitsch, A. Zidanšek, Z. Kutnjak
The effect of graphene on liquid-crystalline blue phases
Applied Physics Letters 103 (14), art. no. 143116 (Sept. 2013)

M. Lučić Lavčević, P. Dubček, S. Bernstorff, M. Pavlović, and L. Šilović
A Grazing-Incidence Small-Angle X-Ray Scattering View of Vertically Aligned ZnO Nanowires
Journal of Nanomaterials 2013, Article ID 381519, 9 pages (2013)

S.S. Mandal, B. Nagarajan, H. Amenitsch, A.J. Bhattacharyya
Probing hemoglobin confinement inside submicron silica tubes using synchrotron SAXS and electrochemical response
European Biophysics Journal 42 (5), pp. 371-382 (2013)

S. Manso, F. Cacho-Nerin, R. Becerril, C. Nerin
Combined analytical and microbiological tools to study the effect on Aspergillus flavus *of cinnamon essential oil Contained In Food packaging*
Food Control 30 (2), 370–378 (2013)

G.R. Mitchell
Characterization of Safe Nanostructured Polymeric Materials Book: *Ecosustainable Polymer Nanomaterials for Food Packaging*
Editor: Clara Silvestre, Sossio Cimmino, Published by CRC Press, Boca Raton FL USA, Vol. 978-90-0420-737-0, pp. 87-118 (2013), http://www.crcpress.com/product/isbn/9789004207370

G. Pabst, B. Kollmitzer, P. Heftberger, and M. Rappolt
Cholesterol stabilizes ion channel function during sphingomyelinase hydrolysis
Biophysical Journal 01/2013 104(2):433

S. Palchetti, D. Pozzi, A. Riccioli, E. Ziparo, V. Colapicchioni, H. Amenitsch and G. Caracciolo
Structural characterization of cationic liposome/poly(I:C) complexes showing high ability in eliminating prostate cancer cells
RSC Advances, Vol. 3 - 46, pp. 24597-24604 (Jan 2013)

P. Pandit, A. Gupta, D. Kumar, M. Banerjee and S. Bernstorff
Effect of confinement on melting behaviour of cadmium arachidate Langmuir-Blodgett multilayer
Langmuir, *29* (12), pp 3950–3956 (2013)

B. Pivac, P. Dubček, I. Capan, H. Zorc, Jasna Dasović, S. Bernstorff, M. Wu, B. Vlahovic
GISAXS study of Si nano structures in SiO_2 matrix for solar cell applications
Physica Status Solidi A 210 (4), 755-759 (2013)

G. Polt, F. Spieckermann, H. Wilhelm, M. B. Kerber, E. Schafler, S. Bernstorff, M. Zehetbauer
The Role of Dislocations in y-iPP under Plastic Deformation investigated by X-ray Line Profile Analysis
Mechanics of Materials, Vol. 67, pp. 126-132 (dec 2013)
doi: 10.1016/j.mechmat.2013.05.010

D. Pozzi, F. Cardarelli, F. Salomone, C. Marchini, H. Amenitsch, G. Caracciolo
Effect of cholesterol on the transfection efficiency of DOTAP-containing lipoplexes
Proceedings of the 2013 NSTI-Nanotech 2013 Conference and Expo, Volume 3, 2013, Pages 274-277

C. Pucci, A. Salvia, M.G. Ortore, C. La Mesa
The DODAB-AOT-water system: vesicle formation and interactions with salts or synthetic polyelectrolytes
Soft Matter, Vol. 9 - 37, pp. 9000-9007 (2013)

F. Di Puccio, L. Mattei, M. D'Acunto, S. Battaglia, S. Affattato, R. Ishak, S. Dinarelli, H. Amenitsch
Experimental and Numerical Analysis of UHMWPE acetabular cups after wear test: a preliminary study
Proceedings of the World Tribology Conference 2013, Turin, Italy, 2013

M. Rappolt
Formation of Curved Membranes and Membrane Fusion Processes Studied by Synchrotron X-ray-Scattering Techniques
Advances in Planar Lipid Bilayers and Liposomes, Vol. 17, pp. 29-54 (Chapter Two), 2013

M. Rappolt, F. Cacho-Nerin, C. Morello, A. Yaghmur
How the chain configuration governs the packing of inverted micelles in the cubic Fd 3 m-phase
Soft Matter 9, 6291-6300 (2013)

M. Rittman, H. Amenitsch, M. Rappolt, B. Sartori, B.M.D. O'Driscoll and A. M. Squires
Control and Analysis of Oriented Thin Films of Lipid Inverse Bicontinuous Cubic Phase using Grazing Incidence Small Angle X-ray Scattering
Langmuir 29 (31), pp 9874–9880 (2013)

D. Russo, M.G. Ortore, F. Spinozzi, P. Mariani, C. Loupiac, B. Annighofer, A. Paciaroni
The impact of high hydrostatic pressure on structure and dynamics of beta-lactoglobulin
Biochimica et Biophysica Acta 1830 (10), pp. 4974-4980 (2013)

K. Salamon, O. Milat, N. Radić, P. Dubček, M. Jerčinović and S. Bernstorff
Structure and morphology of magnetron sputtered W films studied by X-ray methods
J. Phys. D: Appl. Phys. **46** (march 2013) 095304 (10pp);
Figure 5 was selected as cover picture of jornal issue.

A. Schiener, T. Wlochowitz, S. Gerth, T. Unruh, A. Rempel, H. Amenitsch and A. Magerl
Nucleation and growth of CdS nanoparticles observed by ultrafast SAXS
MRS Proceedings Volume 1528, mrsf12-1528-vv10-04 doi:10.1557/opl.2013.572 (2013)

A.W. Thornton, C.M. Doherty, P. Falcaro, D. Buso, H. Amenitsch, S.H. Han, Y.M. Lee, A.J. Hill
Architecturing nanospace via thermal rearrangement for highly efficient gas separations
Journal of Physical Chemistry C 117 (46), pp. 24654-24661 (2013)

A. Turković, P. Dubček, K. Juraić, S. Bernstorff, M. Buljan
Study of polymer electrolyte for Zn rechargeable nanostructured galvanic cells via combined in situ SAXS/DSC/WAXD measurements
American Journal of Nanoscience and Nanotechnology 1(1), 6-10, (2013)

E.M.F. Vieira, S. Levichev, C.J. Dias, R. Igreja, M. Buljan, S. Bernstorff, O. Conde, A. Chahboun, A.G. Rolo and M.J.M. Gomes
Charge storage behavior of nanostructures based on SiGe nanocrystals embedded in Al_2O_3 matrix
The European Physical Journal B, Vol. 86 - 7, pp. 336-1-336-7 (2013)

E. M. F. Vieira, J. Martín-Sánchez, M. A. Roldan, M. Varela, M. Buljan, S. Bernstorff, N. P. Barradas, N. Franco, R. Correia, A. G. Rolo, S. J. Pennycook, S. I. Molina, E. Alves, A. Chahboun and M. J. M. Gomes
Influence of RF-power on vertically stacked $Si_{1-x}Ge_x$ nanocrystals formation between ultra-thin amorphous Al_2O_3 layers by sputtering: structural and photoluminescence properties
J. Phys. D: Appl. Phys. **46** (2013) 385301 (10pp)

A. Yaghmur and M. Rappolt
The micellar cubic Fd3m phase. Recent advances in the structural characterization and potential applications.
Advances in Planar Lipid Bilayers and Liposomes, Vol. 18, pp. 111-145 (chapter 5) (2013)

Yaghmur, A., Rappolt, M., Larsen, S.W.
In situ forming drug delivery systems based on lyotropic liquid crystalline phases: Structural characterization and release properties
Journal of Drug Delivery Science and Technology, 23 (4), pp. 325-332 (2013)

Publications January to Aug 2014

J. Akbarzadeh, S. Puchegger, A. Stojanovic, H.O.K. Kirchner, W. H. Binder, S. Bernstorff, P. Zioupos, H. Peterlik
Timescales of self-healing in human bone tissue and polymeric ionic liquids
Bioinspired, Biomimetic and Nanobiomaterials Vol. 3, pp. 123-130 (2014)

S. Bernstorff, V. Holý, J. Endres, V. Vales, J. Sobota, Z. Siketic, I. Bogdanovic-Radovic, M. Buljan and G. Drazic
Co nanocrystals in amorphous multilayers - a structure study
J. Appl. Cryst. (2013). 46, 1711-1721

C. Carboni, D.G. Carboni, D. Jozić, S. Bernstorff, M. Rappolt and S. Al-Mahrazi
Synchrotron X-ray investigation of the layer spacing in a series of low molar mass bi-mesogen organosiloxane smectic materials
Phase Transitions: A Multinational Journal 4, pp. 739-745 (2014)

D. Carboni, D. Marongiu, P. Rassu, A. Pinna, H. Amenitsch, M. Casula, A. Marcelli, G. Cibin, P. Falcaro, L. Malfatti, P. Innocenzi
Enhanced photocatalytic activity in low-temperature processed titania mesoporous films
Journal of Physical Chemistry C, 118 (22), pp. 12000-12009 (2014)

Drasler B, Drobne D, Novak S, Valant J, Boljte S, Otrin L, Rappolt M, Sartori B, Iglic A, Kralj-Iglic V, Sustar V, Makovec D, Gyergyek S, Ho¿cevar M, Godec M, Zupanc J *Effects of magnetic cobalt ferrite nanoparticles on biological and artificial lipid membranes*
International Journal of Nanomedicine 9 (1), pp. 1559-1581 (2014)

S. Dunst, T. Rath, A. Radivo, E. Sovernigo, M. Tormen, H. Amenitsch, B. Marmiroli, B. Sartori, A. Reichmann, A.-C. Knall, G. Trimmel
Nanoimprinted Comb Structures in a Low Bandgap Polymer: Thermal Processing and Their Application in Hybrid Solar Cells
ACS Appl Mater Interfaces 6 (10), pp. 7633 - 7642 (2014)

M. Erceg, D. Jozić, I. Banovac, S. Perinović Jozić, S. Bernstorff
Preparation and characterization of melt intercalated poly(ethylene oxide)/lithium montmorillonite nanocomposites
Thermochimica Acta 579, 86–92 (2014)

P. Heftberger, B. Kollmitzer, F.A. Heberle, J. Pan, M. Rappolt, H. Amenitsch, N. Kucerka, J. Katsaras and G. Pabst
Global small-angle X-ray scattering data analysis for multilamellar vesicles: the evolution of the scattering density profile model
J. Appl. Cryst. 47, 173–180 (2014)

M. Jerčinović, N. Radić, M. Buljan, J. Grenzer, I. Delač Marion, M. Kralj, I. Bogdanović Radović, R. Hübner, P. Dubček, K. Salamon and S. Bernstorff
Self-assembled growth of Ni nanoclusters in amorphous alumina matrix
J Nanopart Res 16, 2296 (2014)

K. Kornmueller, I. Letofsky-Papst, F. Cacho-Nerin, G. Leitinger, H. Amenitsch, R. Prassl
Self-Assembly of an Amphiphilic Designer-Peptide into Double Helical Superstructures
Biophysical Journal 106(2), 58a (2014) (Published abstract)

L. Malfatti, P. Falcaro, A. Pinna, B. Lasio, M.F. Casula, D. Loche, A. Falqui, B. Marmiroli, H. Amenitsch, R. Sanna, A. Mariani, P. Innocenzi
Exfoliated graphene into highly ordered mesoporous titania films: Highly performing nanocomposites from integrated processing
ACS Applied Materials and Interfaces, Vol. 6 - 2, pp. 795-802 (2014)

B. Marmiroli, F. Cacho-Nerin, B. Sartori, J. Pérez, H. Amenitsch
Thorough small-angle X-ray scattering analysis of the instability of liquid micro-jets in air
Journal of Synchrotron Radiation 21 (1), pp. 193-202 (2014)

M. Mozetic , K. Ostrikov , D.N. Ruzic , D Curreli , U Cvelbar , A Vesel , G Primc , M Leisch , K Jousten , O B Malyshev , J H Hendricks , L Koever , A Tagliaferro , O Conde , A J Silvestre , J Giapintzakis , M Buljan , N Radić , G Dražić , S Bernstorff , H Biederman , O Kylian , J Hanuš , S Milosevic , A Galtayries , P Dietrich , W Unger , M Lehocký , V Sedlarik , K Stana-Kleinschek , A Drmota-Petrič , J J Pireaux , J W Rogers , M Anderle
Recent advances in vacuum sciences and applications
Journal of Physics D 47 (15), article 153001 (2014)

D. Pozzi, V. Colapicchioni, G. Caracciolo, S. Piovesana, A.L. Capriotti, S. Palchetti, S. De Grossi, A. Riccioli, H. Amenitsch, A. Laganà
Effect of polyethyleneglycol (PEG) chain length on the bio-nano- interactions between PEGylated lipid nanoparticles and biological fluids: From nanostructure to uptake in cancer cells
Nanoscale 6 (5), pp. 2782-2792 (2014)

T. Rath, J. Novák, H. Amenitsch, A. Pein, E. Maier, W. Haas, F. Hofer, G. Trimmel
Real time X-ray scattering study of the formation of ZnS nanoparticles using synchrotron radiation
Materials Chemistry and Physics, Vol. 144 - 3, pp. 310-317 (2014)

K.C. Sekhar, S. Levichev, M. Buljan, S. Bernstorff, K. Kamakshi, A. Chahboun, A. Almeida, J. Agostinho Moreira, M. Pereira, M.J.M. Gomes
Effect of bi-layer ratio in ZnO/Al2O3 multilayers on microstructure and functional properties of ZnO nanocrystals embedded in Al2O3 matrix
Applied Physics A115 (1), pp. 283-289 (2014)

P. Sharifi, B. Marmiroli, B. Sartori, F. Cacho-Nerin, J. Keckes, H. Amenitsch, O. Paris
Humidity-driven deformation of ordered mesoporous silica films
Bioinspired, Biomimetic and Nanobiomaterials 3 (3), pp. 183-190 (2014)

F. Spinozzi, C. Ferrero, M.G. Ortore, A. De Maria Antolinos, P. Mariani
GENFIT: software for the analysis of small-angle X-ray and neutron scattering data of macromolecules in solution
Journal of Applied Crystallography 47 (3), pp. 1132-1139 (2014)

V. Valeš, M. Buljan, V. Janicki, S. Bernstorff, S.Mangold, Z. Siketić, O. Schneeweiss, V. Holy
Fe_2O_3/TiO_2 nanoparticles—a complex structural study
Thin Solid Films 564 (2014) 65–72

S. Vilasi, R. Carrotta, M.R. Mangione, C. Campanella, F. Librizzi, L. Randazzo, V. Martorana, A. Marino Gammazza, M.G. Ortore, A. Vilasi, G. Pocsfalvi, G. Burgio, D. Corona, A. Palumbo Piccionello, G. Zummo, D. Bulone, E. Conway de Macario, A.J. Macario, P.L. San Biagio, F. Cappello
Human Hsp60 with Its Mitochondrial Import Signal Occurs in Solution as Heptamers and Tetradecamers Remarkably Stable over a Wide Range of Concentrations.
PLoS One. 9(5):e97657. doi: 10.1371/journal.pone.0097657. eCollection 2014

International Conferences and Workshops in 2013

N. Akhtar, A. Aqeel, A. O. Polyakov, P. Rudolf and T. T. M. Palstra
A supramolecular approach to ultra-thin magnetic films
Ameland PhD Summer school, Hollum, Ameland, The Netherlands, 16-21 June 2013 (poster)

H. Amenitsch
Synchrotron Radiation – Instrumentation and Techniques
8th European NESY Winter-School & Symposium on Neutrons and Synchrotron Radiation, Planneralm, Austria, 11.3.2013 (invited lecture)

H. Amenitsch
The Austrian SAXS beamline as tool in Chemistry
Workshop "Luce di Sincrotrone e Chemistry", Trieste, Italy, 11.4.2013 (Lecture)

H. Amenitsch
Small Angle X-ray Scattering and other games
Zernike Seminars, University of Groeningen, 18.4.2013 (Lecture)

H. Amenitsch
SAXS beamline at ELETTRA and its application in aerosol research
Institutsseminar Aerosolscience, Universität Wien, Austria, 5.6.2013 (lecture)

H. Amenitsch
Chemistry at the Austrian Small Angle X-ray Scattering beamline @ELETTRA
Institutsseminar TUG Chemie, Graz, Austria, 26.6.2013 (Lecture)

H. Amenitsch, K. Kornmueller, C. Vonach, K. Gradauer, C. Mikl, F. Cacho-Nerin, G. Leitinger, R. Prassl
Small Angle Scattering Study of the self-assembly of an amphiphilic designer peptide from the monomer to a helical superstructure
Joint Annual Meeting of the Austrian Physical Society and Swiss Physical Society, JKU Linz, Austria, 3.-6.9.2013 (talk)

H. Amenitsch
SAXS and GISAXS for Biomembranes and Nanotechnology
Advanced School on Synchrotron Radiation Techniques and Nanotechnology: A Synergic Approach to Life Sciences and Medicine. Stellenbosch, Austria, 11.11.2013 (talk)

H. Amenitsch
The Austrian SAXS beamline as tool in Chemistry
Chimica e Luce di Sincrotrone. Trieste, Italy, 11.4.2013 (talk)

H. Amenitsch
ELETTRA & Beamlines
Tutorial for students from Montanuniverstät Leoben, at Elettra, Trieste, Italy, 2.4.2013 (talk)

H. Amenitsch, B. Marmiroli, B. Sartori, S. Bernstorff
The Austrian SAXS beamline at ELETTRA: Science Highlights
Workshop: "Research at European Neutron and Synchrotron facilities by Austrian researchers", Vienna, Austria, 11.11.2013 (poster)

H. Amenitsch, D. Pozzi, F. Cardarelli, F. Salomone, C. Marchini, G. Caracciolo
Effect of cholesterol on the transfection efficiency of DOTAP-containing lipoplexes
Nanotechnology Conference and Expo, NSTI-Nanotech 2013, Washington, DC, USA, 12-15.5.2013

H. Amenitsch, P. Sharifi, B. Marmiroli, B. Sartori, F. Cacho-Nerin, C. Ganser, C. Teichert, E. Martinelli, A. Weinberg, O. Paris
A bioinspired microactuator based on humidity driven bending of a nanoporous bilayer structure
Graz, Austria, 6.11.2013 (talk)

S. Bernstorff
Small Angle X-ray Scattering (SAXS) in materials and environmental science
Advanced school on "Application of synchrotron techniques in environmental science", ICTP, Trieste, Italy, 19 April 2013 (invited lecture)

S. Bernstorff, D. Gracin, K. Juraić, A. Gajović, D. Meljanac, P. Dubček, A. Drašner and M. Čeh
The influence of thermal treatment on the structural and optical properties of amorphous-nano-crystalline thin Si films
19th International Vacuum Congress IVC-19, International conference on Nanoscience and Technology ICNT 2013, Paris, France, 9-13.September 2013 (talk)

A. Bonasera
Perylene Core-Based Derivatives: Towards Applications in Electronic Devices
Nanosolar Project meeting, Grado, Italy, 28-30.1.2013

M. Buljan
Self-assembly of semiconductor quantum dots in amorphous dielectric matrices
19th International Vacuum Congress IVC-19, International conference on Nanoscience and Technology ICN=T 2013, Paris, France, 9-13. September 2013 (invited talk)

M. Buljan
Grazing incidence small angle x-ray scattering-GISAXS
9th Autumn school on x-ray Scattering from Surfaces and Thin films, Smolenice, Slovakia, 25-28.09.2013 (Invited (tutorial) lecture)

M. Buljan, O. Roshchupkina, A. Šantić, V. Hol´y, C. Baehtz, N. Radić, S. Bernstorff and Joerg Grenzer
Growth of anisotropic lattice of Ge quantum dots in alumina matrix
8th Scientific meeting of Croatian Physical Society, Primosten, Croatia, 06-08.10.2013 (oral)

F. Cacho-Nerin
Recent research relevant to coherent imaging activities
Seminar talk at Diamond Light Source, UK, 9.4.2013

F. Cacho-Nerin
Recent research relevant to the Hard X-ray Nanoprobe beamline
Seminar talk at Diamond Light Source, UK, 9.5.2013

C. Carboni, D. Carboni, D. Jozic, S. Bernstorff and M. Rappolt
Synchrotron X-ray investigation of the layer spacing in a series of low molar mass bi-mesogen organosiloxane smectic materials
XX Conference on "Liquid Crystals Chemistry, Physics and Applications", 15-20.9.2013, Mikołajki, Poland

G. Cordoyiannis et al.
Nanoparticle-induced and stabilized liquid-crystalline phases
Gordon Research Conference on Liquid Crystals, University of New England (ME), USA, June 16-21, 2013 (poster)

F. Di Puccio, L. Mattei, M. D'Acunto, S. Battaglia, S. Affattato, R. Ishak, S. Dinarelli, H. Amenitsch
Experimental and Numerical Analysis of UHMWPE acetabular cups after wear test: a preliminary study
World Tribology Conference 2013, Turin, Italy, 2013 (talk)

I. Delač Marion, K. Salamon, D. Grgičin, S. Bernstorff, and T. Vuletić
SAXS study of binary mixtures of DNA and HA
8th Christmas Biophysics Workshop, Dobrna, Slovenia 15-16.12.2013

P. Dubcek, B. Pivac, J. Dasovic, R. Slunjski, N. Radic, H. Zorc, S. Bernstorff
Structural investigation of Si nanoparticles embedded in oxide film
19th International Vacuum Congress IVC-19, International conference on Nanoscience and Technology ICN=T 2013, Paris, France, 9-13.September 2013 (poster)

A. Ghaffar, W. Pichl, G. Krexner, I. Zizak, S. Bernstorff and H. Amenitsch
Effects of geometrical confinement on Li and Na in nanoporous glasses
8th European NESY Winter-School & Symposium on Neutrons and Synchrotron Radiation, Planneralm, Austria, 11.3.2013 (poster)

J. Grenzer, M. Buljan, V. Holy, C. Baehtz, L. Horak, S. Bernstorff and N. Radic
In-situ real-time observation of the self-assembled growth of ordered germanium nanocrystals embedded within a dielectric matrix
11th Biennial Conference on High Resolution X-Ray Diffraction and Imaging (XTOP), Saint-Petersburg, Russia, September 15-20, 2012 (talk)

P. Heftberger, B. Kollmitzer, and G. Pabst
Advancing Global SAXS Data Analysis
8th European NESY Winter-School & Symposium on Neutrons and Synchrotron Radiation, Planneralm, Austria, 12. 03. 2013 (poster)

P. Heftberger, B. Kollmitzer, F. Heberle, J. Pan, J. Katsaras, N. Kucerka, and G. Pabst
Advancing high resolution structural analysis of lipid membranes using a genetic algorithm
9th European Biophysics Congress, Lisbon, Portugal, 15. 07. 2013 (poster)

P. Heftberger, B. Kollmitzer, F. Heberle, J. Pan, J. Katsaras, N. Kucerka, and G. Pabst
Advancing high resolution structural analysis of lipid membranes using a genetic algorithm
Joint Meeting of the Austrian and Swiss Physical Societies, Linz, Austria, 04. 09. 2013 (poster)

P. Heftberger, B. Kollmitzer, and G. Pabst
Advancing Global SAXS Data Analysis
Joint Meeting of the Austrian and Swiss Physical Societies, Linz, Austria, 04. 09. 2013 (talk)

P. Heftberger, B. Kollmitzer, F. Heberle, J. Pan, J. Katsaras, N. Kucerka, and G. Pabst
Advancing high resolution structural analysis of lipid membranes using a genetic algorithm
5th Life Science Meeting, Innsbruck, Austria, 26. 09. 2013 (poster)

P. Heftberger, B. Kollmitzer, A. Rieder, H. Amenitsch, M. Rappolt, and G. Pabst
The evolution of a high resolution global SAXS data analysis for multilamellar lipid vesicles
8th Christmas Biophysics Workshop (XBW 2013), 16. 12. 2013 (talk)

M. Jerčinović, M. Buljan, N. Radić, P. Dubček, S. Bernstorff, G. Dražić, D. Pajić and K. Zadro
Self-organization of nickel nanoparticles in dielectric matrices
19th International Vacuum Congress, Paris, France, September 9-13, 2013 (poster)

M. Jerčinović, M. Buljan, N. Radić, P. Dubček, S. Bernstorff, G. Dražić, D. Pajić and K. Zadro
Self-organization of nickel nanoparticles in dielectric matrices
20th International Scientific Meeting on Vacuum Science and Technologies, Jeruzalem, Ljutomersko-Ormoške gorice, Slovenija, May 9-10, 2013 (poster)

B. Kollmitzer, P. Heftberger, M. Rappolt and G. Pabst
Spontaneous curvature of liquid ordered lipid domains
8th European NESY Winter-School & Symposium on Neutrons and Synchrotron Radiation, Planneralm, Austria, 11.3.2013 (talk)

B. Kollmitzer, P. Heftberger, G. Khelashvili, D. Harries and G. Pabst
Protein partitioning in liquid-ordered (Lo)/liquis-disordered (Ld) domains
9th European Biophysics Congress, Lisbon, Portugal, 15. 07. 2013 (poster)

B. Kollmitzer, P. Heftberger, G. Khelashvili, D. Harries and G. Pabst
Protein partitioning in liquid-ordered (Lo)/liquis-disordered (Ld) domains
Joint Meeting of the Austrian and Swiss Physical Societies, Linz, Austria, 04. 09. 2013 (talk)

B. Kollmitzer, P. Heftberger, G. Khelashvili, D. Harries and G. Pabst
Protein partitioning in liquid-ordered (Lo)/liquis-disordered (Ld) domains
8th Christmas Biophysics Workshop (XBW 2013), 16. 12. 2013 (talk)

K. Kornmüller
Self-Assembly and Applications of Amphiphilic Designer-Peptides
PhD Seminar, Graz, Austria, 10. 1. 2013 (talk)

K. Kornmüller
Self-assembly of an amphiphilic designer peptide into a double helix superstructure revealed by Synchrotron SAXS
PhD Seminar, Graz, Austria, 16. 5. 2013 (talk)

K. Kornmüller, C. Vonach, F. Cacho-Nerin, C. Mikl, H. Amenitsch and R. Prassl
*Amphiphilic Designer-Peptides Explored as **D**etergents to Solubilize and **S**tabilize Apolipoprotein B-100*
Instruct Biennial Structural Biology Meeting**,** EMBL Advanced Training Centre, Heidelberg, Germany**,** 22-24 May 2013 (poster)

K. Kornmüller, C. Vonach, K. Gradauer, F. Cacho-Nerin, C. Mikl, G. Leitinger, H. Amenitsch and R. Prassl
Double helical superstructures from the self-assembly of an amphiphilic designer-peptide – a Synchrotron SAXS study
DocDay 10, Graz, Austria, 12.7.2013 (poster, received a Poster Presentation Award)

K. Kornmüller, F. Cacho-Nerin, G. Leitinger, H. Amenitsch, and R. Prassl
Double helix superstructures from the self-assembly of an amphiphilic designer-peptide revealed by Synchrotron SAXS
ÖGMBT Annual Meeting 2013, Innsbruck, Austria, 25. – 27. 09. 2013 (poster)

Kornmüller, K.; Vonnach, C.; Gradauer, K.; Mikl, C.; Cacho-Nerin, F.; Leitinger, G.; Amenitsch, H.; Prassl, R.:
Small Angle Scattering Study of the self-assembly of an amphiphilic designer peptide from the monomer to a helical superstructure
ÖEPG Linz, Austria, 3.09.2013 (talk)

Rainer T. Lechner
In-situ synchrotron SAXS studies on Colloidal Nanocrystal Formation
Annual Meeting of the Oesterreichischen Physikalischen Gesellschaft, Linz, Austria, 03. - 06. September 2013 (talk)

D. Lombardo, L. Bonaccorsi , P. Calandra, M.A. Kiselev, E. Proverbio
Dendrimer-based Host/Guest Systems for Drug Delivery
Workshop on Biomaterials and their Interactionswith Biological and Model membranes, Salou, Spain 24-26 February 2013 (poster)

A. Magerl, A. Schiener, H. Amenitsch, N. Kirby
Nucleation and Growth Observed by Ultrafast SAXS and WAXS
The 8th Pacific Rim International Congress on Advanced Materials and Processing (PRICM-8), Waikoloa, Hawaii, USA, August 4-9, 2013

M. Manno
Electrostatic repulsion mimics crowding and selects the fibrillation pathways in fibril-forming protein solutions
Int. conference on "Macromolecular crowding effects in cell biology: models and experiments", Orléans, France, October 24-25, 2013 (invited lecture)

F. Marino
The N-terminus of human and Xenopus RecQ4 contain a putative zinc-knuckle domain
SIBBM meeting, Pavia, Italy, June 2013 (poster)

F. Marino
Structural studies on RecQ4 helicase
Cold Spring Harbour meeting, Cold Spring Harbour, NY, USA, September 2013 (poster)

B. Marmiroli
Deep X-RAY Lithography for chemistry and materials science
DÖF MHC6 meeting, Bonn, Germany, 5.4.2013 (talk)

B. Marmiroli
Combining Small Angle X-ray Scattering and Deep X-Ray Lithography for material science
Materials Day 2013, Graz, Austria, 24.10.2013 (talk)

B. Marmiroli, P. Falcaro, L. Malfatti, S.H. Han, A. Pinna, L.F. Dumee, P. Innocenzi, H. Amenitsch
Radiation assisted material synthesis and processing by deep X-ray lithography
Annual Meeting of the Austrian Physical Society, Linz, Austria, 3. - 6. September 2013 (talk)

B. Marmiroli and H. Amenitsch
Combining deep X-ray lithography and small angle X-ray scattering for biology and material science
XCIX Congresso Nazionale Societá italiana di fisica, Trieste, 23-27.9.2013 (talk)

B. Marmiroli, L. Malfatti, L.F. Dumee, S.H. Han, P. Innocenzi, P. Falcaro, H. Amenitsch
Deep X-ray Lithography for Material Science
Nanotech Italy 2013, Venezia, Italy, 27.11.2013 (poster)

B. Marmiroli, P. Falcaro, L. Malfatti, M. Faustini, C.M. Doherty, D. Grosso, P. Innocenzi, H. Amenitsch
Materials synthesis and processing by deep X-ray lithography
HARMNST 2013 (10th International Workshop on High Aspect Ratio Micro and Nano System Technology), Berlin, Germany, 21.04.2013 (poster)

B. Marmiroli, P. Falcaro, L. Malfatti, S.H. Han, L.F. Dumee, C.M. Doherty, P. Innocenzi, H. Amenitsch
Deep X-ray Lithography for Biology and Material Science
NESY meeting 2013, Vienna, Austria, 11.11.2013 (poster)

B. Medagli
MCM2-7 vs MCM8-9: same family but different stories
SIBBM meeting, Pavia, Italy, June 2013 (poster)

O. Milat, K. Salamon, Z. Kovačević, P. Dubček, M. Jerčinović and N. Radić
Morphology and Structure of Sputtered W Thin Films
19th International Vacuum Congress, Paris, France, September 9-13, 2013 (poster)

A. Mojumdar
Structural insight into RecQ4 helicases
Symposium in honor of Prof. Rudy Ledeistein, Stockholm, Sweden, May 2013 (Invited Speaker)

J. Novak, R. Banerjee, Y. Busby, D. Soraruf, H. Amenitsch, G. Casula, P. Cosseddu, S. Nau, S. Sax, E.J.W. List-Kratochvil, A. Bonfiglio, J.-J. Pireaux, and F. Schreiber
X-ray structural characterization of hybrid thin films for non-volatile memory elements
Seminar presentations at Semestrial HYMEC meeting (EU project FP7-NMP-2010-SMALL-4 program, project number 263073), Namur, Belgium, 10. 4. 2013

S. Onesti
Synchrotron radiation in structural biology: unravelling the molecular basis of DNA replication
Iranian Light Source Facility 5th User meeting, Qazvin, Iran, February 2013 (Invited Speaker)

G. Pabst
Physics of cell communication
Montan Universität Leoben, Leoben, Austria, 22. 1. 2013

G. Pabst
Biomembrane physics of cellular signaling
Oak Ridge National Laboratories, Oak Ridge, TN, USA, 29. 1. 2013

G. Pabst
Biomembrane physics of cellular signaling
Stony Brook University,Stony Brook, NY, USA, 31. 1. 2013

G. Pabst
Biomembrane physics of cellular signaling
Weill Cornell Medical College, New York, NY, USA, 1. 2. 2013

G. Pabst, B. Kollmitzer, P. Heftberger, and M. Rappolt
Cholesterol stabilizes ion channel function during sphingomyelinase hydrolysis
57th Annual Meeting of the Biophysical Society, Philadelphia, PA., 2. -6. 2. 2013

G. Pabst, B. Kollmitzer, Benjamin, P. Heftberger and M. Rappolt
Cholesterol stabilizes ion channel function during sphingomyelinase hydrolysis
57th Annual Meeting of the Biophysical Society, Philadelphia, PA, 07. 02. 2013 (poster)

G. Pabst, B. Kollmitzer, P. Heftberger and M. Rappolt
Modulation of ion-channel activity by cholesterol and ceramide, 5th Life Science Meeting, Innsbruck, Austria, 26. 09. 2013 (poster)

G. Pabst, B. Kollmitzer, Benjamin, P. Heftberger and M. Rappolt
Modulation of ion-channel activity by cholesterol and ceramide
9th European Biophysics Congress, Lisbon, Portugal, 16. 07. 2013 (talk)

G. Polt, F. Spieckermann, H. Wilhelm, E. Schafler, M. Kerber and M. Zehetbauer
Investigating the Thermal Stability of Dislocations in Semicrystalline Polymers using Synchrotron Radiation
8th European NESY Winter-School & Symposium on Neutrons and Synchrotron Radiation, Planneralm, Austria, 11.3.2013 (poster)

G. Polt, F. Spieckermann, H. Wilhelm, Erhard Schafler, M.J. Zehetbauer
The thermal stability of dislocations in α - phase polypropylene
Advances in Polymer Science and Technology (APST) 3, Linz, Austria, 9-10 September 2013 (oral)

D. Pozzi, F. Cardarelli, F. Salomone, C. Marchini, H. Amenitsch, G. Caracciolo
Effect of cholesterol on the transfection efficiency of DOTAP-containing lipoplexes
2013 NSTI Nanotechnology Conference and Expo, Washington, DC, USA, 12-16 May 2013

C. Prehal, M. Yarema, H. Amenitsch, W. Heiss, O. Paris and R.T. Lechner
Self Assembling of Colloidal Nanocrystal Solids investigated by in-situ synchrotron SAXS studies
8th European NESY Winter-School & Symposium on Neutrons and Synchrotron Radiation, Planneralm, Austria, 11.3.2013 (poster)

F. Di Puccio, L. Mattei, M. D'Acunto, S. Battaglia, S. Affattato, R. Ishak, S. Dinarelli, H. Amenitsch
Experimental and Numerical Analysis of UHMWPE acetabular cups after wear test: a preliminary study
World Tribology Conference 2013, Turin, Italy, 2013

B. Sartori, B. Marmiroli, F. Cacho-Nerin and H. Amenitsch
Unveiling the architecture of mesostructures with SAXS
DOF meeting, Bonn, Germany, 5-7 April 2013 (talk)

B. Sartori, B. Marmiroli, F. Cacho-Nerin and H. Amenitsch
In-situ and ex-situ study of mesostructured silica synthesized in the gas phase
Annual Meeting of the Austrian Physical Society,, Linz, Austria, 3. - 6. September 2013 (talk)

B. Sartori, B. Marmiroli, F. Cacho-Nerin and H. Amenitsch
Investigation of hierarchical mesostructured silica synthesized in the gas phase
XCIX Congresso Nazionale della Società Italiana di Fisica, Trieste, Italy, 27.9.2013 (?talk / poster)

B. Sartori, B. Marmiroli, F. Cacho Nerin, H. Amenitsch
Investigation of hierarchical mesostructured silica synthesized in the gas phase
Materials Day 2013, Graz, Austria, 24.10.2013 (poster)

Sartori, B.; Marmiroli, B.; Cacho Nerin, F.; Amenitsch, H.:
Investigation of Hierarchical Mesostructured Silica Synthesized in the Gas-phase
NESY Meeting 2013, Vienna, Austria, 11.11.2013 (poster)

E. Schafler, M. Kerber, R. Schuster, F. Spieckermann, H. Wilhelm, G. Polt, S. Bernstorff, M. Zehetbauer and T. Ungar
Characterisation of deformation induced microstructures by in-situ X-ray Synchrotron Bragg Profile Analysis
TMS 2013 142nd Annual Meeting & Exhibition, Symposium: Neutron and X-Ray Studies of Advanced Materials VI: Centennial and Beyond, San Antonia, Texas, US, 5.3.2013 (invited oral)

Andreas Schiener, Kerstin Willnauer and Andreas Magerl
An in-situ SAXS study on the influence of EDTA on the formation of CdS quantum dots
THERMEC 2013, Las Vegas, Nevada, USA, December 2-6, 2013 (poster)

K.C. Sekhar, S. Levichev, O. Karzazi, S. Bernstorff, S. Doyle, A. Chahboun, M.J.M. Gomes
Microstructure and optical properties of ZnOnanocrystals embedded in Al_2O_3 matrix
2nd ENURS and ESRF-Day - Meeting of Synchrotron Radiation Users from Portugal, Lisboa, 14-15th February 2013

F. Spieckermann, G. Polt, H. Wilhelm, S. Bernstorff, E. Schafler, M. Zehetbauer
In-Situ Synchrotron Multi Reflection X - ray Line Profile Analysis of Semicrystalline Polymers
NESY Workshop: Research at European Neutron and Synchrotron facilities by Austrian researchers, 11-12 November 2013, Vienna, Austria (oral)

F. Spieckermann, H. Wilhelm, G. Polt, S. Ahzi, M.J. Zehetbauer
Rate mechanism and dislocation generation in polyethylene
Advances in Polymer Science and Technology (APST) 3, Linz, Austria, 9-10 September 2013 (oral)

F. Spieckermann,
Rate mechanism and dislocation generation in polyethylene
Experimental Polymer Physics Seminar, Institue of Physics, Albert Ludwigs Universität Freiburg im Breisgau, Germany, 15 October 2013 (invited oral)

M. Svec, M. Buljan, S. Novak, R. Hrach, N. Radić, S. Bernstorff
Electrical properties of three-dimensional quantum-dot lattices in oxide matrices
EMRS Spring meeting, Strasbourg, France, May 27-31, 2013

Z. Syrgiannis, A. Sartorel, M. Carraro, H. Amenitsch, G. La Ganga, F. Puntoriero, S. Campagna, M. Bonchio, M. Prato
Synthesis of Hydrid materials with Polyoxometalates (POMs) based on Carbon Nanotubes
1st European Conference on Polyoxometalate Chemistry for Molecular Nanoscience (PoCheMoN 2013), Tenerife, Spain, 16 – 19 May 2013

Z. Syrgiannis, A. Sartorel, M. Carraro, H. Amenitsch, G. La Ganga, F. Puntoriero, S. Campagna, M. Bonchio, M. Prato
Supramolecular Nanostructures of Photosensitizer and Polyoxometalate Dyads: Structural Aspects as a Driving Force for New Routes
Nanosolar Project meeting, Grado, Italy, 28-30.1.2013

M. Trček et al.
Nanoparticle-induced liquid-crystalline phases
European Conference on Liquid Crystals, Rhodes, Greece, September 22-27, 2013 (oral)

V. Valeš, M. Buljan, S. Bernstorff, S. Mangold, V. Holy
Fe_2O_3/TiO_2 nanoparticles – a complex structural study
9th Autumn School on "X-ray Scattering from Surfaces and Thin Layers", Smolenice Castle, Slovakia, 25.-28.9.2013

F. Valle, B. Marmiroli, H. Amenitsch and R. Taccani
SAXS characterisation of proton electrolyte membrane fuel cells catalyst degradation
8th European NESY Winter-School & Symposium on Neutrons and Synchrotron Radiation, Planneralm, Austria, 11.3.2013 (poster)

S. Vilasi, R. Carrotta, M.R. Mangione, C. Campanella, F. Librizzi, V. Martorana, M.G. Ortore, A. Marino Gammazza, A. Vilasi, G. Burgio, D. Corona, G. Zummo, D. Bulone, E. Conway de Macario, A.J.L. Macario, P.L. San Biagio and F. Cappello
Naïve Hsp60, similarly to GroEL, oligomerizes to build heptameric and tetradecameric structures
VI International Congress on Stress Proteins in Biology and Medicine, Sheffield, UK, 18-22 August 2013 (poster)

A. Yaghmur
In situ forming of drug delivery systems based on lyotropic liquid crystalline phases
Lipid Minisymposium 20th June 2013, Department of Pharmacy, Copenhagen University, Denmark (Invited talk)

ELETTRA Highlights 2012-2013

L. Bonaccorsi, P. Calandra, M.A. Kiselev, H. Amenitsch, E. Proverbio and D. Lombardo
Growth of LTA zeolite nanoclusters using a block copolymer template
Elettra Research Highlight, pp. 36-37 (2012-2013)

M. Buljan, O. Roschupkina, A. Šantić, V. Holy, C. Baehtz, A. Muecklich, L. Horak, V. Valeš, N. Radić, S. Bernstorff, J. Grenzer
Growth of anisotropic Ge quantum dot lattices in alumina matrix.
Elettra Research Highlight, pp. 18-19 (2012-2013)

C.M. Doherty, Y. Gao, B. Marmiroli, H. Amenitsch, F. Lisi, L. Malfatti, K. Okada, M. Takahashi, A.J. Hill, P. Innocenzi and
P. Falcaro
Deep x ray lithography of mesoporous silica encapsulated enzymes for micro-device fabrication
Elettra Research Highlight, pp. 26-27 (2012-2013)

A. Yaghmur, B. Sartori, M. Rappolt
Control of lipid structuring by trans- and cis-fatty acids
Elettra Research Highlight, pp. 112-113 (2012-2013)

Contributions to "communicate science in public"

"Lange Nacht der Forschung" - an open day at Austrian research facilities, IBN, Graz, Austria, and Outstation (SAXS-beamline at Elettra), Trieste, Italy, 4.4.2014 (presentations life from the members of the SAXS beamline to Graz by connection via Skype).

SAXS training courses

Third tutorial on "Advanced Synchrotron Techniques at ELETTRA" (AST3 **)**
During 18. and 19.3.2013 took place at Elettra Sincrotrone Trieste the third edition of this Tutorial, coorganized again by Rainer Lechner, Oskar Paris (Montan Universität Leoben, Austria), H. Amenitsch (TU Graz, Austria) and S. Bernstorff (Elettra-Sincrotrone). During the first afternoon, the 16 students from Leoben and Graz followed a general introduction of ELETTRA, and then got a tour of ELETTRA (H. Amenitsch), FERMI (Stefano Cleva) and several beamlines. The second day was dedicated to several "hands-on experiments" performed by small groups of 4 students each at the beamlines SAXS, DXRL, XRD e XAFS. The tutors were Heinz Amenitsch, Sigrid Bernstorff (SAXS), Benedetta Marmiroli (DXRL), Luca Olivi, Giuliana Aquilanti, Antonella Iadecola (EXAFS), Giorgio Bais, Nicola Demitri, Maurizio Polentarutti (XRL).

Advanced School on "Application of Synchrotron Techniques in Environmental Science", 15-26 April 2013, Trieste. Organized by SESAME *(H. Hoorani)*, Elettra Sincrotrone Trieste *(M. Kiskinova)* and ICTP *(J. Niemela)*. Participants: scientists and students from countries which are members of the United Nations, UNESCO and/or IAEA. Also 8 scientists from Elettra gave lectures, and on 22.+ 23.4.2013 several beamlines at ELETTRA (SAXS, XRD, X-ray fluorescence, X-ray absorption spectroscopy e X-ray imaging and spectromicroscopy) offered three 3-hour practical tutorials for small student groups. Contribution from SAXS-group: one invited lecture (S. Bernstorff: "Small Angle X-Ray Scattering (SAXS) in materials and environmental science") and three practical tutorials at the SAXS-beamline (by S. Bernstorff and H. Amenitsch).

PhD Theses

Naureen Akhtar
Multifunctinal Organic-Inorganic Hybrid Films Deposited by the Langmuir-Blodgett Techinque
University of Groningen, Netherlands

Soumit Sankar Mandal
Investigations of molecular structure and function under confinement
Indian Institute of Science, Bangalore, India

K.V. Sarathlal
Preparation and study of patterned magnetic thin films
Devi Ahilya University, Indore, India

Eliana M. F. Vieira
Estruturas baseadas em nanocristais de $Si_{1-x}Ge_x$ em dielétricos com vista à aplicação em memórias
University of Minho, Braga, Portugal

Bachelor Theses

Kerstin Willnauer
Millisekunden aufgelöste SAXS Untersuchung zum Wachstum von Cadmiumsulfid Nanopartikeln
Friedrich-Schiller-Universität, Jena, Germany

Authors Index

SCIENCE ▪ PASSION ▪ TECHNOLOGY

TU Graz

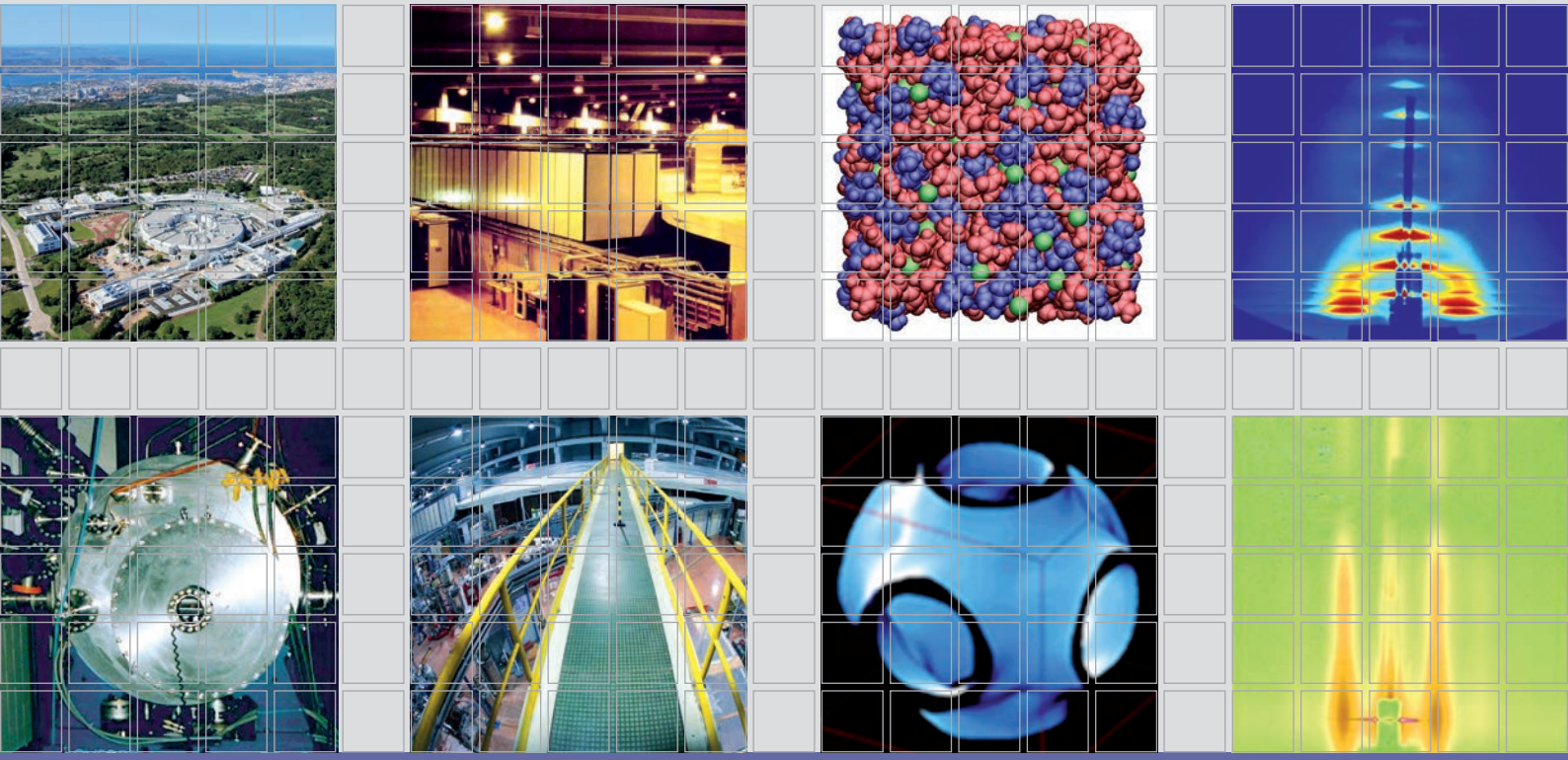

Institute of Inorganic Chemistry
Graz University of Technology
Faculty of Technical Chemistry,
Chemical and Process Engineering,
Biotechnology – TCVB
Stremayrgasse 9/IV, 8010 Graz, Austria
Tel.: +43 316 873 32145
Fax: +43 316 873 32102
E-mail: amenitsch@tugraz.at
Web: http://ac.tugraz.at

Elettra-Sincrotrone Trieste
Strada Statale 14, Km 163,5
34149 Basovizza (TS), Italy
Tel.: +39 040 375 8572
Fax: +39 040 9380 902
E-mail: bernstorff@elettra.eu
Web: www.elettra.eu

Austrian SAXS Beamline
Outstation of the Institute of
Inorganic Chemistry
Graz University of Technology
c/o Elettra-Sincrotrone Trieste
Strada Statale 14, km 163.5
34149 Basovizza (TS) Italy
E-mail: amenitsch@tugraz.at